Living Reviews in Relativity (2023)26:3
https://doi.org/10.1007/s41114-023-00044-3

REVIEW ARTICLE

Searches for continuous-wave gravitational radiation

Keith Riles[1]

Received: 13 June 2022 / Accepted: 20 February 2023

Abstract

Now that detection of gravitational-wave signals from the coalescence of extra-galactic compact binary star mergers has become nearly routine, it is intriguing to consider other potential gravitational-wave signatures. Here we examine the prospects for discovery of continuous gravitational waves from fast-spinning neutron stars in our own galaxy and from more exotic sources. Potential continuous-wave sources are reviewed, search methodologies and results presented and prospects for imminent discovery discussed.

Keywords Gravitational waves · Gravitational-wave detectors · Gravitational-wave sources

Contents

✉ Keith Riles
kriles@umich.edu

[1] Physics Department, University of Michigan, Ann Arbor, MI 48109, USA

Published online: 17 April 2023

1 Introduction

The LIGO (Aasi et al. 2015a) and Virgo (Acernese et al. 2014) gravitational wave detectors have made historic discoveries over the last seven years. The first direct detection in September 2015 of gravitational waves marked a milestone in fundamental science (Abbott et al. 2016b), confirming a longstanding prediction of Einstein's General Theory of Relativity (Einstein 1916, 1918). That the detection came from the first observation of a binary black hole merger provided a bonus not only in verifying detailed predictions of General Relativity, but in establishing unambiguously that stellar-mass black holes exist in the Universe. More than 80 binary black hole (BBH) systems have been observed since GW150914 (Abbott et al. 2016d, 2017h, i, j, 2019b, 2021e, f). Merging binary neutron star (BNS) systems (Abbott et al. 2017k, 2020a) have also been observed, including GW170817 (Abbott et al. 2017k), which was accompanied by a multitude of electromagnetic observations (Abbott et al. 2017l). Those observations confirmed the association of at least some short gamma ray bursts with binary neutron star mergers (Abbott

et al. 2017g) and the onset of kilonovae in BNS mergers that contribute substantially to the heavy element production in the Universe (Abbott et al. 2017l). More recently came detections of merging neutron star—black hole (NSBH) systems (Abbott et al. 2021g). These discoveries of transient gravitational wave signals have ignited the field of gravitational wave astronomy.

This review concerns a quite different and as-yet-undiscovered gravitational wave signal type, one defined by stability and near-monochromaticity over long time scales, namely *continuous waves*. CW signals with strengths detectable by current and imminent ground-based gravitational wave interferometers could originate from relatively nearby galactic sources, such as fast-spinning neutron stars exhibiting non-axisymmetry (Thorne 1989), or more exotically, from strong extra-galactic sources, such as super-radiant Bose–Einstein clouds surrounding black holes (Arvanitaki et al. 2010).

We already know from prior LIGO and Virgo searches that the strengths of CW signals must be exceedingly weak [$\sim 10^{-24}$ or less], which is consistent with theoretical expectation, from which we expect plausible CW strain amplitudes to be orders of magnitudes lower than the amplitudes of the transient signals detected to date [$\sim 10^{-21}$]. This disparity in signal strength holds despite the much nearer distance of galactic neutron stars ($\sim$ kpc) compared to the compact binary mergers ($\sim$ 40 Mpc to multi-Gpc) seen to date. In fact, it is only their long-lived nature that gives us any hope of detecting CW signals through integration over long data spans, so as to achieve a statistically viable signal-to-noise (SNR) ratio. As discussed below, however, that SNR increases, at best, as the square root of observation time, but for most CW searches, increases with an even lower power of observation time, while computational cost increases with much higher powers. These different scalings of signal sensitivity and cost have led to a variety of approaches in targeting signals, depending on the size of signal parameter space searched.

The search for continuous gravitational radiation has been under way since the 1970's, using data from interferometers (Levine and Stebbins 1972) and bars (Hirakawa et al. 1978; Suzuki 1995), including from early prototypes (Livas 1989) for the large gravitational wave detectors to come later. This review focuses primarily on the most recent searches from the Advanced LIGO and Virgo detectors, although summaries of search algorithm developments in the initial LIGO and Virgo era (and before) provide some historical context. For reference, the Advanced LIGO and Virgo runs to date comprise (with selected highlighted detections):

- The O1 observing run (LIGO only): September 12, 2015–January 12, 2016—First detection of gravitational waves from a BBH merger: GW150914 (Abbott et al. 2016b).
- The O2 observing run (LIGO joined by Virgo in last month): November 30, 2016–August 25, 2017—First detection of gravitational waves from a BNS merger: GW170817 (Abbott et al. 2017k).
- The O3 observing run (LIGO and Virgo): April 1, 2019–March 27, 2020—First detection of gravitational waves from the formation of an intermediate-mass black hole: GW190521 (Abbott et al. 2020d) and the first detection of NSBH mergers.

The run was divided into a 6-month "O3a" epoch (April 1, 2019–October 1, 2019) and "O3b" (November 1–March 27, 2020) by a 1-month commissioning break. Many initial publications focused on results from the O3a data.

In the following, Sect. 2 reviews both conventional and exotic potential sources of CW gravitational radiation. Section 3 describes a wide variety of search methodologies being used to address the challenges of detection. Section 4 presents results (so far only upper limits) from searches based on these algorithms, with an emphasis on the most recent results from the Advanced LIGO and Virgo detectors. Finally, Sect. 5 discusses the outlook for discovery in the coming years, including the prospects for electromagnetic observations of the continuous gravitational-wave sources. This review focuses on CW radiation potentially detectable with current-generation and next-generation ground-based gravitational-wave interferometers, which are sensitive to gravitational frequencies in the human-audible band for sound. Past and future searches for lower-frequency CW radiation from supermassive black hole binaries at $\sim$ nHz frequencies using pulsar timing arrays (Manchester 2012) or from stellar-mass galactic binaries at $\sim$ mHz frequencies using the space-based LISA (Bender et al. 1996) are not discussed here.

Textbooks addressing gravitational waves, their detection and their analysis include (Misner et al. 1972; Schutz 1985; Maggiore 2008, 2018; Saulson 2017; Creighton and Anderson 2011; Jaranowski and Królak 2009; Andersson 2019). Review articles and volumes on gravitational-wave science include (Thorne 1989; Blair et al. 1991; Sathyaprakash and Schutz 2009; Pitkin et al. 2011; Freise and Strain 2010; Blair et al. 2012; Riles 2013; Romano and Cornish 2017). This review is a substantial expansion upon a briefer previous article (Riles 2017). Other reviews of CW search methodology include (Prix 2009; Palomba 2012; Lasky 2015; Sieniawska and Bejger 2019; Tenorio et al. 2021b; Piccinni 2022).

2 Potential sources of CW radiation

In the frequency band of present ground-based detectors, the canonical sources of continuous gravitational waves are galactic, non-axisymmetric neutron stars spinning fast enough to produce gravitational waves in the LIGO and Virgo detectable band (at $1\times$, $\sim 4/3\times$ or $2\times$ rotation frequency, depending on the generation mechanism). These nearby neutron stars offer a "conventional" source of CW radiation—as astrophysically extreme as such objects are.

A truly exotic postulated source is a "cloud" of bosons, such as QCD axions, surrounding a fast-spinning black hole, bosons that can condense in gargantuan numbers to a small number of discrete energy levels, enabling coherent gravitation wave emission from boson annihilation or from level transitions. Attention here focuses mainly on the conventional neutron stars, but the exotic boson cloud scenario is also discussed.

2.1 Fast-spinning neutron stars

The following subsections give an overview of neutron star formation, structure, observables and populations, present the phenomenology of neutron-star spin-down, discuss potential sources of non-axisymmetry in neutron stars, and consider a number of particular GW search targets of interest. Although neutron stars were first postulated by Baade and Zwicky (1934) and their basic properties worked out by Oppenheimer and Volkoff (1939), the first definitive establishment of their existence came with the discovery of the first radio pulsar (Hewish et al. 1968) PSR B1919+21 in 1967 with prior theoretical support for neutron star radiation contributing to supernova remnant shell energetics (Pacini 1967) and rapid theoretical follow-up to explain the pulsation mechanism (Gold 1968; Goldreich and Julian 1969; Ruderman and Sutherland 1975).

2.1.1 Neutron star formation, structure, observables and populations

As background, this section surveys at a basic level the fundamentals of neutron star formation, structure, observables and populations. Much more detailed information can be found in the following review articles or volumes on neutron stars (Lattimer and Prakash 2001; Chamel and Haensel 2008; Becker 2009; Özel and Freire 2016), pulsars (Lorimer and Kramer 2005; Lyne and Graham-Smith 2006; Lorimer 2008), and rotating relativistic stars (Paschalidis and Stergioulas 2017).

Neutron stars are the final states of stars too massive to form white dwarfs upon collapse after fuel consumption and too light to form black holes, having progenitor masses in the approximate range 6–15 $M_\odot$ (Lyne and Graham-Smith 2006; Cerda-Duran and Elias-Rosa 2018; Stockinger et al. 2020). These remarkably dense objects, supported by neutron degeneracy pressure, boast near-nuclear densities in their crusts and well-beyond-nuclear densities in their cores. The range of densities and associated total stellar masses and radii depend on an equation of state that is not experimentally accessible in terrestrial laboratories because of the combination of high density and (relatively) low temperature. A variety of equations of state have been proposed (Lattimer and Prakash 2001), with a small subset disfavored by the measurement of neutron stars greater than two solar masses (Buballa et al. 2014), by radii of approximately ten kilometers (Miller et al. 2019b, 2021; Riley et al. 2019, 2021) and by the absence of severe tidal deformation effects in the gravitational waveforms measured for the BNS merger GW170817 (Abbott et al. 2017k, 2018c; Lim and Holt 2019; Essick et al. 2020). The detection of a $\sim$ 2.6-$M_\odot$ object in the GW190814 merger (Abbott et al. 2020e) poses a challenge to the nuclear equation of state if the object is indeed a neutron star instead of a light black hole.

In broad summary, a neutron star is thought to have a crust with outer radius between 10 and 15 km and a thickness of $\sim$ 1 km (Shapiro and Teukolsky 1983), composed near the top of a tight lattice of neutron-rich heavy nuclei, permeated by neutron superfluid. Deeper in the star, as pressure and density increase, the nuclei may become distorted and elongated, forming a "nuclear pasta" of ordered nuclei and gaps (Ravenhall et al. 1983; Caplan and Horowitz 2017). Still deeper, the pasta gives

way to a hyperdense neutron fluid and perhaps undergoes phase transitions involving hyperons, perhaps to a quark-gluon plasma, or even perhaps to a solid strange-quark core (Shapiro and Teukolsky 1983; Lattimer and Prakash 2001).

Uncertainties in equation of state lead directly to uncertainties in the expected maximum mass and radius of a neutron star (Lattimer and Prakash 2001), but theoretical prejudice is consistent with the absence of observation in binary systems of neutron star masses much higher than two solar masses (Özel and Freire 2016; Demorest et al. 2010; Arzoumanian et al. 2018; Antoniadis et al. 2013; Cromartie et al. 2020; Fonseca et al. 2021). Neutron star radii are especially challenging to measure directly, with older measurements coming from X-ray measurements, where inferences are drawn from brightness of the radiation, its temperature and distance to the source, assuming black-body radiation, with corrections for the strong space-time curvature affecting the visible surface area (Özel and Freire 2016; Degenaar and Suleimanov 2018). New measurements from the NICER X-ray satellite are improving upon the precision with which mass and radius can be determined simultaneously from individual stars, constraining more tightly the allowed equations of state (Miller et al. 2019b, 2021; Bogdanov et al. 2019a, b, 2021; Raaijmakers et al. 2019, 2021; Riley et al. 2019, 2021).

Measurements of the gravitational waveform from the binary neutron star merger GW170817 have also provided new constraints and disfavor very stiff equations of state that lead to large neutron star radii (Abbott et al. 2018c). Detection of additional binary neutron star mergers in the coming years should improve these constraints. Broadly, one expects average neutron star densities of $\sim 7 \times 10^{14}$ g cm^{-3}, well above the density of nuclear matter ($\sim 3 \times 10^{14}$) (Lorimer and Kramer 2005), with densities at the core likely above 10^{15} g cm^{-3} (Shapiro and Teukolsky 1983). See Yunes et al. (2022) for a recent review of what has been learned about the neutron star equation of state from gravitational-wave and X-ray observations. A recent Bayesian combined analysis (Huth et al. 2022) of predictions from chiral effective field theory of QCD, measured BNS gravitational waveforms, NICER X-ray observations and measurements from heavy ion (gold) collisions indicate a somewhat stiffer equation of state than previously favored and hence larger allowed radii of neutron stars.

Given the immense pressure on the nuclear matter, one expects a neutron star to assume a highly spherical shape in the limit of no rotation and, with rotation, to become an axisymmetric oblate spheroid. True axisymmetry would preclude emission of quadrupolar gravitational waves from rotation alone. Hence CW searchers count upon a small but detectable mass (or mass current) non-axisymmetry, discussed in detail in Sect. 2.1.3.

During the collapse of their slow-spinning stellar progenitors, neutron stars can acquire an impressive rotational speed as angular momentum conservation spins up the infalling matter. Even the two slowest-rotating known pulsars spin on their axes every 76 s (Caleb et al. 2022) and 24 s (Tan et al. 2018; Manchester and Hobbs 2005), implying rotational kinetic energies greater than $\sim 10^{35}$ J, and other young pulsars with spin frequencies of tens of Hz have rotational energies of $\sim 10^{43}$ J. Recycled millisecond pulsars acquire even higher spins via accretion from a binary

companion star, leading to measured spin frequencies above 700 Hz (Hessels et al. 2006; Bassa et al. 2017) and a rotational energy of $\sim 10^{45}$ J, or several percent of the magnitude of the gravitational bound energy of the star. This immense reservoir of rotational energy might appear to bode well for supporting detectable gravitational-wave emission, but vast energy is required to create appreciable distortions in highly rigid space-time. From the perspective of gravitational-wave energy density (Misner et al. 1972), one can define an effective, frequency-dependent Young's modulus $Y_{\rm eff} \sim \frac{c^2 f_{\rm GW}^2}{G}$ ($\sim 10^{31}$ Pa for $f_{\rm GW} \approx 100$ Hz, or 20 orders of magnitude higher than steel). As a result, one must tap a significant fraction of the reservoir's energy loss rate in order to produce detectable radiation, as quantified below.

Most of the $\sim$ 3300 known neutron stars in the galaxy are pulsars, detected via pulsed electromagnetic emission, primarily in the radio band, but also in X-rays and γ-rays (with a small number detected optically) (Lyne and Graham-Smith 2006; Manchester and Hobbs 2005). Pulses are typically observed at the rotation frequency of the star, as a beam of radiation created by curvature radiation (Buschauer and Benford 1976) from particles that are flung out in a plasma from the magnetic poles (misaligned with the spin axis) and accelerated transversely by the magnetic field, sweeps across the Earth once per rotation (see Melrose et al. 2021, however, for a critique of this model). A subset of neutron stars presumed to have magnetic poles tilted nearly 90 degrees from the spin axis display two distinct pulses.

Other neutron stars are known from detection of X-rays from thermal emission (heat from formation and perhaps from magnetic field decay), particularly at sites consistent with the birth locations and times of supernova remnants (Lyne and Graham-Smith 2006). Still other neutron stars are inferred from accretion X-rays observed in binary systems, particularly low-mass X-ray binaries with accretion disks (Lyne and Graham-Smith 2006), although some accreting binaries with compact stars contain black holes, such as the high-mass X-ray binary Cygnus X-1. Figure 1 shows nearly the entire population of currently known pulsars (Manchester and Hobbs 2005) with spin period P shorter than 20 s[1] in the P–$\dot{P}$ plane, where $\dot{P}$ is the first time derivative of the period. Red triangles show isolated pulsars, and blue circles show binary pulsars.

Neutron stars have strong magnetic field intensities as a natural result of their collapse. If the magnetic flux is approximately conserved, the reduction of the outer surface of the star to a radius of $\sim$ 10 km ensures a static surface field far higher than achievable in a terrestrial laboratory (Pacini 1967), with inferred values (see below) ranging from 10^8 G to more than 10^{15} G (Lyne and Graham-Smith 2006). The strongest fields are seen in so-called "magnetars," young neutron stars with extremly rapid spin-down, for which dynamo generation is also likely relevant (Guilet and Müller 2015; Mösta et al. 2015). Both in young pulsars and in binary millisecond pulsars, there is reason to believe that stronger magnetic fields are "buried" in the star from accreting plasma (Payne and Melatos 2004), although the burial mechanism is not confidently understood (Chevalier 1989; Geppert et al. 1999; Lyne and Graham-

[1] The longest known pulsation period is 76 s from the recently discovered PSR J0901-4046 (Caleb et al. 2022), which also displays unusual pulse length and variability and which may represent a new pulsar class.

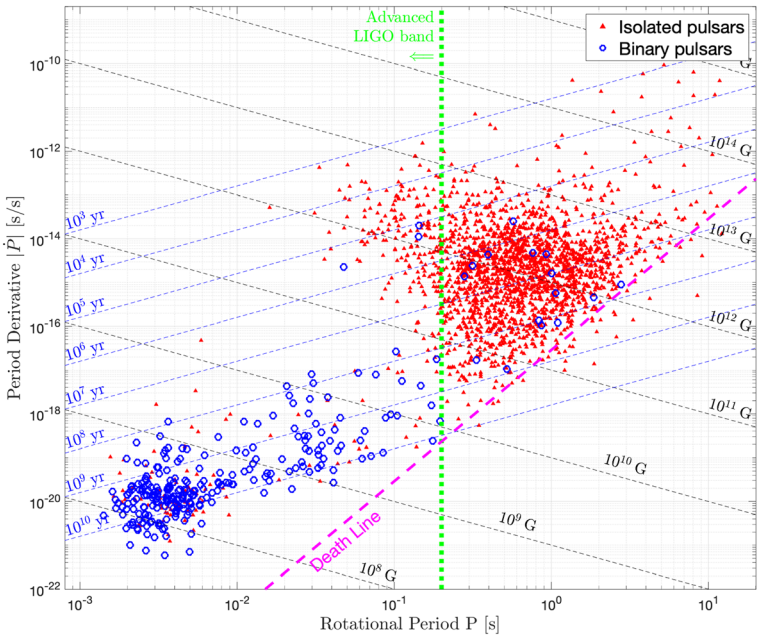

Fig. 1 Measured rotational periods and period derivatives for known pulsars. Closed red triangles indicate isolated stars. Open blue circles indicate binary stars. The vertical dotted line denotes the approximate sensitivity band for Advanced LIGO at design sensitivity ($f_{\rm GW} > 10$ Hz, assuming $f_{\rm GW} = 2f_{\rm rot}$). A similar band applies to design sensitivities of the Advanced Virgo and KAGRA detectors (Abbott et al. 2020b)

Smith 2006; Bernal et al. 2010). It has been suggested there is evidence in at least some pulsars for slowly re-emerging (strengthening) magnetic field (Ho 2011; Espinoza et al. 2011). Energy density deformation from a potentially non-axisymmetric buried field is another potential source of GW emission (Bonazzola and Gourgoulhon 1996). See Cruces et al. (2019) for a discussion of magnetic field decay preceding the accretion stage.

In principle, there should be $\sim 10^{8-9}$ neutron stars in our galaxy (Narayan 1987; Treves et al. 2000). That only a small fraction have been detected is expected, for several reasons. Radio pulsations require high magnetic field and rotation frequency. Early studies (Goldreich and Julian 1969; Sturrock 1970; Ruderman and Sutherland 1975; Lorimer and Kramer 2005) implied the relation

$$B \cdot f_{\rm rot}^2 > 1.7 \times 10^{11}\,{\rm G} \cdot ({\rm Hz})^2, \tag{1}$$

based on a model of radiation dominated by electron-positron pair creation in the stellar magnetosphere, a model broadly consistent with empirical observation, although the resulting "death line" (see Fig. 1) in the plane of period and period derivative is perhaps better understood to be a valley (Chen and Ruderman 1993; Zhang et al. 2000; Beskin and Litvinov 2022; Beskin and Istomin 2022).

The death line can be understood qualitatively from the following argument. The rotating magnetic field of a neutron star creates a strong electric field that pulls

charged particles from the star, forming a plasma with charge density ρ_0 that satisfies (SI units): (Chen and Ruderman 1993)

$$\rho_0 = -\epsilon_0 \nabla \cdot \left[(\vec{\Omega} \times \vec{r}) \times \vec{B}(\vec{r}) \right] \tag{2}$$

$$\approx -2\epsilon_0 \vec{\Omega} \cdot \vec{B}(\vec{r}), \tag{3}$$

where $\vec{\Omega}$ is the angular velocity of the star, and $\vec{B}$ is the local magnetic field at location $\vec{r}$ with respect to the star's center. In steady-state equilibrium, one expects $\vec{E} \cdot \vec{B} \approx 0$ since free charges can move along B-field lines. In so-called "gaps," however, where the plasma density is low, a potential difference large enough to produce spontaneous electron-positron pair production can lead to radio-frequency synchrotron radiation as the accelerated particles encounter curved magnetic fields. This emission is thought to account for most radio pulsations (Lyne and Graham-Smith 2006), where an "inner gap" refers to a region just outside the magnetic poles above the star's surface, and an "outer gap" refers to a region where a nominally dipolar magnetic field is approximately perpendicular to the rotation direction, separating regions of proton and electron flow from the star to the region beyond the "light cylinder," defined by the cylindrical radius at which a co-rotating particle in the magnetosphere must travel at the speed of light. For the inner gap to have a voltage drop high enough to induce an amplifying cascade of pair production leading to coherent radio wave emission imposes a minimum value on the gap potential difference ΔV which, in general, can be approximated by (SI units): (Goldreich and Julian 1969; Sturrock 1970; Ruderman and Sutherland 1975; Chen and Ruderman 1993)

$$\Delta V \sim \frac{B\Omega^2 R^3}{2c}, \tag{4}$$

where R is the neutron star radius, leading (in a more detailed calculation) to Eq. (1) and via magnetic dipole emission assumptions (see Sect. 2.1.2) to the death line shown in Fig. 1 (but see Smith et al. 2019 for evidence of selection effects and Pétri 2019 for a discussion of potentially important effects from higher order multipoles). Presumably, the vast majority of neutron stars created in the galaxy's existence to date are now to the right of the line. Additional negative-sloped dashed lines in the figure indicate different nominal magnetic dipole field strengths and positive-sloped dashed lines indicate different nominal ages, based on observed present-day periods and period derivatives $P/(2\dot{P})$ (see Sect. 2.1.2).

Two distinct major pulsar populations are apparent in Fig. 1, defined by location in the diagram. The bulk of the population lies above and to the right of the line corresponding to $B \sim 10^{11}$ G. The bulk also lies above and to the left of the line corresponding to ages younger than $\sim 10^8$ years. Assuming a star's magnetic field strength is stable, stars are expected to migrate down to the right along the B-field contours. Isolated pulsars seem to have typical pulsation lifetimes of $\sim 10^7$ years (Lyne and Graham-Smith 2006), after which they become increasingly difficult to observe in radio. On this timescale, they also cool to where thermal X-ray emission is

difficult to detect (Potekhin et al. 2015). There remains the possibility of X-ray emission from steady accretion of interstellar medium (ISM) (Ostriker et al. 1970; Blaes and Madau 1993), but it appears that the kick velocities from birth highly suppress such accretion (Hoyle and Lyttleton 1939; Bondi and Hoyle 1944) which depends on the inverse cube of the star's velocity through the ISM, and steady-state X-ray emission from accretion onto even slow-moving neutron stars can be highly suppressed, consistent with non-observation to date of such accretion (Popov et al. 2015).

The remaining population, in the lower left of the figure, is characterized by shorter periods and smaller period derivatives. These are so-called "millisecond pulsars" (MSPs), thought to arise from "recycling" of rotation speed due to accretion of matter from a binary companion. MSPs are stellar zombies, brought back from the dead with immense rotational energies imparted by infalling matter (Alpar et al. 1982; Radhakrishnan and Srinivasan 1982). The rotation frequencies achievable through this spin-up are impressive—the fastest known rotator is PSR J1748 −2446ad at 716 Hz (Hessels et al. 2006). One progenitor class for MSPs is the set of low mass X-ray binaries (LMXBs) in which the neutron star ($\sim$ 1.4 $M_\odot$) has a much lighter companion ($\sim$ 0.3 $M_\odot$) (Lyne and Graham-Smith 2006) that overfills its Roche lobe, spilling material onto an accretion disk surrounding the neutron star or possibly spilling material directly onto the star, near its magnetic polar caps. When the donor companion star eventually shrinks and decouples from the neutron star, the neutron star can retain a large fraction of its maximum angular momentum and rotational energy. Because the neutron star's magnetic field decreases during accretion (through processes that are not well understood), the spin-down rate after decoupling can be very small. The minority of MSPs that are isolated are thought to have lost their one-time companions via consumption and ablation. A bridging class called "black widows" and "redbacks" refer to binary systems with actively ablating companions, such as B1957+20 (Fruchter et al. 1988; Strader et al. 2019; Roberts and van Leeuwen 2013), where black widows denote the extreme subclass with companion masses below 0.1 $M_\odot$ (Roberts and van Leeuwen 2013).

A nice confirmation of the link between LMXBs and recycled MSPs comes from "transitional millisecond pulsars" (tMSPs) in which accreting LMXB behavior alternates with detectable radio pulsations. The first tMSP found was PSR J1023+0038 (Bond et al. 2002; Thorstensen and Armstrong 2005; Archibald et al. 2009), with two more systems since detected (Weltevrede et al. 2018). The nominal ages of MSPs extend beyond 10^{10} years, that is, some have apparent ages greater than that of the galaxy (or even that of the Universe). One possible explanation of this anomaly is reverse-torque spin-down during the Roche decoupling phase (Tauris 2012), although a recent numerical study suggests a more complex frequency evolution before and during the decoupling (Bhattacharyya 2021).

An obvious pattern in Fig. 1, consistent with the recycling model, is the higher fraction of binary systems at lower periods. For example, binary systems account for 3/4 of the lowest 200 pulsar periods (below $\sim$ 4 ms).

Aside from the disappearance of stars from this diagram as they evolve toward the lower right and cease pulsations, there are also strong selection effects that suppress

the visible population. We observe pulsars only if their radiation beams cross the Earth, only if that radiation is bright enough to be seen in the observing band, and only if the radiation is not sufficiently absorbed, scattered or frequency-dispersed to prevent detection with current radio telescopes. When the Square Kilometer Array project comes to fruition in the late 2020's, it is estimated that the current known population of pulsars will grow tenfold (Kramer and Stappers 2015).

2.1.2 Neutron star spin-down phenomenology and mechanisms

Nearly every known pulsar is observed to be spinning down, that is, to have a negative rotational frequency time derivative, implying loss of rotational kinetic energy. As discussed below in detail, there are many physical mechanisms, electromagnetic and gravitational, that can lead to this energy loss. For CW signal detection we want a gravitational-wave component, but there is good reason to believe that electromagnetic processes dominate for nearly every known pulsar.

A convenient and commonly used phenomenological model for spin-down is a power law:

$$\dot{f} = Kf^n, \tag{5}$$

where f is the star's instantaneous frequency (rotational $f_{\rm rot}$ or gravitational: $f_{\rm GW} \propto f_{\rm rot}$), $\dot{f}$ is the first time derivative, and K is a negative constant for all but a handful of stars (thought to be experiencing large acceleration toward us because of nearness to a deep gravitational well, such as in the core of a globular cluster). The exponent n depends on the spin-down mechanism and is known as the *braking index*. The four most common theoretical braking indices discussed in the literature are the following:

- $n = 1$—"Pulsar wind" (extreme model)
- $n = 3$—Magnetic dipole radiation
- $n = 5$—Gravitational mass quadrupole radiation ("mountain")
- $n = 7$—Gravitational mass current quadrupole radiation (r-modes).

In principle, other oscillation modes that can generate gravitational waves are also possible, but the $n = 5$ and $n = 7$ modes discussed below are thought to be the most promising.

Assuming the same power law has applied since the birth of the star, the age τ of the star can be related to its birth rotation frequency f_0 and current frequency f by ($n \neq 1$):

$$\tau = -\left[\frac{f}{(n-1)\dot{f}}\right]\left[1 - \left(\frac{f}{f_0}\right)^{(n-1)}\right], \tag{6}$$

and in the case that $f \ll f_0$,

$$\tau \approx -\left[\frac{f}{(n-1)\dot{f}}\right]. \tag{7}$$

A common baseline assumption in radio pulsar astronomy is that the braking index is $n = 3$ from which the nominal magnetic dipole age of a star can be defined

$$\tau_{\rm mag} \equiv -\frac{f}{2\dot{f}}, \tag{8}$$

again, under the assumption $f \ll f_0$.

From the more generic power-law spin-down model (Eq. (5)), the 2nd frequency derivative can be written:

$$\ddot{f} = nKf^{n-1}\dot{f} = nK^2 f^{2n-1}, \tag{9}$$

from which the current braking index can be determined if the spin frequency's 2nd time derivative can be measured reliably:

$$n = \frac{f\ddot{f}}{\dot{f}^2}. \tag{10}$$

Before examining the empirical measurements of the braking indices, which are mostly inconsistent with $n = 3$, let's briefly review spin-down mechanisms with well defined braking indices, when dominant. For GW radiation spin-down dominance, related "spin-down" limits on strain amplitude will also be presented.

2.1.2.1 "Pulsar wind" ($n = 1$) Early on in pulsar astronomy (Michel 1969; Michel and Tucker 1969) it was recognized that the streaming of relativistic particles (electrons and positrons mainly, with some ions) away from the magnetosphere of a fast-spinning neutron star would lead to a spin-down torque that could, in principle, rival that from magnetic dipole radiation, in addition to distorting the shape of the magnetic field lines and affecting the dipole radiation (Gaensler and Slane 2006). In this perhaps too-simple model, the spin-down is dominated by a braking torque from a return current (predominantly counter-flowing electrons and positrons) crossing magnetic field lines in the polar cap regions of the star (Contopoulos et al. 1999), leading to a braking index of one. A more recent study of magnetar spin-down (Harding et al. 1999) considered a model with sporadic high winds following bursts, with magnetic dipole emission dominating spin-down between bursts. In the steady state, however, considering the interaction of the magnetic field and the plasma of the magnetosphere, both magnetic dipole emission and pulsar wind contributions tend to yield a braking index of about three (Michel and Li 1999; Spitkovsky 2004), discussed next. A phenomenological model (Melatos 1997) that is a variant of the vacuum dipole mode, featuring an inner magnetosphere strongly coupled to the star, accounts successfully for the braking indices of the Crab and other young pulsars with $n < 1$.

2.1.2.2 Magnetic dipole ($n = 3$) The radiation energy loss due to a rotating magnetic dipole moment is (Pacini 1968)

$$\left(\frac{dE}{dt}\right)_{\rm mag} = -\frac{\mu_0 M_\perp^2 \omega_{\rm rot}^4}{6\pi c^3}, \tag{11}$$

where $\omega_{\rm rot}$ is the rotational angular speed and $M_\perp$ is the component of the star's magnetic dipole moment perpendicular to the rotation axis (taken to be the z axis): $M_\perp = M\sin(\alpha)$, with α the angle between the axis and north magnetic pole.

In a pure dipole moment model, the magnetic pole field strength at the surface is $B_0 = \mu_0 M / 2\pi R^3$. Equating the radiation energy loss to that of the (Newtonian) rotational energy $\frac{1}{2} I_{zz}\omega_{\rm rot}^2$ leads to the prediction:

$$\frac{d\omega_{\rm rot}}{dt} = -\frac{2\pi}{3}\frac{R^6}{\mu_0 c^3 I_{zz}} B_\perp^2 \omega_{\rm rot}^3. \tag{12}$$

Hence the magnetic dipole spin-down rate is proportional to the square of $B_\perp = B_0\sin(\alpha)$ and to the cube of the rotation frequency, giving $n = 3$.

2.1.2.3 Gravitational mass quadrupole ("mountain", $n = 5$) Let's now consider the gravitational radiation one might expect from these stars. It is conventional to characterize a star's mass quadrupole asymmetry by its equatorial ellipticity:

$$\epsilon \equiv \frac{|I_{xx} - I_{yy}|}{I_{zz}}. \tag{13}$$

An oblate spheroid naturally has a polar ellipticity, but in the absence of precession,[2] such a deformation does not lead to GW emission. Henceforth "ellipticity" will refer to equatorial ellipticity, often attributed to a "mountain". For a star at a distance d away and spinning about the approximate symmetry axis of rotation (z), (assumed optimal—pointing toward the Earth), then the expected intrinsic strain amplitude h_0 is

$$h_0 = \frac{4\pi^2 G \epsilon I_{zz} f_{\rm GW}^2}{c^4 d} \tag{14}$$

$$= (1.1\times 10^{-24})\left(\frac{\epsilon}{10^{-6}}\right)\left(\frac{I_{zz}}{I_0}\right)\left(\frac{f_{\rm GW}}{1\,{\rm kHz}}\right)^2\left(\frac{1\,{\rm kpc}}{d}\right), \tag{15}$$

where $I_0 = 10^{38}\,{\rm kg}\cdot{\rm m}^2 (10^{45}\ {\rm g}\cdot{\rm cm}^2)$ is a nominal moment of inertia of a neutron star used throughout this article, and the gravitational radiation is emitted at frequency $f_{\rm GW} = 2 f_{\rm rot}$. The total power emission in gravitational waves from the star (integrated over all angles) is

[2] Free precession of an oblate neutron star can lead to gravitational radiation at the rotation frequency (Zimmermann and Szedenits 1979), but there is little empirical evidence for such precession in pulsars and good reason to expect that such precession would be rapidly damped by internal dissipation (Jones and Andersson 2002).

$$\frac{dE}{dt} = -\frac{32}{5}\frac{G}{c^5} I_{zz}^2 \epsilon^2 \omega_{\rm rot}^6 \tag{16}$$

$$= -(1.7 \times 10^{33}\,{\rm J/s})\left(\frac{I_{zz}}{I_0}\right)^2 \left(\frac{\epsilon}{10^{-6}}\right)^2 \left(\frac{f_{\rm GW}}{1\,{\rm kHz}}\right)^6. \tag{17}$$

Equating this loss to the reduction of rotational kinetic energy $\frac{1}{2} I_{zz} \omega_{\rm rot}^2$ leads to the spin-down relation:

$$\dot{f}_{\rm GW} = -\frac{32\,\pi^4}{5}\frac{G}{c^5} I_{zz} \epsilon^2 f_{\rm GW}^5 \tag{18}$$

$$= -(1.7 \times 10^{-9}\,{\rm Hz/s})\left(\frac{\epsilon}{10^{-6}}\right)^2 \left(\frac{f_{\rm GW}}{1\,{\rm kHz}}\right)^5, \tag{19}$$

in which the braking index of 5 is apparent.

For an observed neutron star of measured f and $\dot{f}$, one can define the "spin-down limit" on maximum allowed strain amplitude by equating the power loss in Eq. (16) to the time derivative of the (Newtonian) rotational kinetic energy: $\frac{1}{2} I_{zz} \omega_{\rm rot}^2$, as above for magnetic dipole radiation. One finds:

$$\begin{aligned} h_{\rm spin-down} &= \frac{1}{d}\sqrt{-\frac{5}{2}\frac{G}{c^3} I_{zz} \frac{\dot{f_{\rm GW}}}{f_{\rm GW}}} \\ &= (2.6 \times 10^{-25})\left[\frac{1\,{\rm kpc}}{d}\right]\left[\left(\frac{1\,{\rm kHz}}{f_{\rm GW}}\right)\left(\frac{-\dot{f_{\rm GW}}}{10^{-10}\,{\rm Hz/s}}\right)\left(\frac{I_{zz}}{I_0}\right)\right]^{\frac{1}{2}}. \end{aligned} \tag{20}$$

Hence for each observed pulsar with a measured frequency, spin-down and distance d, one can determine whether or not energy conservation even permits detection of gravitational waves in an optimistic scenario. Unfortunately, nearly all known pulsars have strain spin-down limits below what can be detected by the LIGO and Virgo detectors at current sensitivities, as detailed below.

2.1.2.4 Gravitational mass current quadrupole (*r*-modes, $n = 7$) Different frequency scalings apply to mass quadrupole and mass current quadrupole emission. The most promising source of the mass current non-axisymmetry in neutron stars is thought to be "*r*-modes," due to fluid motion of neutrons (or protons) in the crust or core of the star. Like jet streams in the Earth's atmosphere that manifest Rossby waves, these currents are deflected by Coriolis forces, giving rise to spatial oscillations (Andersson 1998; Bildsten 1998; Friedman and Morsink 1998; Owen et al. 1998). These *r*-modes can be inherently unstable, arising from azimuthal interior currents that are retrograde in the star's rotating frame, but which are prograde in an external reference frame. As a result, the quadrupolar gravitational-wave emission due to these currents leads to an *increase* in the strength of the current. This positive-feedback loop leads to a potential intrinsic (Chandrasekhar–Friedman–Schutz; Chandrasekhar 1970; Friedman and Schutz 1978) instability. The

frequency of such emission is expected to be a bit more than approximately 4/3 the rotation frequency (Andersson 1998; Bildsten 1998; Friedman and Morsink 1998; Owen et al. 1998; Kojima 1998; Caride et al. 2019).

Following the notation of Owen (Owen 2010; Caride et al. 2019), the mass current can be treated as due to a velocity field perturbation δv_j, integration over which leads to the following expression for the intrinsic strain amplitude seen at a distance d:

$$h_0 = \sqrt{\frac{512\,\pi^7}{5}}\frac{G}{c^5}\frac{1}{d}f_{\rm GW}^3\alpha M R^3\tilde{J} \tag{21}$$

$$= 3.6\times10^{-26}\left(\frac{1\,\mathrm{kpc}}{d}\right)\left(\frac{f_{\rm GW}}{100\,\mathrm{Hz}}\right)^3\left(\frac{\alpha}{10^{-3}}\right)\left(\frac{R}{11.7\,\mathrm{km}}\right)^3, \tag{22}$$

where α is the dimensionless r-mode amplitude, M is the stellar mass, R its radius, and $\tilde{J}$ is a dimensionless functional of the stellar equation of state, which for a Newtonian polytrope with index 1 gives $\tilde{J}\approx .0164$ (Owen 2010), assumed in the fiducial Eq. (22).

The energy loss in this model is (Thorne 1980; Owen 2010)

$$\frac{dE}{dt} = -\frac{1024\,\pi^9}{25}\frac{G}{c^7}f_{\rm GW}^8\alpha^2M^2R^6\tilde{J}^2. \tag{23}$$

Equating this loss to the reduction of rotational kinetic energy $\frac{1}{2}I_{zz}\omega_{\rm rot}^2$, as above, leads to the spin-down relation:

$$\dot{f}_{\rm GW} = -\frac{4096\,\pi^7}{225}\frac{G}{c^7}\frac{M^2R^6\tilde{J}^2}{I_{zz}}\alpha^2f_{\rm GW}^7 \tag{24}$$

$$= -9.0\times10^{-14}\,\mathrm{Hz/s}\left(\frac{R}{11.7\,\mathrm{km}}\right)^6\left(\frac{\alpha}{10^{-3}}\right)^2\left(\frac{f_{\rm GW}}{100\,\mathrm{Hz}}\right)^7, \tag{25}$$

in which the braking index of 7 is apparent.

As before, one can define a spin-down limit, but one based on pure r-mode radiation:

$$h_{\rm spin-down} = \frac{1}{r}\sqrt{-\frac{45}{8}\frac{G}{c^3}I_{zz}\frac{\dot{f}_{\rm GW}}{f_{\rm GW}}}, \tag{26}$$

where the ratio of this spin-down limit to the one given in Eq. (20) is 3/2, which arises simply from the different ratios of GW signal frequency to spin frequency for mass quadrupole vs. mass current quadrupole radiation.[3]

2.1.2.5 Measured braking indices Figure 2 shows the distribution of 12 reliably measured braking indices from a recent snapshot of the $\sim$ 3300 pulsars listed in the

[3] The 4/3 ratio assumed here for $f_{\rm GW}/f_{\rm rot}$ is a slow-rotation approximation in Newtonian gravity; the ratio changes by tens of percent for fast rotation in General Relativity (Idrisy et al. 2015; Caride et al. 2019) (see Sect. 4.2).

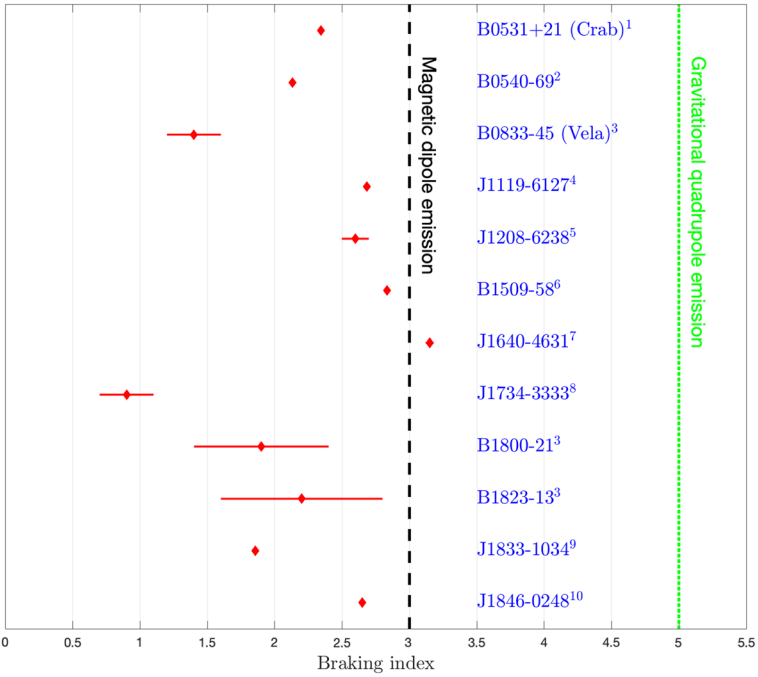

Fig. 2 Measured braking indices inferred from frequency derivatives of young pulsars with rotation frequencies greater than 10 Hz. For frequently glitching pulsars, such as Vela, the braking index is computed as a long-term average (Espinoza et al. 2017). Horizontal bars indicate uncertainties and are smaller than the plot markers for several pulsars. Vertical lines at braking indices of 3 and 5 denote the nominal expectations for magnetic dipole and gravitational quadrupole emission, respectively. References: 1 (Lyne et al. 2015), 2 (Ferdman et al. 2015), 3 (Espinoza et al. 2017), 4 (Weltevrede et al. 2011), 5 (Clark et al. 2016), 6 (Livingstone and Kaspi 2011), 7 (Archibald et al. 2016), 8 (Espinoza et al. 2011), 9 (Roy et al. 2012), 10 (Livingstone et al. 2007)

ATNF catalog [release V1.66—January 10, 2022 (Manchester and Hobbs 2005)]. Nearly all have values below the nominal value of 3 for a magnetic dipole radiator, although several have large uncertainties.

This distribution suggests that the model of a neutron star spinning down with constant magnetic field is, most often, inaccurate (Lyne and Graham-Smith 2006). All measured values for this collection lie below 3.0, except X-ray pulsar PSR J1640 −4631 with a measured index of 3.15 ± 0.03 (Archibald et al. 2016). It is possible that for many stars the departure of the measured braking index from the nominal value is due to an admixture of magnetic dipole radiation and other steady-state processes (Melatos 1997), although secular mechanisms may also play a role. See Palomba (2000, 2005) for discussions of spin-down evolution in the presence of both gravitational-wave and electromagnetic torques. Other suggested mechanisms for less-than-3 braking indices are decaying magnetic fields (Romani 1990), re-emerging buried magnetic fields (Ho 2011), a changing inclination angle between the magnetic dipole axis the spin axis (Middleditch et al. 2006; Tauris and Konar 2001; Ho 2015;

Lyne et al. 2015; Johnston and Karastergiou 2017), and a changing superfluid moment of inertia (Ho and Andersson 2012).

An interesting observation of the aftermath of two short GRBs noted indirectly inferred braking indices near or equal to three (Lasky et al. 2017a), suggesting the rapid spin-down of millisecond magnetars, possibly born from neutron star mergers. (No direct gravitational-wave evidence of a such a post-merger remnant has been observed from GW170817 (Abbott et al. 2017o, 2019d).) Similarly, a recent analysis of X-ray afterglows of gamma-ray bursts (Sarin et al. 2020) argues that at least some have millisecond magnetar remnants powering their emission, with GRB 061121 yielding a braking index $n = 4.85^{+0.11}_{-0.15}$, consistent with gravitational radiation dominance (albeit with large required ellipticity, Ho 2016; Kashiyama et al. 2016). See Strang et al. (2021), however, for an alternative study in which radiation driven from a millisecond magnetar can account for short GRB X-ray afterglows. See Dall'Osso and Stella (2022) for a recent brief review of millisecond magnetars, including evidence of their serving as central engines to create GRBs, and see Jordana-Mitjans et al. (2022) for evidence of a protomagnetar remnant in the aftermath of GRB 180618A.

It has been argued that the inter-glitch evolution of spin for the X-ray pulsar PSR J0537−6910 displays behavior consistent with a braking index of 7, (Andersson et al. 2018; Ho et al. 2020) consistent with *r*-mode emission, while the long-term trends points to an underlying braking index of -1.25 ± 0.01 (Ho et al. 2020). When intepreting the generally low values of well measured braking indices, one must bear in mind the potential for selection bias. Baysesian analysis of the spin evolution of 19 young pulsars (Parthasarathy et al. 2019, 2020), taking into account timing noise and extracting the long-term behavior from short-term, glitch-driven fluctuations, leads to braking indices *much larger* than 3. A similar follow-up analysis of an ensemble of glitching and non-glitching pulsars (Lower et al. 2021) confirmed that braking indices exceeding 100 are observed (see Fig. 3), albeit for stars in which a simple power-law spin-down is clearly inappropriate.

2.1.2.6 The gravitar model and associated figures of merit Gravitars refer to neutron stars with spin-down dominated by gravitational-wave energy loss (Palomba 2005). Although there is good reason to believe that most known pulsars are *not* gravitars, nonetheless the model is useful in bounding expectation on what is *possibly* detectable. Figure 4 shows a subset of the pulsars from Fig. 1, now graphed in the $f_{\rm GW}$–$\dot{f}_{\rm GW}$ plane, under the assumption that $f_{\rm GW} = 2f_{\rm rot}$. Again, isolated and binary stars are denoted by closed circles and open triangles, respectively. A vertical dashed line bounds the approximate detection bandwidth for Advanced LIGO at design sensitivity ($\sim$ 10 Hz and above). The same approximate frequency boundary applies to the design sensitivities of the Advanced Virgo and KAGRA detectors (Abbott et al. 2020b). As in Fig. 1, contours are shown for constant magnetic field, assuming spin-down dominated by magnetic dipole emission ($n = 3$). In addition, contours of higher slope are shown for constant ellipticity. An intriguing deficit of millisecond pulsars with extremely low period derivatives appears consistent (Woan et al. 2018) with a population of sources with a minimum ellipticity of about $\sim 10^{-9}$

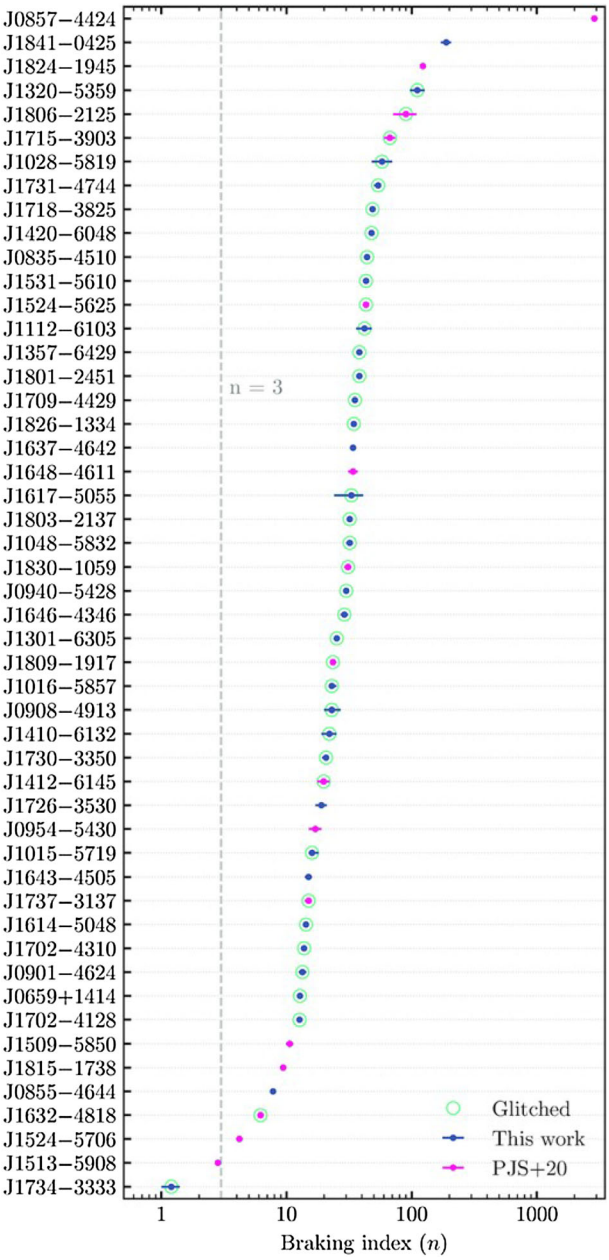

Fig. 3 Measured braking indices inferred from frequency derivatives of pulsars compiled in [Lower et al. (2021)—"this work", including from Parthasarathy et al. (2020)—PJS]. An ensemble of glitching (open green circles) and non-glitching pulsars are included. For most of the glitching stars, the braking indices are representative of their average inter-glitch braking, not their long-term evolution

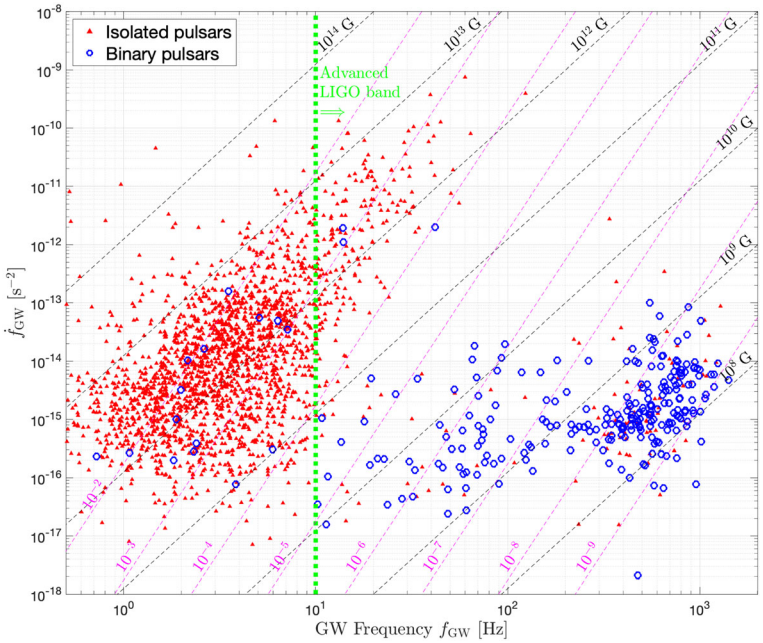

Fig. 4 Nominal expected GW frequencies and frequency derivatives for known pulsars. Closed triangles indicate isolated stars. Open circles indicate binary stars. Contours are shown for constant magnetic fields (ellipticities) for spin-down dominated by magnetic dipole (gravitational mass quadrupole) emissions. In this figure and in Figs. 5, 6, 7 and 8, the frequency derivatives have been corrected for the Shklovskii effect (Shklovskii 1970) (apparent negative frequency derivative due to proper motion orthogonal to the line of sight). The vertical dotted line denotes the approximate sensitivity band for Advanced LIGO at design sensitivity. A similar band applies to design sensitivities of the Advanced Virgo and KAGRA detectors (Abbott et al. 2020b)

with additional spin-down losses from magnetic dipole radiation (see near absence of sources in Fig. 4 to the right of the $\epsilon = 10^{-9}$ line). At the other extreme are lower-frequency, younger pulsars with high spin-downs, the highest of which is 7.6×10^{-10} Hz/s (Crab pulsar).

Using Eq. (20), these known pulsars can be mapped onto a plane of $f_{\rm GW}$–h_0 *under the gravitar assumption*, indicated in Fig. 5. That is, the spin-down strain limit (for $n = 5$) is shown on the vertical axis. Also shown are corresponding contours of constant implied values of ϵ/d, under the gravitar assumption, where d is the distance to the star. In addition, detector network sensitivities are shown for advanced detectors at design sensitivity (Abbott et al. 2020b) and for two proposed configurations of the "3rd-generation" Einstein Telescope (ET) (Maggiore et al. 2020) (ETB and ETC, for three detectors for five observing years). Another 3rd-generation proposal is for the "Cosmic Explorer" (Abbott et al. 2017c) which would have performance comparable to that of ET, being more sensitive at frequencies above $\sim$ 10 Hz and less sensitive at lower frequencies. To avoid clutter in these figures, only the ET sensitivities are shown.

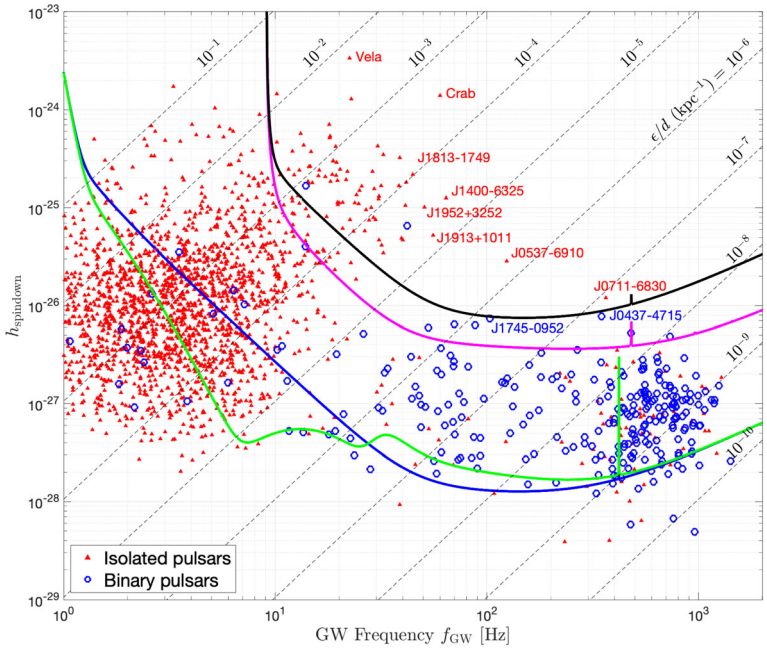

Fig. 5 Nominal expected GW frequencies and nominal strain spin-down limits for known pulsars. Closed triangles indicate isolated stars. Open circles indicate binary stars. The solid curves indicate the nominal (idealized) strain noise sensitivity for the O3 observing run (black), and expected sensitivities for 2-year advanced detector data run at design sensitivity (magenta) and a 5-year Einstein Telescope data run for two different detector designs: ETB (blue) and ETC (green). Dashed diagonal lines correspond to particular quotients of ellipticity over distance. A subset of pulsars of particular interest are labeled on the figure

In Fig. 5 and in succeeding figures, the "advanced detector" sensitivities are represented by those computed for two Advanced LIGO detectors running continuously for two observing years, henceforth designated as the "O4/O5 run". Although the O4 run scheduled to start near the start of 2023 will likely run for only $\sim$ 1 year (Abbott et al. 2020b) and may not quite reach the original Advanced LIGO design sensitivity, the succeeding O5 run in the "A$^+$" configuration is expected to exceed Advanced LIGO sensitivity significantly and to last for more than a year, making the detector sensitivities assumed here conservative, in principle. Including Advanced Virgo and KAGRA into the network sensitivity would improve these sensitivities still further. On the other hand, the O4/O5 observing time assumed here does not account for realistic deadtime losses, which can be substantial ($\sim$ 25% per detector, Davis et al. 2021). The detection sensitivities shown in Fig. 5 assume a *targeted search* (discussed below) using known pulsar ephemerides. If a star is marked above a sensitivity curve, then it is at least possible to detect it if its spin-down makes it a gravitar. Note, however, that Eq. (20) has been applied with a nominal moment of inertia I_{zz}, but the uncertainty in I_{zz} is of order a factor of two, depending on equation of state and stellar mass (Worley et al. 2008).

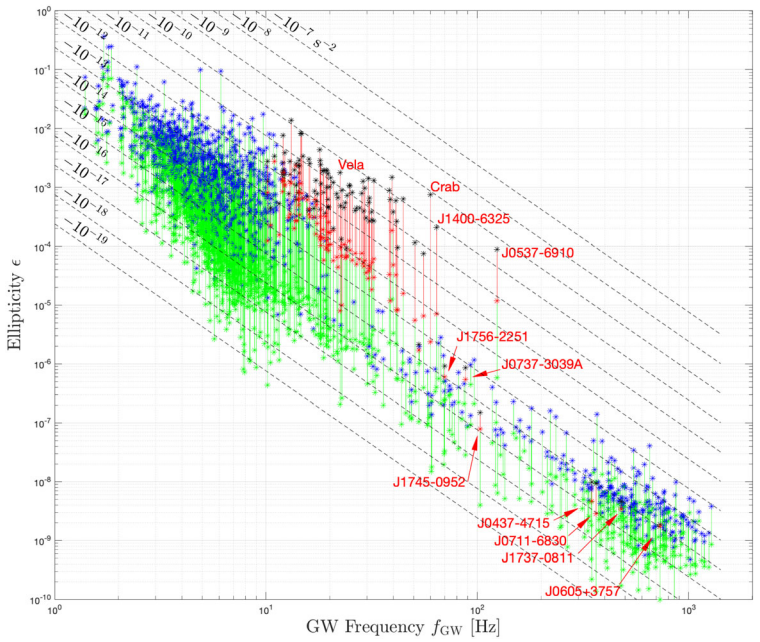

Fig. 6 Nominal expected GW frequencies and maximum allowed ellipticities for known pulsars. Black or blue asterisks indicate ellipticities accessible with advanced detectors or ETC sensitivities (3 detectors, 5 years), respectively, using targeted searches, where red vertical lines terminated by red asterisks indicate ellipticity sensitivity range for advanced detectors, and green vertical lines and green asterisks indicate additional ellipticity sensitivity range for ETC. A selection of pulsars accessible with advanced detector sensitivity are labeled in red. Diagonal dashed lines correspond to corresponding $\dot{f}_{\mathrm{GW}}$ values under the gravitar model

Another take on the pulsars with accessible spin-down limits is shown in Fig. 6, where accessible ellipticity ϵ values are shown for advanced detector and Einstein Telescope (ETC) sensitivities. Each vertical bar represents a range of ellipticities detectable for that star (red = accessible to advanced detectors, green = accessible to Einstein Telescope), where the asterisk at the top of the each bar is the ellipticity corresponding to that star's spin-down limit, given its f_{GW}, $\dot{f}_{\mathrm{GW}}$ and distance d values, while the depth to which the bar falls indicates the lowest detectable ellipticity. Straight dashed lines of negative slope depict corresponding $\dot{f}_{\mathrm{GW}}$ values *under the mass quadrupole gravitar model*. The actual $\dot{f}_{\mathrm{GW}}$ may be significantly higher because of the spin-down mechanisms discussed earlier. A striking feature of this figure is that sensitivities to very low ellipticities come almost entirely from the highest-frequency stars (as a reminder from Eq. (14), $h_0 \propto \epsilon f_{\mathrm{GW}}^2$). For example, no known pulsar with an ellipticity below 10^{-6} and that is accessible to advanced detectors has a f_{GW} value lower than 70 Hz, and no ellipticity below 10^{-8} is accessible to advanced detectors below 300 Hz.

Another figure of merit is the distance to which searches can detect sources of a particular ellipticity. Figure 7 shows the estimated distances to known pulsars over

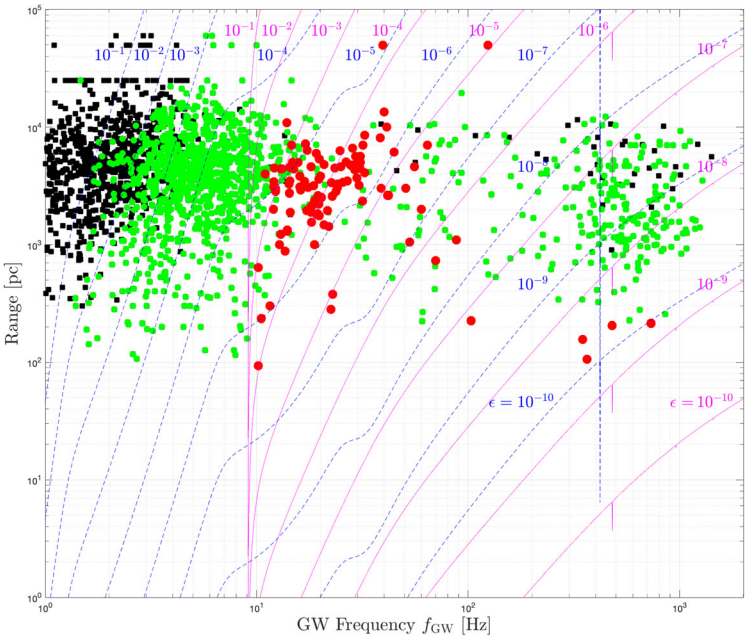

Fig. 7 Maximum allowed targeted-search ranges for gravitars versus GW frequencies for different assumed ellipticities for advanced detector sensitivity (solid magenta curves) and corresponding ranges for ETC sensitivity (dashed blue curves). Known pulsar distances are shown versus the expected GW frequencies, where red dots indicate pulsars with accessible spin-down limits for advanced detector sensitivity, and smaller green dots indicated pulsars with accessible spin-down limits for ETC sensitivity. Known pulsars in distinct horizontal bands (common distance) arise from stars in clusters or from distance capping in the galactic electron density model (Yao et al. 2017) used in the ATNF catalog (Manchester and Hobbs 2005)

the detection frequency band. Also shown are solid contours of advanced detector sensitivity range for different ellipticity values and dashed contours for Einstein Telescope. Pulsars with spin-down limits accessible to advanced detectors are shown in red, and those accessible to Einstein Telescope are shown in green. Only a handful of pulsars within 500 pc are accessible to advanced detectors with ellipticities below 10^{-8}. On the other hand, to reach the galactic center ($\sim$ 8.5 kpc) at a signal frequency of 1 kHz requires an ellipticity larger than $\sim 3 \times 10^{-8}$, and at 100 Hz requires an ellipticity greater than $\sim 3 \times 10^{-6}$.

As discussed in detail below, all-sky searches for unknown neutron stars necessarily have reduced sensitivity, such that the ranges shown for targeted searches using known pulsar timing do not apply. Figure 8 shows another range versus frequency plot, but for which (optimistic) advanced detector and Einstein Telescope all-sky sensitivities are assumed. For reference, the all-sky strain sensitivity is taken to be about 20 times worse than its targeted-search sensitivity for advanced detector

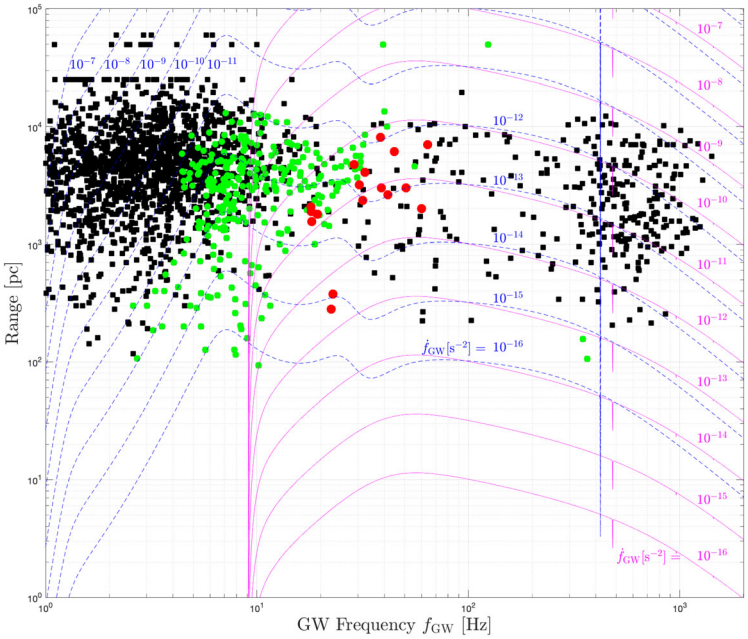

Fig. 8 Maximum allowed (optimistic) all-sky-search ranges for gravitars versus GW frequencies for different assumed spin-down derivatives for advanced detector sensitivity (solid magenta curves) and corresponding ranges for ETC sensitivity (dashed green curves). Known pulsar distances are shown versus the expected GW frequencies, where red dots indicate pulsars with accessible spin-down limits for advanced detector sensitivity, and smaller green dots indicated pulsars with accessible spin-down limits for ETC sensitivity. These all-sky search ranges assume an optimistic sensitivity depth of 50 $\mathrm{Hz}^{-1/2}$ (see Sect. 3.8)

and the corresponding ratio about 40 times worse for Einstein Telescope.[4] Consequently, the all-sky range contours corresponding to those in Fig. 7 would be reduced by the same ratios. Alternatively, to obtain the same ranges in the all-sky search would require ellipticities higher by the same ratios. The all-sky ranges in Fig. 8, in contrast, are shown as contours for different assumed $\dot{f}_{GW}$ values under the gravitar assumption. These contours are useful in assessing all-sky searches, since those searches are defined, in part, by their maximum spin-down range, which affects computational cost. Once again, known pulsars for which this search technique can reach the spin-down limit are shown in red for advanced detector and in green for Einstein Telescope. We see that for the advanced detectors to reach the galactic center at a signal frequency of 1 kHz requires a minimum spin-down magnitude greater than 10^{-9} Hz/s (minimum because another mechanism, such as magnetic dipole emission, may contribute to a higher spin-down magnitude), and at 100 Hz requires a minimum spin-down magnitude just less than 10^{-10} Hz/s. The corresponding required

[4] Because targeted-search strain sensitivity improves as the square root of time, while all-sky search sensitivity improves, at best, as only the fourth root of time (see Sect. 3.1), the disparity between targeted and all-sky sensitivity increases for longer observing times.

ellipticities at those frequencies are $\sim 8 \times 10^{-5}$ and $\sim 8 \times 10^{-7}$, respectively.

A simple steady-state argument by Blandford (Thorne 1989) led to an early estimate of the maximum detectable strain amplitude expected from a population of isolated gravitars of a few times 10^{-24}, independent of typical ellipticity values, in the optimistic scenario that most neutron stars become gravitars. A later detailed numerical simulation (Knispel and Allen 2008) revealed, however, that the steady-state assumption does not generally hold for mass quadrupole radiation, leading to ellipticity-dependent expected maximum amplitudes that can be 2–3 orders of magnitude lower in the LIGO/Virgo/KAGRA band for ellipticities as low as 10^{-9} and a few times lower for ellipticity of about 10^{-6}. Mass current quadrupole (*r*-mode) emission, however, would spin stars down faster, leading back to more optimistic maximum amplitudes (Owen 2010). A more detailed simulation including both electromagnetic and gravitational wave spin-down demonstrated the potential for setting joint constraints on natal neutron star magnetic fields and ellipticities (Wade et al. 2012). A recent population simulation study (Reed et al. 2021) estimated fractions of neutron stars probed by previous CW searches for different assumed ellipticities and concluded that the greatest potential gain from improving detector sensitity in accessing more neutron stars of plausible ellipticity comes at higher frequencies.

The spin-down limit on strain defined in Eq. (20) for known pulsars requires knowing the frequency f_{GW}, its first derivative $\dot{f}_{\mathrm{GW}}$ and the distance d to the star. There are other neutron stars for which no pulsations are observed, hence for which neither f_{GW} nor $\dot{f}_{\mathrm{GW}}$ is known, but for which the distance and the age of the star are known with some precision. For such stars one can define an "age-based" limit—under the assumption of gravitar behavior since the neutron star's birth in a supernova event. Using Eq. (7) and a braking index of 5 for mass quadrupole radiation gives the gravitar age:

$$\tau_{\mathrm{gravitar}} = -\frac{f_{\mathrm{rot}}}{4\dot{f}_{\mathrm{rot}}}. \tag{27}$$

Therefore, if one knows the distance and the age of the star, e.g., from the expansion rate of its visible nebula, then under the assumption that the star has been losing rotational energy since birth primarily due to gravitational-wave emission, then one has the following *frequency-independent* age-based limit on strain (Wette et al. 2008):

$$h_{\mathrm{age}} = (2.3 \times 10^{-24}) \left(\frac{1\,\mathrm{kpc}}{r}\right) \sqrt{\left(\frac{1000\,\mathrm{yr}}{\tau}\right)\left(\frac{I_{zz}}{I_0}\right)}, \tag{28}$$

along with a corresponding frequency-dependent but distance-independent ellipticity upper limit (Wette et al. 2008):

$$\epsilon_{\rm age} = (2.2 \times 10^{-4}) \left(\frac{100\,{\rm Hz}}{f_{\rm GW}}\right)^2 \sqrt{\left(\frac{1000\,{\rm yr}}{\tau}\right)\left(\frac{I_0}{I_{zz}}\right)}. \tag{29}$$

The corresponding calculation for r-mode emission leads to the age-based strain limit relation (Owen 2010):

$$h_{\rm age}^{r-{\rm mode}} = (1.9 \times 10^{-24}) \left(\frac{1\,{\rm kpc}}{r}\right) \sqrt{\left(\frac{1000\,{\rm yr}}{\tau}\right)\left(\frac{I_{zz}}{I_0}\right)}, \tag{30}$$

along with a corresponding frequency-dependent but distance-independent r-mode amplitude upper limit (Wette et al. 2008):

$$\alpha_{\rm age} = 0.076 \left(\frac{1000\,{\rm yr}}{\tau}\right)^{1/2} \left(\frac{100\,{\rm Hz}}{f_{\rm GW}}\right)^2. \tag{31}$$

Yet another empirically determined strain upper limit can be defined for accreting neutron stars in binary systems, such as Scorpius X-1. The X-ray luminosity from the accretion is a measure of mass accumulation rate at the surface. As the material rains down on the surface it can add angular momentum to the star, which in equilibrium may be radiated away in gravitational waves. Hence one can derive a torque-balance limit (Wagoner 1984; Papaloizou and Pringle 1978; Bildsten 1998) in the form (Watts et al. 2008):

$$\begin{aligned} h_{\rm torque} \sim (3 \times 10^{-27}) &\left(\frac{R}{10\,{\rm km}}\right)^{\frac{3}{4}} \left(\frac{M_\odot}{M}\right)^{\frac{1}{4}} \\ &\times \left(\frac{1000\,{\rm Hz}}{f_{\rm rot}}\right)^{\frac{1}{2}} \left(\frac{\mathcal{F}_{\rm x}}{10^{-8}\,{\rm erg/cm^2/s}}\right)^{\frac{1}{2}}, \end{aligned} \tag{32}$$

where $\mathcal{F}_{\rm x}$ is the observed energy flux at the Earth of X-rays from accretion, M is the neutron star mass and R its radius. Taking nominal values of $R = 10$ km, $M = 1.4 M_\odot$ and reformulating in terms of the gravitational-wave frequency $f_{\rm GW}$ (benchmarked to 600 Hz), one obtains:

$$h_{\rm torque} \sim (5 \times 10^{-27}) \left(\frac{600\,{\rm Hz}}{f_{\rm GW}}\right)^{\frac{1}{2}} \left(\frac{\mathcal{F}_{\rm x}}{10^{-8}\,{\rm erg/cm^2/s}}\right)^{\frac{1}{2}}. \tag{33}$$

Equations 32 and 33 assume the radius at which the accretion torque is applied is the stellar surface. If one assumes the torque lever arm is the Alfvén radius because of the coupling between the stellar rotation and the magnetosphere, then the implied equilibrium strain is $\sim$ 2.4 times higher (Abbott et al. 2019e). This limit is independent of the distance to the star. In general, variations in accretion inferred from X-ray flux fluctuations suggest similar (slower) fluctuations in the equilibrium frequency, which could degrade GW detection sensitivity for coherent searches that assume exact equilibrium. A first attempt to address these potential frequency fluctuations for Scorpius X-1 may be found in (Mukherjee et al. 2018). See Serim et al.

(2022) for a recent compilation of timing fluctuations of seven accretion-powered pulsars, providing evidence that accretion fluctuations indeed dominate timing noise.

2.1.3 Assessing potential sources of neutron star non-axisymmetry

From the above, it is clearly *possible* for neutron stars in our galaxy to produce continuous gravitational waves detectable by current ground-based detectors, but is it *likely* that putative emission mechanisms are strong enough to give us a detection in the next few years. Let's look more critically at those mechanisms.[5]

Isolated neutron stars may exhibit intrinsic non-axisymmetry from residual crustal deformation—e.g., from "starquakes" due to cooling and cracking of the crust (Pandharipande et al. 1976; Kerin and Melatos 2022) or due to changing centrifugal stress induced by stellar spin-down (Ruderman 1969; Baym et al. 1969; Fattoyev et al. 2018; Giliberti and Cambiotti 2022)—from non-axisymmetric distribution of magnetic field energy trapped beneath the crust (Zimmermann 1978; Cutler 2002) or from a pinned neutron superfluid component in the star's interior (Jones 2010; Melatos et al. 2015; Haskell et al. 2022). See Haskell et al. (2015); Singh et al. (2020) for a discussion of emission from magnetic and thermal "mountains" and Lasky (2015); Glampedakis and Gualtieri (2018) for recent, comprehensive reviews of GW emission mechanisms from neutron stars.

Maximum allowed asymmetries depend on the neutron star equation of state (Johnson-McDaniel and Owen 2013; Krastev et al. 2008) and on the breaking strain of the crust. Detailed molecular dynamics simulations borrowed from condensed matter theory have suggested in recent years that the breaking strain may be an order of magnitude higher than previously thought feasible (Horowitz and Kadau 2009; Caplan and Horowitz 2017). Analytic treatments (Baiko and Chugunov 2018) indicate, however, that anisotropy may be important and caution that simulations based on relatively small numbers of nuclei may not capture effects due to a polycrystalline structure in the crust. A recent cellular automaton-based simulation (Kerin and Melatos 2022) of a spinning-down neutron star used nearest-neighbour tectonic interactions involving strain redistribution and thermal dissipation. That study found the resulting annealing led to emitted gravitational strain amplitudes too low to be detected by present-generation detectors.

A recent revisiting of the mountain-building scenario (Gittins et al. 2020) finds systematically lower ellipticities to be realistic. It is argued in Woan et al. (2018) that a possible minimum ellipticity in millisecond pulsars may arise from asymmetries of buried internal magnetic field B_i (Cutler 2002; Lander et al. 2011; Lander 2014) of order of Woan et al. (2018)

$$\epsilon \sim 10^{-8} \left(\frac{<B_i>}{10^{12}\,\mathrm{G}} \right) \left(\frac{<H_c>}{10^{16}\,\mathrm{G}} \right), \tag{34}$$

where H_c is the lower critical field for superconductivity (protons in the stellar core are assumed to form a Type II superconductor). Hence, a buried toroidal (equatorial)

[5] This section draws, in part, from a recent review (Glampedakis and Gualtieri 2018) of gravitational-wave emission from neutron stars.

field of $\sim 10^{11}$ G could yield an ellipticity at the 10^{-9} level. It has been argued, on the other hand, that an explicit model of braking dynamics with non-axisymmetry due to magnetic field non-axisymmetry leads to still smaller ellipticities, based on observed braking indices of younger pulsars (de Araujo et al. 2016, 2017), where the magnetic contribution to the ellipticity depends quadratically on the field strength (Bonazzola and Gourgoulhon 1996; Konno et al. 1999; Regimbau and de Freitas Pacheco 2006). An analysis (Osborne and Jones 2020) of internal magnetic field contributions to non-axisymmetric temperature distributions in the neutron star crust finds that high field strengths ($> 10^{13}$ G) are needed in an accreting system for GW emission to halt spin-up from the accretion, four orders of magnitude higher than is expected for surface fields in LMXBs. A follow-up study (Hutchins and Jones 2022) finds more optimistically large thermal asymmetries to be possible deeper in a star, and another study (Morales and Horowitz 2022) finds a maximum allowed ellipticity of $\sim 7.4 \times 10^{-6}$.

r-modes (mass current quadrupole, see Sect. 2.1.2) offer an intriguing alternative GW emission source (Mytidis et al. 2015). Serious concerns have been raised, (Arras et al. 2003; Glampedakis and Gualtieri 2018) however, about the detectability of the emitted radiation for young isolated neutron stars, for which mode saturation appears to occur at low *r*-mode amplitudes because of various dissipative effects (Owen 2010). Another study, (Alford and Schwenzer 2014) though, is more optimistic about newborn neutron stars. The same authors, on the other hand, find that *r*-mode emission from millisecond pulsars is likely to be undetectable by advanced detectors (Alford and Schwenzer 2015).

The notion of a runaway rotational instability was first appreciated for high-frequency *f*-modes, (Chandrasekhar 1970; Friedman and Schutz 1978) (Chandrasekhar–Friedman–Schutz instability), but realistic viscosity effects seem likely to suppress the effect in conventional neutron star production (Lindblom and Detweiler 1977; Lindblom and Mendell 1995). Moreover, (Ho et al. 2019) set limits on the *r*-modes amplitude α for J0952−0607 below 10^{-9} based on the absence of heating observed in its X-ray spectrum, despite its high rotation frequency (707 Hz) which places it in the nominal *r*-modes instability window. Similarly, (Boztepe et al. 2020) set limits on α as low as 3×10^{-9}, based on observations of two other millisecond pulsars (PSR J1810+1744 and PSR J2241−5236) which also sit in the instability window. Another potential source of *r*-modes dissipation is from the interaction of "ordinary" and superfluid modes, leading to a stabilization window for LMXB stars (Gusakov et al. 2014; Kantor et al. 2020). The *f*-mode stability could play an important role, however, for a supramassive neutron star formed as the remnant of a binary neutron star merger (Doneva et al. 2015) (spinning too fast to collapse immediately despite exceeding the nominal maximum allowed neutron star mass).

In addition, as discussed below, a binary neutron star may experience direct non-axisymmetry from non-isotropic accretion (Owen 2005; Ushomirsky et al. 2000; Melatos and Payne 2005) (also possible for an isolated young neutron star that has experienced fallback accretion shortly after birth), or may exhibit *r*-modes induced by accretion spin-up.

Given the various potential mechanisms for generating continuous gravitational waves from a spinning neutron star, detection of the waves should yield valuable information on neutron star structure and on the equation of state of nuclear matter at extreme pressures, especially when combined with electromagnetic observations of the same star.

The notion of gravitational-wave torque equilibrium is potentially important, given that the maximum observed rotation frequency of neutron stars in LMXBs is substantially lower than one might expect from calculations of neutron star breakup rotation speeds ($\sim$ 1400 Hz) (Cook et al. 1994). It has been suggested (Chakrabarty et al. 2003) that there is a "speed limit" due to gravitational-wave emission that governs the maximum rotation rate of an accreting star. In principle, the distribution of frequencies could have a quite sharp upper frequency cutoff, since the angular momentum emission is proportional to the 5th power of the frequency for mass quadrupole radiation. For example, for an equilibrium frequency corresponding to a particular accretion rate, doubling the accretion rate would increase the equilibrium frequency by only about 15%. For *r*-mode GW emission, with a braking index of 7, the cutoff would be still sharper.

Note, however, that a non-GW speed limit may well arise from interaction between the neutron star's magnetosphere and an accretion disk (Ghosh and Lamb 1979; Haskell and Patruno 2011; Patruno et al. 2012). It has also been argued (Ertan and Alpar 2021) that correlation between the accretion rate and the frozen surface dipole magnetic field resulting from Ohmic diffusion through the neutron star crust in the initial stages of accretion in low mass X-ray binaries can explain a minimum rotation period well above the naive expectation.

A number of mechanisms have been proposed by which the accretion leads to gravitational-wave emission in binary systems. The simplest is localized accumulation of matter, e.g., at the magnetic poles (assumed offset from the rotation axis), leading to a non-axisymmetry. One must remember, however, that matter can and will diffuse into the crust under the star's enormous gravitational field. This diffusion of charged matter can be slowed by the also-enormous magnetic fields in the crust, but detailed calculations (Vigelius and Melatos 2010) indicate the slowing is not dramatic. Relaxation via thermal conduction is considered in (Suvorov and Melatos 2019).

Another proposed mechanism is excitation of *r*-modes in the fluid interior of the star, (Andersson 1998; Bildsten 1998; Friedman and Morsink 1998; Owen et al. 1998) with both steady-state emission and cyclic spin-up/spin-down possible (Levin 1999; Heyl 2002; Arras et al. 2003). Intriguing, sharp lines consistent with expected *r*-mode frequencies were reported in the accreting millisecond X-ray pulsar XTE J1751−305 (Strohmayer and Mahmoodifar 2014a) and in a thermonuclear burst of neutron star 4U 1636−536 (Strohmayer and Mahmoodifar 2014b). The inconsistency of the observed stellar spin-downs for these sources with ordinary *r*-mode emission, however, suggests that a different type of oscillation is being observed (Andersson et al. 2014) or that the putative r-modes are restricted to the neutron star crust and hence gravitationally much weaker than core r-modes (Lee 2014). Another recent study (Patruno et al. 2017) suggests that spin frequencies observed in accreting LMXB's are consistent with two sub-populations, where the narrow higher-

frequency component ($\sim$ 575 Hz with standard deviation of $\sim$ 30 Hz) may signal an equilibrium driven by gravitational-wave emission. It has been suggested (Haskell and Patruno 2017) that the transitional millisecond pulsar PSR J1023+0038 (for which spin-down has been measured in both accreting and non-accreting states) shows evidence for mountain building (or *r*-modes) during the accretion state, based on different spin-downs observed in accreting vs. non-accreting states. It has also been argued (Bhattacharyya 2020) that J1023+0038 shows evidence for a permanent ellipticity in the range $0.48 - 0.93 \times 10^{-9}$. An analysis (Chen 2020) of three transitional millisecond pulsars and ten redbacks concluded their ellipticities ranged over $0.9 - 23.4 \times 10^{-9}$.

A recent analysis (De Lillo et al. 2022) based on the absence of evidence of a stochastic gravitational-wave background emitted by a population of neutron stars with a rotational frequency distribution similar to that of known pulsars inferred that the average ellipticity of the galactic population is less than $\sim 2 \times 10^{-8}$.

2.1.4 Particular GW targets

In the following, particular neutron star targets for gravitational-wave searches are discussed in the following categories: known young pulsars with high spin-down rates; known high-frequency millisecond pulsars; neutron stars in supernova remnants, neutron stars in low-mass X-ray binary systems; and particular directions on the sky.

2.1.4.1 Known young pulsars with high spin-down rates A young pulsar with a high spin-down rate presents an attractive target. Its age offers the hope of a star not yet annealed into smooth axisymmetry, a hope strengthened by the prevalence of observed timing glitches among young stars. A high spin-down rate not only makes it more likely that the spin-down limit is accessible, but also suggests a star with a reservoir of magnetic energy, some of which could give rise to non-axisymmetry. From the Advanced LIGO/Virgo O1, O2 and O3 data sets more than 20 pulsars were spin-down accessible (Abbott et al. 2019b, 2022j) (see Sect. 4.1), but most correspond to ellipticities of $\sim 10^{-4}$–10^{-3}. A small number are highlighted here, for which ellipticities below 10^{-5} are accessible already or with a 2-year data run at advanced detector design sensitivity ("O4/O5 run").

- **Crab (PSR J0534+2200)**—This pulsar, created in a 1054 A.D. supernova observed by Chinese astronomers and discovered in 1968 (Staelin and Reifenstein 1968), has received more attention from LIGO / Virgo analysts than any other. Its spin-down limit was first beaten in the initial LIGO data set S5 (Abbott et al. 2008b), and now has been beaten (O3 data) by a factor of $\sim$ 100 (Abbott et al. 2022j) (see Sect. 4.1), leading to a 95% upper limit on ellipticity of 1.0×10^{-5}. For a 2-year O4/O5 run, this sensitivity reaches $\sim 2 \times 10^{-6}$. Spinning at just below 30 Hz, its nominal f_{GW} is just below 60 Hz, making the detector spectrum susceptible to power mains contamination (including non-linear upconversion, see Sect. 3.7) in the LIGO and KAGRA interferometers, but not in the Virgo

interferometer, which uses 50 Hz power mains. Its inferred rotational kinetic energy loss rate based on its spin-down is $dE/dt \sim -5 \times 10^{38}$ erg s^{-1}, assuming the nominal $I_{zz} = 10^{38}$ kg m^2 (10^{45} g cm^2).

- **Vela (PSR J0835-4510)**—Although older and lower in frequency than the Crab with a higher ellipticity spin-down limit (1.9×10^{-3}), the Vela pulsar, discovered in 1968 (Large et al. 1968), is nonetheless interesting, given its frequent glitches (Manchester 2018; Ashton et al. 2019). Its O4/O5 ellipticity sensitivity reaches $\sim 8 \times 10^{-6}$. Spinning at just above 11 Hz, its nominal f_{GW} is about 22 Hz, where detector noise is several times higher than at the Crab frequency. Its inferred $dE/dt \sim -7 \times 10^{36}$ erg s^{-1}.
- **PSR J0537-6910**—This pulsar, observed to pulse only in X-rays, is distant ($\sim$ 50 kpc in the Large Magellanic Cloud). With a rotation frequency of $\sim$ 62 Hz, its nominal GW frequency of 124 Hz is quite high for a young pulsar (magnetic dipole spin-down age $\sim$ 5000 years), and its spin-down energy loss is comparable to the Crab's. It is also extremely glitchy ($\sim$ 1 per 100 days) (Antonopoulou et al. 2018; Ferdman et al. 2018) and as noted above, may show evidence of *r*-mode emission between glitches (Andersson et al. 2018; Ho et al. 2020) (which would imply a GW frequency at $\sim$ 90 Hz). Its inferred $dE/dt \sim -5 \times 10^{38}$ erg s^{-1}.
- **PSR J1400-6325**—This relatively recently discovered X-ray pulsar (Renaud et al. 2010) lies in a supernova remnant 7–10 kpc away and displays a spin-down energy about 1/10 of the Crab pulsar's, but may be younger than 1000 years. With a spin frequency of $\sim$ 32 Hz, its nominal f_{GW} is 64 Hz, comparable to the Crab's, but farther from the troublesome 60 Hz power mains. Its inferred $dE/dt \sim -5 \times 10^{37}$ erg s^{-1}.
- **PSR J1813-1749**—First detected as a TeV γ-ray source (Aharonian et al. 2005), this star was found to exhibit non-thermal X-ray emission and to have a tentative association with a radio supernova remnant G12.8−0.0 (Brogan et al. 2005) suggesting a distance greater than 4 kpc and an age perhaps younger than 1000 years. X-ray pulsations detected still later with a period of 44 ms confirmed a pulsar source and posited an association with a young star cluster at 4.7 kpc (Gotthelf and Halpern 2009), while yielding a nominal pulsar spin-down age of 3.3−7.5 kyr. A more recent detection of highly dispersed radio pulsations, however, suggest a distance of 6 or 12 kpc (Camilo et al. 2021), depending on electron dispersion model, casting doubt on the association with the star cluster. The spin frequency of 22 Hz yields a nominal GW frequency of $\sim$ 45 Hz, and the frequency derivative imply $dE/dt \sim -6 \times 10^{37}$ erg s^{-1}.

2.1.4.2 Known high-frequency millisecond pulsars Because nearly all millisecond pulsars are old, with some characteristic ages greater than 10 billion years, they can be assumed to retain little asymmetry from their initial formation or from the accretion that spun them up. Thus one sees low spin-down for this population in Fig. 5 and hence low inferred maximum ellipticities in Fig. 6. On the other hand, the

vast energy reservoirs in their rotation and the quadratic dependence of h_0 on frequency still makes these stars potentially intriguing. As noted above, there may be empirical evidence for a minimum ellipticity of order $\sim 10^{-9}$ (Woan et al. 2018). Highlighted below are particular millisecond pulsars of interest in the coming years.

- **PSR J0711-6830** This isolated star at a distance of 0.11 kpc, with a nominal $f_{\rm GW} \sim$ 364 Hz, a spin-down upper limit of 1.2×10^{-26} and corresponding maximum ellipticity of 9.4×10^{-9}, is the first MSP to have its spin-down limit beaten (in early O3 data, see Sect. 4.1).
- **PSR J0437–4715** This binary star at a distance of 0.16 kpc, with a nominal $f_{\rm GW} \sim$ 347 Hz, a spin-down upper limit of 7.8×10^{-27} and corresponding maximum ellipticity of 9.7×10^{-9} also had its spin-down limit beaten (in the full O3 data).
- **PSR J1737–0811** This binary star at a distance of 0.21 kpc, with a nominal $f_{\rm GW} \sim$ 479 Hz, a spin-down upper limit of 5.3×10^{-27} and corresponding maximum ellipticity of 4.6×10^{-9}, will likely have its spin-down limit beaten by the O4/O5 data set.
- **PSR J1231–1411** This binary star at a distance of 0.42 kpc, with a nominal $f_{\rm GW} \sim$ 543 Hz, a spin-down upper limit of 2.8×10^{-27} and corresponding maximum ellipticity of 3.8×10^{-9}, will likely have its spin-down limit beaten by the O4/O5 data set.
- **PSR J2124–3358** This binary star at a distance of $\sim$ 0.4 kpc, with a nominal $f_{\rm GW} \sim$ 406 Hz, a spin-down upper limit of 2.3×10^{-27} and corresponding maximum ellipticity of 5.6×10^{-9}, will likely have its spin-down limit beaten by the O4/O5 data set.
- **PSR J1643–1224** This binary star at a distance of 0.79 kpc,[6] with a nominal $f_{\rm GW} \sim$ 433 Hz, a spin-down upper limit of 2.1×10^{-27} and corresponding maximum ellipticity of 8.0×10^{-9}, may *not* have its spin-down limit beaten by the O4/O5 data set, but as noted by Woan et al. (2018), would have the highest GW SNR of any known star if its ellipticity were 10^{-9}.

2.1.4.3 Central compact objects and Fomalhaut b Not every neutron star of interest has been detected to pulsate. Central compact objects (CCOs) at the heart of supernova remnants present especially intriguing targets, especially those in remnants inferred from their size and expansion rate to be young (De Luca 2008). There may be direct evidence of a neutron star, such as from thermal X-rays emitted from a hot surface or from X-rays due to interstellar accretion, or there may be indirect evidence from a pulsar wind nebula driven by a fast-spinning star at the core. Most GW searches to date for a CCO lacking detected pulsations have focused on the particularly promising source, Cassiopeia A, but in recent years, such searches have also been carried out for as many as 15 supernova remnants (Abbott et al.

[6] A recent parallax measurement (Reardon et al. 2021), though, finds a distance for J1643−1224 of $1.2^{+0.4}_{-0.3}$ kpc.

2019a, 2021i). Highlighted below are particular supernova remnants ("G" naming terminology based on the Green Catalog (Green 2014), see also Ferrand and Safi-Harb 2012) with known or suspected central compact objects, in addition to an object, Fomalhaut b, originally thought to be an exoplanet, but which may be a nearby neutron star. Results from searches for these targets are presented further below in Sect. 4.2.

- **Cassiopeia A**—Cas A (G111.7−2.1) is perhaps the most promising example of gravitational-wave CCO source in a supernova remnant. Its birth aftermath may have been observed by Flamsteed (Hughes 1980) $\sim$ 340 years ago in 1680, and the expansion of the visible shell is consistent with that date (Fesen et al. 2006). Hence Cas A, which is visible in X-rays (Tananbaum 1999; Ho et al. 2021) but shows no pulsations (Halpern and Gotthelf 2009), is almost certainly a very young neutron star at a distance of about 3.3 kpc (Reed et al. 1995; Alarie et al. 2014). From Eq. (28), one finds an age-based strain limit of $\sim 1.2 \times 10^{-24}$, which is readily accessible to LIGO and Virgo detectors in their most sensitive band.
- **Vela Jr.**—This star (G266.2−1.2) is observed in X-rays (Pavlov et al. 2001; Kargaltsev et al. 2002; Becker et al. 2006) and is potentially quite close ($\sim$ 0.2 kpc) and young (690 years) (Iyudin et al. 1998), but searches have also conservatively assumed more a more pessimistic distance (0.9 kpc) and age (5100 years), based on other measurements (Allen et al. 2015). The optimistic age and distance assumptions lead to an age-based strain limit of $\sim 1.4 \times 10^{-23}$, even more accessible than the Cas A limit. Even the pessimistic age-base limit of 1.1×10^{-24} is only slightly lower than that of Cas A. It has been argued (Ming et al. 2016) that a search over multiple CCOs, optimized for most likely detection success given fixed computing resources, favors focusing those resources on Vela Jr. over other CCOs, including Cas A.
- **G347.3–0.5**—An X-ray source (Slane et al. 1999; Ho et al. 2021) is consistent with the core of this supernova remnant, the nearness ($\sim$ 0.9 kpc) and youth (1600 years) of which make a search aimed at the remnant's center intriguing, as they yield an age-based strain limit of $\sim 2.0 \times 10^{-24}$—higher than that of Cas A.
- **G1.9+0.3** This supernova remnant, the youngest in the galaxy at 100 years (Reynolds et al. 2008), has no detected CCO at its core, which is consistent with a Type IA supernova's having left no neutron star behind. Nonetheless, its youth make it interesting despite this doubt and its distance (8.5 kpc), yielding an age-based strain limit of $\sim 8.4 \times 10^{-25}$.
- **Fomalhaut b** This object was assumed to be an extrasolar planet (Kalas et al. 2008) until (Neuhäuser et al. 2015) noted that the absence of detected infrared radiation could indicate the object is a remarkably nearby neutron star ($\sim$ 0.01 kpc). The absence of attempted X-ray detection with *Chandra* observations (Poppenhaeger et al. 2017), however, disfavors its being a young, hot neutron star. More recent evidence (Gáspár and Rieke 2020) argues, in fact, that the optical observations point to a planetesimal collision.

2.1.4.4 Neutron stars in low-mass X-ray binary systems Because of its high X-ray flux ($\mathcal{F}_{\rm x} \sim 3.9 \times 10^{-7}$ erg cm^{-2} s^{-1}, Watts et al. 2008) and the torque-balance relation for low-mass X-ray binaries (Eq. 32), Scorpius X-1 is thought to be an especially promising search target for advanced detectors and has been the subject of multiple searches in initial and Advanced gravitational-wave detector data. From Eq. (33), one expects a strain amplitude limited by Abbott et al. (2007a) and Messenger et al. (2015)

$$h \sim (3 \times 10^{-26}) \left(\frac{600\,\mathrm{Hz}}{f_{\rm GW}}\right)^{\frac{1}{2}}. \tag{35}$$

While Sco X-1's rotation frequency remains unknown (Galaudage et al. 2021), its orbital period is well measured, (Gottlieb et al. 1975; Wang et al. 2018) which allows substantial reduction in search space. A similar but less bright LMXB system is Cygnus X-2 (Premachandra et al. 2016) at a distance of 7 kpc and an average flux $\mathcal{F}_{\rm x} = 11 \times 10^{-9}$ erg/cm^2 s^{-1} (Galloway et al. 2008), yielding a torque-balance strain limit about 20 times lower than that of Sco X-1. Unlike Sco X-1 which is assumed but not known to contain a neutron star (as opposed to a black hole with an accretion disk), Cyg X-2 has displayed thermonuclear bursts, confirming the presence of a neutron surface.

Another interesting class contains "accreting X-ray millisecond pulsars" (AXMPs) which are fast-spinning neutron stars in LMXBs that show sporadic outbursts during accretion episodes (when "active") from which rotation frequencies can be determined. When active, the frequencies can increase or decrease, while frequencies between outbursts (when "quiescent") generally decrease. One could hope to detect CW radiation from either active or quiescent phases. Although the limited durations of bursts and their stochastic nature constrain potential search sensitivity, it is during such outbursts when one might expect the largest generation of non-axisymmetries or excitation of r-modes. The fastest-spinning stars, such as IGR J00291+5934 at $f_{\rm rot} \sim$ 599 Hz and a distance of $\sim$ 4 kpc (Torres et al. 2008; Patruno 2017), offer deeper probing of equatorial ellipticity and r-mode amplitude. Current search sensitivities to strain amplitude (Abbott et al. 2022g) remain an order of magnitude or more away from inferred spin-down limits ($\sim 10^{-28}$–10^{-27}), but improvements in detector sensitivity, search methodology and potential future electromagnetic observations make this type of source potentially intriguing in the coming years.

2.1.4.5 Particular sky directions In addition to known (or suspected) neutron stars, there are other localized sky regions or points where a directed search might yield a continuous gravitational-wave detection. Listed below are possibilities that have attracted attention in recent years.

- **Galactic center**—The vicinity of the galactic center (Sgr A*) is particularly interesting (Aasi et al. 2013a), as an active, star-forming region with known pulsars (Deneva et al. 2009). Moreover, it is highly likely that only a small fraction of pulsars near the galactic center have been detected to date, since there

is extreme dispersion and scattering of radio signals along the propagation line to the Earth (Lazio and Cordes 1998). The inference of there being many hidden pulsars is supported by $\sim$ 20 pulsar wind nebula candidates detected within 20 pc of Sgr A* (Muno et al. 2008). In addition, searches for dark-matter annihilation signals have detected an excess of high-energy gamma ray emission from the galactic center region above what is expected from conventional models of diffuse gamma-ray emission and catalogs of known gamma-ray sources (Ackermann et al. 2017), a tension which may be resolved by the existence of a hidden population of millisecond pulsars (Abazajian 2011). A systematic radio survey of the central 1 parsec of Sgr A* at a frequency of 15 GHz (Macquart and Kanekar 2015), high enough to reduce dispersion and scattering substantially, yielded no detections, but the rapidly falling spectrum of most pulsars makes detection at 15 GHz at that distance difficult. This survey obtained a 90% CL upper limit of 90 on the number of pulsars within 1 parsec of Sgr A*, assuming the population there is similar to known pulsars. Unfortunately, the $\sim$ 8.5 kpc distance to the galactic center makes CW searches challenging with present detector sensitivities. Only stars with extreme ellipticities are accessible to advanced detectors at design sensitivity (see Fig. 8). At the same time, however, young neutron stars are those most likely to exhibit such ellipticities.

- **Globular cluster cores**—One normally associates globular clusters with ancient stellar populations and might expect, at best, to see only pulsars that are themselves ancient – recycled and well annealed millisecond pulsars. Indeed many MSPs are seen in globular clusters (Freire 2012). For example, Tucanae 47 is known to host at least 25 MSPs (Freire et al. 2017). Nonetheless, not all observed pulsars in globular clusters seem to be old (Freire 2012). A plausible explanation is that the dense core of a globular cluster leads to multibody exchange interactions in which a previously recycled but decoupled neutron star acquires a close new companion that proceeds to overflow its Roche lobe, leading to new accretion. Another, related mechanism is possible debris accretion triggered by multibody interactions, given that some pulsars are known to host debris disks and even planets (Abbott et al. 2017m). The well localized core of a globular cluster makes a deep, directed search tractable.
- **High-latitude Fermi sources** The Fermi satellite's LAT experiment has detected $\sim$ 100 previously unknown gamma ray pulsars since observing began in 2008. Gamma ray pulsars tend to be sources with low variability and relatively low spectral cutoffs, and most lie near the galactic plane, as expected. Fermi-LAT point sources well outside the galactic plane tend to be extagalactic, e.g., active galactic nuclei, but an intriguing possiblity is that a source with high galactic latitude could be a galactic neutron star, in which case the high latitude favors a nearby source (Sanders 2016), consistent with a scale height of $\sim$ 600 pc with respect to the galactic plane observed for known pulsars (Lyne and Graham-Smith 2006). Arguing against this possibility, however, are extensive searches for gamma-ray pulsations from pulsar-like Fermi-LAT sources (see, e.g., Clark et al. 2018), based in part on algorithms developed for CW gravitational-wave searches (Pletsch et al. 2011). On the other hand, such searches are challenged to probe

binary sources with large accelerations, suggesting that CW searches directed at such sources include algorithms sensitive to binary sources (Neunzert 2019).

In between all-sky searches and directed searches for single sky points reside "spotlight" searches, in which a patch of sky is searched more deeply than in all-sky searches (with increased computational cost), but less deeply than is computationally feasible for a single sky location. Such spotlights have been applied in searches for a broad star-forming region along two directions of the Orion spur of the local galactic spiral arm (Aasi et al. 2016b) and toward the galactic center region, including the globular cluster Terzan 5 (Dergachev et al. 2019).

2.2 Axion clouds bound to black holes

An intriguing potential connection between gravitational waves and the still-unknown missing dark matter of the Universe comes from the possibility that the dark matter is composed of ultralight, electromagnetically invisible bosons, such as axions. One novel idea is that these bosons could be disproportionately found in the vicinity of rapidly spinning black holes (Arvanitaki et al. 2010; Arvanitaki and Dubovsky 2011). The ultralight particles could, in principle, be spontaneously created via energy extraction from the black hole's rotation (Penrose 1969; Christodoulou 1970) and form a Bose–Einstein "cloud" with nearly all of the quanta occupying a relatively small number of energy levels. For a cloud bound to a black hole, the approximate inverse-square law attraction outside the Schwarzchild radius ($r_{\text{Schwarz.}} \equiv \frac{2\,GM_{\text{BH}}}{c^2}$) leads to an energy level spacing directly analogous to that of the hydrogen atom (Arvanitaki et al. 2010; Baumann et al. 2019). The number of quanta occupying the low-lying levels can be amplified enormously by the phenomenon of superradiance in the vicinity of a rapidly spinning black hole (with angular momentum that is a signficant fraction of the maximum value allowed in General Relativity). The bosons in a non-s ($\ell > 0$) negative-energy state can be thought of as propagating in a well formed between an ℓ-dependent centrifugal barrier at $r > r_{\text{Schwarz.}}$ and a potential rising toward zero as $r \to \infty$; wave function penetration into the black hole ergosphere permits transfer of energy from the black hole spin (Zel'dovich 1971; Misner 1972; Starobinskiĭ 1973) into the creation of new quanta.

Two particular gravitational-wave emission modes of interest here can arise in the axion scenario, both potentially leading to intense coherent radiation (Arvanitaki et al. 2015). In one mode, axions can annihilate with each other to produce gravitons with frequency double that corresponding to the axion mass: $f_{\text{graviton}} = 2m_{\text{axion}}c^2/h$. In another mode, emission occurs from level transitions of quanta in the cloud. This Bose condensation is most pronounced when the reduced Compton wavelength of the axion is comparable to but larger than the scale of the black hole's Schwarzchild radius:

$$\lambda\!\!\!^{-} \equiv \frac{\lambda}{2\,\pi} = \frac{\hbar}{m_{\rm axion} c} \gtrapprox \frac{2\,G M_{\rm BH}}{c^2} \tag{36}$$

$$\Rightarrow \quad m_{\rm axion} \lessapprox (7 \times 10^{-11}\,{\rm eV/c^2}) \frac{M_\odot}{M_{\rm BH}}, \tag{37}$$

where $\hbar$ is the reduced Planck constant and G is Newton's gravitational constant. A key parameter governing detectability is a parameter analogous to the electromagnetic fine structure constant:

$$\alpha \equiv \frac{G m_{\rm axion} M_{\rm BH}}{\hbar c}, \tag{38}$$

where both the growth rate of a cloud upon black hole formation and the amplitude of gravitational-wave emission due to axion annihilation depend on high powers of α. Hence small α impedes detection; at the same time, superradiance itself requires (Isi et al. 2019):

$$\alpha < \frac{1}{2} m \chi \left(1 + \sqrt{1 - \chi^2}\right)^{-1} < \frac{m}{2}, \tag{39}$$

where χ is the dimensionless black hole spin proportional to its total angular momentum magnitude J: $\chi = \frac{cJ}{GM_{\rm BH}^2}$, and m is the quantum number corresponding to the axion's orbital angular momentum projection along the spin axis of the black hole (the first level to be populated in a newborn black hole is $m = 1$, Isi et al. 2019). Hence the range of α (and therefore axion mass) for which a particular black hole produces superradiance may be narrow. In general, more massive black holes produce stronger signals over wider ranges in axion mass. Clouds composed of ultralight vector or tensor bosons would lead to stronger, but shorter-lived signals (Siemonsen and East 2020; Brito et al. 2020). Nominal limits on axion masses can be placed based on the existence of high-spin binary black holes in our galaxy (Arvanitaki et al. 2017; Cardoso et al. 2018), but those limits are subject to uncertainties in inferred black hole spins (Reynolds 2014; McClintock et al. 2014) and may be invalidated by tidal disruption effects from the companion star (Cardoso et al. 2020). Constraints have also been inferred from spin measurements in the population of binary black hole merger detections (Ng et al. 2021).

Given the many orders of magnitude of uncertainty in, for example, axion masses that could account for dark matter (Bertone 2010), the relatively narrow mass window accessible to currently feasible CW searches (1–2 orders of magnitude) makes searching for such an emission a classic example of "lamppost" physics, where one can only hope that nature places the axion in this lighted area of a vast parameter space.

In principle, searching for these potential CW sources requires no fundamental change in the search methods described below, but search optimization can be refined for the potentially very slow (and positive) frequency evolution expected during

annihilation emission (as the relative magnitude of the axion field's binding energy decreases). In addition, for a known black hole location, a directed search can achieve better sensitivity than an all-sky search. For string axiverse models, however, the axion cloud (Arvanitaki et al. 2010; Arvanitaki and Dubovsky 2011; Yoshino and Kodama 2014, 2015) can experience significant self-interactions which can lead to appreciable frequency evolution of the signal and to uncertainty in that evolution, a complication less important for the postulated QCD axion (Arvanitaki et al. 2015). In an optimistic scenario with many galactic black holes producing individually detectable signals, (Zhu et al. 2020) points out that the signals would all lie in a very narrow band, complicating CW searches, which typically implicitly assume no more than one detectable signal in narrow bands. A later study (Pierini et al. 2022), however, finds that semi-coherent searches can be robust with respect to potential signal confusion.

Until recently, most published searches have not been tailored for a black hole axion cloud source, but instead existing (non-optimized) limits on neutron star CW emission could be reinterpreted as limits on such emission (Arvanitaki et al. 2015; Dergachev and Papa 2019; Palomba et al. 2019). More recently, though, searches have been carried out that exploit the narrow spin-up parameter space expected for such sources (Sun et al. 2020; Abbott et al. 2022c).

One interesting suggestion includes the possibility that a black hole formed from the detected merger of binary black holes or neutron stars could provide a natural target for follow-up CW searches (Arvanitaki et al. 2017; Ghosh et al. 2019; Isi et al. 2019). Recent studies (Brito et al. 2017a, b; Tsukada et al. 2019, 2021) argue that the lack of detection of a stochastic gravitational radiation background from the superposition of extragalactic black holes already places significant limits on axion masses relevant to CW searches. Another recent study (Isi et al. 2019) examined in detail the prospects for detecting superradiance from both post-merger black hole remnants and known black holes in galactic X-ray binaries, such as Cygnus X-1.

3 Continuous Wave Search Methods

Being realistic, we must acknowledge that the first discovered CW signal will be exceedingly weak compared to the transient signals detected to date, an assumption borne out by many unsuccessful CW searches to date. One must integrate the signal over a long duration to observe it with statistical significance. Those long integrations in noise that is instantaneously much higher in amplitude require application of assumed signal templates to the data. In general, the more restrictive is the model, the better is the achievable signal-to-noise ratio, as one can search over a smaller volume of source parameter space. The following sections discuss the challenges faced in searching over larger parameter space volumes, a common classification of general search methods, and specific algorithms devised to meet the challenges.

3.1 Challenges in CW signal detection and types of searches

At first glance, it may seem puzzling that a signal due to a rapidly spinning neutron star is challenging to find. One might expect a simple discrete Fourier transform of the data stream to reveal a sharp spike at the nominal frequency. There are several severe complications, however, for most CW searches. For concreteness, imagine that a signal is weak enough to require a coherent, phase-preserving 1-year integration time $T_{\rm coh}$. The nominal frequency resolution from a discrete Fourier transform (DFT[7]) is then 1/year $\sim$ 30 nHz. In order for the signal's central frequency to remain in the same DFT bin (integer index into the transform result, see Eq. (52) below) during that year, its first derivative $\dot{f}$ would need to satisfy $\dot{f}T_{\rm coh} \lesssim 1/T_{\rm coh}$, or $\dot{f} \lesssim 10^{-15}$ Hz/s and its second derivative $\ddot{f} \lesssim 6 \times 10^{-23}$ Hz/s^2. In practice, not only are Doppler modulations of detected frequency due to the Earth's motion much larger than these values, as discussed below, but the frequency derivative of a detectable source is typically also much larger, in order for its rotational kinetic energy loss to be compatible with detection (detectable spin-down limit). If the precise frequency evolution of the source is known already from radio or gamma-ray pulsar timing (assuming a fixed EM/GW phase relation), then one can make corrections for that evolution via *barycentering*, discussed below, without SNR degradation as long as the uncertainties in frequency derivatives are well below the above constraints.

For sources with large frequency uncertainties, however, especially those with unknown frequencies, correcting for intrinsic source frequency evolution and for modulations due to the Earth's motion incurs a substantial computing cost for searching over parameter space. Because of these costs, it is useful to categorize CW searches broadly into three categories (Prix 2009) (while recognizing there are special cases that fall near the boundaries).

1. *Targeted* searches in which the star's position and rotation frequency are known, i.e., known radio, X-ray or γ-ray pulsars;
2. *Directed* searches in which the star's position is known, but rotation frequency is unknown, e.g., a non-pulsating X-ray source at the center of a supernova remnant; and
3. *All-sky* searches for unknown neutron stars.

The volume of parameter space over which to search increases in large steps as one progresses through these categories. In each category a star can be isolated or binary. For 2) and 3) any unknown binary orbital parameters further increase the search volume, making a subclassification helpful, as discussed below. In general, the greater the *a priori* knowledge of sources parameters, the more computationally feasible it is to integrate data coherently for longer time periods in order to improve strain amplitude sensitivity.

[7] CW search literature frequently refers to SFTs, "Short" discrete Fourier transforms, where short is relative to the span of an observing run, but which may correspond to coherence times as long as hours.

To illustrate, consider a directed search for a source of known location but with unknown frequency and unknown frequency derivatives, where the signal phase is expanded in truncated Taylor form in the source frame time τ with respect to a reference time τ_0:

$$\Phi(\tau) \approx \Phi_0 + 2\pi\left[f_s(\tau-\tau_0) + \frac{1}{2}\dot{f}_s(\tau-\tau_0)^2 + \frac{1}{6}\ddot{f}_s(\tau-\tau_0)^3\right]. \tag{40}$$

Using the phase evolution model of Eq. (40), if we wish to preserve phase fidelity to a tolerance $\Delta\Phi$ over a coherence time $T_{\rm coh} \approx \tau - \tau_0$, then we need (in a naive estimate) to know the frequency and derivatives to a tolerance better than

$$\Delta f_{\rm GW} \approx \frac{\Delta\Phi}{2\pi}\frac{1}{T_{\rm coh}}, \tag{41}$$

$$\Delta \dot{f}_{\rm GW} \approx \frac{\Delta\Phi}{2\pi}\frac{2}{T_{\rm coh}^2}, \tag{42}$$

$$\Delta \ddot{f}_{\rm GW} \approx \frac{\Delta\Phi}{2\pi}\frac{6}{T_{\rm coh}^3}. \tag{43}$$

Hence the numbers of steps to take in $f_{\rm GW}$, $\dot{f}_{\rm GW}$, and $\ddot{f}_{\rm GW}$ to cover a given range in the parameters are proportional to $T_{\rm coh}$, $T_{\rm coh}^2$ and $T_{\rm coh}^3$, respectively—if it's necessary to step at all in those derivatives. Naively, for a search over a long enough coherence time to require multiple steps in $\ddot{f}_{\rm GW}$, one has a template count proportional to $T_{\rm coh}^6$ and, presumably, pays a price proportional to another factor of $T_{\rm coh}$ in computational cost in processing the associated data volume. In principle, then, the computational cost of a coherent search scales as the 7th power of the coherence time used, although, in practice the scaling tends not to be as extreme because the numbers of steps needed for $\ddot{f}_{\rm GW}$ can be small integers that take on new discrete values only slowly with increased $T_{\rm coh}$. In practice, these considerations for a 2nd frequency derivative come into play for only directed searches or for the deep follow-up of outliers from all-sky searches, when segment coherence times exceed several days. Section 3.6 will discuss more quantitatively the placement of search templates in parameter space to maintain acceptable phase tolerance.

In carrying out *all-sky* searches for unknown neutron stars, the computational considerations grow worse. The corrections for Doppler modulations and antenna pattern modulation due to the Earth's motion must be included, as for the targeted and directed searches, but the corrections are sky-dependent, and the spacing of the demodulation templates is dependent upon the inverse of the coherence time of the search. Specifically, for a coherence time $T_{\rm coh}$ the required angular resolution is (Abbott et al. 2008a)

$$\delta\theta \approx \frac{0.5\,\mathrm{c}\,\delta\mathrm{f}}{f\,[v\sin(\theta)]_{\rm max}}, \tag{44}$$

where θ is the angle between the detector's velocity relative to a nominal source

direction, where the maximum relative frequency shift $[\nu \sin(\theta)]_{\max}/c \approx 10^{-4}$, and where δf is the size of the frequency bins in the search. For $\delta f = 1/T_{\rm coh}$, one obtains:

$$\delta\theta \approx 9 \times 10^{-3}\,\text{rad}\left(\frac{30\,\text{minutes}}{\text{T}_{\text{coh}}}\right)\left(\frac{300\,\text{Hz}}{\text{f}_{\text{s}}}\right), \tag{45}$$

where $T_{\rm coh}$ = 30 min has been used in several all-sky searches to date. Because the number of required distinct points on the sky scales like $1/(\delta\theta)^2$, the number of search templates scales like $(T_{\rm coh})^2(f_s)^2$ for a fixed signal frequency f_s. Now consider attempting a search with a coherence time of 1 year for a signal frequency $f_s = 1$ kHz. One obtains $\delta\theta \sim 0.3$ μrad and a total number of sky points to search of $\sim 10^{14}$—again, for a fixed frequency. Adding in the degrees of freedom to search over ranges in f_s, $\dot{f}_s$ and $\ddot{f}_s$ (and higher-order derivatives, as needed) makes a brute-force, fully coherent 1-year all-sky search hopelessly impractical, given the Earth's present total computing capacity.

As a result, tradeoffs in sensitivity must be made to achieve tractability in all-sky searches. The simplest tradeoff is to reduce the observation time to a computationally acceptable coherence time. It can be more attractive, however, to reduce the coherence time still further to the point where the total observation time is divided into $N = T_{\rm obs}/T_{\rm coh}$, segments, each of which is analyzed coherently and the results added incoherently to form a detection statistic. One sacrifices intrinsic sensitivity per segment in the hope of compensating (partially) with the increased statistics from being able to use more total data. In practice, for realistic data observation spans (weeks or longer), the semi-coherent approach gives better sensitivity for fixed computational cost and hence has been used extensively in both all-sky and directed searches (Prix and Shaltev 2012). One finds a strain sensitivity (threshold for detection) that scales approximately as the inverse fourth root of N (Abbott et al. 2005a). Hence, for a fixed observation time, the strain sensitivity degrades roughly as $N^{\frac{1}{4}}$ as $T_{\rm coh}$ decreases (see Wette 2012) for a discussion of variations from this scaling). This degradation is a price one pays for not preserving phase coherence over the full observation time, in order to make the search computationally tractable. An important virtue of semi-coherent searches methods, however, is robustness with respect to deviations of a signal from an assumed coherent model.

In general, fully coherent search methods are potentially the most sensitive, but their applicability depends on several considerations, perhaps the most important being sheer computational tractability. Even when tractable for a particular search, moreover, a fully coherent initial search stage may incur a statistical trials factor large enough to make a putative detection questionable, because of the necessarily ultra-fine search needed to probe coherently a multi-dimensional signal parameter space. That is, the statistical significance of a nominally "loud" detection statistic must account for the number of independent trials carried out in the search. Applying *a priori* constraints instead, when available from electromagnetic observations or theoretical expectation, can reduce the parameter space volume and hence trials factor, making a detection more convincing. For example, a "5 σ" detection of a signal from a known pulsar in a targeted search might not qualify as even a weak

outlier in an all-sky search, much less as a discovery. (Dergachev 2010b) discusses the tradeoff between fully templated and "loose coherence" methods (see Sect. 3.3.4) in a broad parameter space, arguing against brute-force template application.

In the next sections, a variety of general approaches and specific algorithms will be presented, methods that attempt to achieve tradeoffs best suited to particular CW search types.

3.2 Signal model

CW searches must account for large phase modulations (or, equivalently, frequency modulations) of the source signal due to detector motion and potentially due to source motion (expecially for binary sources). The precision of the applied modulation corrections must be high in the case of *targeted* searches, which use measured ephemerides from radio, optical, X-ray or γ-ray observations valid over the gravitational-wave observation time. The precision must also be high in following up outliers from *directed* or *all-sky* searches, while much less precision is needed in the first stage of hierarchical searches. This section describes the intrinsic signal model assumed, along with the expected modulations due to detector motion.

For the Earth's motion, one has a daily relative frequency modulation of $v_{\mathrm{rot}}/c \approx 10^{-6}$ and a much larger annual relative frequency modulation of $v_{\mathrm{orb}}/c \approx 10^{-4}$. The pulsar astronomy community has developed a powerful and mature software infrastructure for measuring ephemerides and applying them in measurements, using the TEMPO 2 program (Hobbs et al. 2006). The same physical corrections for the Sun's, Earth's and Moon's motions (and for the motion of other planets), along with general relativistic effects including gravitational redshift in the Sun's potential and Shapiro delay for waves passing near the Sun, have been incorporated into the LIGO and Virgo software libraries (LIGO Scientific Collaboration 2018; Astone et al. 2002a).

Consider an isolated, rotating rigid triaxial ellipsoid (conventional model for a GW-emitting neutron star), for which the strain waveform detected by an interferometer can be written as

$$h(t) \;=\; F_{+}(t,\psi)\,h_0\,\frac{1+\cos^2(\iota)}{2}\,\cos(\Phi(t)) \;+\; F_{\times}(t,\psi)\,h_0\,\cos(\iota)\,\sin(\Phi(t)), \qquad (46)$$

where ι is the angle between the star's spin direction and the propagation direction $\hat{k}$ of the waves (pointing toward the Earth). F_+ and $F_\times$ are the (real) detector antenna pattern response factors ($-1 \le F_+, F_\times \le 1$) to the $+$ and $\times$ polarizations. F_+ and $F_\times$ depend on the orientation of the detector and the source, and on the polarization angle ψ (Abbott et al. 2004). Here, $\Phi(t)$ is the phase of the signal, which can often usefully be Taylor-expanded as in Eq. (40), in the solar system barycenter (SSB) time τ with apparent frequency derivatives with respect to detector-frame time arising from source motion. A more general signal model with GW emission at both once and twice the rotation frequency is considered in Jaranowski et al. (1998), with effects of free precession addressed in Jones and Andersson (2001), Jones and

Andersson (2002), and Van Den Broeck (2005); Gao et al. (2020), and a convenient reparametrization is presented in Jones (2015).

Explicitly, the time of arrival of a signal at the solar system barycenter, $\tau(t)$, can be written in terms of the signal time of arrival t at the detector:

$$\tau(t) \equiv t + \delta t = t - \frac{\vec{r}_d \cdot \hat{k}}{c} + \Delta_{E\odot} + \Delta_{S\odot}, \tag{47}$$

where $\vec{r}_d$ is the position of the detector with respect to the SSB, and $\Delta_{E\odot}$ and $\Delta_{S\odot}$ are solar system Einstein and Shapiro time delays, respectively (Taylor 1992; Hobbs et al. 2006).

Equation 47 implicitly assumes planar gravitational wavefronts and neglects proper motion of the source (transverse to the line of sight), corrections for which are common in radio pulsar astronomy (Lorimer and Kramer 2005; Lyne and Graham-Smith 2006). In principle, long-duration (multi-year) fully coherent observations of a near-enough ($\sim$ 100 pc), high-frequency ($\sim$ 1 kHz) CW source would allow inference of its distance from determination of the wavefront curvature (Seto 2005). Similarly, multi-year coherent observations of a high-frequency source would need to account for significant proper motions ($\sim$ 50 mas/year, typical of known pulsars) (Covas 2020). Both wavefront curvature and proper motion have been neglected in CW searches for unknown sources to date because the coherence times used in the searches don't require those corrections, but in the happy event of a future detection and subsequent extended observations, these corrections may become relevant.

Existing gravitational-wave detectors are far from isotropic in their response functions. In the long-wavelength limit, Michelson interferometers have an antenna pattern sensitivity with polarization-dependent maxima normal to their planes and nodes along the bisectors of the arms. As the Earth rotates at angular velocity Ω_r with respect to a fixed source, the antenna pattern modulation is quite large and polarization dependent via the functions $F_+(t)$ and $F_\times(t)$ which depend on the orientation of the detector and the source.

A commonly used parametrization of these amplitude response modulations is defined in (Jaranowski et al. 1998).

$$F_+(t) = \sin(\zeta)[a(t)\cos(2\psi) + b(t)\sin(2\psi)], \tag{48}$$

$$F_\times(t) = \sin(\zeta)[b(t)\cos(2\psi) - a(t)\sin(2\psi)], \tag{49}$$

where ζ is the angle between the arms of the interferometer (nearly or precisely 90 degrees for all major ground-based interferometers), and where ψ defines the polarization angle of the source wave frame (e.g., angle between neutron star spin axis projected onto the plane of the sky and local Cartesian coordinates aligned with its right ascension and declination directions). The antenna pattern functions $a(t)$ and $b(t)$ depend on the position and orientation of the interferometer on the Earth's surface, the source location and sidereal time:

$$
\begin{aligned}
a(t) = & \frac{1}{16}\sin(2\gamma)(3-\cos(2\lambda))(3-\cos(2\delta))\cos[2(\alpha-\phi_r-\Omega_r t)] \\
& -\frac{1}{4}\cos(2\gamma)\sin(\lambda)(3-\cos(2\delta))\sin[2(\alpha-\phi_r-\Omega_r t)] \\
& +\frac{1}{4}\sin(2\gamma)\sin(2\lambda)\sin(2\delta)\cos[(\alpha-\phi_r-\Omega_r t] \\
& -\frac{1}{2}\cos(2\gamma)\cos(\lambda)\sin(2\delta)\sin[(\alpha-\phi_r-\Omega_r t] \\
& +\frac{3}{4}\sin(2\gamma)\cos^2(\lambda)\cos^2(\delta),
\end{aligned}
\tag{50}
$$

$$
\begin{aligned}
b(t) = & \cos(2\gamma)\sin(\lambda)\sin(\delta)\cos[2(\alpha-\phi_r-\Omega_r t)] \\
& +\frac{1}{4}\sin(2\gamma)(3-\cos(2\lambda))\sin(\delta)\sin[2(\alpha-\phi_r-\Omega_r t)] \\
& +\cos(2\gamma)\cos(\lambda)\cos(\delta)\cos[\alpha-\phi_r-\Omega_r t] \\
& +\frac{1}{2}\sin(2\gamma)\sin(2\lambda)\cos(\delta)\sin[\alpha-\phi_r-\Omega_r t].
\end{aligned}
\tag{51}
$$

Specifically, in these equations, λ is the interferometer's latitude, and γ is the counterclockwise angle between the bisector of its arms and the eastward direction. The source direction is specified by right ascension α and declination δ, while ϕ_r is a deterministic phase defined implicitly by the interferometer's longitude. These functions reveal amplitude modulations with periods of 1/2 and 1 sidereal day, and in the case of $a(t)$, a constant term independent of time. As a result, the interferometer's response to a monochromatic source in the Earth center's reference frame will, in general, display five distinct frequency components, corresponding to the "carrier" frequency and two pairs of positive and negative sidebands, with a splitting between adjacent frequencies of $\frac{\Omega_r}{2\pi} \approx 1.16 \times 10^{-5}$ Hz.

Searches for CW signals must take into account the phase/frequency modulations embodied in Eq. (47) due to detector translational motion and the antenna pattern modulations embodied in Eqs. (48)–(51) due to detector orientation changes.

Figure 9 shows a sample spectrogram of a pure signal simulation using one of the so-called "hardware injections" used in LIGO data runs. These signal simulations are used to verify end-to-end the detector's response to a CW signal, including sustained phase coherence over long durations. The simulations are injected via "photon calibrators," which are auxiliary lasers shining on mirrors with a modulated intensity. The imposed relative motion of the mirror mimics (in the long-wavelength regime) the response of the interferometer to a gravitational wave. Various such signals, ranging in nominal frequency from 12 to 2991 Hz were injected into the LIGO detectors over the O1, O2 and O3 observation runs (Biwer et al. 2017). In the example shown, a signal ("Pulsar 2") with source frequency 575.163573 Hz (reference time = November 1, 2003 00:00 UTC) and spin-down -1.37×10^{-13} Hz/s is simulated at a sky location of right ascension $\alpha = 3.75692884$ radians (14 h 21 m 1.48 s) and declination $\delta = 0.060108958$ radians (3° 26' 38.36"). Its orientation is defined by inclination angle $\iota = 2.76$ radians (158. deg), and polarization angle $\psi =$

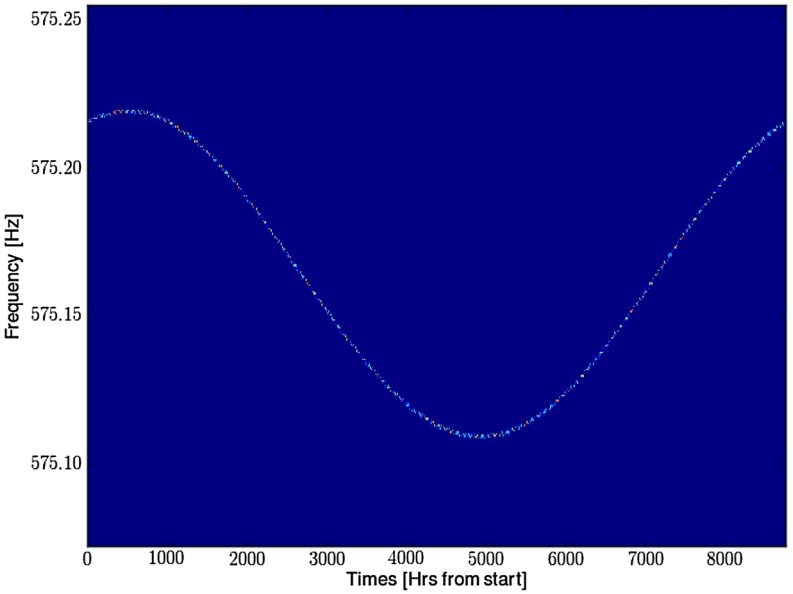

Fig. 9 Sample signal spectrogram for a LIGO "hardware injection" (negligible noise), where the pixel dimensions are 0.5 h by 0.556 mHz

−0.222 radians (−12.7 deg). The simulation shown (with negligible noise for clarity) in Fig. 9 applies over a duration of the calendar year 2019 UTC. One can see the annual modulation from the Earth's orbit imposed on an imperceptible decrease in the intrinsic frequency. A zoom of 100-h duration is also shown in Fig. 10, to indicate the much smaller frequency modulation (by $\sim$ 2 orders of magnitude), along with the intensity modulation.

As seen from the spectrogram, the frequency modulations lead to stationary bands at the turning points of the modulation. As a result, the spectrum averaged over the signal duration peaks at the turning points, as shown in Fig. 11. These "horns" are a characteristic spectral signature of expected signals, where the relative heights of the horns depend on the duration of the observation and on the Earth's orbital phase at the start. For a signal with negligible spin-down and a duration equal to a multiple of a year, the horns are approximately symmetric, but in the general case that includes observations of a few months or less, one or both horns may not be apparent. A more detailed analysis of the Fourier transform of a CW signal can be found in Valluri et al. (2021).

In the following, we discuss in more detail the implementations of a selection of these methods developed in searches of the initial LIGO and Virgo data sets (2001–2011) and that have been further refined for searches of advanced detector data. Section 4 presents the results of each type, from searches in the data of Advanced LIGO's and Virgo's observing runs O1, O2 and O3.

The volume of parameter space over which to search increases in large steps as one progresses through these categories. In each category a star can be isolated or

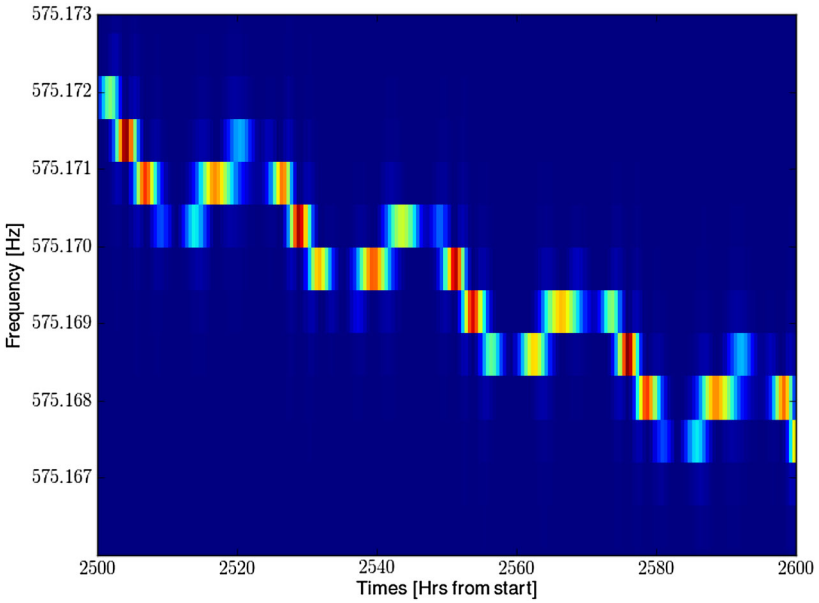

Fig. 10 Zoomed-in sample signal spectrogram for a LIGO "hardware injection" (100 h from spectrogram in Fig. 9). The sidereal Doppler modulations ($\sim$ 24 h) of frequency and amplitude modulations ($\sim$ 12 and 24 h) are more apparent

binary. Any unknown binary orbital parameters further increase the search volume. In all cases we expect (and have now verified from unsuccessful searches to date) that source strengths are very small. Hence one must integrate data over long observation times to have any chance of signal detection. How much one knows about the source governs the nature of that integration. In general, the greater that knowledge, the more computationally feasible it is to integrate data coherently (preserving phase information) over long observation times, for reasons explained below.

3.3 Broad approaches in CW searches

Computational cost depends critically upon the search method used, which in turn, depends on the *a priori* knowledge one has about the source. In the following, a broad overview is given of a few key search methods used in published searches to date. More details of implementation are presented in Sect. 4, where a selection of these methods is applied to particular classes of potential CW sources.

In this overview, a simplified "toy model" will be used to illustrate scaling relations. Methods specific to correcting for modulations will be addressed further below in the presentation of particular search implementations. For now, amplitude modulation of the signal strength due to rotation of the GW detectors with respect to the source is ignored in the following, along with Doppler modulations.

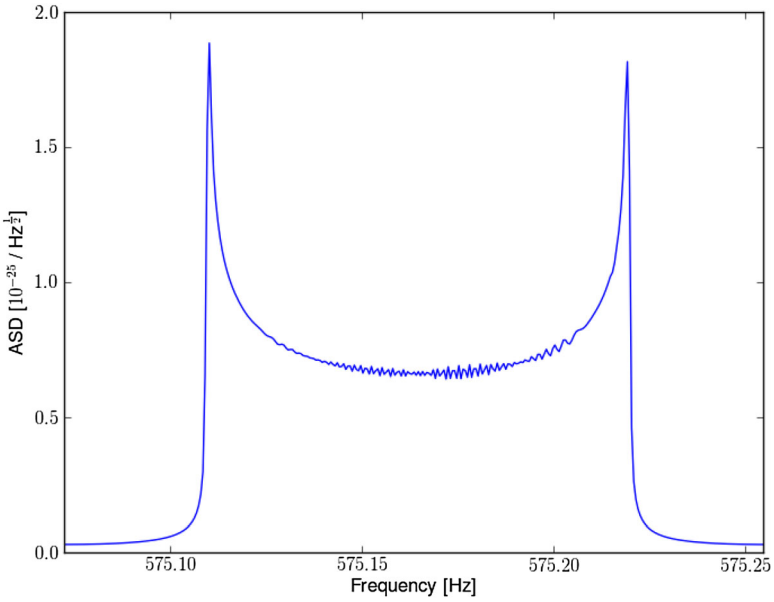

Fig. 11 Sample signal amplitude spectral density for a LIGO "hardware injection" (same injection as for spectrograms in Fig. 9)

3.3.1 Fully coherent methods

When applicable, as discussed in Sect. 3.1, fully coherent methods provide the best sensitivity. Explicit search methods, taking into account source frequency and amplitude evolution along with detector noise non-stationarity, are discussed in Sect. 4.1. Here, though, let's consider the highly simplified problem of detecting a sinuosidal signal of amplitude h_0 and known frequency $f_{\rm sig}$, but with unknown phase constant, in random Gaussian noise.

Imagine the data observation is continuous of duration $T_{\rm obs}$ and has a one-sided power spectral noise density function $S_h(f_{\rm GW})$, and for convenience, assume $f_{\rm sig}$ is an integer multiple of $1/T_{\rm obs}$ (see (Allen et al. 2002) for a didactic treatment of the more general case). The DFT bin $\tilde{D}_i$ is defined by the following sum over a real time series of length $N_{\rm sample} = f_{\rm sample} T_{\rm obs}$ with values d_j ($j = 0...N_{\rm sample}$) where $f_{\rm sample}$ is the sampling frequency of the data stream:

$$\tilde{D}_i = \sum_{j=0}^{N_{\rm sample}-1} d_j e^{-{\rm i}2\pi {\rm j}i/{\rm N}_{\rm sample}}. \tag{52}$$

From the DFT, one can define the one-sided power spectral noise density estimate S_{h_i}:

$$S_{h_i} = \frac{2\left\langle\left[\left(\Re\{\tilde{D}_i\}\right)^2 + \left(\Im\{\tilde{D}_i\}\right)^2\right]\right\rangle T_{\mathrm{obs}}}{N_{\mathrm{sample}}^2} = \frac{2\langle|\tilde{D}_i|^2\rangle T_{\mathrm{obs}}}{N_{\mathrm{sample}}^2}, \tag{53}$$

for $0 < i < N_{\mathrm{sample}}/2$ and where "$\langle\ \rangle$" indicates an expectation value in the absence of signal (e.g., determined from an average over many nearby bins *and excluding the bin i itself*). Then one can construct a dimensionless detection statistic ρ_i^2 using the measured strain power in the DFT bin $\tilde{D}_i$ corresponding to a signal frequency f_{sig}:

$$\rho_i^2 = 4\frac{|\tilde{D}_i|^2 T_{\mathrm{obs}}}{N_{\mathrm{sample}}^2 S_{h_i}}, \tag{54}$$

which follows a non-central χ^2 distribution with two degrees of freedom and a non-centrality parameter $\lambda(h_0) = \frac{h_0^2 T_{\mathrm{obs}}}{S_{h_i}}$, which implies an expectation value $2 + \frac{h_0^2 T_{\mathrm{obs}}}{S_{h_i}}$ and variance $4 + 4\frac{h_0^2 T_{\mathrm{obs}}}{S_{h_i}}$. In Gaussian noise one expects a χ^2 distribution with two degrees of freedom from summing the squares of the normally distributed real and imaginary DFT coefficients.

In the absence of a signal, one can define a threshold value ρ_i^* corresponding to a false alarm probability α such that the cumulative density probability function satisfies:

$$\mathrm{CDF}_{\mathrm{noise}}[\rho_{\mathrm{i}}^{*2}] \equiv \int_0^{\rho_{\mathrm{i}}^{*2}} \mathrm{p}_{\mathrm{noise}}(\rho_{\mathrm{i}}^2; 2)\,\mathrm{d}(\rho_{\mathrm{i}}^2) \equiv 1 - \alpha, \tag{55}$$

where the probability density function is (χ^2 with two degrees of freedom)

$$p_{\mathrm{noise}}(x; 2) = \frac{1}{2}e^{-x/2}. \tag{56}$$

From this threshold and a desired false dismissal rate β, one can then determine the corresponding signal amplitude $h_0^{1-\beta}$ from

$$\mathrm{CDF}_{\mathrm{signal+noise}}[\rho_{\mathrm{i}}^{*2}] \equiv \int_0^{\rho_{\mathrm{i}}^{*2}} \mathrm{p}_{\mathrm{signal+noise}}(\rho_{\mathrm{i}}^2; 2, \lambda(\mathrm{h}_0^{1-\beta}))\,\mathrm{d}(\rho_{\mathrm{i}}^2) = \beta, \tag{57}$$

where the probability density function is (non-central χ^2 with two degrees of freedom)

$$p_{\mathrm{signal+noise}}(x; 2, \lambda) = \frac{1}{2}e^{-(x+\lambda)/2} I_0(\sqrt{\lambda x}), \tag{58}$$

and where $I_0(y)$ is a modified Bessel function of the first kind:

$$I_0(y) = \sum_{j=0}^{\infty} \frac{(y^2/4)^j}{(j!)^2}. \tag{59}$$

Choosing a 1% false alarm probability ($\alpha = 0.01$) leads to $\rho_i^{*2} \approx 9.21$, from which numerical evaluation of Eq. 57 for a false dismissal probability $\beta = 5\%$ leads to an expected sensitivity $h_0^{95\%}$ of

$$h_0^{95\%} \approx 4.54 \sqrt{\frac{S_{h_i}}{T_{\mathrm{coh}}}}, \tag{60}$$

which can be taken as a proxy for the expected 95% confidence level upper limit on signal amplitude based simply on an observation that an observed ρ_i does not exceed ρ_i^*. In practice, many CW search upper limits are based on the loudest statistic found in a search, (e.g., largest ρ^2 value for multiple computations at different frequencies), regardless of whether or not a pre-defined threshold has been exceeded. (Tenorio et al. 2022) discusses the statistics of loudest candidates using extreme value theory.

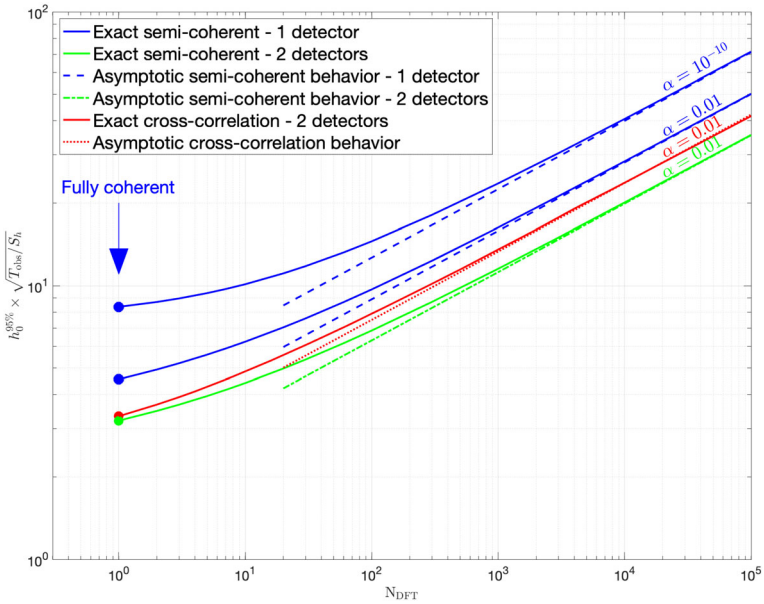

Fig. 12 Strain sensitivities (defined by $\alpha = 0.01$ or $\alpha = 10^{-10}$; and $\beta = 0.05$) of various search methods to a bin-centered sinusoidal signal in noise of power spectral density S_h versus the number of DFT segments into which a fixed observing time T_{obs} is divided. Curves are shown for $h_0^{95\%}$ for $\alpha = 0.01$ and $\alpha = 10^{-10}$ for semi-coherent searches in a single detector's data (blue) and for $\alpha = 0.01$ in two-detector searches (green). Asymptotic expressions based on the large-N_{seg} Gaussian approximation are shown as dashed lines. The points at the bottom left of each curve represent the fully coherent search sensitivities for 1 and 2 identical detectors. Semi-coherent curves for two detectors assumed coherent summing of simultaneous DFTs for the 2 detectors. Sensitivities for cross-correlation of simultaneous data from two detectors are also shown (red)

The sensitivity expression in Eq. (60) is shown as the leftmost point of the lower blue curve in Fig. 12, where it can be compared to sensitivities from other methods, discussed below.

If simultaneous data sets from two independent detectors of identical sensitivity are added coherently (and a phase correction applied, to account for detector separation and source direction), one can construct a combined averaged detection statistic $\rho^2_{i,\mathrm{comb}}$ using the measured power from the square of the sum of the simultaneous DFT bin coefficients $\tilde{D}_{1,i}$ and $\tilde{D}_{2,i}$ containing f_{sig}:

$$\rho^2_{i,\mathrm{comb}} = \frac{1}{2}\left[4\frac{|\tilde{D}_{1,i} + \tilde{D}_{2,i}|^2\, T_{\mathrm{obs}}}{N^2_{\mathrm{sample}} S_{h_i}}\right] \tag{61}$$

which has an expectation value of $2 + \frac{2\,h_0^2 T_{\mathrm{obs}}}{S_{h_i}}$ and a variance of $4 + \frac{8\,h_0^2 T_{\mathrm{obs}}}{S_{h_i}}$, that is, it follows a non-central χ^2 distribution with two degrees of freedom and a non-centrality parameter $\lambda(h_0) = \frac{2\,h_0^2 T_{\mathrm{obs}}}{S_{h_i}}$. Applying the same methodology as above for a single detector, one obtains an expected sensitivity of

$$h_0^{95\%} \approx \frac{1}{\sqrt{2}} \times 4.54 \sqrt{\frac{S_{h_i}}{T_{\mathrm{coh}}}}, \tag{62}$$

indicating an improvement by $\sqrt{2}$ with respect to a single detector. This sensitivity is shown as the leftmost point of the green curve in Fig. 12. More generally, N identical detectors with simultaneous data sets,[8] for which phase corrections are known, gain a sensitivity improvement of $\sqrt{N}$ with respect to a single detector, as one would naively expect. Put another way, combining the N sets gives a sensitivity equal to that of a single detector with an amplitude spectral noise density of $\sqrt{S_{h_i}/N}$. Again, this is a simplified model. In practice, detectors have different, frequency-dependent S_{h_i} noise levels and unequal live times of observing, in addition to different orientations affecting antenna pattern sensitivity, ignored here.

3.3.2 Semi-coherent methods

Fully coherent methods are computationally costly when covering a large parameter space because of the fine steps needed to avoid missing a signal as coherence times increase. A crude solution is simply to reduce the coherence time and suffer the reduction in strain sensitivity, by approximately $\sqrt{T_{\mathrm{coh}}}$. A better solution is to apply a *semi-coherent* method in which the observation time is divided into N_{seg} segments of equal length $T_{\mathrm{coh}} = T_{\mathrm{obs}}/N_{\mathrm{seg}}$, where the detection statistic is constructed from an incoherent sum of powers from the individual segments. This method sacrifices the constraint of phase consistency among the different segments and hence is less sensitive than a fully coherent method, but is more sensitive than analysis of a single

[8] Simultaneity is not strictly required, if phase corrections for time offsets between detectors can be computed precisely enough.

segment alone. As shown below, the strain sensitivity scales with $1/N_{\rm seg}^{\frac{1}{4}}$ for fixed coherence time and large $N_{\rm seg}$.

For illustration, consider a detection statistic constructed from the sum of $N_{\rm seg}$ individual DFT powers covering the observation time $T_{\rm obs}$, and once again, each normalized by its power spectral density (taken to be stationary here, for convenience):

$$R_i \equiv \sum_{k=1}^{N_{\rm seg}} 4\frac{|\tilde{D}_i^{(k)}|^2 T_{\rm coh}}{N_{\rm sample}^2 S_{h_i}}, \tag{63}$$

where $N_{\rm seg} = 1$ yields $R_i = \rho_i^2$ in Eq. (54). The underlying statistical distribution of R_i is that of a non-central χ^2 with $2N_{\rm seg}$ degrees of freedom and a non-centrality parameter of $\lambda(h_0) = N_{\rm seg}\frac{h_0^2 T_{\rm coh}}{S_{h_i}}$.

In the absence of signal a false alarm probability α implies a threshold R_i^*, found from requiring that the cumulative probability density function satisfy:

$$\mathrm{CDF}_{\rm noise}[R_i^*] \equiv \int_0^{R_i^*} p_{\rm noise}(R_i; 2)\, dR_i \equiv 1 - \alpha, \tag{64}$$

where the probability density function is

$$p_{\rm noise}(x; 2N_{\rm seg}) = \frac{x^{N_{\rm seg}-1} e^{-x/2}}{2^{N_{\rm seg}}\Gamma(N_{\rm seg})}, \tag{65}$$

which reduces to Eq. (56) for $N_{\rm seg} = 1$. R_i^* can be determined numerically for arbitrary $N_{\rm seg}$, but in the limit of large $N_{\rm seg}$, $p_{\rm noise}$ reduces to a normal distribution with a mean of $2N_{\rm seg}$ and variance $4N_{\rm seg}$, in which approximation $R_i^*(\alpha = 0.01) \approx 2N_{\rm seg} + 4.65\sqrt{N_{\rm seg}}$.

In the presence of a signal, the $h_0^{95\%}$ value can be obtained numerically from the cumulative probability density function:

$$\mathrm{CDF}_{\rm signal+noise}[R_i^*] \equiv \int_0^{R_i^*} p_{\rm signal+noise}(R_i; 2, h_0)\, dR_i = \beta, \tag{66}$$

where the probability density function is

$$p_{\rm signal+noise}(x; 2N_{\rm seg}, h_0) = \frac{1}{2} e^{-\frac{1}{2}\left(x + \frac{h_0^2 T_{\rm obs}}{S_h}\right)} \left(\frac{x S_h}{h_0^2 T_{\rm obs}}\right)^{\frac{N_{\rm seg}-1}{2}} I_{N_{\rm seg}-1}\left(h_0\sqrt{\frac{x T_{\rm obs}}{S_h}}\right) \tag{67}$$

which reduces to Eq. (58) for $N_{\rm seg} = 1$, where $T_{\rm obs} = N_{\rm seg} T_{\rm coh}$ has been used.

In the limit of large $N_{\rm seg}$ and weak signal, however, the distribution approaches that of a Gaussian with variance $4N_{\rm seg}$, from which an approximate expression for $h_0^{95\%}$ can be obtained:

$$h_0^{1-\beta} \approx \sqrt{2}\left[\sqrt{2}\left(\mathrm{erfc}^{-1}(2\alpha) + \mathrm{erfc}^{-1}(2\beta)\right)\right]^{1/2} N_{\mathrm{seg}}^{\frac{1}{4}} \sqrt{\frac{S_h}{T_{\mathrm{obs}}}}, \tag{68}$$

where erfc is the inverse complementary error function. This scaling of sensitivity with $N_{\mathrm{seg}}^{\frac{1}{4}}$ for fixed observation time is a universal result in semi-coherent searches with large N_{seg} (Krishnan et al. 2004; Mendell and Landry 2005; Prix and Shaltev 2012; Wette 2012). It can be understood qualitatively from the SNR of an approximately Gaussian detection statistic (large N_{seg}) scaling with $\sqrt{N_{\mathrm{seg}} T_{\mathrm{coh}}} = \sqrt{T_{\mathrm{obs}}/N_{\mathrm{seg}}}$ and the direct dependence of that detection statistic on the squared signal amplitude.

For $\alpha = 0.01$ and $\beta = 0.05$, Eq. 68 yields $h_0^{95\%} \approx 2.82 N_{\mathrm{seg}}^{\frac{1}{4}} \sqrt{S_h/T_{\mathrm{obs}}}$. This expression does *not* agree with Eq. (60) when $N_{\mathrm{seg}} = 1$ because the Gaussian approximation breaks down for small N_{seg}. For the much lower false alarm probability $\alpha = 10^{-10}$, Eq. (68) yields $h_0^{95\%} \approx 4.00 N_{\mathrm{seg}}^{\frac{1}{4}} \sqrt{S_h/T_{\mathrm{obs}}}$. These asymptotic approximations are shown as dashed lines in Fig. 12, together with numerically evaluated values from Eq. (66).

As is the case for combining data in a fully coherent search from two identical detectors with simultaneous data sets, there is a gain of $\sqrt{2}$ in sensitivity for combining simultaneous DFTs from two detectors in a semi-coherent search—as long as the DFT coefficients are combined coherently for each segment (otherwise, the gain is only $2^{1/4}$ from semi-coherent combination of DFT powers). Figure 12 shows exact (solid green curve) and asymptotic (dashed green line) results for two detectors.

An important variation on semi-coherent methods, used in Hough transform methods described below, applies *thresholding* to DFT powers prior to summing. By applying a threshold corresponding to a relatively high false alarm rate (and relatively high false dismissal rate for weak signals), one can reduce the data volume in processing, to reduce computational cost. In addition, by adding integer counts (or, optimally, pre-computed weights) instead of measured DFT powers, one's detection statistic is less susceptible to distortions from transient, non-Gaussian outliers from instrumental contamination. The optimum false alarm probability for thresholding in this idealized sine-wave detection analysis (weak-signal limit) is ≈20% (Allen et al. 2002).

3.3.3 Cross-correlation methods

Another attractive approach uses cross correlation between independent (and ideally, simultaneous) data streams. The canonical example is cross correlation between coincident data sets taken with the nearly aligned Hanford and Livingston interferometers, but cross correlation can also be used with poorly aligned detector pairs and with non-coincident data streams—if sufficient signal coherence can be established over longer time scales. In this section, only truly coincident data sets will be considered, for simplicity.

Once again, let's use the artificial but informative toy model of a bin-centered, constant-amplitude sinusoidal signal in Gaussian noise. Let's also assume two identically oriented detectors (approximation to Hanford-Livingston, which have normal vectors to their planes only 27.3 degrees apart (Althouse et al. 1998), in addition to a 90-degree relative rotation about the normal, leading to a sign flip in GW response). Also assume that the relative positions of the detectors can be accounted for via a signal phase correction for any given source direction. In the following, that phase correction is assumed to have been applied.

Using the notation from Sect. 3.3.2, we can combine the two independent data streams via DFT coefficients in a narrow band of interest to define a new detection statistic:

$$\rho_{\mathrm{CC}} = \frac{2\sqrt{2}\,\Re\left\{\tilde{D}_{1,i}\tilde{D}^{*}_{2,i}\right\}T_{\mathrm{obs}}}{N^{2}_{\mathrm{sample}}S_{h_i}}. \tag{69}$$

In the absence of a signal, this statistic has an expectation value of zero and (by construction) a variance of one. The underlying statistical distribution is far from Gaussian, however. In the absence of a signal, one has the sum of two normal product distributions (from $\Re\left\{\tilde{D}_{1,i}\tilde{D}^{*}_{2,i}\right\} = \Re\left\{\tilde{D}_{1,i}\right\}\Re\left\{\tilde{D}_{2,i}\right\} + \Im\left\{\tilde{D}_{1,i}\right\}\Im\left\{\tilde{D}_{2,i}\right\}$), which can be obtained analytically, using characteristic functions.

Specifically, a single normal production distribution for the product of two zero-mean normal distributions of variance σ_1^2 and σ_2^2 is

$$p_{1\,\mathrm{normal\,product}}(x) = \frac{1}{\pi\sigma_1\sigma_2}K_0\left(\frac{|x|}{\sigma_1\sigma_2}\right), \tag{70}$$

where K_0 is a modified Bessel function of the second kind, and for which the characteristic function is (McNolty 1973)

$$\mathrm{CF}[\mathrm{K}_0\left(\frac{|\mathrm{x}|}{\sigma_1\sigma_2}\right)] = \frac{1}{\sqrt{1+\sigma_1^2\sigma_2^2\mathrm{t}^2}}. \tag{71}$$

Inverting the product of characteristic functions gives the following probability distribution for the sum of two such (signal-free) normal product distributions:

$$p_{2\,\mathrm{normal\,products}}(x) = \frac{1}{2\sigma_1\sigma_2}e^{-\frac{|x|}{\sigma_1\sigma_2}}. \tag{72}$$

For identical detectors ($\sigma_1 = \sigma_2 \equiv \sigma$) of power spectral density S_{h_i} with a signal present of amplitude h_0, the expectation value of ρ_{CC} is $\frac{h_0^2 T_{\mathrm{obs}}}{\sqrt{2}\,S_{h_i}}$, and the variance is $1 + \frac{h_0^2 T_{\mathrm{obs}}}{S_{h_i}}$.

In the presence of a common signal h_0 in both data streams, one can evaluate numerically the value $h_0^{1-\beta}$ for which the false dismissal rate is β for a threshold on the detection statistic corresponding to the signal-free false alarm probability α. In the absence of a signal, the threshold on ρ_{CC} for a false alarm probability $\alpha = 0.01$ is

approximately 2.766. For $\beta = 0.05$ one then finds $h_0^{95\%} \approx 3.335\sqrt{S_{h_i}/T_{\rm obs}}$, which is only slightly higher than that obtained for a fully coherent search using data from two identical detectors (see Fig. 12).

As with semi-coherent searches, discussed in Sect. 3.3.2, one typically finds it necessary in wide-parameter searches to segment the data. As before, consider dividing the observation time $T_{\rm obs}$ into $N_{\rm seg}$ equal-duration segments of coherence time $T_{\rm coh}$. In the presence of a signal of amplitude h_0, the following detection statistic,

$$\rho_{\rm CC}^{N_{\rm seg}} = \frac{1}{N_{\rm seg}} \sum_{i=1}^{N_{\rm seg}} \rho_{\rm CC}^{i}, \tag{73}$$

has a mean value of $\frac{h_0^2 T_{\rm coh}}{\sqrt{2} S_{h_i}} = \frac{1}{N_{\rm seg}} \frac{h_0^2 T_{\rm obs}}{\sqrt{2} S_{h_i}}$ and variance $\frac{1}{N_{\rm seg}} \left[1 + \frac{h_0^2 T_{\rm obs}}{S_{h_i}}\right]$.

In the regime of large $N_{\rm seg}$ and weak signal, the underlying probability distribution approaches that of a Gaussian for which one expects:

$$h_0^{1-\beta} \approx \sqrt{2} \left[\sqrt{2}\left(\mathrm{erfc}^{-1}(2\alpha) + \mathrm{erfc}^{-1}(2\beta)\right)\right]^{1/2} \left[\frac{N_{\rm seg}}{2}\right]^{\frac{1}{4}} \sqrt{\frac{S_h}{T_{\rm obs}}}. \tag{74}$$

This asymptotic expectation is shown as a dotted red line in Fig. 12, together with results from numerical simulation over a range of $N_{\rm seg}$ values (solid red curve). This detection statistic is $2^{1/4}$ more sensitive than the asymptotic 1-detector semicoherent sensitivity (lower dashed blue curve), equally sensitive to the asymptotic 2-detector semicoherent sensitivity for which powers from separate detectors are added (not shown), and $2^{1/4}$ less sensitive than the asymptotic 2-detector semicoherent behavior with coherent summing of simultaneous DFTs from the 2 detectors before computing power, as in Eq. (61) (green dash-dotted curve).

One practical consideration to keep in mind for these comparisons is that while coherent summing or cross-correlation of simultaneous DFTs provides improved sensitivity where possible, those gains are limited by achievable livetimes of interferometers that operate near their technological limits.

One can compute nominal signal-to-noise ratios for given signal strengths for the coherent, semi-coherent and cross-correlations methods from the noise-only variances and the expectation value dependences on signal h_0 presented above. Those SNRs allow sensible direct comparisons among semi-coherent and cross-correlation methods when $N_{\rm seg}$ is large enough for the noise-only detection statistics to exhibit approximate Gaussian behavior over the range of interest, but for small $N_{\rm seg}$, including especially the fully coherent case of $N_{\rm seg} = 1$, the underlying statistics are highly non-Gaussian, requiring care in making comparisons.

3.3.4 Long-lag cross-correlation and loose coherence

Fully coherent, long integrations seem distinctly different from the multiple-short-segment searches based on semi-coherent and cross-correlation described (in simplified form) above, and in fact, using fully coherent methods to follow up on

outliers produced by the latter methods is challenging because of the typical mismatch in parameter space fineness. Nonetheless, between these extremes exist bridges that offer the possibility of both systematic follow-up of outliers and more sensitive initial stages for multi-segment searches. The first method is long-lag correlation (Dhurandhar et al. 2008), and the second method is known as loose coherence (Dergachev 2010b).

Each method benefits from coherently summing DFT coefficients from data segments offset in time, which can be motivated by considering the segmentation of a single (continuous) Fourier transform of a strain signal $h(t)$ into $N_{\rm seg}$ segments:

$$F(\omega;[t_A,t_B]) \equiv \frac{1}{T}\int_{t_A}^{t_B} h(t)e^{-i\omega(t-t_A)}dt \tag{75}$$

$$= \frac{e^{i\omega t_A}}{N_{\rm seg}}\sum_{i=1}^{N_{\rm seg}} \frac{e^{-i\omega t_{i-1}}}{T_{\rm seg}}\int_{t_{i-1}}^{t_i} h(t)e^{-i\omega(t-t_{i-1})}dt \tag{76}$$

$$= \frac{e^{i\omega t_A}}{N_{\rm seg}}\sum_{i=1}^{N_{\rm seg}} e^{-i\omega t_{i-1}}F(\omega;[t_{i-1},t_i]) \tag{77}$$

$$= \frac{e^{i\omega t_A}}{N_{\rm seg}}\sum_{i=1}^{N_{\rm seg}} e^{-i\phi_i}F_i(\omega), \tag{78}$$

where $T_{\rm seg} = (t_B - t_A)/N_{\rm seg}$, $t_i = t_A + iT_{\rm seg}$ and $\phi_i = \omega t_{i-1}$. Hence the Fourier transform for the full data span is proportional to the sum of transforms for the individual segment transforms with phase corrections $e^{-i\phi_i}$.

Now consider once again the artificial but informative special case of a monochromatic signal detected via its strength in DFT bins from two detectors 1 and 2 with identical observation periods segmented into $N_{\rm DFT}$ epochs for which DFT are computed. For simplicity, assume the signal is bin-centered for each epoch's DFT and that the detector noise is both stationary and identical for the two detectors. Guided by the relation above, one can then define a detection statistic based on the coherent sum of *all* DFTs from both detectors:

$$P = \left|\sum_{i=1}^{N_{\rm DFT}}\left[\tilde{D}_{1,i}e^{-i\phi_{1,i}} + \tilde{D}_{2,i}e^{-i\phi_{2,i}}\right]\right|^2 \tag{79}$$

$$= \sum_{I,J=1}^{2}\sum_{i,j=1}^{N_{\rm DFT}} \tilde{D}_{I,i}\tilde{D}^*_{J,j}e^{-i(\phi_{I,i}-\phi_{J,j})}, \tag{80}$$

where $\phi_{1,i}$ and $\phi_{2,i}$ account for the signal phase evolution for each detector for each DFT i and for any geometric offset between the detectors relative to the source direction (see Eq. 47). This full double sum is computationally costly to evaluate explicitly, not only because of the additional operations, but more important, because the implicit full coherence requires a fine stepping in parameter space. The form,

however, makes more clear the relations between full coherence and both semi-coherence and cross-correlations (Dhurandhar et al. 2008), which can be viewed as subsets of the double sum. A semi-coherent sum of powers from individual detectors can be represented by

$$P_{\text{semi-coherent}} = \sum_{I=1}^{2} \sum_{i=1}^{N_{\text{DFT}}} \tilde{D}_{I,i} \tilde{D}^{*}_{I,i}, \tag{81}$$

while cross-correlation of simultaneous amplitudes (see Eq. 73) from the two detectors is proportional to

$$P_{\text{cross-correlation}} = \sum_{(I \neq J)=1}^{2} \sum_{i=1}^{N_{\text{DFT}}} \tilde{D}_{I,i} \tilde{D}^{*}_{J,i} e^{-i(\phi_{I,i} - \phi_{J,j})}. \tag{82}$$

This last relation suggests the possibility of following up an interesting search outlier from the first stage of a simultaneous-segment cross-correlation search by increasing the number of terms kept from the full double sum, allowing non-simultaneous cross terms and allowing self-correlation terms. For example, allowing an offset of up to N_{lag} segment durations would yield:

$$P_{\text{cross-correlation}(\text{N}_{\text{lag}})} = \sum_{I,J=1}^{2} \sum_{\substack{i,j=1; \\ |i-j| \leq N_{\text{lag}}}}^{N_{\text{DFT}}} \tilde{D}_{I,i} \tilde{D}^{*}_{J,j} e^{-i(\phi_{I,i} - \phi_{J,j})}. \tag{83}$$

This approach can also be used at the first stage if rapid frequency evolution of the source, such as in a short-period binary system or in young object, argues for short DFT coherence times.

Another, related approach is to define a "loosely coherent" detection statistic as a subset of the original sum for which phase correlation between nearby (small-lag) DFT coefficients is favored (as opposed to the completely random relation allowed by semi-coherent sums). To illustrate,[9] consider for simplicity a sum restricted to a single detector. Assume the phase correction applied to a product of DFT coefficients for segments separated by a single segment lag is taken to be unknown but uniformly distributed in probability between $-\delta$ and $+\delta$. A useful detection statistic can then be formed by (Dergachev 2010b)

[9] For simplicity, the initial implementation of loose coherence is described here. Later refinements (Dergachev 2012, 2018; Dergachev and Papa 2019) led to substantial performance improvements.

$$P_{\text{loose-coherence}} = \frac{1}{(2\delta)^{N_{\text{seg}}-1}} \int_{-\delta}^{+\delta} d\Delta\phi_{1,2} \int_{-\delta}^{+\delta} d\Delta\phi_{2,3} \ldots \int_{-\delta}^{+\delta} d\Delta\phi_{N_{\text{seg}}-2,N_{\text{seg}}-1} \sum_{i,j}^{N_{\text{seg}}} \tilde{D}_{I,i} \tilde{D}^{*}_{I,j} e^{-i(\Delta\phi_{i',i'+1}+\Delta\phi_{i'+1,i'+2}+\ldots+\Delta\phi_{j'-1,j'})}, \tag{84}$$

where $i'(j') = \min(\max)\{\mathrm{i},\mathrm{j}\}$ and $\Delta\phi_{m,n} = \phi_n - \phi_m$. Evaluation of the integrals leads to

$$P_{\text{loose-coherence}} = \sum_{i,j}^{N_{\text{seg}}} \tilde{D}_{I,i} \tilde{D}^{*}_{I,j} \left(\frac{\sin(\delta)}{\delta}\right)^{|i-j|}, \tag{85}$$

where the factor $\left(\frac{\sin(\delta)}{\delta}\right)^{|i-j|}$ weights adjacent-lag products more heavily than those with longer lags (and yields unity for $i = j$). The single-detector semicoherent power sum is recovered by setting $\delta = \pi$. In practice, to reduce computational cost, the factor is replaced by a discrete kernel function that truncates terms for which the weight contribution is too small to warrant the additional operations. A generalized version of this detection statistic, including more than one detector and non-integer segment lags, has been used in multi-stage searches with decreasing δ at each stage, e.g., $\delta = \pi \rightarrow \pi/2 \rightarrow \pi/4 \rightarrow \pi/8$. Each reduction in δ brings an increase in computational cost per parameter space volume as more terms are retained in the sum and the parameter space is searched more finely ("zooming in").

3.4 Barycentering and coherent signal demodulation

Taking into account the phase/frequency modulations of Eq. (47) due to detector translational motion and the antenna pattern modulations embodied in Eqs. (48)–(51) due to detector orientation changes requires an accurate model of relevant solar system motions. As noted above, the gravitational-wave community has adopted techniques of pulsar astronomy researchers, with many LIGO data searches using the TEMPO 2 program (Hobbs et al. 2006) as a guide and for cross-checking (LIGO Scientific Collaboration 2018; Abbott et al. 2004). Correction for the Earth's and a detector's motions with respect to the solar system barycenter is called barycentering. Independently, Virgo analysts developed another barycentering software package (Astone et al. 2008), also checked against TEMPO 2 and the LIGO software. These packages choose steps in time fine enough to allow reliable interpolation of detector motion between sampled times.

Several approaches to incorporating the corrections have been developed for continuous gravitational-wave searches. These include time-domain heterodyning, Fourier-domain decomposition and hybrid techniques, as discussed below. More recently, techniques have been developed for more computationally efficient barycentering for use in targeted searches (Pitkin et al. 2018) and all-sky searches (Sauter et al. 2019).

3.4.1 Heterodyne method

Since CW signals are inherently quite narrowband with respect to deviations from idealized models, a heterodyning procedure using a base frequency near the nominal signal frequency, followed by a low-pass filter allows a large reduction in the number of data samples required to capture the signal modulations. Conceptually, if one has a pure signal $h(t)$ that can be expressed as a slowly varying amplitude function $A(t)$ times a sinusoid of base frequency f_{base}, namely, $h(t) = \Re\{A(t)e^{\mathrm{i}(2\,\pi \mathrm{f}_{\text{base}}\tau(\mathrm{t})+\phi_0)}\}$, one can apply the following heterodyne for a base frequency f_{base}:

$$H_{f_{\text{base}}}(t) \equiv h(t)\, e^{-\mathrm{i}2\,\pi \mathrm{f}_{\text{base}}\tau(\mathrm{t})} = A(t)\, e^{\mathrm{i}\phi_0}, \tag{86}$$

where $\tau(t)$ relates the SSB time to detector time. This approach allows the heterodyned function to have a low effective bandwidth. Applying a low-pass filter and then downsampling allows a large reduction in data volume while preserving signal fidelity.

In practice, the heterodyne used in targeted CW searches applies not a pure sinusoid factor, but rather a slowly modulated sinusoidal phase $\phi_{\text{model}}(t)$ dependent on the topocentric (observatory-centric) time t, a model that includes the effects of Eqs. (40) and 47 on signal frequency evolution and propagation delays:

$$H_{\text{model}}(t) \equiv d(t)\, e^{-\phi_{\text{model}}(t)}, \tag{87}$$

where it is assumed the signal is well approximated by the model: $h(t) = \Re\{f(t)e^{\mathrm{i}(\phi_{\text{model}}(\mathrm{t}))}\}$, and the data stream $d(t)$ contains $h(t)$ and a (much larger-amplitude) random noise $n(t)$. The resulting heterodyne product $H_{\text{model}}(t)$ can then be interrogated for consistency with noise in addition to a signal amplitude function subject to antenna pattern modulations. Small residual deviations from the model ("timing noise") measured empirically from electromagnetic pulsation observations can also be taken into account straightforwardly.

This technique is well suited to searches for known pulsars, for which the nominal frequency is precisely known from ephemeris measurements. For example, it has been customary in many LIGO and Virgo targeted searches to heterodyne, low-pass filter and then downsample to 1 data sample per minute, starting from a raw data stream of 16384 Hz. This technique assumes the residual intrinsic bandwidth of the signal following the heterodyne is no greater than the Nyquist frequency of 8.3 mHz, which is an excellent approximation for effects due to Earth / detector motion. This specific implementation is not as well suited to wide-parameter searches, for which the bandwidth must be increased or many distinct heterodynes be carried out.

The resulting heterodyned data samples have had frequency / phase modulations due to detector motion removed, but they retain antenna pattern due to detector rotation about the Earth's spin axis. Section 4.1 below presents a Bayesian analysis method for such samples (Dupuis and Woan 2005).

3.4.2 Resampling methods

An alternative barycentering technique to heterodyning is to "resample" the detector data in order to transform it into SSB time (Schutz 1991; Jaranowski et al. 1998; Brady et al. 1998). A mundane but difficult nuisance is that data samples uniformly in detector frame time is *not* uniformly sampled in SSB time, making it difficult to apply conventional discrete Fourier transforms to the SSB samples. Two distinct methods have been used to date in CW analysis, to make the SSB samples uniform in time. The first (Patel et al. 2010; Meadors et al. 2018) uses spline interpolation of the non-uniformly sampled data to create uniformly sampled data. In practice, this interpolation is carried out on heterodyned subbands, much wider than those used in targeted searches, but much narrower than the full bandwidth of the original data collected. Another method (Astone et al. 2014b; Singhal et al. 2019) is based on selective data sample deletions and duplications, where narrow bands of data are temporarily upsampled to much higher frequencies, allowing smaller errors when extra samples are deleted or duplicated as SSB time appears to run faster or slower than detector-frame time (as defined by successive gravitational wavefronts), depending on the relative velocity of the detector with respect to the source. As for the heterodyne method, the result in both methods is a data stream for which detector translational motion has been corrected, but which still contains antenna pattern modulations from daily detector rotation.

3.4.3 Dirichlet kernel method

An alternative method can be applied in the Fourier domain by breaking the observation time into segments of short-enough duration that the signal frequency has negligible evolution during that duration, that is, the frequency change during the time $T_{\rm seg}$ is small relative to intrinsic frequency resolution of a discrete Fourier transform over that duration: $\frac{1}{T_{\rm seg}}$. In a templated search for a particular signal, the frequency for that segment is known, and a Dirichlet filter (Dirichlet 1829) can be applied to the DFT coefficients in a narrow band surrounding the nominal frequency (e.g., ±4 DFT bins), using the expected weights for those bins for the nominal central frequency.

For a bin-centered signal and rectangular windowing, the filter would be a Kronecker delta, but in general, spectral leakage favors use of a handful of neighboring bins, to recover the full signal strength. By coherently combining the resulting extracted complex coefficients from the observed segments, one can achieve a full, coherent demodulation of the signal.[10] Table 1 shows example power fractions in adjacent DFT bins (using rectangular windowing) for a monochromatic signal that is bin-centered or offset positively from the bin center by bin fractions of $0.1-0.5$ in increments of 0.1. One sees that the bulk of signal power can be recovered by a modest number of neighboring bins. Figure 13 shows a visual representation of the values in Table 1.

[10] An algorithm commonly used is known as LALDemod (Williams and Schutz 2000; Prix 2018).

Table 1 Fractional powers in neighboring DFT bins (rectangularly windowed) for a monochromatic signal with a frequency that ranges from bin-centered (bin 0 of the 10 bins shown) to a positive offset of a half-bin

	Fractional bin offset of signal from bin center					
	0.0	**0.1**	**0.2**	**0.3**	**0.4**	**0.5**
Bin +5:	0	0.0004	0.0015	0.0030	0.0043	0.0050
Bin +4:	0	0.0006	0.0024	0.0048	0.0071	0.0083
Bin +3:	0	0.0012	0.0045	0.0091	0.0136	0.0162
Bin +2:	0	0.0027	0.0108	0.0229	0.0358	0.0450
Bin +1:	0	0.0119	0.0547	0.1353	0.2546	0.4053
Bin 0:	1	0.9675	0.8751	0.7368	0.5728	0.4053
Bin −1:	0	0.0080	0.0243	0.0392	0.0468	0.0450
Bin −2:	0	0.0022	0.0072	0.0125	0.0159	0.0162
Bin −3:	0	0.0010	0.0034	0.0061	0.0079	0.0083
Bin −4:	0	0.0006	0.0020	0.0036	0.0047	0.0050
Sum:	1.000	0.9982	0.9933	0.9874	0.9825	0.9807

The last row gives the total fractional power in these 10 bins

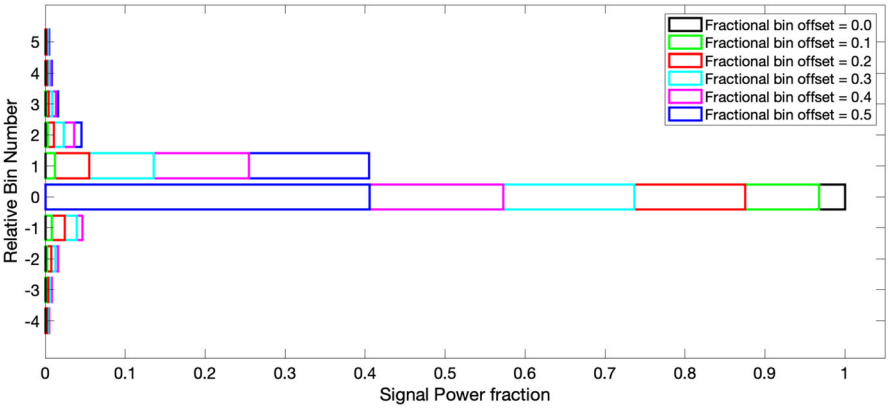

Fig. 13 Visual representation of the fractional power values listed in Table 1

3.4.4 Time-domain parameter extraction

After frequency demodulation for detector translational motion, one has a highly reduced band-limited, data stream (time-domain for heterodyne or resampling, Fourier-domain for the Dirichlet filter) implicitly containing the amplitude modulations embodied in Eqs. (48)–(51), which can be considered deterministic functions of time, dependent upon the putative signal parameters. In the case of a source of known position and phase evolution but unknown orientation, as for many known pulsars, the unknown source parameters can be taken to be the strain amplitude h_0, the signal phase constant ϕ_0, the inclination angle ι and the polarization angle ψ. The data stream can then be analyzed to extract those parameters.

For direct time-domain analysis, the principal method used to date for LIGO and Virgo data analysis has been a Bayesian inference (Abbott et al. 2004; Dupuis and Woan 2005). In brief, the heterodyned data samples $\{B_k\}$ can be expressed as complex quantities, with signal template expectations: (adopting the notation of Abbott et al. 2004):

$$\begin{aligned} y(t_k, \vec{a}) = & \frac{1}{4} F_+(t_k;\psi) h_0 (1+\cos^2(\iota)) e^{\mathrm{i}2\phi_0} \\ & - \frac{\mathrm{i}}{2} F_\times(t_k;\psi) h_0 \cos(\iota) e^{\mathrm{i}2\phi_0}, \end{aligned} \tag{88}$$

where $\vec{a}$ is a vector with components $(h_0, \iota, \psi, \phi_0)$ and t_k is the time stamp of the kth sample.

With a set of priors on the $\vec{a}$ parameters one can extract a joint posterior probability density function for these parameters:

$$\begin{aligned} p(\vec{a}|\{B_k\}) \propto & p(\vec{a}) \exp\left[-\sum_k \frac{\Re\{B_k - y(t_k;\vec{a})\}^2}{2\,\sigma^2_{\Re\{B_k\}}} \right] \\ & \times \exp\left[-\sum_k \frac{\Im\{B_k - y(t_k;\vec{a})\}^2}{2\,\sigma^2_{\Im\{B_k\}}} \right], \end{aligned} \tag{89}$$

where $p(\vec{a})$ is the prior on $\vec{a}$ (uniform for $\cos(\iota)$, ψ and ϕ_0 and h_0), and $\sigma^2_{\Re\{B_k\}}$ and $\sigma^2_{\Im\{B_k\}}$ are the variances on the real and imaginary parts of B_k. This posterior distribution can be examined for evidence of a signal present. In the absence of a signal, an upper limit on strain amplitude h_0 can be found via marginalization over the other three signal parameters to obtain a marginalized posterior:

$$p(h_0|\{B_k\}) \propto \iiint p(\vec{a}|\{B_k\})\, d\iota\, d\psi\, d\phi_0, \tag{90}$$

normalized so that $\int_0^\infty p(h_0|\{B_k\}) dh_0 = 1$. Unlike a frequentist confidence level, the resulting curve versus h_0 represents the distribution of degree of belief in any particular value of h_0, given the signal model, the parameter priors and the data observations $\{B_k\}$. One can derive a 95% credible Bayesian upper limit $h_0^{95\%\,\mathrm{UL}}$ for which the probability lies below $h_0^{95\%\,\mathrm{UL}}$ via

$$0.95 = \int_0^{h_0^{95\%\,\mathrm{UL}}} p(h_0|\{B_k\}) dh_0. \tag{91}$$

The combined posterior distribution from multiple, independent detectors can be obtained via the product of the individual likelihoods (Dupuis and Woan 2005). In the event that estimates of ι and ψ can be inferred from electromagnetic measurements of the source, e.g., from images of jets assumed to be emitted along the spin axis of a star, then the precision on h_0 can be improved by assigning much narrower priors to the parameters.

3.4.5 Five-vector method

The so-called "Five-vector" method exploits the property that the complexity in Eqs. (46) and 48-51 can be distilled down to five terms (Astone et al. 2010b)

$$h(t) = h_0 \vec{A} \cdot \vec{W} e^{\mathrm{i}(\omega_0 \mathrm{t} + \phi_0)}, \tag{92}$$

where ω_0 is the signal frequency in the SSB frame, where $\vec{A}$ can be decomposed into plus- and cross-polarized terms that depend on complex amplitudes H_+ and $H_\times$:

$$\vec{A} = H_+ \vec{A}^+ + H_\times \vec{A}^\times, \tag{93}$$

and where $\vec{A}^+$ and $\vec{A}^\times$ can be expressed in terms of trigonometic functions, using Eqs. (48)–(51) (see Astone et al. 2010b for detailed expressions). The vector $\vec{W}$ is a five-component set of basis functions, indexed by $k = [-2, -1, 0, 1, 2]$:

$$\vec{W}_k = e^{-\mathrm{ik}\Theta}, \tag{94}$$

where Θ is the detector's local sidereal time in radians.

The data stream $x(t)$ too can be decomposed using these basis functions:

$$\vec{X} = \int_T x(t) \vec{W} e^{-\mathrm{i}\omega_0 \mathrm{t}} dt. \tag{95}$$

One can then construct a detection statistic using a weighted sum of the squared projections:

$$S = c_+ |\hat{h}_+|^2 + c_\times |\hat{h}_\times|^2, \tag{96}$$

where the projections are defined by

$$\hat{h}_+ = \frac{\vec{X} \cdot \vec{A}^+}{|\vec{A}^+|^2}; \qquad \hat{h}_\times = \frac{\vec{X} \cdot \vec{A}^\times}{|\vec{A}^\times|^2}. \tag{97}$$

Empirically (Astone et al. 2010b), it is found that best performance for known ι, ψ can be obtained with the weightings: $c_{+,\times} = |\vec{A}^{+,\times}|^4$, while estimation of signal amplitude can be obtained from

$$\hat{h}_0 = \sqrt{|\hat{h}_+|^2 + |\hat{h}_\times|^2}. \tag{98}$$

3.4.6 The $\mathcal{F}$-statistic

The most pervasive detection statistic used in broadband CW searches can also be used for targeted searches, namely the $\mathcal{F}$-statistic (Jaranowski et al. 1998). As above, the $\mathcal{F}$-statistic is constructed to take into account not only the frequency / phase modulation of the detector's translational motion (using time-domain or frequency-domain techniques), but also the amplitude modulation from daily detector rotation.

It is constructed from a general maximum likelihood approach, where the data is taken to be a sum of random noise $n(t)$ and a signal $h(t)$:

$$x(t) = n(t) + h(t), \tag{99}$$

where $h(t)$ from Eqs. (48)–(51) can be written[11]

$$h(t) = \sum_{i=1}^{4} A_i h_i(t), \tag{100}$$

where the coefficients A_i are inferred from Eqs. (48)–(51):

$$\begin{aligned} A_1 =& h_0 \sin(\zeta) \left[\frac{1}{2}(1 + \cos^2(\iota) \cos(2\psi) \cos(2\,\Phi_0) \right. \\ & \left. - \cos(\iota) \sin(2\psi) \sin(2\Phi_0) \right], \end{aligned} \tag{101}$$

$$\begin{aligned} A_2 =& h_0 \sin(\zeta) \left[\frac{1}{2}(1 + \cos^2(\iota) \sin(2\psi) \cos(2\,\Phi_0) \right. \\ & \left. + \cos(\iota) \cos(2\psi) \sin(2\Phi_0) \right], \end{aligned} \tag{102}$$

$$\begin{aligned} A_3 =& h_0 \sin(\zeta) \left[-\frac{1}{2}(1 + \cos^2(\iota) \cos(2\psi) \sin(2\,\Phi_0) \right. \\ & \left. - \cos(\iota) \sin(2\psi) \cos(2\Phi_0) \right], \end{aligned} \tag{103}$$

$$\begin{aligned} A_4 =& h_0 \sin(\zeta) \left[-\frac{1}{2}(1 + \cos^2(\iota) \sin(2\psi) \sin(2\,\Phi_0) \right. \\ & \left. + \cos(\iota) \cos(2\psi) \cos(2\Phi_0) \right], \end{aligned} \tag{104}$$

and the time-dependent functions h_i have the form:

$$h_1 = a(t) \cos(2\Phi(t)), \quad h_2(t) = b(t) \cos(2\Phi(t)) \tag{105}$$

$$h_3 = a(t) \sin(2\Phi(t)), \quad h_4(t) = b(t) \sin(2\Phi(t)), \tag{106}$$

where $\Phi(t)$ is the phase of the signal, including modulations.

[11] In the original $\mathcal{F}$-statistic article (Jaranowski et al. 1998), a two-component signal model is assumed, corresponding to frequencies at once and twice the source rotation frequency. Only the component at twice the rotational frequency is considered here where the wobble angle θ in Jaranowski et al. (1998) is taken to be $\pi/2$ for a triaxial ellipsoid, allowing a simplification of notation.

A log-likelihood function $\log(\Lambda)$ is constructed via:

$$\log(\Lambda) = (x|h) - \frac{1}{2}(h|h), \tag{107}$$

where the scalar product $(\,|\,)$ is defined by a filter matched to the detection noise spectrum:

$$(x|y) := 4\Re\left\{\int_0^\infty \frac{\tilde{x}(f)\tilde{y}^*(f)}{S_h(f)}df\right\}, \tag{108}$$

where $\tilde{}$ denotes a Fourier transform, $*$ is the complex conjugation, and S_h is the one-sided power spectral density.

Following Jaranowski et al. (1998), the narrowband signal allows, in principle, conversion of the scalar product to a time-domain expression:

$$(x|h) \approx \frac{2}{S_h(f_0)}\int_0^{T_{\rm obs}} x(t)h(t)dt, \tag{109}$$

where stationarity of the noise over the observation period $T_{\rm obs}$ is implicitly assumed, which unfortunately, is rarely a good assumption for interferometers at the frontier of technology. Nonetheless, practical implementations of the $\mathcal{F}$-statistic are not limited by this assumption. Defining a time-domain scalar product:

$$(x||y) := \frac{2}{T_{\rm obs}}\int_0^{T_{\rm obs}} x(t)y(t)dt, \tag{110}$$

the log-likelihood function can be approximated via

$$\log(\Lambda) \approx \frac{T_{\rm obs}}{S_h(f_0)}\left[(x||h) - \frac{1}{2}(h||h)\right], \tag{111}$$

which is proportional to a normalized log-likelihood $\log(\Lambda')$:

$$\log(\Lambda') = (x||h) - \frac{1}{2}(h||h), \tag{112}$$

which does not depend explicitly on the spectral noise density. The signal depends linearly on the four amplitudes A_i and can, in principle, be extracted from a likelihood maximization:

$$\frac{\partial \log \Lambda'}{\partial A_i} = 0, \tag{113}$$

from which a set of linear algebraic equations can be derived:

$$\sum_{i=1}^{4} \mathcal{M}_{ij}A_j = (x||h_i), \tag{114}$$

where the components of the matrix $\mathcal{M}_{ij}$ are given by

$$\mathcal{M}_{ij} := (h_i||h_j). \tag{115}$$

Cross-terms of the $\cos(\Phi(t))$ and $\sin(\Phi(t))$ terms in Eqs. (105)–106 can be neglected in the time integrations. The surviving terms can be expressed:

$$\begin{aligned}(h_1|h_1) &\approx (h_3|h_3)\\ (h_2|h_2) &\approx (h_1|h_4)\\ (h_1|h_2) &\approx (h_3|h_4)\end{aligned} \tag{116}$$

where $A := (a||a)$, $B := (b||b)$ and $C := (a||b)$. With these approximations, the matrix $\mathcal{M}$ becomes

$$\mathcal{M} = \begin{pmatrix} \mathcal{C} & \mathcal{O} \\ \mathcal{O} & \mathcal{C} \end{pmatrix}, \tag{117}$$

where $\mathcal{O}$ is a zero 2×2 matrix, and $\mathcal{C}$ is

$$\mathcal{C} = \frac{1}{2}\begin{pmatrix} A & C \\ C & B \end{pmatrix}, \tag{118}$$

from which maximum-likelihood estimators $\tilde{A}_i$ of the true amplitudes A_i can be obtained:

$$\begin{aligned}\tilde{A}_1 &= 2\frac{B(x||h_1) - C(x|h_2)}{D},\\ \tilde{A}_2 &= 2\frac{A(x||h_2) - C(x|h_1)}{D},\\ \tilde{A}_3 &= 2\frac{B(x||h_3) - C(x|h_4)}{D},\\ \tilde{A}_4 &= 2\frac{A(x||h_4) - C(x|h_3)}{D},\end{aligned} \tag{119}$$

where $D = AB - C^2$. Substituting these expressions into Eqs. (111) leads to the $\mathcal{F}$-statistic (denoted by $2\mathcal{F}$):

$$\begin{aligned}2\mathcal{F} = \frac{T_{\text{obs}}}{S_h(f_0)}\Bigg[&\frac{B(x||h_1)^2 + A(x||h_2)^2 - 2C(x||h_1)(x||h_2)}{D}\\ &+ \frac{B(x||h_3)^2 + A(x||h_4)^2 - 2C(x||h_3)(x||h_4)}{D}\Bigg].\end{aligned} \tag{120}$$

The quantity $2\mathcal{F}$ has a probability distribution of a chi-squared with four degrees of freedom in the absence of a signal and that of a non-central chi-squared with a non-centrality parameter:

$$\lambda \equiv d^2 = (h|h) \tag{121}$$

where d is proportional to signal amplitude (Jaranowski et al. 1998). The probability distributions $p_{\text{noise}}(2\mathcal{F})$ and $p_{\text{signal+noise}}(2\mathcal{F};\, d)$ are hence:

$$p_{\text{noise}}(2\mathcal{F}) = \frac{1}{4}(2\mathcal{F})e^{-(2\mathcal{F})/2}, \tag{122}$$

$$p_{\text{signal+noise}}(2\mathcal{F};\, d) = \frac{(2\mathcal{F})^{\frac{1}{2}}}{d} I_1\left(d\sqrt{(2\mathcal{F})}\right) e^{-\frac{1}{2}(2\mathcal{F})-\frac{1}{2}d^2}, \tag{123}$$

where I_1 is a modified Bessel function of the first kind (order 1).

As discussed in Sect. 3.3, $2\mathcal{F}$ can be used as a detection statistic, where a threshold $2\mathcal{F}_0$ can be chosen to satisfy a desired false alarm probability:

$$\text{CDF}_{\text{noise}}[2\mathcal{F}_0] = \int_0^{2\mathcal{F}_0} p_{\text{noise}}(2\mathcal{F})\, d(2\mathcal{F}) = 1 - \alpha, \tag{124}$$

$$= 1 - \left(1 + 2\mathcal{F}_0 + \frac{1}{2}2\mathcal{F}_0^2 + \frac{1}{6}2\mathcal{F}_0^3\right) e^{-2\mathcal{F}_0}, \tag{125}$$

and where the probability of detection for a given d is

$$P_{\text{detection}}(d, 2\mathcal{F}_0) = \int_{2\mathcal{F}_0}^{\infty} p_{\text{signal+noise}}(2\mathcal{F};\, d)\, d(2\mathcal{F}). \tag{126}$$

The formalism above describes a time-domain implementation (Jaranowski et al. 1998; Astone et al. 2010a), but a narrowband frequency implementation (Prix 2018) has been used extensively in LIGO searches.

In searches for known pulsars for which optical or X-ray observations of pulsar wind nebulae allow inference of ι and ψ, a modified version of the $\mathcal{F}$-statistic known as the $\mathcal{G}$-statistic can be applied to gain slightly in sensitivity, depending on the stellar orientation (Jaranowski and Królak 2010).

Although originally derived in a frequentist, log-likelihood framework, the $\mathcal{F}$-statistic can also be obtained in a Bayesian approach (Prix and Krishnan 2009) with an unphysical prior (non-isotropic in stellar orientation), an alternative framework that has received additional study (Prix et al. 2011; Keitel et al. 2014; Whelan et al. 2014; Dhurandhar et al. 2017; Bero and Whelan 2019; Wette 2021).

3.5 Semi-coherent signal demodulation

Let's now consider a coarser demodulation, in which phase fidelity is not required for the full observation time. Instead, the observation is broken into discrete segments of coherence time T_{coh} which need not be contiguous with each other. The segmentation reduces the fineness with which the parameter space (e.g., frequency, frequency derivatives, sky location) must be sampled, leading to often dramatic reduction in computing cost to search a given parameter space volume, albeit with a degradation of achievable strain sensitivity.

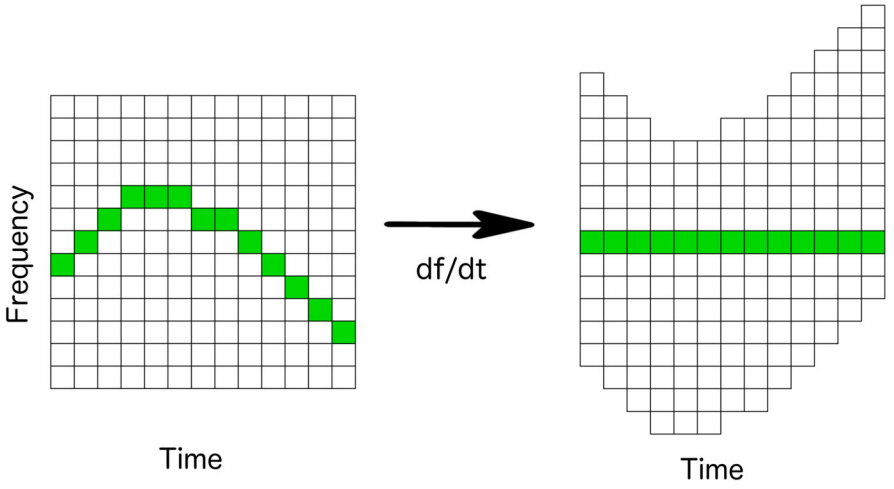

Fig. 14 Conceptual illustration of the "stack-slide" method in which rows of a spectrogram are shifted up or down in frequency to account for Doppler modulations

3.5.1 The stack-slide method

For short-enough $T_{\rm coh}$, no frequency demodulation need be applied within a single segment. One can simply sum the strain power from each bin in an DFT containing the frequency of the signal for that time interval. Figure 14 illustrates the simplest version of this approach, known as "stack-slide" (Brady et al. 1998; Mendell and Landry 2005). In a spectrogram where each column represents DFT powers for a given $T_{\rm coh}$, the bin containing the signal frequency (indicated by the green square) varies in frequency from one column to the next. Correcting for the frequency modulation by shifting columns up or down leads to the signal's power being contained in a horizontal track in the demodulated spectrogram. For a relatively narrow frequency band, the amount of vertical shift for a given column is nearly the same for all frequencies in the band, for a given set of source parameters, including sky location. Hence by stacking powers across rows in the demodulated spectrogram, one can look for an outlier indicating a signal.

To be concrete, define the power $\tilde{P}_i^{(k)}$ to be the strain power spectral density measured in bin i of DFT k, where the bin i is the appropriate bin after "sliding":

$$\tilde{P}_i^{(k)} = \frac{2|\tilde{D}_{i(\rm demod)}^{(k)}|^2}{T_{\rm coh}}. \tag{127}$$

Following Abbott et al. (2008a), Mendell and Landry (2005), this power is renormalized to form a dimensionless quantity η_i^k

$$\eta_i^k = \frac{\tilde{P}_i^{(k)}}{S_{h_i}^k}, \tag{128}$$

where $S_{h_i}^k$ is the one-sided power spectral density expected in the absence of signal. This quantity differs from the ρ_i^2 defined in Eq. (54), both in the implicit demodulation associated with bin i and in a factor of 2. Here η_i^k has an expectation value of 1 in the absence of signal.

The stack-slide detection statistic $P_{i(\mathrm{SS})}^{(k)}$ then is the average value of η_i^k over the N_{DFT} DFT's used in the analysis:

$$P_{i(\mathrm{SS})}^{(k)} = \frac{1}{N_{\mathrm{DFT}}} \sum_{k=1}^{N_{\mathrm{DFT}}} \eta_i^k. \tag{129}$$

This quantity has an expectation value of 1 in the absence of signal and a variance of $1/N_{\mathrm{DFT}}$. Signal candidates are chosen based on exceeding a threshold corresponding to a false alarm probability α, from which detection sensitivity is determined from a desired false dismissal probability β. Appendix B of Abbott et al. (2008a) details the statistical behavior. In brief, the quantity (similar to R_i of Eq. (63) above)

$$\mathcal{P}_{i(\mathrm{SS})} = 2N_{\mathrm{DFT}}\eta_i^k \tag{130}$$

has the probability density distribution of a non-central χ^2 with $2N_{\mathrm{DFT}}$ degrees of freedom and a non-centrality parameter $2N_{\mathrm{DFT}} <d^2>$ which is the expectation value of the estimator in Eq. (121) when evaluated over a single DFT. Hence the probability density distribution for $\mathcal{P}_{i(\mathrm{SS})}$ follows:

$$p_{\mathrm{signal+noise}}(\mathcal{P}_{i(\mathrm{SS})}; N_{\mathrm{DFT}}, d) = \frac{I_{N_{\mathrm{DFT}}-1}\left(\sqrt{\mathcal{P}_{i(\mathrm{SS})} N_{\mathrm{DFT}} <d^2>}\right)}{(N_{\mathrm{DFT}} <d^2>)^{N_{\mathrm{DFT}}-1}} \times \mathcal{P}_{i(\mathrm{SS})}^{\frac{N_{\mathrm{DFT}}-1}{2}} e^{-\left(N_{\mathrm{DFT}} + <\frac{d^2}{2}>\right)}. \tag{131}$$

Numerical evaluation (Abbott et al. 2008a) for $\alpha = 0.01$ and $\beta = 0.10$ leads (in the large N_{DFT} limit) to a sensitivity $<d^2>^{(90)} \approx 7.385/\sqrt{N_{\mathrm{DFT}}}$ and to a strain sensitivity *for a single template search* of $h_0^{(90)} \approx 7.7\sqrt{S_h}/(T_{\mathrm{coh}}T_{\mathrm{obs}})^{1/4}$, where T_{obs} refers here to the total observing time analyzed and where stationary data is implicitly assumed. In practice, however, this method is applied to wide-parameter searches for which trials factors lead to much worse strain sensitivities (Tenorio et al. 2022). Prix and Shaltev (2012) carry out a detailed analysis of maximizing sensitivity at fixed computational cost for different stack-slide search configurations.

3.5.2 The powerflux method

The PowerFlux method (Abbott et al. 2008a), in its simplest form, is similar to the stack-slide method, with the following refinements: (1) an explicit polarization is assumed for each signal template searched, with an antenna pattern correction

applied; (2) detection statistic variance is minimized in the presence of non-stationary noise; and the detection statistic itself is a direct measure of strain amplitude.

Using the same notation as above (see Eq. 127), the PowerFlux detection statistic $R_{\rm PF}$ for a given set of orientation parameters ι and ψ is written:

$$R_{\rm PF} = \frac{2}{T_{\rm coh}} \frac{\sum_{i=1}^{N_{\rm DFT}} W_i \tilde{P}_i^{(k)} / (F_i(\iota,\psi))^2}{\sum_{i=1}^{N_{\rm DFT}} W_i}, \tag{132}$$

where the weights are defined as

$$W_i = [(F_i(\iota,\psi))^2]^2 / S_{h_i}^2, \tag{133}$$

and where $F_i(\iota,\psi)$ is the antenna pattern weight calculated for the midpoint of the time segment i for the assumed polarization such that the detector amplitude response can be written as $h_{\rm det,i} = h_0 F_i(\iota,\psi)$. In practice, searches have been carried out for circular polarization ($\iota = 0$ or π) and for particular linear polarization angles ψ (with $\iota = \pi/2$) to define "best-case" and "worst-case" orientations, respectively.

The choice of weight definition comes from minimizing the variance of the strain amplitude estimator $\tilde{P}_i^{(k)} / (F_i(\iota,\psi))^2$, where the noise (in the weak signal regime) is assumed to be dominated in each time segment i by a power spectral density S_{h_i} with underlying Gaussian distributions for real and imaginary DFT components. Under that assumption, the variance of the noise is proportional to $(S_{h_i})^2$. As a result, each term in the numerator of Eq. (132) is proportional to $(F_i(\iota,\psi))^2 \tilde{P}_i^{(k)} / S_{h_i}^2$, which gives higher weight to segments with higher $F_i(\iota,\psi)$ magnitude and lower noise S_{h_i}, as one would wish. For a given polarization choice defined by (ι,ψ) the detection statistic $R_{\rm PF}$ is a direct measure of total strain power such that subtracting the expectation value based on neighboring bin yields a direct estimator for signal power.

3.5.3 Hough transform methods

Hough transform methods refer, in practice, to an application of a pattern recognition algorithm first developed for use in the 1960's by high energy particle physicists (Hough 1959, 1962) to reconstruct a charged particle's trajectory from discrete positions ("hits"), measured by a tracking detector. The method is best suited to data that is "sparse" and for which a simple transformation from the raw measurements to the signal parameter space can amplify the detection statistic. In the original application to particle tracking, the hits were two-dimensional projections for which looking for straight lines built out of all hit combinations was computationally intensive (especially in the 1960's!). To represent a straight line, instead of offset and slope, the vector of its minimum distance to the origin, in polar coordinates (r,θ), is used. A point (x, y) belonging to that line sets the relation $r = x\cos\theta + y\sin\theta$ which is a sinusoidal curve in the θ-r plane. Cells in that plane count how many curves pass within their boundaries, and the most occupied cell identifies (r,θ) of the original track.

In the case of CW searches, two different Hough transform methods ("Sky Hough" and "Frequency Hough") have been used in recent years, both of which accumulate excess power from frequency-demodulated DFTs. In the Sky Hough method (Krishnan et al. 2004), the transformation is from a narrow frequency band and frequency derivative to right ascension and declination, where broad patches of sky are searched collectively. In the Frequency Hough method (Antonucci et al. 2008; Astone et al. 2014a), the transform is from a time-frequency plane to a plane of frequency and frequency derivative. In each case, one searches for a statistically significant excess among the pixels and applies a thresholding to individual accumulated powers, in order to reduce computational cost in the accumulation.

The Hough number count is defined as a weighted sum of binary counts n_i:

$$n = \sum_{i=1}^{N_{\mathrm{DFT}}} w_i n_i, \tag{134}$$

where $n_i = 1$ if the normalized segment power η_i^k exceeds a threshold η^* and zero otherwise, and where the weights favor low-noise times and are optimized for circular polarization (Antonucci et al. 2008; Abbott et al. 2008a):

$$w_i \propto \frac{1}{S_{h_i}} \left[(F_i^+)^2 + (F_i^\times)^2 \right], \tag{135}$$

with a normalization chosen to satisfy:

$$\sum_{i=1}^{N_{\mathrm{DFT}}} w_i = N_{\mathrm{DFT}}. \tag{136}$$

In the Sky Hough method (Krishnan et al. 2004), so-called "Hough maps" in right ascension and declination are created for each assumed frequency and frequency derivative, where signal outliers produce "hot" pixels in the sky patch for which the map applies. In the Frequency Hough method (Antonucci et al. 2008; Astone et al. 2014a), the Hough map is created instead in the plane of frequency and frequency derivative for each localized sky point. The primary motivations for this alternative mapping to parameter space are reduction of inaccuracies arising from approximations and non-linearities in the mapping to the sky; avoidance of artifact "pileup" in which certain regions of the sky are contaminated over subbands by particular narrowband artifacts; and the possibility to use over-resolution in frequency, at negligible additional computational cost (Antonucci et al. 2008).

Regardless of the choice of parameter space mapping, the statistical character of the Hough number counts is governed by the value of the threshold used to define the binary counts n_i. The mean number count in the absence of a signal is $\bar{n} = N_{\mathrm{DFT}} p$, where p is the probability that the normalized power η_i^k exceeds a threshold value η^*. For unity weighting, the standard deviation is $\sigma_{\bar{n}} = N_{\mathrm{DFT}} p(1-p)$. For the more general weighting, this becomes:

$$\sigma = \left[p(1-p) \sum_{i=1}^{N_{\rm DFT}} w_i^2 \right]^{1/2}. \tag{137}$$

For $N_{\rm DFT} \gg 1$, the underlying distribution can be approximated as Gaussian, in which case a threshold $n_{\rm th}(\alpha)$ corresponding to a false alarm rate α is given by (Krishnan et al. 2004)

$$n_{\rm th} = N_{\rm DFT}\, p + \sqrt{2}\, \sigma\, {\rm erfc}^{-1}(2\alpha), \tag{138}$$

where it is natural to regard the significance of a given measured n to be

$$s = \frac{n - \bar{n}}{\sigma}. \tag{139}$$

In Krishnan et al. (2004), Abbott et al. (2005a), and Abbott et al. (2008a) an optimal choice of the normalized power threshold parameter is found to be $\eta^* \approx 1.6$, for which $p = e^{-\eta^*} \approx 0.2$.

One can compute (Abbott et al. 2008a) a sensitivity $h_0^{1-\beta}(\alpha)$ for a false dismissal probability β and false alarm probability α:

$$h_0^{1-\beta}(\alpha) \approx 3.38 (S)^{1/2} \left(\frac{||\vec{w}||}{\mathbf{w} \cdot \mathbf{X}} \right)^{1/2} \sqrt{\frac{1}{T_{\rm coh}}}, \tag{140}$$

where $||\vec{w}|| = \sum_{i=1}^{N_{\rm DFT}} w_i^2$ and

$$\mathcal{S} = {\rm erfc}^{-1}(2\alpha) + {\rm erfc}^{-1}(2\beta), \tag{141}$$

$$X_i = \frac{1}{S_{h_i}} \left[\left(F_+^i\right)^2 + \left(F_\times^i\right)^2 \right], \tag{142}$$

and where $F^i_{+/\times}$ refer to the antenna pattern functions for the $+$ and $\times$ polarizations evaluated at the midpoint of time segment i.

Other improvements to the Sky Hough method have included incorporating a hierarchical approach (Sancho de la Jordana 2010), adaptation to a search for stars in binary systems (Covas and Sintes 2019) (see Sect. 4.5), clustering of outliers (Tenorio et al. 2021c) and systematic outlier follow-up (Tenorio et al. 2021a).

3.5.4 The stacked $\mathcal{F}$-statistic method

The semi-coherent approach used above (in various approaches) with DFT coefficients can also be applied to longer segments of time for each of which the coherent $\mathcal{F}$-statistic is computed. This approach permits deeper sensitivity since the $\mathcal{F}$-statistic can be computed without degradation of signal coherence for arbitrarily long periods of time. The disadvantage is that the much finer resolution in parameter space associated with such sensitivity leads to much greater computational cost, coming from the fine stepping needed within each segment and from the mapping with negligible signal loss from one segment to the next. A variety of $\mathcal{F}$-statistic

"stacking" methods[12] have been implemented over the years, both inside and outside of the framework of the Einstein@Home distributed computing system (see Sect. 4.4). When computing the $\mathcal{F}$-statistic over short time segments, a modified variation, the $\mathcal{F}_{\mathrm{AB}}$-statistic, which avoids degeneracy due to minimal antenna pattern modulation can be more effective (Covas and Prix 2022b).

Many of the considerations discussed in semi-coherent summing of DFT power have analogs in $\mathcal{F}$-statistic summing, including the use of thresholding and the use of Hough transform mapping. Particular implementations will be discussed below in Sects. 3.6.1 and 4.4. One critical issue in these computationally costly searches is the optimum placement of signal templates in parameter space, to be discussed next, more generally. Another important consideration is clustering of initial outlier candidates (Steltner et al. 2022a) to reduce computational cost in hierarchical searches prior to follow up with deeper search algorithms.

3.6 Template placement

Computationally demanding searches must choose step sizes in signal parameter space, with finer spacing leading to greater cost, in general. The choices are typically governed by what is considered an acceptable maximum "mismatch", normally parametrized by the fractional decrease in detection statistic for a given offset in parameter space.

For an n-dimensional, hypercubic grid defined by n search parameters, one can regard the mismatch parameter μ as governing the maximum half-length of the diagonal of the n-dimensional cell containing the correct signal parameters. Conceptually, we imagine having made the least optimum choice of grid offset such that the true parameters lie at the center of the cell, and no matter which of the 2^n corners of the cell is sampled, the value of the detection statistic is no smaller than $1-\mu$ of the value obtained, had the center of the cell been sampled. Figure 15 illustrates the concept with a detection statistic "surface" above a plane in two signal parameters, where the contours correspond to mismatch values of 20%, 40%, 60% and 80%.

In the following, general considerations of template placement are considered, first for directed searches for particular points on the sky, for which placement is relatively straightforward, and then for all-sky searches, where template placement is quite subtle and remains an active research front.

3.6.1 Template placement in directed searches

For coherent directed searches, the phase evolution Eq. (40) governs template placement, where for multi-day analyses, the effects of amplitude modulation can be safely neglected in choosing template spacing (Prix 2007a, b). Consider for a moment a highly simplified detection statistic based on multiplying in the time

[12] "Stacking" the $\mathcal{F}$-statistic values is more subtle than in the stacking used in the stack-slide and other semi-coherent methods based on summing DFT powers because the demodulations to obtain the $\mathcal{F}$-statistic values differ across time segments.

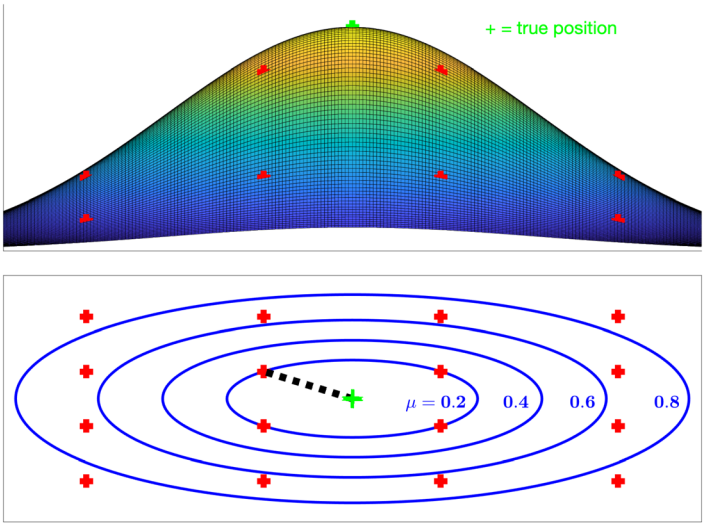

Fig. 15 Illustration of mismatch for a generic detection statistic. The upper panel shows a "surface" of height equal to the detection statistic for a pure signal above a plane defined by two signal-defining parameters (with zero covariance for simplicity). The green cross marks the true location for the two parameters and the maximum possible detection statistic. The lower panel shows detection statistic contours in the two-parameter space, where the contours correspond to mismatch values of 20%, 40%, 60% and 80%. The red crosses define a search template grid chosen to be least optimal for this signal location in that the true signal location is centered in a 2-dimensional cell, which maximizes the possible minimum mismatch (20%) between the detection statistics for the true signal and the closest template. The dashed diagonal line defines the "distance" in the 2-dimensional parameter space between the true signal location and the closest search template

domain an assumed sinusoidal signal template having a particular phase constant ϕ_0 and frequency f_0 against the raw data $x(t)$, assumed to be a sum of random Gaussian noise $n(t)$ and a sinusoid signal having amplitude h_0, phase constant ϕ_0' and frequency f_0':

$$F(\phi_0', f_0') = \left| \frac{2}{T} \int_0^T e^{-i(\phi_0 + 2\pi f_0 t)} x(t) dt \right|^2 \tag{143}$$

$$= \left| \frac{2}{T} \int_0^T e^{-i(\phi_0 + 2\pi f_0 t)} \left[n(t) + h_0 \cos(\phi_0' + 2\pi f_0' t) \right] dt \right|^2 . \tag{144}$$

In the limit of large T and strong signal (neglecting $n(t)$), the expectation value of F when maximized over possible template values for f_0 is simply h_0^2, independent of ϕ_0, ϕ_0' and f_0', where F is maximized for $\Delta f \equiv f_0' - f_0 = 0$. To understand how rapidly F decreases as $|\Delta f|$ departs from zero, it's helpful to rewrite $\cos(\phi_0' + 2\pi f_0' t) = \frac{1}{2}(e^{i(\phi_0' + 2\pi f_0' t)} + e^{-i(\phi_0' + 2\pi f_0' t)})$, where in the strong-signal limit of large T and for small $|\Delta f|$ such that the second term of the cosine expansion can be neglected, F approaches

$$F \approx \left| \frac{h_0}{T} \int_0^T e^{i[\Delta\phi + 2\pi \Delta f t]}\, dt \right|^2 \tag{145}$$

$$= h_0^2 |\mathrm{sinc}(\pi \Delta \mathrm{fT})|^2 \tag{146}$$

$$\approx h_0^2 \left[1 - \frac{1}{3} (\pi \Delta f T)^2 \right], \tag{147}$$

where $\Delta\phi \equiv \phi_0' - \phi_0$ drops out and where the convention $\mathrm{sinc}(\mathrm{x}) \equiv \frac{\sin(\mathrm{x})}{\mathrm{x}}$ is chosen. If we rewrite this last result as $F \approx h_0^2 \cos^2(\Delta\phi_{\mathrm{mismatch}})$, then the tolerance in Δf for a phase mismatch value $\Delta\phi_{\mathrm{mismatch}}$ is

$$\Delta f_{\mathrm{mismatch}} \approx \frac{\sqrt{3}}{\pi T} \Delta\phi_{\mathrm{mismatch}}, \tag{148}$$

which is $2\sqrt{3}$ larger than the naive underestimate of Eq. (41). Consequently, in a search that automatically maximizes F over the unknown phase constant, one need not search as finely in frequency as suggested by Eq. (41), which implies reduced computational costs in large-scale searches.

Given the importance of template placement to those costs, in fact, a systematic approach is merited. Following methodology developed originally for template placement in compact binary merger searches (Sathyaprakash and Dhurandhar 1991; Owen 1996; Balasubramanian et al. 1996), one can rewrite and generalize the simplified detection statistic in Eq. (143), replacing the data with another template and address the reduction in F's value due to mismatch of template parameters

$$F(\vec{\lambda}, \vec{\lambda}') = \left| \frac{1}{T} \int_0^T e^{-i\Phi(t;\vec{\lambda})} e^{i\Phi(t;\vec{\lambda}')}\, dt \right|^2 \tag{149}$$

$$= \left| \frac{1}{T} \int_0^T e^{i\Delta\Phi(t;\vec{\lambda},\Delta\vec{\lambda})}\, dt \right|^2, \tag{150}$$

where $\vec{\lambda}$ and $\vec{\lambda}'$ refer to a set of N parameters, such as phase and frequency derivatives, and where $\Delta\vec{\lambda} \equiv \vec{\lambda}' - \vec{\lambda}$ is taken small enough that 2nd-order $\Delta\vec{\lambda}$ corrections in $\Delta\Phi \equiv \Phi(t;\vec{\lambda} + \Delta\vec{\lambda}) - \Phi(t;\vec{\lambda})$ can be neglected. Clearly, for $\Delta\vec{\lambda} = 0$, $F = 1$ and is maximum, with vanishing first partial derivatives. Hence we expect F to have the following form in the vicinity of $\Delta\vec{\lambda} = 0$:

$$F \approx 1 + \frac{1}{2} \sum_{k,\ell=1}^{N} \left. \frac{\partial^2 F}{\partial \Delta\lambda_k \partial \Delta\lambda_\ell} \right|_{\Delta\vec{\lambda}=0} \Delta\lambda_k \Delta\lambda_\ell, \tag{151}$$

where the diagonal 2nd-partial derivatives are negative and which leads to the definition of a *metric*:

$$g_{k\ell} = -\frac{1}{2}\frac{\partial^2 F}{\partial \Delta\lambda_k \partial \Delta\lambda_\ell}\bigg|_{\Delta\vec{\lambda}=0}, \tag{152}$$

such that the *mismatch* μ of a template deviation is $\mu = \sum_{k,\ell} g_{k\ell}\Delta\lambda_k\Delta\lambda_\ell$. Hence the appropriate spacing of templates in parameter space to avoid excessive mismatch is governed by the form of $g_{k\ell}$.

A general treatment of finding $g_{k\ell}$ (Owen 1996) can be approached by Taylor-expanding the exponential in Eq. 150: $e^{i\Delta\Phi} \approx 1 + i\Delta\Phi - \frac{1}{2}\Delta\Phi^2$ and evaluating the second derivatives of F with respect to $\Delta\lambda_k$ and $\Delta\lambda_\ell$. In the limit $\Delta\vec{\lambda} \to 0$, one finds:

$$-\frac{1}{2}\frac{\partial^2 F}{\partial \Delta\lambda_k \partial \Delta\lambda_\ell}\bigg|_{\Delta\lambda=0} = \left[\left\langle \frac{\partial\Delta\Phi}{\partial\Delta\lambda_k}\frac{\partial\Delta\Phi}{\partial\Delta\lambda_\ell}\right\rangle - \left\langle\frac{\partial\Delta\Phi}{\partial\Delta\lambda_k}\right\rangle\left\langle\frac{\partial\Delta\Phi}{\partial\Delta\lambda_\ell}\right\rangle\right]_{\Delta\lambda=0}, \tag{153}$$

where

$$\langle f(t)\rangle \equiv \frac{1}{T}\int_0^T f(t)\,dt. \tag{154}$$

More specifically, in the context of the Taylor Nth-order expansion of the phase function (henceforth omitting $\vec{\lambda}$ dependence in $\Delta\Phi$):

$$\Delta\Phi(t;\Delta\vec{\lambda}) \approx \Delta\phi_0 + 2\pi\sum_{m=0}^{N}\frac{\Delta f^{(m)} t^{m+1}}{(m+1)!}, \tag{155}$$

where $f^{(m)} = \frac{d^m f}{dt^m}\big|_{t=0}$, and the set of frequency derivatives can be treated as a parameter vector $\mathbf{f} \equiv [f^{(0)}, f^{(1)}, ..., f^{(N)}]$. The detection statistic F can be expanded:

$$F \approx \left|\frac{1}{T}\int_0^T e^{i\left(\Delta\phi_0 + 2\pi\sum_{m=0}^{N}\frac{\Delta f^{(m)} t^{m+1}}{(m+1)!}\right)}\,dt\right|^2 \tag{156}$$

$$\begin{aligned}\approx |e^{i\Delta\phi_0}|^2\bigg|\frac{1}{T}\int_0^T\bigg[1 + i\,2\pi\sum_{m=0}^{N}\frac{\Delta f^{(m)} t^{m+1}}{(m+1)!} \\ -\frac{1}{2}(2\pi)^2\sum_{m,n=0}^{N}\frac{\Delta f^{(m)}\Delta f^{(n)} t^{m+n+2}}{(m+1)!(n+1)!}\bigg]\,dt\bigg|^2\end{aligned} \tag{157}$$

$$\begin{aligned}\approx\bigg|\frac{1}{T}\bigg[T + i\,2\pi\sum_{m=0}^{N}\frac{\Delta f^{(m)} T^{m+2}}{(m+2)!} \\ -\frac{1}{2}(2\pi)^2\sum_{m,n=0}^{N}\frac{\Delta f^{(m)}\Delta f^{(n)} T^{m+n+3}}{(m+1)!(n+1)!(m+n+3)}\bigg]\bigg|^2\end{aligned} \tag{158}$$

$$\approx\Bigg[1+(2\pi)^2\sum_{m,n=0}^{N}\frac{\Delta f^{(m)}\Delta f^{(n)}T^{m+n+2}}{(m+2)!(n+2)!} - (2\pi)^2\sum_{m,n=0}^{N}\frac{\Delta f^{(m)}\Delta f^{(n)}T^{m+n+2}}{(m+1)!(n+1)!(m+n+3)}\Bigg] \tag{159}$$

$$=1-(2\pi)^2\sum_{m,n=0}^{N}\frac{\Delta f^{(m)}\Delta f^{(n)}T^{m+n+2}(m+1)(n+1)}{(m+2)!(n+2)!(m+n+3)}. \tag{160}$$

Terms higher in order than $\Delta f^{(m)}\Delta f^{(n)}$ have been neglected in the above. From this last expression, we conclude that the metric $g_{k\ell}$ can be written:

$$g_{k\ell}=(2\pi)^2\frac{T^{k+\ell+2}(k+1)(\ell+1)}{(k+2)!(\ell+2)!(k+\ell+3)}. \tag{161}$$

See Wette et al. (2008) for the same expression for the metric for the $\mathcal{F}$-statistic (Jaranowski et al. 1998) in a directed search.

As examples, consider the 2-parameter metric with respect to frequency f_0 and its first derivative f_1:

$$g_{00}=\frac{1}{3}(\pi T)^2, \tag{162}$$

$$g_{01}=\frac{1}{6}\left(\pi T^{3/2}\right)^2, \tag{163}$$

$$g_{11}=\frac{4}{45}\left(\pi T^2\right)^2. \tag{164}$$

For a given desired mismatch ΔM, define nominal offsets Δf_0^* and Δf_1^*, using only the diagonal metric elements: ($\Delta f_k^*\equiv\sqrt{\Delta M}/g_{kk}$)

$$\Delta f_0^*=\frac{\sqrt{3\Delta M}}{\pi T}, \tag{165}$$

$$\Delta f_1^*=\frac{3\sqrt{5\Delta M}}{\pi T^2}. \tag{166}$$

Since off-diagonal terms in the metric are non-zero, a rectangular grid using only diagonal terms will, in general, be inefficient. Figure 16 illustrates for a 2-dimensional slice of Δf_0 vs. Δf_1 ($=\Delta\dot{f}_{\mathrm{GW}}$) a template grid that accounts for these correlations in mismatch. A grid placement based on only the diagonal metric elements would lead to inefficient coverage, as shown. Prix (2007b) and Wette (2014) discuss more generally and in more detail template grid placement for CW searches, with special focus on searches over the three-dimensional parameter space ($f_{\mathrm{GW}},\dot{f}_{\mathrm{GW}},\ddot{f}_{\mathrm{GW}}$). As noted above, however, for short coherence times, the range of $\ddot{f}_{\mathrm{GW}}$ searches may

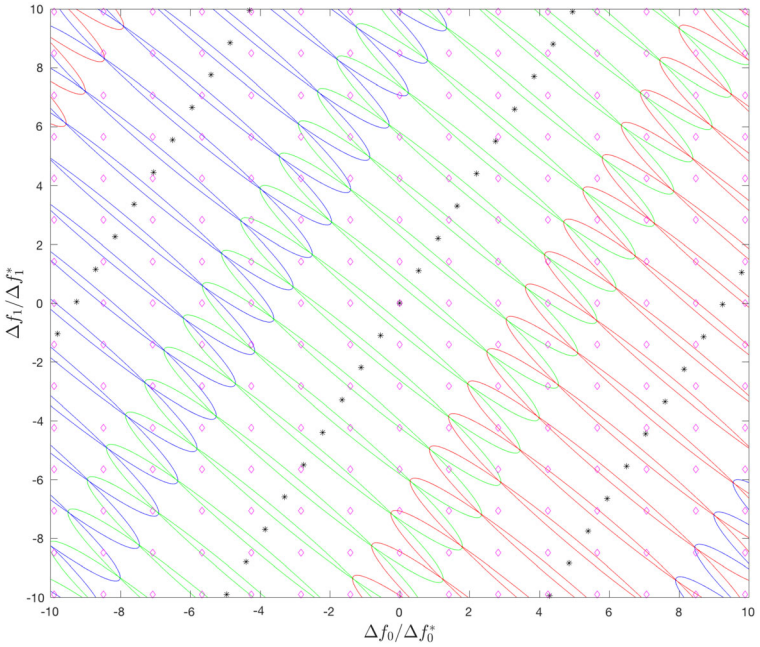

Fig. 16 Illustration of a (Δf_0, Δf_1) template grid (black stars) and constant-mismatch elliptical contours for which the grid point placement gives complete coverage. The values of the frequency and frequency derivative are given in normalized units of Δf_0^* and Δf_1^* defined in Eqs. (165)–166. The magenta diamonds indicate a rectangular grid with full coverage when the off-diagonal metric term is ignored

be smaller than $\Delta \ddot{f}^*_{\rm GW}$ in regions of parameter space, depending on braking-index assumptions and the value of $\dot{f}_{\rm GW}$.

3.6.2 Template placement in all-sky searches

Template placement in all-sky searches is relatively straightforward for semi-coherent searches using short coherence times $T_{\rm coh}$ of $\sim$ h or less, but is quite subtle for coherent searches using much longer coherence times (days) and for semi-coherent searches using long coherence times for each data segment.

Short-$T_{\rm coh}$ template grids can be factorized over sky location (α, δ) and over ($f_{\rm GW}$, $\dot{f}_{\rm GW}$), using isotropic grid point placement, e.g., density proportional to $\cos(\delta)$ and uniform in α, with a rectangular grid in ($f_{\rm GW}$, $\dot{f}_{\rm GW}$), with spacings determined empirically or semi-analytically for a given data run. For example, the rule of thumb given in Eq. (44) overestimates the density needed for short observation times of $\sim$ few months because of correlations (Prix and Itoh 2005) in the dependence of a semi-coherent power sum on sky location and frequency parameters. For a data set collected over 1–2 months of the Earth's orbit, the average acceleration of the detector toward the Sun creates an apparent offset in the spin-down of a putative source. Hence a search over a band of frequencies and 1st derivatives may detect a

signal with nearly as high an SNR as the nominal maximum, but with correlated offsets in the four parameters $(\alpha, \delta, f_{\rm GW}, \dot{f}_{\rm GW})$. For longer observation times, these near degeneracies in parameter space become less helpful; signal templates must be placed more densely. At additional computational cost, these semi-coherent searches may also search explicitly over source polarizations, or may choose to apply a circular polarization weighting and sacrifice some sensitivity to near-linear polarizations (Abbott et al. 2008a).

Template placement for much longer coherence times is more challenging because analytic approximations break down for long coherence times and because naive grid spacings depend on the specific region of the Earth's orbit covered by a particular coherence time, making the systematic matching of signal candidates across different time segments non-trivial in semi-coherent searches. Template placement for the $\mathcal{F}$-statistic has received much attention in the last decade and a half (Whitbeck 2006; Prix 2007a, b; Wette and Prix 2013; Wette 2014), in part because of its use in the Einstein@Home (see Sect. 4.4) distributed computing platform. From Eq. (121), one can define a mismatch analogous to that of Sect. 3.6.1:

$$1 - \mu \equiv \frac{(h_{\vec{\lambda}+\Delta\vec{\lambda}}|h_{\vec{\lambda}+\Delta\vec{\lambda}})}{(h_{\vec{\lambda}}|h_{\vec{\lambda}})}, \tag{167}$$

where we expect an approximately quadratic falloff from unity for small $|\Delta\vec{\lambda}|$ (but see Allen 2019 for a discussion of template placement for larger $|\Delta\vec{\lambda}|$ and see Allen 2021 which distinguishes between optimality for setting rigorous upper limits and optimality for signal detection).

The complexity of the definition of $(h|h)$ (see Eqs. 50–51 and 100–106) do not yield a definition of $(h|h)$ in the convenient form of Eq. (149). In particular, the sidereal antenna pattern modulations due to the Earth's rotation are not accommodated by the phase-only dependence of the simplified form. For long observation times, however, amplitude modulation effects can be averaged with sufficient accuracy (Prix 2007a). Phase modulation from the Earth's motion is captured by Eq. (149), allowing use of Eq. (153) to determine the $\mathcal{F}$-statistic metric with respect to frequency parameters and sky location.

Following the treatment of Prix (2007a), a more explicit phase evolution can be written:

$$\Phi(t) = \phi_0 + 2\pi \sum_{m=0}^{N} \frac{f^{(m)}(\tau_{\rm ref})\, \tau(t)^{m+1}}{(m+1)!}, \tag{168}$$

where $\tau(t)$ is the SSB arrival time of the signal. Ignoring the Shapiro and Einstein delays in Eq. (47) for metric definition, one can write:

$$\tau(t) = t + \frac{\vec{r}(t) \cdot \hat{n}}{c} - \tau_{\rm ref}, \tag{169}$$

where $\vec{r}(t)$ is the position of the detector at time t, $\hat{n}$ is the unit vector pointing from the detector to the source, and $\tau_{\rm ref}$ is the reference time in the SSB frame at which the frequency and its derivatives are defined.

The phase derivatives entering Eq. (153) can then be written:

$$\frac{\partial \Phi}{\partial f^{(k)}} = 2\pi \frac{\tau(t)^{k+1}}{(k+1)!}, \tag{170}$$

$$\frac{\partial \Phi}{\partial n_i} = 2\pi \frac{r_i(t)}{c} \sum_{m=0}^{N} \frac{f^{(m)}(\tau_{\rm ref})\, \tau(t)^m}{m!}, \tag{171}$$

where $\vec{r}(t) \cdot \hat{n} = \sum_i r_i(t) n_i$, from which the metric terms for a particular point in parameter space $(\mathbf{f}, \hat{n})$ can be computed via numerical integration of Eq. (153) over the observation span, with precise description of $\vec{r}(t)$, accounting for the non-zero eccentricity of the Earth's orbit. It is convenient in some studies, though, to make the "Ptolemaic" approximation (Jones et al. 2005; Whitbeck 2006) in which the Earth's orbit is treated as circular, for which analytic but quite lengthy trigonometric expressions can be obtained (Whitbeck 2006).

As shown in Jaranowski et al. (1998), the GW phase described by Eqs. (168)–(169) can be well approximated (setting the reference time $\tau_{\rm ref} = 0$ for convenience) by

$$\Phi(t) = \phi_0 + 2\pi \sum_{m=0}^{N} \frac{f^{(m)} t^{m+1}}{(m+1)!} + 2\pi \frac{\vec{r}(t) \cdot \hat{n}}{c} \left(\sum_{k=0}^{N} \frac{f^{(k)} t^k}{k!} \right). \tag{172}$$

The last term in Eq. 172 can be usefully decomposed into the orbital motion of the Earth's center and the spin of the detector about the Earth's center with orbital and spin phases ($\vec{r}(t) = \vec{r}_{\rm orb}(t) + \vec{r}_{\rm spin}(t)$):

$$\Phi_{\rm orb}(t) = 2\pi \frac{\vec{r}_{\rm orb}(t) \cdot \hat{n}}{c} \left(\sum_{k=0}^{N} \frac{f^{(k)} t^k}{k!} \right), \tag{173}$$

$$\Phi_{\rm spin}(t) = 2\pi \frac{\vec{r}_{\rm spin}(t) \cdot \hat{n}}{c} \left(\sum_{k=0}^{N} \frac{f^{(k)} t^k}{k!} \right). \tag{174}$$

An inconvenient property of the metric defined above using the parameters $(\vec{f}, \hat{n})$ is that converting the 3-D Cartesian $\hat{n}$ components to the 2-D sky coordinates α and δ leads to a sky spacing that depends on the parameter themselves. A metric more convenient for large-scale CW searches over the entire sky can be obtained by using *global correlations* in parameter space (Pletsch 2008; Pletsch and Allen 2009). Some searches exploiting these correlations are known as "GCT" searches for "Global Correlation Transform." For multi-day coherence times short compared to one orbital year, one can Taylor-expand the rescaled position of the Earth's center $\vec{\xi}(t) \equiv \vec{r}_{\rm orb}(t)/c$ in Eq. (169) about the midpoint t_0 of the coherence time span $T_{\rm coh}$:

$$\vec{\xi}(t) = \vec{\xi}(t_0) + \sum_{n=1}^{\infty} \frac{\vec{\xi}^{(n)}(t_0)(t-t_0)^n}{n!}. \tag{175}$$

The Earth's orbital motion contribution to signal phase (Eq. 173) can then be rewritten:

$$\Phi_{\rm orb}(t) = 2\pi \left(\sum_{k=0}^{N} \frac{f^{(k)}(t-t_0)^k}{k!} \right) \left(\sum_{\ell=0}^{\infty} \frac{(t-t_0)^\ell}{\ell!} \vec{\xi}^{(\ell)} \cdot \hat{n} \right) \tag{176}$$

$$= 2\pi \sum_{m=0}^{\infty} (t-t_0)^m \left(\sum_{n=0}^{m'} \frac{f^{(n)} \vec{\xi}^{(m'-n)}}{n!(m'-n)!} \cdot \hat{n} \right), \tag{177}$$

where $m' = \min(m,N)$.

It is also convenient to define new sky coordinates that capture the vector difference in signal phase (radians) between the source direction (α, δ) and the detector's direction from the Earth's center ($\alpha_D(t_0)$, δ_D) at time t_0 (Pletsch 2010):

$$n_x(t_0) \equiv 2\pi f(t_0)\tau_{\rm E} \cos(\delta)\cos(\delta_D)\cos[\alpha - \alpha_D(t_0)], \tag{178}$$

$$n_y(t_0) \equiv 2\pi f(t_0)\tau_{\rm E} \cos(\delta)\cos(\delta_D)\sin[\alpha - \alpha_D(t_0)], \tag{179}$$

where $\tau_{\rm E} = R_{\rm E}/c$ is the light travel time from the Earth's center to the detector. (See Jaranowski and Królak 1999 for a similar sky coordinate definition.)

Using Eqs. (168)–(169) and (175)–(179), including the approximation in Eq. (172), and absorbing phase constants into a single term ϕ_0', one obtains (Pletsch 2010):

$$\begin{aligned} \Phi(t) = {} & \phi_0' + \sum_{k=0}^{N} \nu^{(k)}(t_0) \left(\frac{t-t_0}{T_{\rm coh}} \right)^{k+1} 2^{k+1} \\ & + n_x(t_0)\cos(\Omega t) + n_y(t_0)\sin(\Omega t), \end{aligned} \tag{180}$$

where $\nu^{(k)}$ are new coordinates, serving the role of effective frequencies and effective frequency derivatives and Ω is the Earth's rotational angular velocity (sidereal time):

$$\begin{aligned} \nu^{(k)}(t_0) = {} & 2\pi \left(\frac{T_{\rm coh}}{2} \right)^{k+1} \left[\frac{f^{(k)}(t_0)}{(k+1)!} + \right. \\ & \left. + \sum_{\ell=0}^{k+1} \frac{f^{(\ell)}(t_0)}{\ell!(k-\ell+1)!} \vec{\xi}^{(k-\ell+1)}(t_0) \cdot \hat{n} \right], \end{aligned} \tag{181}$$

where the insertion of powers of $T_{\rm coh}$ is to make the coordinates dimensionless. Since large-parameter-space all-sky searches to date have used only up to 1st-order frequency derivatives in first-stage analysis, it is useful to express $\nu(t_0)$ and $\dot{\nu}(t_0) \equiv \nu^{(1)}(t_0)$ explicitly (neglecting higher-order derivatives and setting $N = 1$ in Eq. (176)). One obtains (Pletsch 2010):

$$v(t_0) = 2\pi \frac{T_{\mathrm{coh}}}{2} \left[f(t_0) + f(t_0)\dot{\vec{\xi}}(t_0) \cdot \hat{n} + \dot{f}(t_0)\vec{\xi}(t_0) \cdot \hat{n} \right], \tag{182}$$

$$\dot{v}(t_0) = 2\pi \left(\frac{T_{\mathrm{coh}}}{2} \right)^2 \left[\frac{\dot{f}(t_0)}{2} + \frac{f(t_0)}{2} \ddot{\vec{\xi}}(t_0) \cdot \hat{n} + \dot{f}(t_0)\dot{\vec{\xi}}(t_0) \cdot \hat{n} \right]. \tag{183}$$

The form of Eq. (180) indicates the phase is linear with respect to the coordinates $v^{(k)}$, n_x and n_y, which permits an analytic evaluation of the metric components (Pletsch 2010) for a coherent search. Expressions appropriate for searching over a 2nd-order frequency derivative can be found in Pletsch (2010)

Further, in the context of a semi-coherent search constructed from N_{coh} coherently analyzed segments, one can systematically apply a refined metric in summing $\mathcal{F}$-statistic values over the segments. In practice, a "coarse grid" for each segment j is defined by evaluating Eq. (153) to obtain the $g^{[j]}_{\alpha\beta}$. In summing the $\mathcal{F}$-statistic values, one must use a "fine grid" to avoid needless loss of SNR from signal evolution over the full observation period. As shown in (Pletsch 2010), for the global correlation parameters, one can obtain the following approximation to the fine-grid metric from

$$\bar{g}_{\alpha\beta} = \frac{1}{N_{\mathrm{coh}}} \sum_{j=1}^{N_{\mathrm{coh}}} g^{[j]}_{\alpha\beta}. \tag{184}$$

Explicit evaluation of $\bar{g}_{\alpha\beta}$ over many sidereal days leads to a fine grid that scales as $\frac{1}{N_{\mathrm{coh}}}$ for only the $\dot{v}$ coordinate (Pletsch 2010), which is unsurprising, since the frequency derivative is the parameter driving the evolution of the frequency over time. Explicit expressions for $g^{[j]}_{\alpha\beta}$ and $\bar{g}_{\alpha\beta}$ may be found in (Pletsch 2010). One criticism (Wette 2015) of this fine-grid metric approximation, however, is that it does not explicitly take into account the changes in reference time implicit in each Taylor expansion for each segment. Nonetheless, one finds empirically (Wette 2016) that for semi-coherent searches the effective $\mathcal{F}$-statistic mismatch grows much more slowly than implied by the Taylor expansion in Eq. (175), allowing Eq. (184) to be used successfully in Einstein@Home searches with large nominal metric mismatches.

The Weave software infrastructure provides a more systematic approach to covering the parameter space volume in a templated search to ensure acceptable loss of SNR for true signals lying between template points (Wette et al. 2018). The Weave program combines together recent developments in template placement to use an optimal parameter-space metric (Wette and Prix 2013; Wette 2015) and optimal template lattices (Wette 2014). The package is versatile enough to be used in all-sky searches for unknown sources and in directed searches for particular sources, such as the Cas A and Vela Jr. supernova remnants (Abbott et al. 2022i).

In brief, Weave creates a template grid in the parameter space for each time segment, a grid that is appropriate to computing the $\mathcal{F}$-statistic for a coherence time T_{coh} equal to the total observation period T_{obs} divided by N_{seg}. The spacing of the grid points in parameter space is set according to a metric (Wette and Prix 2013; Wette 2015) that ensures a worst-case maximum mismatch m_{coh} defined by the fractional

loss in summed $\mathcal{F}$-statistic value due to a true signal not coinciding with a search template.

Separately, a much finer grid is defined for the full observation period with respect to the midpoint of the observation period, one with its own mismatch parameter $m_{\mathrm{semi-coh}}$, analogous to m_{coh}, where the semi-coherent metric is the average of all the coherent metrics, which (unlike in the (GCT) approximation) use a common reference time. The choice of the $m_{\mathrm{semi-coh}}$ value is set empirically in a tradeoff between sensitivity and computational cost. The Weave package creates at initialization a mapping between each point in the semi-coherent template grid and a nearest corresponding point in each of the separate, coarser segment grids, accounting for frequency evolution.

The discussion above has implicitly assumed analysis of data from a single detector. One may wonder if detection statistics based on two or more detectors require a finer template spacing, given the potential for better discrimination of signals by requiring coherent signal phase consistency among the detectors. For short coherence times there is indeed a finer discrimination from coherent summing when phase consistency is enforced and hence a need for finer sampling of frequency and sky location (Goetz and Riles 2016). For much longer coherence times, however, this statement no longer holds. For example, the multi-detector $\mathcal{F}$-statistic (Cutler and Schutz 2005) has a coherent parameter space metric that is essentially unchanged from that of a single-detector $\mathcal{F}$-statistic (Prix 2007a).

This perhaps surprising result can be understood from considering the intrinsic motions of the detectors on the surface of an Earth in orbit. In order to maintain phase coherence for a single detector over the course of one day, one must track the detector's relative motion around the Earth's center a distance of order the diameter of the Earth ($\sim$ 13,000 km), larger than any detector pair separation. In addition, the Earth's center travels a distance in its orbit of about 2.6 million km in one day, and more important to template spacing, deviates from a straight line by approximately 22,000 km. Given the phase fidelity needed to account for these Earth-induced motions over coherence times much longer than this, the incorporation of additional detectors on the face of the Earth does not impose an extra burden on template placement. Note, though, that combining data coherently from N_{det} detectors of equal sensitivity and similar livetime fractions does improve SNR by the nominal desired $\sqrt{N_{\mathrm{det}}}$ (Prix 2007a).

Finally, although the above approach of defining the template spacing according to a metric computed in the strong-signal regime is widespread in the CW literature, an important alternative instead places templates according to isoheights of the autocovariance function of the *signal-free* detection statistic (Astone et al. 2002a; Jaranowski and Królak 2009; Astone et al. 2010a; Pisarski et al. 2011; Pisarski and Jaranowski 2015). See Appendix A of Pisarski and Jaranowski (2015) for a comparison of these two approaches for searches based on the $\mathcal{F}$-statistic.

3.6.3 Viterbi methods and machine learning

All of the search methods described so far use signal templates, explicitly or implicitly via favored frequency evolution. When searching a large parameter space volume with fine resolution, computational cost becomes formidable and often determinative of achievable sensitivity. Alternative approaches receiving increased attention rely upon more generic pattern recognition.

The generic approach that has received most attention in recent years is based on Viterbi dynamical programming (Viterbi 1967). To illustrate with a simplified example, consider finding a signal "trajectory" in a spectrogram, such as shown in Fig. 9. A templated search might sum up the power for every possible trajectory allowed by the signal model and declare one or more candidate outliers based on a summed power of spectrogram pixels exceeding a pre-determined threshold. The Viterbi method (in its simplest form) dispenses with templates, seeking instead for the loudest trajectory that "moves" in time from left to right, where the degree of contiguity from one vertical column to the next is tunable. For example, a trajectory traveling from a pixel in column n and row m_n to column $n+1$ may be constrained to change by no more than one row: $|m_{n+1} - m_n| \leq 1$. For a trajectory that begins in row m_1 in column 1 and travels to row m_N in the last column (N), the number of possible trajectories is 3^{N-1}. Maximizing the power over all possible such trajectories does not, however, require explicitly evaluating each power. The Viterbi algorithm leads to the insight that the trajectory with the highest summed power (for a strong enough signal) is also locally maximum, which allows rapid elimination of the vast majority of non-optimum trajectory segments and a remarkably fast evaluation of the detection statistic.

The Viterbi method was first demonstrated in CW searches via a "spectrogram" with each pixel representing a Bessel-weighted $\mathcal{F}$-statistic evaluated over a 10-day period for Scorpius X-1 (Suvorova et al. 2016) over the course of the initial LIGO S6 run (part of a Sco X-1 mock data challenge Messenger et al. 2015). Follow-up analyses with additional refinements have been applied to Suvorova et al. (2017) or proposed (Melatos et al. 2021) for searches from the Advanced LIGO and Advanced Virgo O1, O2 and O3 data (Abbott et al. 2017n, 2019e; Sun et al. 2020) (see Sect. 4.3). Simultaneous tracking of stellar rotational phase and orbital phase (Melatos et al. 2021) offers a significant improvement in strain sensitivity relative to tracking of orbital phase alone (Suvorova et al. 2017). In addition, the Viterbi method has also been applied to searches for accreting millisecond pulsars (Middleton et al. 2020; Abbott et al. 2022g), isolated neutron stars (Sun et al. 2018; Millhouse et al. 2020; Abbott et al. 2021i) and for a post-merger remnant from the BNS merger GW170817 (Abbott et al. 2019d). The Viterbi method may see its largest gain in computation cost, though, from application to all-sky searches (Bayley et al. 2020; Abbott et al. 2022b).

Although the hidden Markov Viterbi method has dramatic potential for reducing computational cost, it also has another important virtue; it is robust with respect to unknown and potentially stochastic frequency evolution that deviates from templated models. That flexibility makes the methodology especially important for accreting

systems like LMXBs (see Sect. 2.1.4) and for extremely young sources, such as newborn neutron stars and post-merger hypermassive neutron stars (see Sect. 3.10).

Machine learning techniques, such as convolutional neural networks, have received less attention, but offer similar gains in computational cost. One trains an algorithm on noise samples and signal+noise samples, for which machine learning detects an underlying pattern, producing an opaque but potentially effective algorithm for quickly yielding high detection statistic values for true signals. An early study (Dreissigacker et al. 2019) of single-detector data confirms the enormous gain in computing cost possible, but does not suggest such automated algorithms achieve greater sensitivity. A follow-up study (Dreissigacker and Prix 2020) examined machine learning on multi-detector data sets with realistic data gaps and non-Gaussian noise. Another study (Beheshtipour and Papa 2020) found that a convolutional neural network proved efficient in clustering Einstein@Home search outliers, to reduce computational cost in follow-up, with a different tuning found effective for identifying weak signals (Beheshtipour and Papa 2021). Another recent study examined the potential for combining convolutional neural network analysis with Doppler demodulation for the Earth's diurnal rotation in an all-sky search (Yamamoto and Tanaka 2021).

These generic methods are powerful in yielding rapid results, but require some care in use. For example, when searching a narrow band with instrumental artifacts, the Viterbi method may seize upon the artifact and miss a nearby signal, although imposing consistency between different detectors can mitigate this problem (Bayley et al. 2020). An area of active research is understanding better the statistics of the loudest outlier in a Viterbi search, specifically, to understand the effective trials factor, a large value of which degrades strain sensitivity. In the event of a first detection via non-templated methods, there remain, of course, fully templated methods available to assess more quantitatively a candidate signal's credibility and to estimate source parameters.

3.7 Coping with non-Gaussian instrumental artifacts

Non-Gaussian instrumental artifacts, especially spectral line artifacts, degrade CW searches. The degradation depends on the nature of the search. Stationary, narrow line artifacts generally do not significantly degrade targeted searches for known pulsars, for which long observation times permit extremely fine frequency resolution and known ephemerides permit that resolution to be exploited. Periods during which a frequency-modulated signal overlaps with a known artifact can be vetoed or deweighted. On the other hand, an all-sky search is prone to contamination, especially in short data runs for which frequency modulation from certain sky directions may be limited, making a stationary instrumental line resemble a signal template, at least in the first stage of a hierarchical search.

For low assumed source spin-down (and no binary source modulation), the templates most prone to contamination lie near the ecliptic poles, where signal frequency modulation due to the Earth's orbital motion would be small. At larger spin-down magnitudes, a stationary line can also lead to contamination of signal templates for which the frequency shift due to the Earth's average acceleration

toward the Sun largely cancels the assumed source spin-down. The associated templates tend to lie in a circular band concentric with the Sun's average direction during the run with a radius and skyband thickness depending on the assumed frequency, spin-down and on the coherence time of the search (Abbott et al. 2008a). Such contamination is most pronounced for data runs short relative to a year.

In principle, even a stationary line near an ecliptic pole should not be mistaken for a true signal once a fully coherent algorithm is applied to assess that discrimination. The chance of an instrumental line displaying the residual frequency modulation (including that due to the Earth's daily rotation) and associated phase modulation of a true signal is quite small. Moreover, the chance that two different detectors would display the same line artifact with precisely the right time-dependent offset in phase to account for the daily change in relative positions of the detectors is quite small. For example, one veto method (Zhu et al. 2017) is based on turning off demodulation in the vicinity of an outlier template to determine if an even louder candidate is found. Another veto method, specific to the Frequency Hough search pipeline (see Sect. 3.5.3), exploits characteristic patterns in the detection statistic variation across search template parameter space created by stationary lines (Intini et al. 2020a). Similar considerations can be applied to following up outliers from Viterbi-based searches (Jones et al. 2022) (see Sect. 3.6.3). Nonetheless, lines are a major problem in CW searches because at initial stages of hierarchical searches, such discrimination is not available with tractable computational cost. Strong lines can trigger apparent loud signal outliers over regions of parameter space, making outlier follow-up challenging. Simply vetoing such a region because of a known contamination risks overlooking a true signal that would be recoverable in a deep search.

Several methods have been developed for coping with these line-induced problems in early search stages (Astone et al. 2014a; Leaci 2015; Tenorio et al. 2021b), to reduce the burden of needless outlier followup while maintaining satisfactory detection efficiency for true signals. The simplest method is to veto outliers known to be contaminated by a known line. This approach is effective in reducing computational cost, but does risk throwing away real and detectable signals. A more refined approach, one that need not rely upon prior knowledge of particular lines is imposing consistency in signal strength seen in two or more detectors. For example, for two detectors of similar sensitivity one can require that individual detection statistic strengths in both detectors exceed a threshold and that the combined detection strength exceed both individual-detector strengths. Similarly, in a Bayesian approach one can impose consistency in the definition of the combined detections statistic (Keitel et al. 2014; Keitel and Prix 2015; Keitel 2016). An empirical background estimation to account for non-Gaussian contribution can be obtained (Isi et al. 2020) via "sky-shifting," that is, by evaluating template recovery strengths for identical source parameters except for offsets in sky location. One can also require consistency in SNR across different data subsets for a putative outlier template, such as via a χ^2 test for the separate contributions to the detection statistic (Sancho de la Jordana and Sintes 2008).

Another approach is "cleaning" of data prior to searching for CW signal templates. Time-domain data cleaning has been used for general-purpose analysis

(Allen et al. 1999; Meadors et al. 2014; Tiwari et al. 2015; Driggers et al. 2019; Davis et al. 2019; Vajente et al. 2020; Davis et al. 2021; Viets and Wade 2021) where an auxiliary witness channel permits regression of known noise. Such cleaning can remove both broadband and narrow contamination (Driggers et al. 2019). A more CW-specific procedure can be carried out in the frequency domain in the absence of a witness channel—if a non-astrophysical source is clear. After creating DFTs one can replace bins known to be contaminated with randomly generated DFT coefficients consistent in magnitude with noise in neighboring bins (Abbott et al. 2009c). This approach potentially renders particular true signals less detectable or undetectable, particularly for sky locations near the ecliptic poles; hence injection simulations are needed to assess efficiency loss when setting upper limits in the absence of a signal.

Many spectral lines in a detector's gravitational-wave strain channel can be identified via correlation/coherence with lines observed in auxiliary channels, such as for magnetometers or accelerometers, that monitor the environment and that have no sensitivity to true astrophysical systems (Aasi et al. 2015b; Covas et al. 2018). Others may not have a reliable witness channel, but come in "combs" of many lines with equal frequency spacings between adjacent lines, inconsistent with a plausible astrophysical source, allowing safe veto or cleaning (Goetz et al. 2021). Efficient tracking of known lines is an active area of investigation, including tracking of lines that wander slightly in frequency (Daw et al. 2022).

Traditionally, transient instrumental glitches in LIGO data that create nuisances (sometimes severe) in searches for transient gravitational wave signal have not troubled CW searches much because their effect on overall noise level integrated over long time periods has been small. In the LIGO O3 data, however, a new class of extremely loud glitches with spectra peaking at low frequencies but visible as high as $\sim$ 500 Hz appeared. These glitches of uncertain origin plagued both LIGO interferometers and occurred loudly and frequently enough to degrade sensitivity to CW signals in the low-frequency band. To cope with this new artifact, an *ad hoc* "self-gating" algorithm (Zweizig and Riles 2021) was developed to taper the data in the time domain to zero during the affected intevals of $\sim$seconds before creating DFTs for Fourier analysis. A more sophisticated, adaptive self-gating method (Steltner et al. 2022b) achieved transient suppression with reduced deadtime. An earlier gating algorithm (Astone et al. 2005) was developed to cope with loud gltiches in initial Virgo data and later refined (Astone et al. 2014a).

3.8 Sensitivity depth

A rough rule of thumb is convenient when assessing the detectability of a prospective CW signal for a given data set. Such a figure of merit is the *sensitivity depth* (Behnke et al. 2015). Its use arose in part because of the large variations in (1) methodologies with cost/sensitivity dependence on parameter space volume searched; (2) durations T_{obs} of data runs (or subsets) used in analyses; and (3) intrinsic detector sensitivity versus frequency. In part too, it avoids sometimes unwarranted assumptions based on idealized scaling with observation time. For example, a semi-coherent search with sensitivity improvements proportional to $T_{\mathrm{obs}}^{1/4}$ may require more computational

resources than are available if T_{obs} becomes too large, especially since increasing T_{obs} usually requires stepping more finely in parameter space.

Instead, the sensitivity depth (Dreissigacker et al. 2018) addresses the "bottom line" with respect to a given intrinsic detector strain amplitude spectral noise density (square root of power spectral noise density S_h):

$$\mathcal{D} \equiv \frac{\sqrt{S_h}}{h_0}, \tag{185}$$

where h_0 is the quantity of interest, typically the 90% or 95% upper limit on a strain amplitude. By design the depth does not include a parametrized scaling with observation time. Hence the values for a given algorithm do depend on the particular data set. Dreissigacker et al. (2018) examines in detail the sensitivity depths achieved in searches of LIGO and Virgo data from the early initial LIGO S2 run to the first Advanced LIGO / Virgo run O1. Values range for templated searches from $\sim$ 1000 for targeted searches of $\sim$ 2 years down to $\sim$ 20 for the most sensitive all-sky search for CW signals in unknown binary systems.

3.9 Upper limits and sensitivities

The CW search literature is rife with different conventions on how negative results (non-discoveries) are reported. This section gives a brief guide to the reader in understanding those variations and the reasons for them.

Most analyses have produced frequentist upper limits at 95% (or 90%) confidence level, meaning that in a hypothetical ensemble of repeated experiments with the same underlying random noise contributions (but the same, non-random instrumental artifacts), a signal at the nominal upper limit value would have yielded a higher detection statistic 95% (90%) of the time. These upper limits are derived from or at least validated by simulated signals (injections) and are quoted over narrow bands in frequency (usually 1 Hz or less), where wider bands necessarily have somewhat higher upper limits than most of the narrower bands from which they are composed.

Deriving rigorous upper limits with extensive simulations in each individual band is computationally expensive (particularly for 95% C.L.), so it has become common in recent years to derive instead "sensitivities" at, say, 95% efficiency after following up and ruling out every outlier in each search band that lies above a nominal threshold (where the choice of threshold depends on a target false alarm probability that varies considerably across different searches). These sensitivities are calibrated by deriving upper limits in a sparse sampling of narrow bands over the full search spectrum and finding an empirical scale factor between upper limits and average strain amplitude spectral densities for the data set, using a weighted average appropriate to the search. These sensitivities are not rigorous upper limits, particularly in disturbed bands, but give a useful interpretation of a non-detection.

In highly disturbed bands with one or more strong instrumental lines, it is sometimes impractical to derive rigorous upper limits for some search methods or even to derive useful sensitivities. Such bands are vetoed and no upper limit quoted. As noted in Sect. 3.7, when SFT cleaning of instrumental lines is used, one must take

into account the resulting loss in detection efficiency in quoting upper limits. When strong lines are not vetoed or cleaned, upper limits in affected nearby bands typically suffer and may not apply at all to regions very near the ecliptic poles.

Most quoted frequentist upper limits are population-averaged over the parameter space searched, assuming random orientation of the stellar spin axis, and in the case of all-sky searches, random position on the sky. Detection efficiency varies substantially for different angles of stellar inclination ι (best efficiency for $|\cos(\iota)|$ near one, corresponding to circular polarization), and to a lesser extent over different regions of the sky. Because of this variation in sensitivity, the PowerFlux pipeline (see Sect. 3.5.2) derives separate upper limits for circular polarization and linear polarization, where in each case the 95% C.L. upper limits are strict in the sense that 95% coverage is maintained separately for every position on the sky. Approximate population-averaged upper limits can then be derived from the strict circular-polarization limits via multiplying by a scale factor (typically $\sim$ 2.3) empirically determined from simulations in a given data set, including its non-stationarity and non-Gaussian contaminations (Abbott et al. 2017d, 2021a).

As described in Sect. 3.4.4, an alternative Bayesian analysis technique has been applied to targeted searches for known pulsars. In that approach a 95% credible Bayesian upper limit on strain amplitude is obtained, which is interpreted as the analyst's confidence that the true amplitude of a signal lies below that value, given the observed data and (conservative) prior beliefs in the parameter values. Bayesian notions of prior expectation have also influenced the construction of frequentist detection statistics.

3.10 Transient CW sources

In recent years, and particularly since the discovery of the binary neutron star merger GW170817, attention has turned to signal models that deviate from the canonical CW source of near-constant amplitude and very low intrinsic frequency evolution. Searches for two distinct classes of "near-CW" signals have been developed, one for sources of stable intrinsic frequency, but of large amplitude variations, and one for sources of rapid spin-down and concomitant amplitude decrease. The primary target motivating the first type of search is a neutron star glitch, in which a sudden stellar deformation appears, such as a ruptured crust, causing a sudden increase in the strength of gravitational waves emitted at twice the spin frequency of the star (Prix et al. 2011; Yim and Jones 2020). The resulting stellar spin-down would be modest, leading to only small relative changes in frequency during the time required for the deformation to heal. Hence the search methods differ from "standard" CW methods primarily in allowing for a time-dependent strength.

The danger in using the standard methods on a "transient CW" signal is that the data used prior to the glitch tends to reduce the integrated SNR, as does amplitude decay. To avoid this problem, an $\mathcal{F}$-statistic-based method segments the data and look separately for signals within individual segments and coherently or semi-coherently across different combinations of segments (Prix et al. 2011; Keitel 2016; Keitel et al. 2019; Keitel and Ashton 2018; Abbott et al. 2022f; Modafferi et al. 2021). See Moragues et al. (2023) for a recent, detailed assessment of the prospects

(near-term and long-term) for detecting quasi-monochromatic gravitational emission in the aftermath of glitches, based on a study of 726 previously observed electromagnetic glitches.

Another class of near-CW source is a post-merger remnant, in which two neutron stars form a hypermassive neutron star (2–3 solar masses). Although one naively expects such a star to collapse promptly into a black hole, rapid rotation (rigid-body or differential) can delay the collapse for certain equations of state (Baiotti and Rezzolla 2017; Piro et al. 2017; Ravi and Lasky 2014). In extreme equations of state, the collapse may be delayed until the star's rotation frequency has decreased dramatically (Ravi and Lasky 2014). Given the enormous initial quadrupole asymmetry as two neutron stars begin to merge, one might hope for a substantial residual asymmetry in the minutes, hours or even days during which a post-merger remnant persists. That asymmetry might well lead to a rapid spin-down, one for which the truncated Taylor expansion in Eq. (40) is a poor approximation.

A recent search in LIGO data for a post-GW170817 remnant (Abbott et al. 2019d) used instead a model (for sensitivity determination) in which the frequency has an evolution similar to that of Eq. (5), but with a different normalization convention:

$$\frac{d\Omega}{dt} = -k\Omega^n, \tag{186}$$

where $\Omega(t)$ is the angular frequency of rotation, n is the braking index and k is a positive real constant. This equation leads to an explicit form for $f_{\rm GW}(t)$ (Lasky et al. 2017b; Sarin et al. 2018):

$$f_{\rm GW}(t) = \frac{f_{\rm GW}(0)}{\left(1 + \frac{t}{\tau_{\rm SD}}\right)^{\frac{1}{n-1}}}, \tag{187}$$

where $\tau_{\rm SD}$ is a characteristic time scale for spin-down:

$$\tau_{\rm SD} = \frac{1}{k(n-1)\Omega_0^{n-1}}, \tag{188}$$

and where $\Omega_0 = \Omega(t = 0)$.

Since the amplitude depends on frequency for fixed ellipticity (see Eq. (14)), one expects the amplitude to decrease monotonically too:

$$h_0 = \frac{4\pi^2 G\epsilon I_{zz} f_{\rm GW}^2(0)}{c^4 r} \frac{1}{\left(1 + \frac{t}{\tau_{\rm SD}}\right)^{\frac{2}{n-1}}}. \tag{189}$$

In addition, the product ϵI_{zz} is likely to decrease as the post-merger remnant spins down.

A more significant hurdle to detection than fidelity of the signal model, however, is the typical distance at which binary neutron star mergers occur. GW170817 lay approximately 40 Mpc away, several orders of magnitude farther than the neutron stars sought in our own galaxy. The necessary ellipticity to generate a detectable signal is hence enormous; at the same time, such an ellipticity ensures a rapid-enough

spin-down that no appreciable SNR could be achieved through integration over the signal's duration at current detector sensitivities. Based on the total number of definitive BNS detections (two) (Abbott et al. 2017k, 2020a, 2021f) during the O1 through O3 data runs and on the volume-time sampled in those runs, it appears that GW170817 was closer than the bulk of the BNS mergers expected in future runs. Detecting a CW signal from a post-merger remnant may require significantly more sensitive detectors than those that detected GW170817. Applicable search methods for such a rapidly evolving signal have been developed both well before (Thrane et al. 2011) and especially after (Thrane et al. 2011; Miller et al. 2018; Sun and Melatos 2019; Oliver et al. 2019; Banagiri et al. 2019; Mytidis et al. 2019; Miller et al. 2019a) the discovery of GW170817.

4 Results of continuous wave searches

Searches have been carried out for continuous gravitational waves for five decades, starting with data from early detector prototypes (Levine and Stebbins 1972; Hirakawa et al. 1978; Livas 1989; Suzuki 1995). Although transient gravitational-wave discoveries to date have relied upon coincident signal detections in two or more detectors, a definitive continuous-wave source discovery can be accomplished, at least in principle, with a single gravitational-wave detector. By definition, the source remains on, allowing follow-up verification of the signal strength and of the distinctive Doppler modulations of signal frequency due to the Earth's motion. In the event of an all-sky discovery, for which intrinsic sensitivity is necessarily limited by computational realities (see Sect. 3.1), it is likely that a stable continuous signal could then *a posteriori* be detected in prior data sets via targeted searches. Hence a relatively large number of CW searches were carried out with both bar detectors and interferometer prototypes in the decades before the major 1st-generation interferometers began collecting data, as summarized in Abbott et al. (2004).

The most sensitive of the resulting early upper limits (Hirakawa et al. 1978; Suzuki 1995; Astone et al. 2002b) came from bar detectors in their narrow bands of sensitivity. The Explorer detector reported (Astone et al. 2002b) an upper limit on spin-downless CW signals from the galactic center of 2.9×10^{-24} in a 0.06 Hz band near 921 Hz, based on 96 days of observation. A broader-band ($\sim$ 1 Hz) upper limit of 2.8×10^{-23} was also reported (Astone et al. 2002a) from the Explorer detector based on a coherent 2-day search that allowing for stellar spin-down. In addition, searches for spin-downless CW waves from the galactic center and from the pulsar-rich globular cluster 47 Tucanae in two 1 Hz bands near 900 Hz were carried out in Allegro detector data, yielding upper limits (Mauceli et al. 2000) of 8×10^{-24}. Finally, a narrowband (0.05 Hz) search (Soida et al. 2003) was carried out with the TAMA interferometer near 935 Hz for continuous waves from the direction of Supernova 1987A, with an upper limit of 5×10^{-23} reported.

When the initial LIGO interferometers and later the initial Virgo interferometer began collecting data in the 2000's, CW searches became more sensitive, both from improved detector sensitivity, and to a lesser extent, because search algorithms improved. In the following, brief summaries of the results from those searches will be

given, with emphasis on results from searches in advanced detector data. As of this writing, numerous results from the third LIGO-Virgo observing run (O3) have appeared and will be featured where available, along with many results from the O1 and O2 runs, to illustrate the progression of sensitivities and algorithms during the Advanced LIGO and Virgo era to date. In recent years, research groups outside of the LIGO Scientific Collaboration, Virgo Collaboration and KAGRA Collaboration (LVK) have also carried out analyses of the public GW data, which is released approximately 18 months after collection. Because of that delay, many additional results from the O3 data, beyond those described here, can be expected in the coming months and years, perhaps in parallel with LVK results from the upcoming O4 data run (Abbott et al. 2020b).

4.1 Targeted and narrowband searches for known pulsars

In *targeted* searches for known pulsars using measured ephemerides from radio, optical, X-ray or γ-ray observations valid over the gravitational-wave observation time, one can apply precise, well known corrections for the phase of the signal, including modulations, because one knows the source phase evolution, its location and motion, the Earth's location and motion, and the detector's position and orientation on the Earth.

Various approaches have been used in targeted searches in LIGO and Virgo data to date: 1) A time-domain heterodyne method (Dupuis and Woan 2005) in which Bayesian posteriors are determined on the signal parameters that govern absolute phase, amplitude and amplitude modulations (see Sect. 3.4.4); 2) a Fourier-domain determination of a "carrier" strength along with the strengths of two pairs of sidebands created by amplitude modulation from the Earth's sidereal rotation of each detector's antenna pattern ("5-Vector" method) (Astone et al. 2010b, 2012) (see Sect. 3.4.5); and 3) a matched-filter method in which marginalization is carried out over unknown orientation parameters (the "$\mathcal{F}$-statistic") (Jaranowski et al. 1998; Jaranowski and Królak 2010) (see Sect. 3.4.6).

The first application of the heterodyne Bayesian method (Abbott et al. 2004) in LIGO and GEO 600 S1 data (separately to each interferometer) led to upper limits on h_0 of a few times 10^{-22} for PSR J1939+2134 ($f_{\rm rot}$ = 642 Hz). Comparable upper limits were obtained from an implementation of the (frequentist) $\mathcal{F}$-statistic (Abbott et al. 2004). Later applications of the heterodyne Bayesian method incorporated a variety of improvements, including coherent treatment of multiple interferometers, marginalization over noise parameters, a Markov Chain Monte Carlo search method for parameter estimation and joint searching over one and two times the stellar rotation frequency. At the same time the number of stars searched in each data run increased, along with closer partnership with radio and X-ray astronomers who provided ephemerides. In the S2 data, limits were placed on 28 pulsars, with a lowest strain limit of 1.7×10^{-24} (Abbott et al. 2005b). In the S3 and S4 data (analyzed jointly), limits were placed on 78 pulsars, with a lowest strain limit of 2.6×10^{-25} (Abbott et al. 2007b). In the S5 data, limits were placed on 116 pulsars, with a lowest

strain limit of 2.3×10^{-26} (PSR J1603−7202) (Abbott et al. 2010). The lowest limit placed on ellipticity from the S5 search was 7.0×10^{-8} (PSR J2124−3358).

The final targeted-search results from initial LIGO and Virgo presented joint results from the LIGO S5 and S6 runs, and for the two low-frequency Crab and Vela pulsars, results from the Virgo VSR2 and VSR4 runs (Aasi et al. 2014b). This synoptic paper presented results for 195 pulsars in total, where the lowest obtained strain limit was only slightly better than obtained from the S5 data alone: 2.1×10^{-26} (PSR J1910−5959D), with a lowest ellipticity upper limit of 6.7×10^{-8} (PSR J2124−3358). The use of Virgo VSR2 and VSR4 data in this last analysis did, however, open up a new low-frequency spectrum, giving sensitivities approaching the spin-down limits for several pulsars other than the Crab, most notably the Vela pulsar, for which the spin-down limit was beaten (Abadie et al. 2011; Aasi et al. 2014b). The S5, S6, VSR2 and VSR4 analyses also included searches using the $\mathcal{F}$-statistic and 5-vector algorithms applied to "high value" isolated pulsars for which the spin-down limits were approached or beaten. As expected, sensitivities obtained were comparable to those found in the Bayesian analysis. All three methods typically obtain somewhat better sensitivities when exploiting the inclination and polarization angles ι and ψ inferred from pulsar wind nebulae observations for known pulsars, such as Crab and Vela (for example, the $\mathcal{F}$-statistic is refined to a more specific $\mathcal{G}$-statistic, Jaranowski and Królak 2010), although an unfavorable orientation can also lead to worse h_0 sensitivity.

When Advanced LIGO data collection began in fall 2015 there was a significant improvement in broadband sensitivity and a dramatic improvement at the lowest frequency, thanks to improved seismic isolation (Aasi et al. 2015a; Abbott et al. 2016c). The low-frequency improvements were, of course, helpful to the first binary black hole merger detection (Abbott et al. 2016b), but they also made a large number of known young pulsars accessible with respect to spin-down limit (energy conservation). Targeted searches were carried out in the O1 data using each search program (Abbott et al. 2017f), where method (1) was applied to 200 stars, and methods (2) and (3) were applied to 11 and 10 stars, respectively, for which the spin-down limit (Eq. 20) was likely to be beaten or approached, given the detector sensitivity. Results are shown in Fig. 17, along with those from initial LIGO and Virgo searches. Highlights of these O1 searches included setting a lowest upper limit on strain amplitude of 1.6×10^{-26} (PSR J1918−0642), setting a lowest upper limit on ellipticity of 1.3×10^{-8} (PSR J0636+5129) and beating the spin-down limit on 8 stars (PSR J0205+6449, J0534+2200, J0835−4510, J1302−6350, J1813−1246, J1952+3252, J2043+2740, J2229+6114). Perhaps the most notable result was setting an upper limit on the Crab pulsar's (PSR J0534+2200) energy loss to gravitational radiation at a level of 0.2% of the star's total rotational enegy loss inferred from measured rotational spin-down.

Similar searches were carried out for 221 known pulsars in the O1 and/or O2 data, with results summarized in Fig. 18 (Abbott et al. 2019b). Highlights included beating the spin-down limit on 20 pulsars, a lowest upper limit on strain of 8.9×10^{-27} (PSR J1623−2631), a lowest upper limit on ellipticity of 5.8×10^{-9} (PSR J0636+5129) and an upper limit on the Crab pulsar's fractional energy loss to gravitational

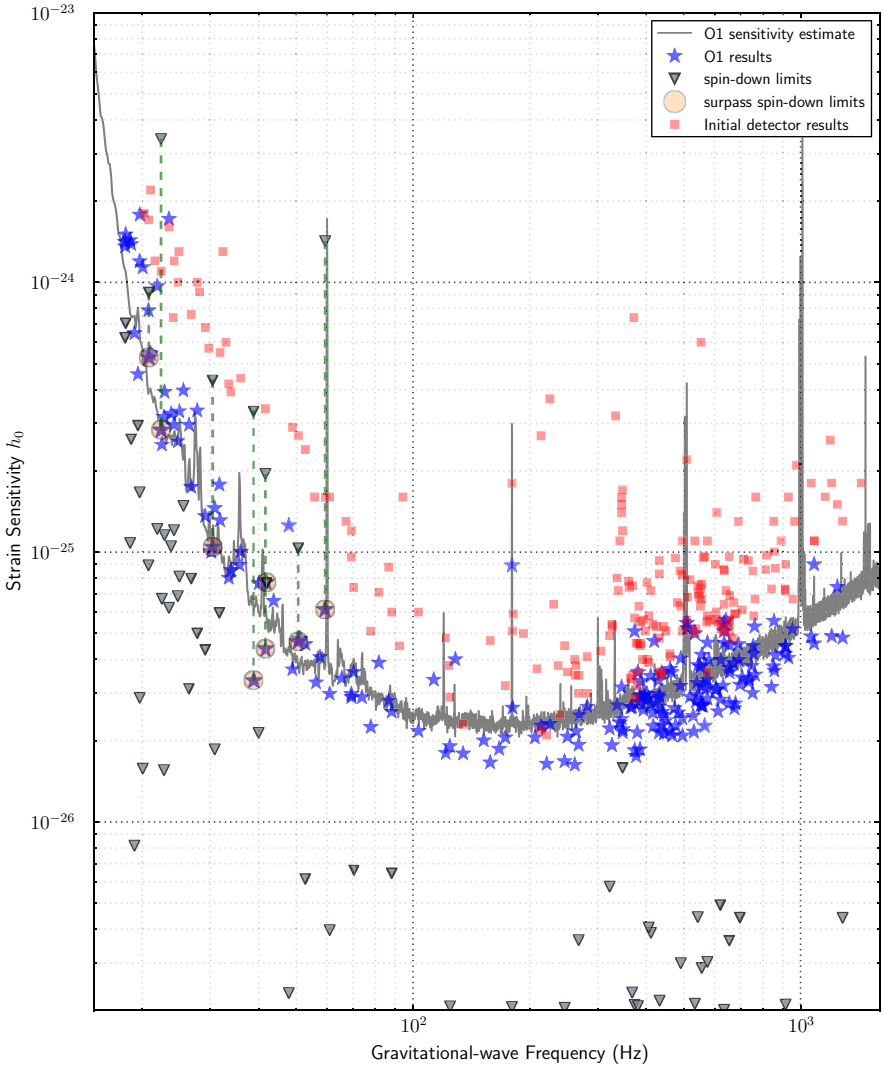

Fig. 17 Upper limits (95% CL) on h_0 for known pulsars from targeted searches in the LIGO O1 data (Abbott et al. 2017f) (closed stars). The gray band shows the *a priori* estimated sensitivity range of the search. Also plotted (closed squares) are the lowest upper limits from searches in initial LIGO and Virgo data and spin-down limits (closed triangles). Upper limits that lie below spin-down limits are outlined with a circle. Image reproduced with permission from Abbott et al. (2017f), copyright by AAS

radiation of 0.02%. In addition, the upper limit on strain amplitude (1.5×10^{-26}) for the MSP PSR J0711−6830 ($f_{\rm rot} = 182$ Hz) was only 30% above the star's spin-down limit, corresponding to an ellipticity upper limit of 1.2×10^{-8}. Upper limits are also presented in Abbott et al. (2019b) on signals at the stellar rotation frequencies, along with upper limits on the mass quadrupole moment $Q_{22} \equiv \epsilon I_{zz}\sqrt{\frac{15}{8\pi}}$ (Ushomirsky et al.

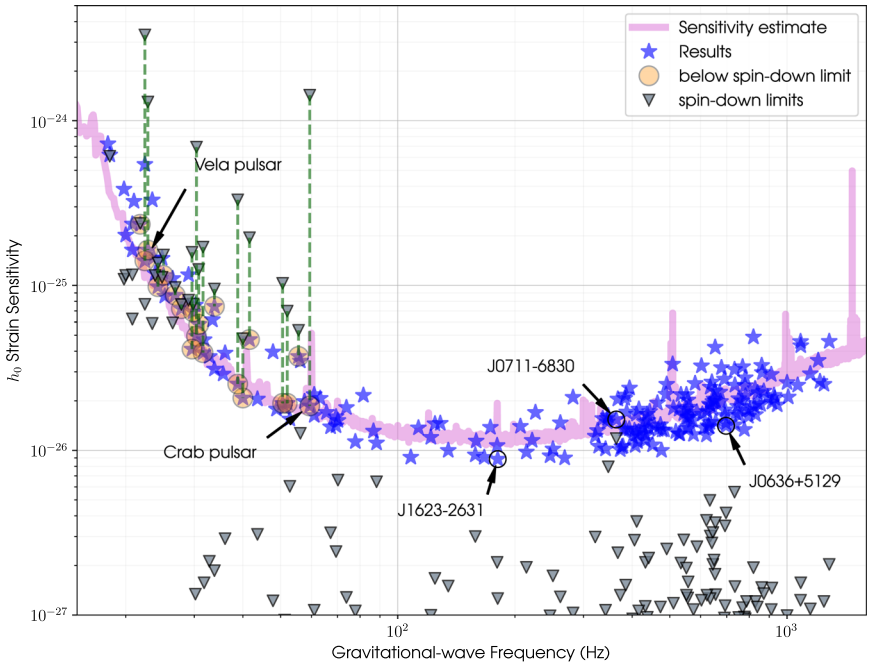

Fig. 18 Upper limits (95% CL) on h_0 for 221 known pulsars from targeted searches in the LIGO O1 and/or O2 data (Abbott et al. 2019b) (closed stars). The pink band shows the *a priori* estimated sensitivity range of the search. Also plotted are spin-down limits (closed triangles). Upper limits that lie below spin-down limits are outlined with a circle. Image reproduced with permission from Abbott et al. (2019b), copyright by AAS

2000). Initial analysis of the first six months of the LIGO and Virgo O3 data set reduced further the upper limits on the Crab and Vela pulsar, along with those of three recycled pulsars, for which the spin-down limit has now been beaten (Abbott et al. 2020c). Similarly, a targeted search for the young, highly energetic star PSR J0537−6910 (Abbott et al. 2021d) dived below the spin-down limit to an upper limit (95% CL) of 1×10^{-26} for a GW frequency (123.8 Hz) of twice the rotation frequency.

A separate analysis (Nieder et al. 2019) of the Advanced LIGO O1 and O2 data for a newly discovered gamma-ray pulsar (PSR J0952−0607) also set an upper limit on emission amplitude of 6.6×10^{-26}. Upper limits on GW emission of amplitude 3.0×10^{-26} were also set on the black widow γ-ray pulsar PSR J1653−0158 (Nieder et al. 2020) discovered in an Einstein@Home search.

Recent cumulative results from targeted searches from the O1, O2 and O3 data runs (Abbott et al. 2022j) for 236 known pulsars in total are shown in Fig. 19. Highlights include beating the spin-down limit on 23 pulsars, a lowest upper limit on strain of 4.7×10^{-27} (PSR J1745−0952), a lowest upper limit on ellipticity of 5.26×10^{-9} (PSR J0711−6830), and an upper limit on the Crab pulsar's fractional energy loss to gravitational radiation of 0.009%. In addition, the spin-down limit was

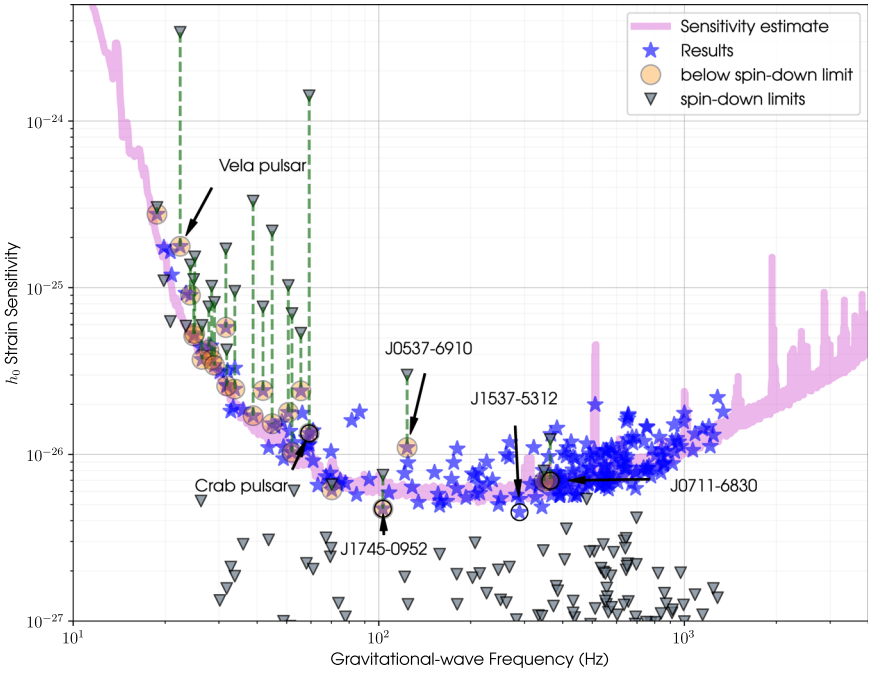

Fig. 19 Upper limits (95% CL) on h_0 for 237 known pulsars from targeted searches in the cumulative LIGO and Virgo O1–O3 data (Abbott et al. 2022j, 2021d). The stars show 95% credible upper limits on the amplitudes of h_0, while gray triangles represent the spin-down limits for each pulsar. For those pulsars which surpass their spin-down limits, their results are plotted within shaded circles. The pink curve gives an estimate of the expected strain sensitivity of all three detectors combined during the course of O3. The highlighted pulsars are those with the best h_0, Q_{22} and spin-down ratio out of the pulsars which surpassed their spin-down limit, as well as the best h_0 limit out of the whole sample. Image reproduced with permission from Abbott et al. (2022j), copyright by AAS

beaten for two millisecond pulsars: PSR J0711−6830 ($h_0 < 7.0 \times 10^{-27}$, $\epsilon < 5.3 \times 10^{-9}$ for $f_{\rm GW} \approx$364 Hz) and PSR J0437−4715 ($h_0 < 6.9 \times 10^{-27}$, $\epsilon < 8.5 \times 10^{-9}$ for $f_{\rm GW} \approx$347 Hz). These results also include a more general analysis searching simultaneously for a signal at one and two times the rotation frequency (Pitkin et al. 2015; Abbott et al. 2022j). Results from cumulative O1–O3a searches for seven additional pulsars were presented in Ashok et al. (2021).

The progressive improvement in noise level for the LIGO and Virgo detectors over the O1, O2 and O3 runs is reflected in Figs. 17, 18, and 19. Although more refined analyses have been brought to bear in parallel, the gains in astrophysical sensitivity come primarily from improving the instruments, for these targeted searches which already approach optimality.

These upper limits assume the correctness of General Relativity in that antenna pattern calculations used in the searches assume two tensor polarizations in strain. Alternative theories of gravity can, in principle, support four additional polarizations (two scalar and two vector modes), which would lead to different antenna pattern sensitivities (Isi et al. 2015). Searches have been carried out for evidence of signals

from the 200 targeted pulsars in the O1 data exhibiting these other polarizations, using the heterodyned data products. In no case was significant evidence of a non-standard signal seen, and upper limits were placed (Abbott et al. 2018a).

The targeted-search upper limits in Fig. 17 assume a fixed phase relation between stellar rotation (measured by electromagnetic pulses) and gravitational-wave emission ($f_s = f_{\rm rot}$). To allow for a more general scenario, such as slight differential rotation of EM- and GW-emitting regions, searches have also been carried out for signals very near in parameter space to those expected from an ideal phase relation. These so-called "narrowband" searches allow a relative frequency deviation of $\sim 10^{-3}$. The first such search, using the $\mathcal{F}$-statistic, was for the Crab pulsar in the Inital LIGO S5 data set (Abbott et al. 2008b), which set a limit slightly below the Crab spin-down limit, despite a large trials factor of 3×10^7, when the orientation of the assumed signal was aligned with observed Crab pulsar wind nebula X-ray jet axes (Ng and Romani 2004), a limit five times higher than achieved in the same data set using a targeted search. A similar narrowband search was later carried out in initial Virgo VSR4 data for the Crab and Vela pulsars, using the 5-vector program, a search which yielded a Crab upper limit about two times below the spin-down limit and a Vela upper limit slightly higher than its spin-down limit (Aasi et al. 2015d).

The 5-vector program was applied again to the Advanced LIGO O1 data set. Results from searches for 11 stars with expected sensitivities near the spin-down limits have been obtained from O1 data (Abbott et al. 2017e). In general, these limits are expected and found to be higher than the corresponding upper limits from targeted searches above because the increased parameter space search implies an additional trials factor. Nonetheless, this first advanced detector narrowband search beat the spin-down limit on the Crab (PSR J0534+2200), Vela (PSR J0835−4510) and PSR J2229+6114. Later, a 5-vector search of LIGO O2 data (Abbott et al. 2019c) for 33 known pulsars yielded the upper limits shown in Fig. 20, along with the 11 (higher) O1 upper limits. In this analysis, the spin-down limit was beaten for 8 known pulsars, despite trials factors ranging from $\sim 10^6$ to $\sim 10^9$. For the Crab pulsar, the strain upper limit was an order of magnitude lower than the spin-down limit, leading to a limit on fractional energy loss to gravitational waves of $\sim$ 1%.

Most recently, further sensitivity improvement was seen in O3 narrowband results (Abbott et al. 2022f), as shown in Fig. 21 for 18 known pulsars with spin-down limits within a factor of 3 of the expected sensitivity for which the spin-down limit is beaten for six pulsars. A separate analysis of O1–O3a data for seven other pulsars was carried out in Ashok et al. (2021).

Searches for accreting X-ray millisecond pulsars (AXMPs) (see Sect. 2.1.4) require a modified narrowband approach in that nominal rotation frequencies are known, but with poor precision compared to that available for pulsars for which sustained monitoring is feasible. Their frequencies can vary rapidly (and likely with significant stochasticity) during active (accreting) phases and during quiescent phases

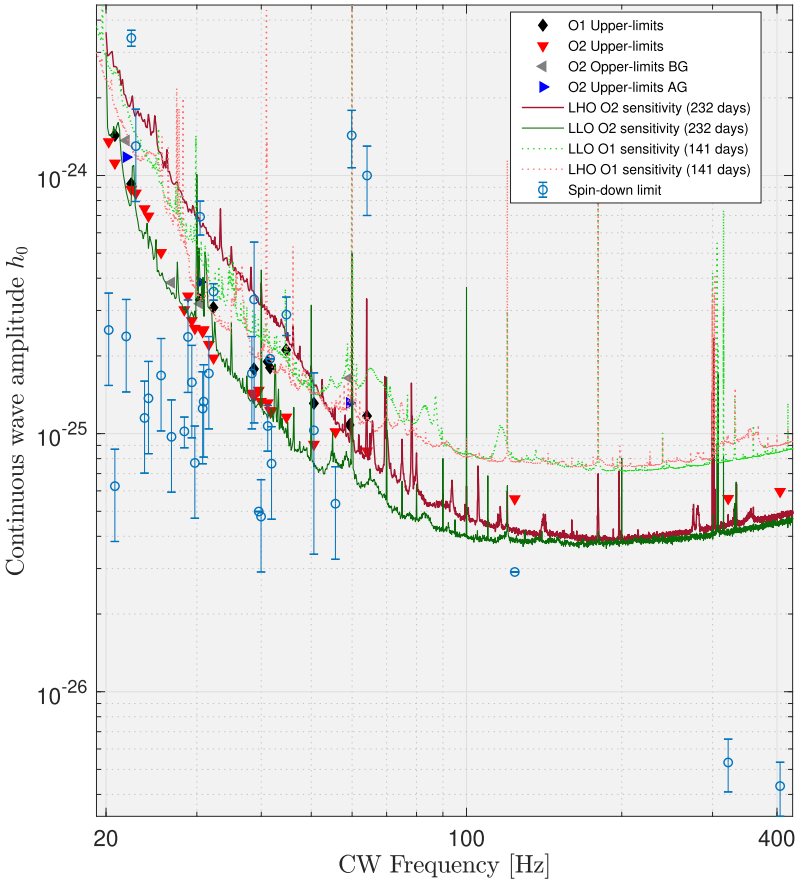

Fig. 20 Upper limits (95% CL) on h_0 for (11) 33 known pulsars from narrowband searches in the LIGO (O1) O2 data (Abbott et al. 2019c) (closed diamonds and triangles), where the GW frequency and derivative are allowed to vary by $\sim 10^{-3}$ with respect to the expectation from electromagnetic observations. For those pulsars known to have glitched in the O2 run, separate upper limits are shown for the epochs before the glitch (BG) and afterward (AG). Spin-down limits are shon as open circles, where error bars denote the uncertainties due to pulsar distances. Curves denote nominal sensitivities for the O1 and O2 runs for the individual LIGO Hanford (LHO) and Livingston (LLO) interferometers. Image reproduced with permission from Abbott et al. (2019c), copyright by APS

can generally only be inferred. Given these uncertainties, including unknown stochastic contributions, a hidden Markov Viterbi method based on the $\mathcal{J}$-statistic[13] has been applied to searches for five AXMPs in the O2 LIGO data (Middleton et al. 2020) and to 20 AXMPs in the O3 LIGO data (Abbott et al. 2022g). The O3 search yielded strain amplitude sensitivities in the range $(5–24)\times 10^{-26}$, where estimated spin-down limits based on measured frequency derivatives lie in the range

[13] The $\mathcal{J}$-statistic is a weighted sum of powers from a large number of orbital sidebands generated by evaluating the $\mathcal{F}$-statistic for a binary source, using a weighting governed by a set of Bessel functions J_n arising from the frequency modulation and incorporating the orbital phase of the binary system (Suvorova et al. 2017).

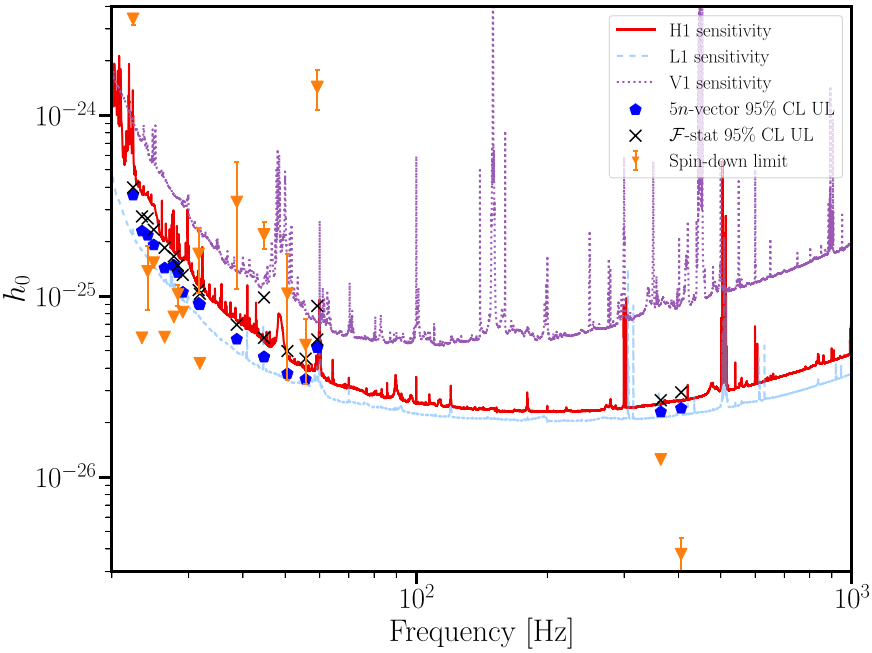

Fig. 21 Upper limits (95% CL) on h_0 for known pulsars from *narrowband* searches in the LIGO O3 data (Abbott et al. 2022f). The red solid, blue dashed, and purple dotted curves show the expected sensitivities for H1, L1, and V1, respectively. The blue pentagons indicate the median 95% CL ULs from the 5*n*-vector search across all 10^{-4} Hz sub-bands for each source. The black crosses indicate 95% CL ULs from the $\mathcal{F}$-statistic search, which are set across the full search range for each target. The orange triangles indicate the spin-down limit, $h_{\mathrm{spin-down}}$, with error bars that reflect uncertainty in the distance to each source. In a few cases the error bars are smaller than the size of the markers. Image reproduced with permission from Abbott et al. (2022f), copyright by the author(s)

10^{-28}–10^{-27} with comparable to somewhat larger estimates based on torque balance (Abbott et al. 2022g) (see Sect. 2.1.2).

4.2 Directed searches for isolated stars

Directed searches are those for which the source location is precisely known, but for which the signal's gravitational-wave phase evolution is unknown or poorly known. As discussed in Sect. 3.6.1, the implied parameter space volume of a truly broadband search will then depend sensitively upon the assumed age of the star. For a very young pulsar, one must search over not only the frequency and first frequency derivative (spin-down), but also over the second and possibly higher derivatives.

Directed-search methods are also appropriate when searching for *r*-modes from known pulsars. The search band lies nominally near 4/3 the star's rotation frequency, but has large systematic uncertainties of order 10% that depend on the unknown equation of state governing the modes (Idrisy et al. 2015; Caride et al. 2019). Hence, while the search band is much smaller than that for, say, a young neutron star with unknown frequency, the band is also much larger than that used in narrowband

searches (see Sect. 4.1), arguing for careful balancing of computational cost against sensitivity (Caride et al. 2019).

The computational cost of fully coherent directed searches can be understood qualitatively from the scalings with coherence time implied by Eqs. (41)–(43), with more quantitative estimates based on the template placement considerations discussed in Sect. 3.6.1. Semi-coherent searches have more complex scalings, but for long observation spans, generally achieve improved strain sensitivity with respect to fully coherent searches carried out over shorter subsets of the data set (which is typically necessary).

The first such analysis in initial LIGO data used the $\mathcal{F}$-statistic algorithm (Abadie et al. 2010) to search for the central compact object (X-ray source) at the center of the Cassiopeia A supernova remnant. As discussed in Sect. 2, given the $\sim$ 300-year presumed age of the star, one can derive a frequency-dependent upper limit on its strain emission of $\sim 1.3 \times 10^{-24}$, assuming its rotational energy loss has been dominated by gravitational-wave emission. A coherent search was carried out in a 12-day period of LIGO S5 data over the band 100–300 Hz, for which it was expected that the age-based limit could be tested with that data set (Wette et al. 2008). The resulting upper limits did indeed beat the age-based limit over that band, reaching a minimum upper limit of 7×10^{-25} at 150 Hz. That the limits were more than an order of magnitude higher than found in the full-S5 targeted searches for known pulsars in that band reflected not only the much shorter observation time used (12 days vs. 23 months), but also the higher SNR threshold necessary to apply when searching over $\sim 10^{12}$ templates in f_s, $\dot{f}_s$ and $\ddot{f}_s$ for a 300-year old star.

This coherent approach over tractable intervals (Wette et al. 2008) was later applied to searches in the data from the last initial LIGO data run (S6) for nine young supernova remnants (Aasi et al. 2015e) and to a possible source at the core of the globular cluster NGC 6544 (Abbott et al. 2017m), achieving upper limits on strain comparable to those found in the S5 data, with lowest values ranging over $\sim$ 4–7×10^{-25}, depending on source age (lower limits for older sources with lower trials factors from searching over frequency derivatives).

The coherent $\mathcal{F}$-statistic approach was applied to Advanced LIGO O1 data (Abbott et al. 2019a) in a search for 15 supernova remnants and one nominal exoplanet with an unusual apparent orbit, which has been suggested to be a very nearby neutron star (Neuhäuser et al. 2015) (see Sect. 2.1.4). Best upper limits obtained ranged over ~ 1–4×10^{-25}, depending on assumed source range. Figure 22 shows sample results for three of the supernova remnants, including Cas A, along with that for Fomalhaut b. In this analysis, separate "deep" and "wide" analyses were applied to three of the supernova remnants, including Vela Jr., to account for large uncertainties in source age, where deep searches could be carried out for older sources, requiring a smaller range in frequency derivatives. A similar approach was used to probe the O2 data for 12 supernova remnants, restricting attention to frequencies below 150 Hz, applying coherence times ranging from 12 to 55.9 days (Lindblom and Owen 2020). A recent coherent search of 8.7-day and 12.8-day subsets O2 LIGO data (Owen et al. 2022) for CW radiation from a Supernova 1987A

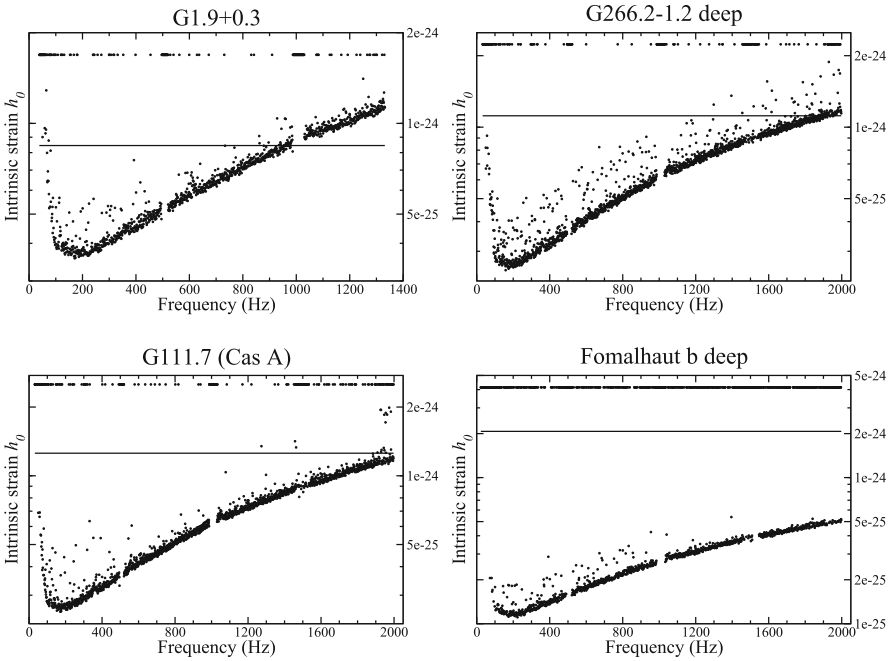

Fig. 22 Upper limits (95% CL) on h_0 (dots) for 3 supernova remnant cores and nominal exoplanet (but possible neutron star) Fomalhaut b, using coherent $\mathcal{F}$-statistic searches of O1 data (Abbott et al. 2019a). Upper left: G1.9+0.3; upper right: Vela Jr.; lower left: Cassiopeia A; lower right: Fomalhaut b. The horizontal lines indicate nominal age-based limits (Eq. 28). Image reproduced with permission from Abbott et al. (2019a), copyright by AAS

remnant beat the age-based indirect limit. A Viterbi-based search for Fomalhaut b was applied to O2 data (Jones and Sun 2021).

As one might imagine, a semi-coherent approach has the potential to improve upon a single coherent directed search. One demonstration of the method in initial LIGO S5 data searched for a source at the galactic center (Aasi et al. 2013a), using 630 segments of 11.5 h each, where $\mathcal{F}$-statistic values averaged over the segments were computed, where the global correlation transform template mapping was used in combining the $\mathcal{F}$-statistic values over the segments. A similar but more sensitive semi-coherent approach was applied in a computationally intensive Einstein@Home (see Sect. 4.4) S6 search for a CW signal from Cas A (Zhu et al. 2016). This search used 44 segments of 140 h, again applying the global correlation transform template gridding and summing.

The same method was applied to an Einstein@Home search in Advanced LIGO O1 data for three supernova remnants: Cas A, Vela Jr. and G347.3 (Ming et al. 2019). Figure 23 shows the results of the three searches, together with results from the coherent search of a subset of the same data set (Abbott et al. 2019a). The semi-coherent search which exploits the full data set, typically achieves a factor of two improvement in strain sensitivity over the coherent search over a data subset. This search also applied a search optimization method (Ming et al. 2016) to choose

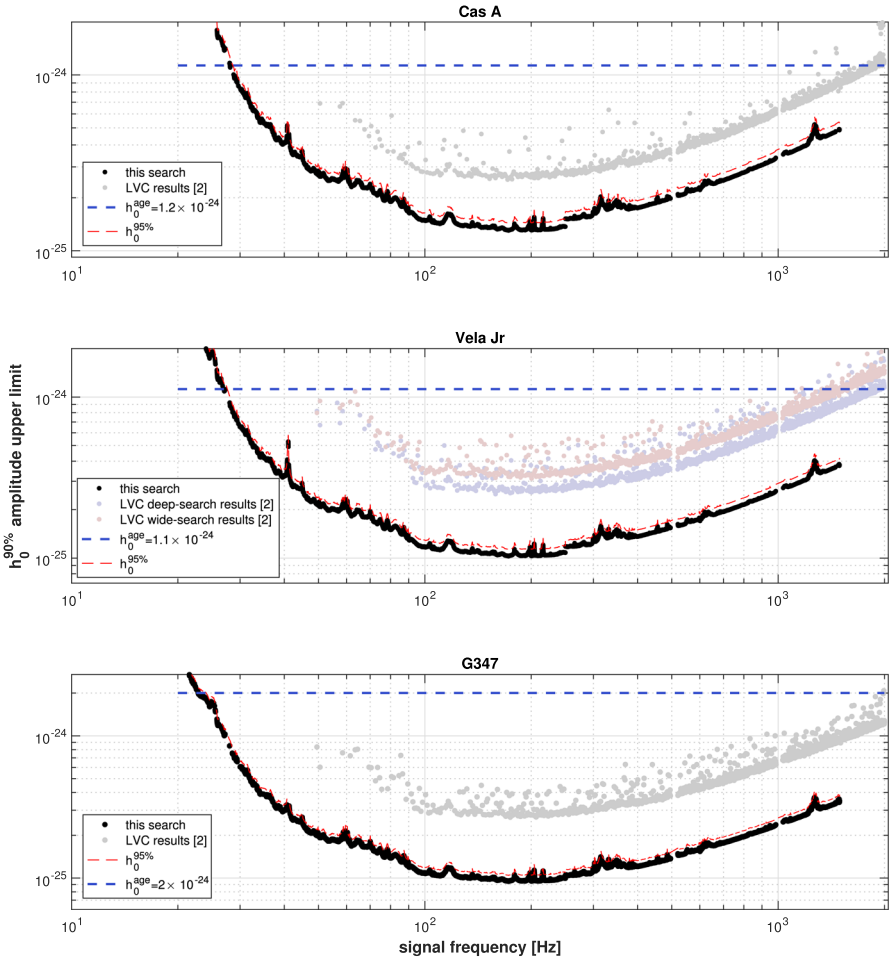

Fig. 23 Upper limits (90% CL) on h_0 for Cassiopeia A, Vela Jr. and G347.3 (dots) from ("this search") semi-coherent Einstein@Home directed $\mathcal{F}$-statistic searches in Advanced LIGO O1 data, (Ming et al. 2019; Papa et al. 2020), shown with previous (higher) coherent-search limits (Abbott et al. 2019a) ("LVC results") using subsets of the O1 data. The dashed curves denote estimated 95% CL upper limits based on the 90% CL values. Image reproduced with permission from Ming et al. (2019), copyright by APS

coherence times and segmentations for each source, where the optimization attempts to take into account relative probabilities for detection, given available astronomical information. In this instance the segmentations chosen were 12 245-h segments (Cas A), 8 369-h segments (Vela Jr.) and 6 489-h segments (G347.3). As seen in Fig. 23, best upper limits obtained were $\sim 1 \times 10^{-25}$. Another semi-coherent directed search for the galactic center, based on the Frequency Hough method (Antonucci et al. 2008), accelerated by the Band-Sampled Data (BSD) use of DFTs (Piccinni et al. 2018), was carried out using the Advanced LIGO O2 data (Piccinni et al. 2020). Another O2 analysis (Ming et al. 2022) searched for a signal from G347.3 using a semi-coherent $\mathcal{F}$-statistic implementation in Einstein@Home.

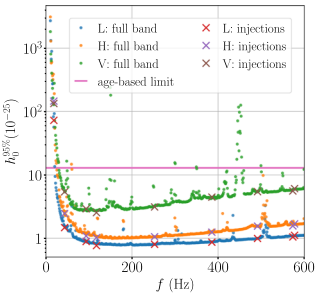

(a) G65.7+1.2

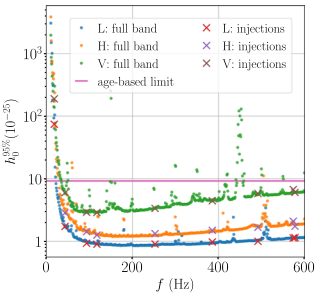

(b) G189.1+3.0

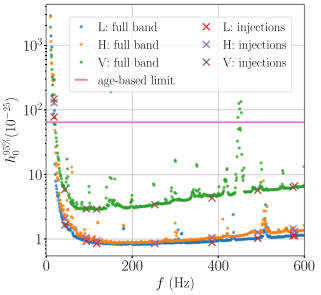

(c) G266.2–1.2/Vela Jr.

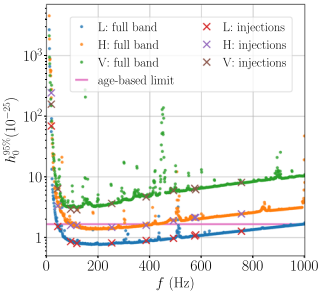

(d) G39.2–0.3

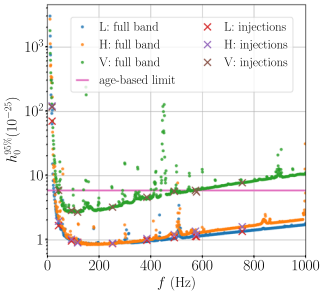

(e) G93.3+6.9

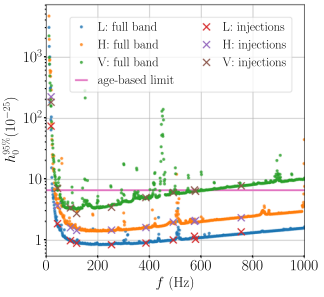

(f) G18.9–1.1

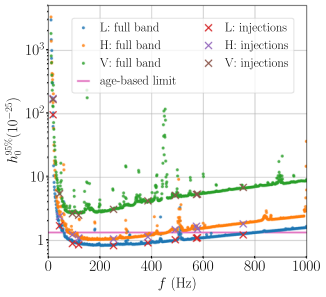

(g) G353.6–0.7

◀**Fig. 24** Sensitivity estimates (95% efficiency) $h_0^{95\%}$ obtained from an O3a semi-coherent Frequency Hough (BSD-accelerated) search (Abbott et al. 2021i). The dotted curves represent the estimated $h_0^{95\%}$ in the full band of H, L and V detectors searched by the pipeline. The crosses represent the frequentist strain upper limits at 95% confidence level obtained empirically in sample sub-bands of 1 Hz. Horizontal lines are the indirect age-based limit (Eq. 28). The limit is beaten across the full band also using Virgo data, except for the most disturbed regions, for G65.7+1.2, G189.1+3.0 and G266.2−1.2/Vela Jr. The remaining curves beat the limit on a limited parameter space and/or not for every detector. Image reproduced with permission from Abbott et al. (2021i), copyright by AAS

Several distinct semi-coherent directed searches have been carried out to date using O3 data. First came results from three methods applied to 15 supernova remnants using the O3a data (Abbott et al. 2021i), one method being a semi-coherent, BSD-accelerated Frequency Hough search and the other two methods being less sensitive but more robust Viterbi (Sun et al. 2018) searches. The two Viterbi methods searched for either signal at only a single frequency (Sun et al. 2018) (assumed to be twice the unknown rotation frequency) or at both one frequency and its doubled value (Sun et al. 2019). All three methods were applied to seven stars, with only the single-frequency Viterbi method applied to another eight stars. The results from the Frequency Hough search are shown in Fig. 24. A separate publication (Beniwal et al. 2022) described a Viterbi search for a potential unidentified pulsar powering HESS J1427-608, a spatially unresolved TeV gamma-ray point source (Aharonian et al. 2008). Another publication described a coherent $\mathcal{F}$-statistic search (2 days from O3b data) for CW emission from the center of the 840-year-old supernova remnant G4.8+6.2 (Liu and Zou 2022).

A separate O3a analysis (Abbott et al. 2022i) used the Weave implementation (see Sect. 3.6.2) of a semi-coherent $\mathcal{F}$-statistic search. While the package is versatile enough to be used in all-sky searches for unknown sources, a simpler configuration, applicable to well localized sources, was used to search in the O3a data for the Cas A and Vela Jr. supernova remnants. Figure 25 shows the results in comparison with earlier searches for these two sources in O1, O2 and O3a data.

These 95%-efficiency sensitivities to Cas A and Vela Jr. can be translated into sensitivities to ellipticity, as shown in Fig. 26. The quadratic dependence of strain on frequency for fixed ellipticity (see Eq. 14) leads to dramatically better sensitivity to ellipticity at higher frequencies, reaching as low as $\epsilon \approx 2 \times 10^{-8}$ near 1000 Hz for the more optimistic assumption of Vela Jr. distance (0.2 kpc).

Another approach (Dhurandhar et al. 2008) for directed searches is based on cross correlation of independent data streams. The most straightforward method defines bins in detector-frame frequency and uses short coherence times, as in directional searches for stochastic gravitational radiation (Ballmer 2006; Abbott et al. 2017b), which can be used to search for both isolated and binary sources, albeit with limited sensitivity. One can use finer frequency binning, however, when correcting explicitly for Doppler modulation of the signal. Cross-correlation methods are especially robust against wrong assumptions about phase evolution and are attractive in searching for a very young object, such as a hypothetical neutron star remaining from Supernova 1987A (see Ashton et al. 2017 for a discussion of potential degradation of coherent searches from neutron star glitches, Page et al. 2020 for evidence of a hidden star from an excess of infrared emission, and Greco et al. 2022 for evidence of pulsar

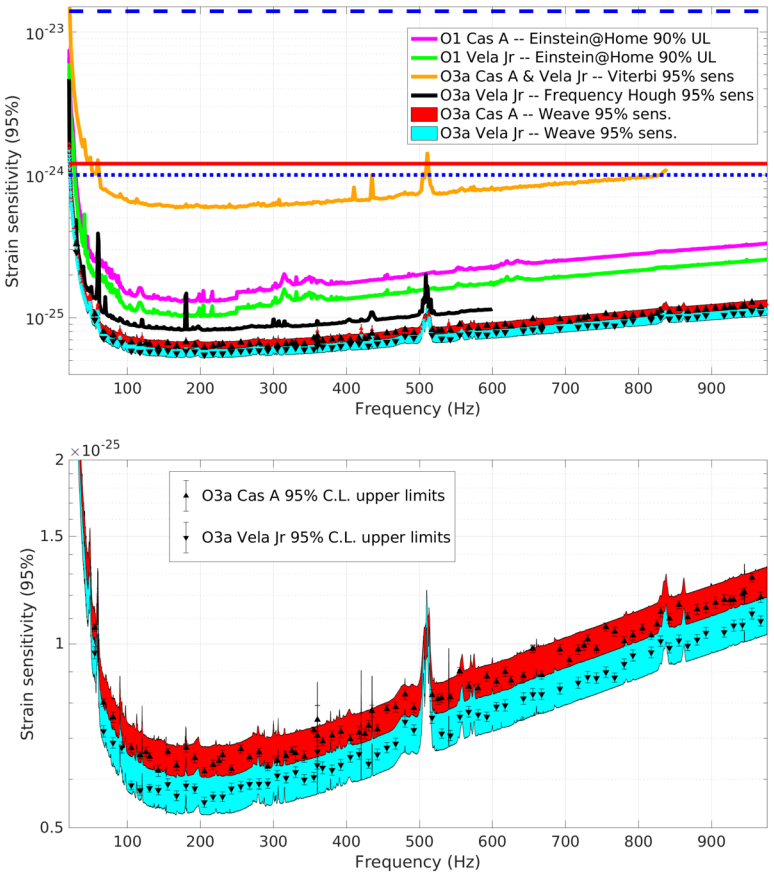

Fig. 25 *Top panel:* Estimated gravitational-wave strain amplitude sensitivities (95% efficiency) in each 0.1 Hz sub-band for the O3a Cas A (red band) and Vela Jr. (cyan band) searches (Abbott et al. 2022i). Conservative uncertainty bands of ±7% are indicated, to account for statistical and systematic uncertainties in estimating sensitivity depths, including calibration uncertainties. Black triangles (upright—Cas A, inverted—Vela Jr.) denote 0.1 Hz bands for which rigorous upper limits are used to determine estimated sensitivity vs. frequency. Additional results from prior searches for Cas A and Vela Jr. are also shown: O1 Einstein@Home 90% C.L. upper limits for Cas A (magenta curve) and for Vela Jr. (green curve) (Ming et al. 2019); O3a Cas A and Vela Jr. 95% C.L. upper limits using a model-robust Viterbi method (orange curve) (Abbott et al. 2021i); O3a Vela Jr. 95% C.L. upper limits using the template-based Frequency Hough method (black curve) (Abbott et al. 2021i). The solid red horizontal line indicates the age-based upper limit on Cas A strain amplitude. The dashed (dotted) horizonal blue lines indicate the optimistic (pessimistic) age-based upper limit on Vela Jr. strain amplitude, assuming an age and distance of 700 years and 0.2 kpc (5100 years and 1.0 kpc). *Bottom panel:* Magnification of the sensitivity bands from the O3a Weave search over most of the search band ($\sim$ 40–976 Hz), with 1-σ statistical uncertainties shown for the individual sparsely sampled upper limits used to estimate the depth. Image reproduced with permission from Abbott et al. (2022i), copyright by APS

wind nebula). A cross-correlation search for SN 1987A, including demodulation for effects from the motion of the Earth (Chung et al. 2011) was carried out in initial LIGO data (Sun et al. 2016). Recent application of cross-correlation methods to directed searches for binary sources will be discussed in the next Sect. 4.3.

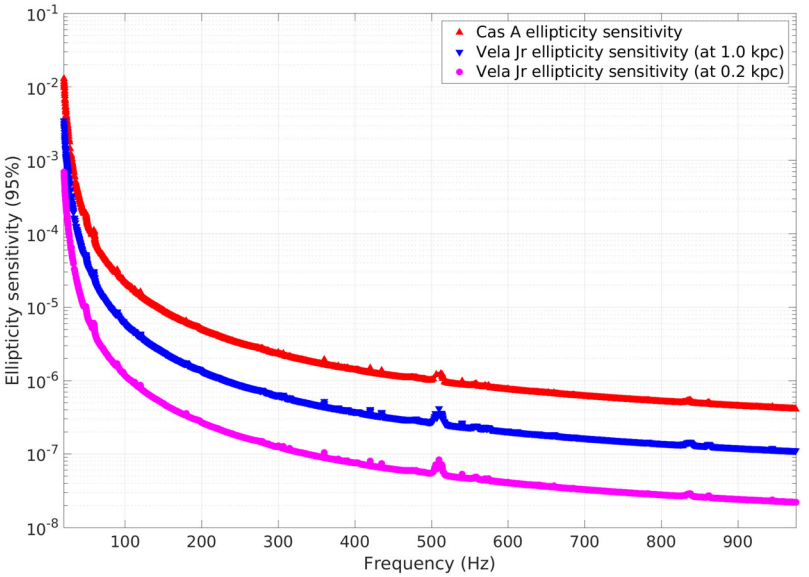

Fig. 26 Estimated ellipticity sensitivities (95% efficiency) in each 0.1 Hz sub-band for the O3a (Weave-based) Cas A (red) and Vela Jr. (blue, magenta) searches, derived from the strain amplitude sensitivities shown in Fig. 25 assuming a source distance of 3.3 kpc for Cas A, and assuming source distances of 1.0 kpc and 0.2 kpc for Vela Jr.

Directed searches for particular sources require making choices, that is, to prioritize among a wide set of potential targets in deciding how best to apply computational resources and analyst time. Recent work (Ming et al. 2016, 2018) has taken a probabilistic approach to address this problem, based on source age and distance information (including sometimes large uncertainties) along with detector sensitivity, an approach that may be generalized to parameter choices in both directed and all-sky searches.

Searches for *r*-modes radiation from known pulsars are less challenging computationally than truly broadband directed searches, because the range of expected frequencies is better known. Nonetheless there is substantial theoretical uncertainty in the ratio between GW emission frequency and rotation frequency. Although the nominal ratio is 4/3 in the slow-spinning, non-relativistic regime, there are substantial corrections for fast-spinning stars and for stellar compactness that depend on the equation of state (Yoshida et al. 2005; Jasiulek and Chirenti 2017; Idrisy et al. 2015; Caride et al. 2019), leading to a significant range in possible ratios. Following Caride et al. (2019), the ratio can be written:

$$\frac{f_{\mathrm{GW}}}{f_{\mathrm{rot}}} \approx A - B\left(\frac{f_{\mathrm{rot}}}{f_{\mathrm{Kepler}}}\right)^2, \tag{190}$$

where f_{Kepler} is the Kepler frequency of the star (rotation frequency at which centrifugal forces destroy the star), A is a parameter dependent on the equation of state, with an estimated allowed range of $1.39-1.57$ (Idrisy et al. 2015) and B is a

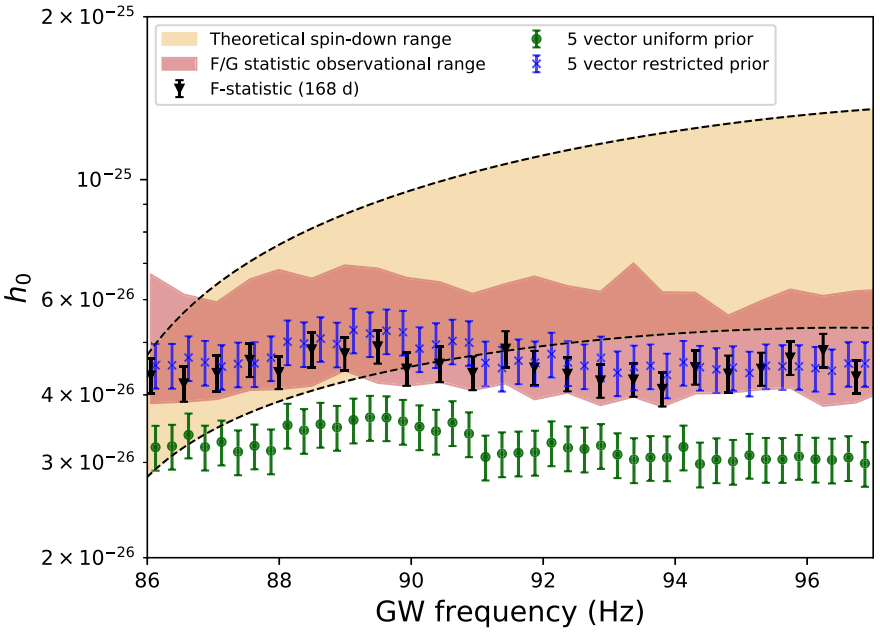

Fig. 27 Upper limits on GW amplitude h_0 obtained from searches for r-modes emission from PSR J0537-6910 in the O3 LIGO data using the $\mathcal{F}$-statistic/$\mathcal{G}$-statistic and 5-vector methods (Abbott et al. 2021c). The shaded band indicates the full range of results of the $\mathcal{F}$-statistic/$\mathcal{G}$-statistic pipeline. The dashed lines are defined by the stiffest and softest equations of state considered in the analysis and enclose a range of theoretical h_0

correction term for high spin with an estimated maximum value of $B_{\max} = 0.195$ (Caride et al. 2019).

Using these assumptions, several searches have been carried out explicitly for such r-modes: (1) an analysis of O1 and O2 data for emission from the young, energetic pulsar PSR J0537−6910 (Fesik and Papa 2020) (see Sect. 2.1.4), which reached to within an order of magnitude of the strain spin-down limit; (2) an analysis of O1 and O2 data for emission from the younger, comparably energetic and much closer Crab pulsar, for which the spin-down limit was surpassed by an order of magnitude (Rajbhandari et al. 2021); and a recent search in the O3 LIGO and Virgo data (Abbott et al. 2021c) which placed stringent constraints on theoretical models for r-mode-driven spin-down in J0537−6910, especially for higher frequencies for which upper limits reach below the spin-down limit. These latter results which attempt to address directly the evidence for r-modes in inter-glitch J0537–6910 spin-down are shown for the frequency band of the search (86–97 Hz) in Fig. 27.

4.3 Directed searches for binary stars

For known binary pulsars with measured timing ephemerides, targeted searches work well, and upper limits have been reported for many stars, as described in Sect. 4.1. But searching for known (possibly accreting) neutron stars in binary systems not

exhibiting pulsations or for entirely unknown stars in binary systems once again significantly increases the parameter space, relative to the corresponding isolated star searches, posing new algorithmic challenges and computing costs.

Searches for Sco X-1 in O1 data were carried out with several methods: (1) a "Sideband" method (Messenger and Woan 2007; Sammut et al. 2014; Suvorova et al. 2016; Abbott et al. 2017n; Sun 2018) based on summing power in orbital sideband frequencies; (2) a non-demodulated cross-correlation method (Ballmer 2006; Abbott et al. 2017b) and (3) a demodulated cross-correlation method (Whelan et al. 2015; Abbott et al. 2017p; Meadors et al. 2018). The demodulated cross-correlation method has proven to be the most sensitive method to date in such searches on a fixed data set for templated signal models without stochasticity, as expected from a previous mock data challenge (Messenger et al. 2015) including these methods and others (Goetz and Riles 2011, 2016; Meadors et al. 2016, 2017; van der Putten et al. 2010), and as shown in Fig. 28. Computationally intensive methods using the $\mathcal{F}$-statistic, however, may eventually improve upon it (Leaci and Prix 2015). Follow-up Sco X-1 searches of the O2 data were based on the Viteri method using the $\mathcal{J}$-statistic (Abbott et al. 2019e, 2022h).

One complication in Sco X-1 searches is potential spin wandering due to fluctuations in accretion from its companion (Mukherjee et al. 2018), which limits the length of a coherence time that can be assumed safe for a signal template. One previous fully coherent search (Aasi et al. 2015c) restricted its coherence length to 10 days, to be conservative. Semi-coherent and cross-correlation methods (Suvorova et al. 2016; Meadors et al. 2016; Ballmer 2006; Whelan et al. 2015) should be more robust against wandering. Figure 29 shows results from the recent Viterbi-based Sco X-1 search (Abbott et al. 2022h) in the O3 data using the $\mathcal{J}$-statistic (Suvorova et al. 2017), in which results for different assumptions about Sco X-1 orientation are made. The implied limits on intrinsic strain amplitude h_0 are lowest in the most favorable case of circular polarization, less favorable for an inclination angle $\iota = 44^\circ$ consistent with observations of its radio lobes (Fomalont et al. 2001), and least favorable for a strain amplitude marginalized over unknown inclination. Also shown are torque-balance limits assuming both a stellar radius and Alfvén radius for the accretion lever arm (see Sect. 2.1.2).

Figure 30 shows a comparison of Sco X-1 upper limits (marginalized over the unknown stellar inclination angle) obtained from the CrossCorr method applied to the O1, O2 and O3 LIGO data, with comparisons to the torque balance limit for a stellar radius lever arm. The O3 inclination-averaged strain upper limits (Abbott et al. 2022h) shown in Fig. 30 now reach as low as the torque-balance benchmark in Eq. (33) for a narrow frequency band below 100 Hz. Less conservatively, Fig. 31 shows the results of three search methods applied to the O3 data in terms of upper limits on "effective strain" amplitude, which takes into account the inclination angle ι of the star:

$$(h_0^{\mathrm{eff}})^2 \equiv (h_+)^2 + (h_\times)^2 \tag{191}$$

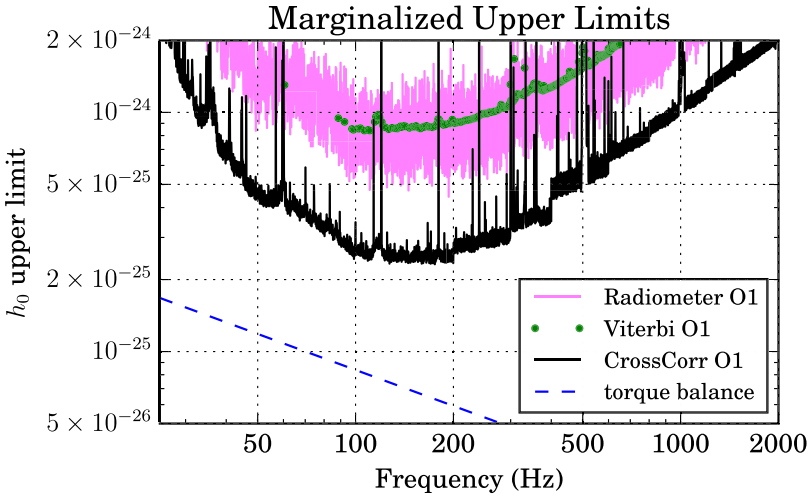

Fig. 28 Upper limits (95% CL) on h_0 for Scorpius X-1 from Advanced LIGO O1 data, using several different search methods: a "radiometer" search using stochastic analysis methods (Abbott et al. 2017b) and fine frequency binning, a Viterbi method based on a Bessel-weighted $\mathcal{F}$-statistic(Abbott et al. 2017n) and a templated cross-correlation method (Abbott et al. 2017p). The dashed line indicates the torque-balance benchmark defined in Eq. (33) for accretion at the stellar radius. Image reproduced with permission from Abbott et al. (2017p), copyright by AAS

$$= h_0^2 \, \frac{[(1+\cos^2(\iota))/2]^2 + \cos^2(\iota)}{2}, \tag{192}$$

where $h_0^{\mathrm{eff}} = h_0$ for circular polarization and $h_0^{\mathrm{eff}} = \frac{1}{\sqrt{8}} h_0$ for linear polarization. The torque-balance upper limit is shown as a band, depending on assumed inclination, with the value favored by radio lobes observations highlighted by the dashed-dotted line. In this comparison, one can see that recent CW searches probe the torque-balance hypothesis over a much broader band below several hundred Hz, depending on inclination assumptions. As advanced detector sensitivities continue to improve and with longer data runs, future searches should progressively probe to higher frequencies along this benchmark.

Possessing more definitive information on the rotation frequency of Sco X-1 could potentially make the difference between missing and detecting its gravitational waves in advanced detector data, by both permitting longer coherence-time searches and reducing the statistical trials factor and thereby the threshold needed to identify an interesting outlier. More intensive measurements and analysis of Sco X-1 X-ray emission could yield a dramatic scientific payoff (Galaudage et al. 2021).

Until recently, CW searches for known LXMB systems focused almost exclusively on Scorpius X-1, although (Meadors et al. 2017) did also include limits from narrowband searches around three particular frequencies of interest for XTE J1751−305, given X-ray observations of a potential r-mode excitation (Strohmayer and Mahmoodifar 2014a). More attention is turning now to other accreting systems,

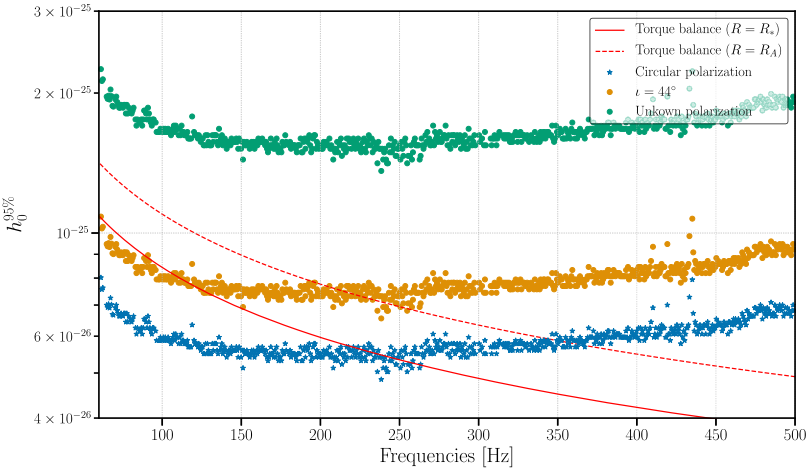

Fig. 29 Upper limits on strain amplitude h_0 from a hidden-Markov model search for Scorpius X-1 at 95% confidence from LIGO O3 data (Abbott et al. 2022h) as a function of sub-band frequency, for three scenarios: circular polarization with $\iota = 0$ (blue stars), $\iota \approx 44°$ based on radio observations (see Fomalont et al. 2001; orange dots), and a flat prior on $cos\,\iota$ (green dots). Indirect torque-balance upper limits (see Sect. 2.1.2) for two torque lever arms are also shown: the stellar radius (red solid line) and the Alfvén radius (dashed red line). Image reproduced with permission from Abbott et al. (2022h), copyright by APS

such as Cygnus X-2 (Premachandra et al. 2016; Galaudage et al. 2021). In addition, recent searches were carried out in Advanced LIGO O2 data for five systems (Middleton et al. 2020) and in O3 data for 20 accreting millisecond pulsars (Abbott et al. 2022g), both using a Viterbi hidden Markov method (Suvorova et al. 2017) and exploiting the relatively good precision with which the stellar rotation frequencies are known (see Sect. 4.1).

4.4 All-sky searches for isolated stars

4.4.1 Overview of search pipelines in use

Various semi-coherent algorithmic approaches have been tried, many based in some way on the "Stack Slide" algorithm (Brady et al. 1998; Brady and Creighton 2000; Cutler et al. 2005; Mendell and Landry 2005) in which the strain powers from Fourier transforms computed over each coherently analyzed segment are stacked on each other after sliding each transform some number of bins to account for Doppler modulation of the source frequency (see Sect. 3.5.1). One algorithm is a direct implementation of this idea called StackSlide (Mendell and Landry 2005).

Other implementations (Krishnan et al. 2004; Antonucci et al. 2008) are based on the Hough transform approach, (Hough 1959, 1962) in which for each segment a detection statistic is compared to a threshold and given a value of 0 or 1. The unity values were later refined to be adaptive non-unity weights, to account for variations in noise and detector antenna pattern (Palomba et al. 2005; Sintes and Krishnan 2006). The sums of those weights are accumulated in parameter space "maps," with

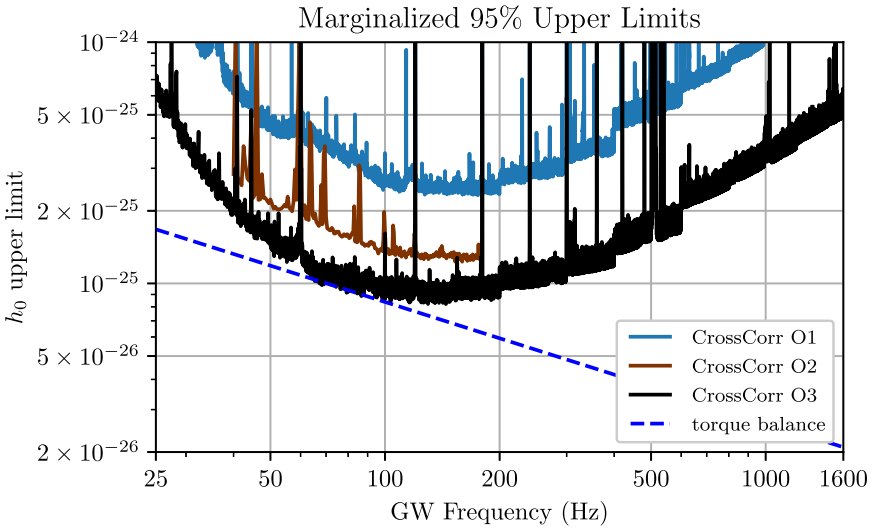

Fig. 30 Comparison of 95% CL upper limits on h_0 due to Sco X-1 emission from searches using the CrossCorr method carried out in O1, O2 and O3 data: blue solid—O1 CrossCorr search (Abbott et al. 2017p), brown solid—O2 CrossCorr search (Zhang et al. 2021), black solid—O3 CrossCorr search Abbott et al. (2022e). The indirect torque-balance upper limits (see Sect. 2.1.2), using the stellar radius are also plotted (blue dashed line), marginalized over stellar inclination angle. Image reproduced with permission from Abbott et al. (2022e), copyright by the author(s)

high counts warranting follow-up. The Hough approach offers greater computational efficiency from reducing floating point operations, along with robustness against non-Gaussian artifacts (Abbott et al. 2008a) (see Sect. 3.7). The Hough approach has been implemented in two distinct search pipelines, the "Sky Hough" (Krishnan et al. 2004; Abbott et al. 2005a) and "Frequency Hough" (Antonucci et al. 2008; Astone et al. 2014a; Aasi et al. 2016a) programs, named after the different parameter spaces chosen in which to accumulate weight sums.

Another implementation, known as PowerFlux, (Abbott et al. 2008a; Dergachev 2005; Dergachev and Riles 2005; Dergachev 2010a, b, 2013) improves upon the StackSlide method by weighting segments by the inverse variance of the estimated (usually non-stationary) noise and by searching explicitly over different assumed polarizations while including the antenna pattern correction factors in the noise weighting (see Sect. 3.5.2).

Yet another method uses coincidences among $\mathcal{F}$-statistic outliers (see Sect. 3.4.6) in multiple time segments typically longer than those used in the semi-coherent approaches (Astone et al. 2010a; Aasi et al. 2014c), where the implementation is carried out in the time domain (hereafter denoted as TD-$\mathcal{F}$-statistic), with systematic follow-up of outliers carried out through progressive increase of coherence time (Sieniawska et al. 2019).

The deepest wideband searches (including wide in frequency derivative range) achieved to date in given fixed data sets have stacked $\mathcal{F}$-statistic values over time segments semi-coherently (see Sect. 3.5.4) and have used the resources of the

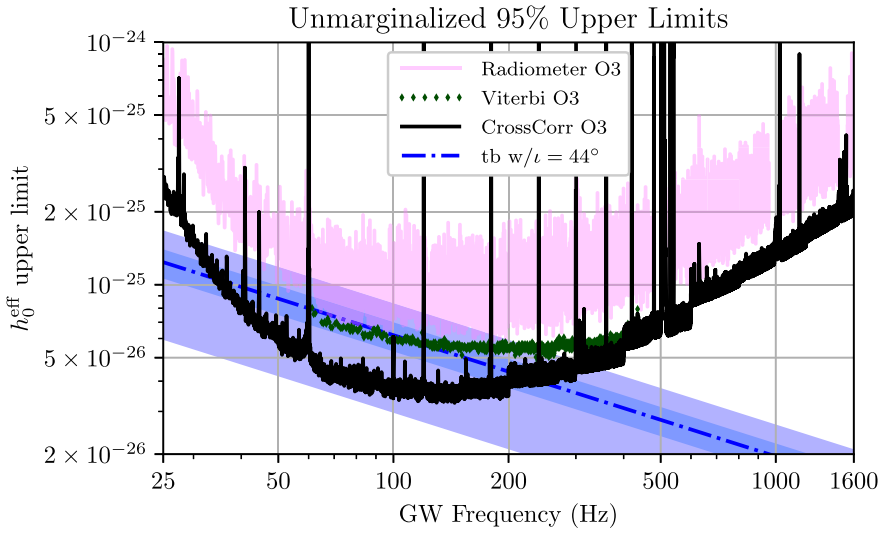

Fig. 31 Upper limits on *effective* strain amplitude $h_0^{\rm eff}$ (defined in text) at 95% confidence from three different searches for Scorpius X-1 emission from LIGO O3 data. The CrossCorr limits (black) (Abbott et al. 2022e) probe the torque-balance limit expectation over a broad frequency band and range of assumed inclinations (light purple band). The Viterbi limits (green) (Abbott et al. 2022h) and Radiometer limits (pink) (Abbott et al. 2021h) shown assume the most favorable inclination ($\iota = 0$ or π, producing circular polarization). The dashed-dotted blue line and darkened blue band show the torque-balance limits and uncertainty, assuming the inclination favored by radio lobe observations (Fomalont et al. 2001). Image reproduced with permission from Abbott et al. (2022e), copyright by the author(s)

distributed computing project Einstein@Home (Abbott et al. 2009c) based on the same software infrastructure (BOINC) (University of California 2002) developed for the Seti@Home project (Anderson et al. 2002). Einstein@Home encourages volunteers to download narrow-band segments of LIGO data and carry out a semi-coherent $\mathcal{F}$-statistic search over a small patch of sky. Results are automatically returned to an Einstein@Home server and recorded, with every set of templates analyzed independently by host computers owned by at least two different volunteers. Einstein@Home scientists then carry out post-processing to follow up on promising outliers found. This project has been remarkably successful in engaging the public (hundreds of thousands of volunteers and 750,000 host computers to date) in forefront science while making good use of idle computer cycles to carry out searches that would otherwise exceed the capacity of dedicated gravitational-wave computing clusters.

The availability of the Einstein@Home platform has driven the evolution of semi-coherent stacked $\mathcal{F}$-statistic techniques. This evolution has led to increased search sophistication and sensitivity over the last decade and a half, in general, including for related pipelines outside of that distributed computing framework, such as Weave (which has a memory footprint incompatible with Einstein@Home). Particular improvements have included search setup optimization (Cutler et al. 2005; Prix and Shaltev 2012; Shaltev 2016), more efficient semi-coherent stacking and template

placement, (Prix 2007a, b; Pletsch 2008; Pletsch and Allen 2009; Wette and Prix 2013; Wette 2014, 2015, 2016; Wette et al. 2018; Walsh et al. 2019) automated vetoing of instrumental lines, (Keitel et al. 2014; Keitel and Prix 2015; Keitel 2016) and hierarchical outlier followup and veto (Shaltev et al. 2014; Papa et al. 2016; Singh et al. 2017; Zhu et al. 2017; Ashton and Prix 2018; Intini et al. 2020b).

Technical challenges in distributed computing include efficient data transfer to/from host computers and running on many computing platforms of greatly varying CPU. GPU and memory capabilities. The large computing resources available via distributed computing can be used to enlarge the parameter space searched or to probe more deeply in the noise than is feasible on current computing clusters, but optimization must account for scaling of computing cost with the target range of frequency and frequency derivative and weigh the benefit of longer coherence time for sensitivity against the incurred cost (see Sect. 3.1).

The $\mathcal{F}$-statistic-stacking techniques can also be used, of course, in less powerful computing environments, with different tunings, e.g., shorter coherence times per segment. These techniques can also be used for systematic follow-up of outliers found in first-stage semi-coherent $\mathcal{F}$-statistic searches or in searches using other semi-coherent methods (Walsh et al. 2019), including both all-sky and directed searches. One general-purpose, multi-stage approach uses the python wrapper PyFstat for $\mathcal{F}$-statistic summing (Ashton and Prix 2018; Keitel et al. 2021) and a Markov Chain Monte Carlo search through parameter space to "zero in" on signals (Tenorio et al. 2021a). This method systematically lengthens segment coherence times (hence reducing segment counts per observational run) simultaneously with narrowing of the parameter space volume, while guided by the parameters of the loudest survivors from each stage.

A comparison of many of these all-sky search methods was carried out via a mock data challenge using initial LIGO data, (Walsh et al. 2016) and these methods have been applied to searches of the Advanced LIGO O1–O3 data sets (Abbott et al. 2017a, d, 2018b, 2019a; Steltner et al. 2021; Abbott et al. 2021a, 2022b). Unsurprisingly, the all-sky search enabled by Einstein@Home computing resources displayed consistently better sensitivity than the other methods in the mock data challenge, given the longer coherence times made possible by those resources.

A newcomer all-sky search pipeline, known as the SOAP pipeline (Bayley et al. 2020), uses a Viterbi approach to seek trajectories in spectrograms for which each time segment is represented by the average spectrum over a 24-h period using a 30-mins coherence time. Although not as sensitive as the pipelines described above, the technique is blazingly fast, in comparison, offering the potential of rapid discovery for observing runs with much improved detector noise. Perhaps more important, because the algorithm is untemplated, it has the additional potential of detecting new (strong) signals that do not follow the models sought by other isolated-star pipelines, including long-period binary systems.

4.4.2 Results from all-sky, isolated-star searches of LIGO and Virgo data

The Sky Hough algorithm was used to produce all-sky upper limits in the 200–400 Hz band of the LIGO S2 data (Abbott et al. 2005a), based on a total of 3800 30-min

segments of data from the three LIGO interferometers. The StackSlide, Sky Hough and PowerFlux methods were used to produce all-sky upper limits in the 50–1000 band of the LIGO S4 data (Abbott et al. 2008a). The first Einstein@Home all-sky search was carried out too on the S4 data (Abbott et al. 2009c).

The PowerFlux algorithm was used to produce all-sky upper limits in the 50–1100 Hz band of the first eight months of LIGO S5 data (Abbott et al. 2009a). The sheer length of data for the full 23-month S5 run required substantial upgrade of the program which was then used to produce all-sky upper limits in the 50–800 Hz band of the full data set, based on a total of more than 80,000 (50%-overlapped) 30-min segments from the H1 and L1 data. This PowerFlux result (Abadie et al. 2012) included a three-stage hierarchical search with a follow-up procedure of loud candidates based on *loose coherence* (see Sect. 3.3.4). A Sky Hough search of the S5 data consisted of a coincidence analysis of data sets from two separate approximately 1-year subsets of the data over the 50–1000 Hz band. Einstein@Home too was applied in sequential analyses to the early S5 (Abbott et al. 2009b) and to the full S5 (Aasi et al. 2013b). A final all-sky initial LIGO PowerFlux analysis of the S6 data set (Abbott et al. 2016a) included a 5-stage hierachical search with longer and longer effective coherence times over 100–1500 Hz within the loose coherence framework. The S6 Einstein@Home search (Abbott et al. 2016e) achieved the most sensitive all-sky results from any of the initial LIGO data sets, reaching upper limit values as low as 5.5×10^{-25}.

When initial Virgo VSR1 data became available, a direct time-domain implementation of the $\mathcal{F}$-statistic (Astone et al. 2010a) was applied to a search of it for the 100–1000 Hz band (Aasi et al. 2014c). Later, the Frequency Hough method was applied to data from the initial Virgo VSR2 and VSR4 runs over the 20–128 Hz band, the first time an all-sky search was applied to frequencies below 50 Hz (Aasi et al. 2016a).

Since Advanced LIGO observing has begun, multiple all-sky search programs have been applied to data from the first three observing runs, O1, O2 and O3. The first publications based on O1 data focused on lower frequencies. Four pipelines (PowerFlux, Sky Hough, Frequency Hough and TD-$\mathcal{F}$-statistic) covered the band 20–475 Hz and a spin-down range $[-1.0 \times 10^{-8}, +1.0 \times 10^{-9}]$ Hz/s (Abbott et al. 2017a). A separate Einstein@Home search using the GCT-$\mathcal{F}$-statistic method drilled deeper in the 20–100 Hz band in a narrower spin-down range $[-2.65 \times 10^{-9}, +2.64 \times 10^{-10}]$ Hz/s (Abbott et al. 2017d). A follow-up publication using three of the first four pipelines (PowerFlux, Sky Hough and TD-$\mathcal{F}$-statistic) covered the broader band 475–2000 Hz (Abbott et al. 2018b).

Figure 32 shows the full-band O1 results from Abbott et al. (2018b) for these three pipelines. The PowerFlux results shown are defined differently from those shown for the other searches. PowerFlux upper limits are derived as strict frequentist over the full sky, that is, a 95% CL limit provides at least 95% coverage, regardless of sky position, making it quite conservative. At the same time, however, limits are shown for an optimistic polarization assumption (circular polarization corresponding to $|\cos(\iota)| = 1$) and for a pessimistic assumption (linear polarization corresponding to $\cos(\iota) = 0$ for the least favorable choice of polarization angle ψ). These limits are

derived directly from the corresponding detection statistics (see Sect. 3.5.2). The other limits shown are conventional frequentist population-based values, averaged over source orientation and sky position. Figure 33 shows the low-frequency band up to 100 Hz, comparing the limits obtained in Abbott et al. (2017a) with those from the GCT-$\mathcal{F}$-statistic search on Einstein@Home (Abbott et al. 2017d) (which use a smaller spin-down range), where the PowerFlux limits have been reevaluated via explicit simulation to produce population-averaged values for comparison.

All-sky results from three pipelines (Sky Hough, Frequency Hough and TD-$\mathcal{F}$-statistic) were applied to the O2 data set (Abbott et al. 2019a; Palomba et al. 2019) over the 20–1922 Hz band and a spin-down range $[-1.0 \times 10^{-8}, +2.0 \times 10^{-9}]$, where frequency coverage varied by pipeline. Resulting upper limits are shown in Fig. 34. The Frequency Hough search was later extended up to 2024 Hz (Palomba et al. 2019) (see Fig. 35). A dedicated Einstein@Home search of the O2 data (Steltner et al. 2021) over the 20–585 Hz band achieved significantly lower upper limits in the overlapping frequency band (see Fig. 35) for a spin-down range about four times smaller.

An intriguing set of O1 and O2 all-sky searches using the Falcon pipeline (derived from PowerFlux, but implemented with approximations and exploiting additional symmetries (Dergachev and Papa 2019, 2020a, b, 2021a, b)), focused on deeper searches. The O1 search (Dergachev and Papa 2019, 2020a) doubled the first-stage

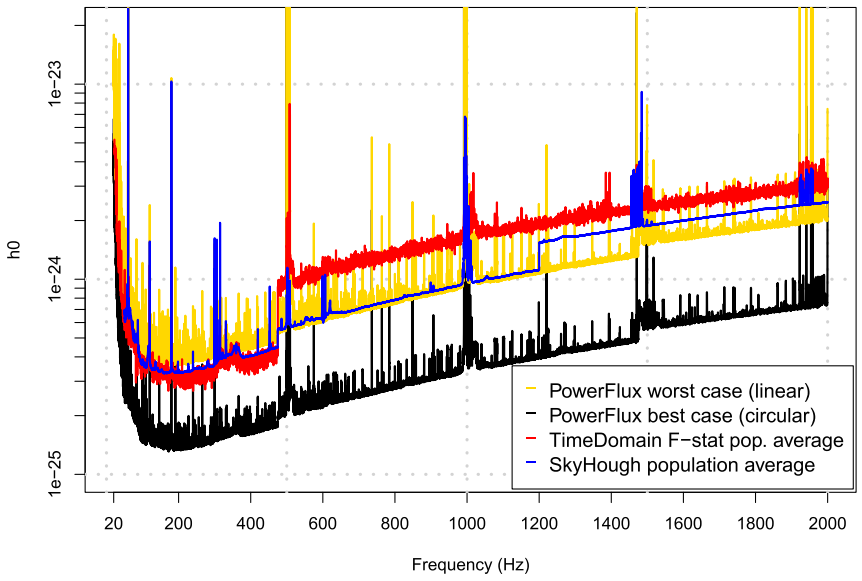

Fig. 32 O1 all-sky upper limits (95% CL) on h_0 for isolated stars from three semi-coherent search pipelines over the band 20–2000 Hz (Abbott et al. 2018b). The limits shown for the PowerFlux method correspond to best-case (circular polarization) and worst-case (linear polarization) over the entire sky, while the limits shown for the time-domain $\mathcal{F}$-statistic and Sky Hough methods correspond to population averages over the sky and source orientations. The steps in sensitivty apparent in the limits correspond to reductions in FFT coherence time as frequencies increase. Image reproduced with permission from Abbott et al. (2018b), copyright by the authors

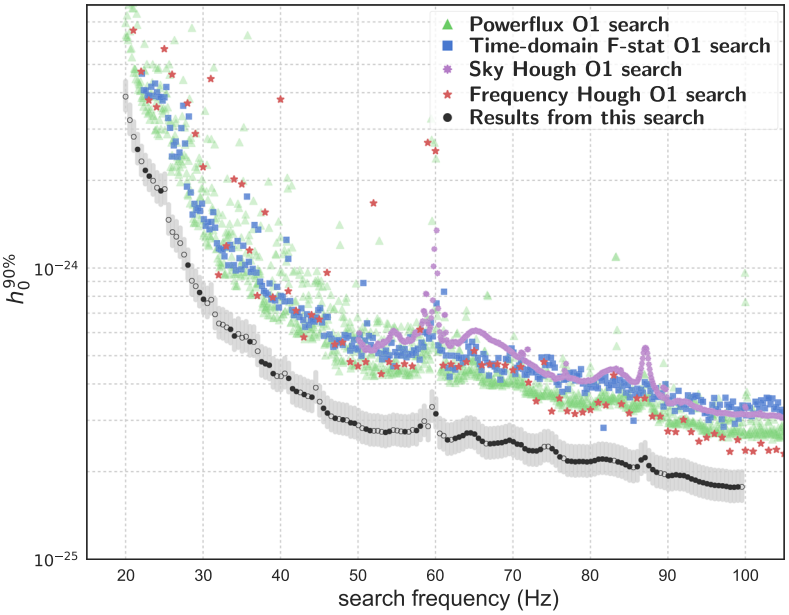

Fig. 33 O1 all-sky upper limits (95% CL) on h_0 for isolated stars in the low-frequency band (20–100 Hz) for five semi-coherent pipelines (Abbott et al. 2017d), including an Einstein@Home GCT-$\mathcal{F}$-statistic search ("this search"). The PowerFlux limits here are population-averaged, unlike those shown in Fig. 32 Image reproduced with permission from Abbott et al. (2017d), copyright by the authors(s)

effective coherence time from that used in the O1 PowerFlux search (Abbott et al. 2017a, 2018b) while covering the same spin-down range over the 100–600 Hz band. The O2 searches, on the other hand, targeted low-ellipticity pulsars (Woan et al. 2018) by severely restricting the spin-down range (e.g., $|\dot{f}_{\rm GW}| < 3 \times 10^{-12}$ Hz/s) in the 500–1500 Hz band. This vast reduction in parameter space permits using loose coherence with an effective coherence time of 12 h in its initial search stage, albeit with a necessarily reduced astrophysical range because of the spin-down restriction.

Another deep O2 search (Wette et al. 2021) focused on the narrow 171–172 Hz band while restricting spin-down magnitudes below $\sim 3 \times 10^{-13}$ Hz/s. This search used a semi-coherent $\mathcal{F}$-statistic technique with Graphics Processing Unit acceleration in the $\mathcal{F}$-statistic computation, where the frequency band chosen was meant to optimize probability density of detection in a narrow band based on detector sensitivity and the known pulsar population.

The first all-sky search of O3 data for isolated CW sources (Abbott et al. 2021a) used the PowerFlux pipeline to examine the O3a data for the same broad parameter space in frequency and spin-down as used in the O1 search. A comparison of upper limits obtained from several O2 searches with those obtained from the O3a search are shown in Fig. 35. Figure 36 shows the corresponding parameter space coverages.

The most sensitive all-sky results to date for broad coverage of both frequency and spin-down were obtained recently from the full O3 data from three pipelines (Sky Hough, Frequency Hough and TD-$\mathcal{F}$-statistic) (Abbott et al. 2022b) and are shown

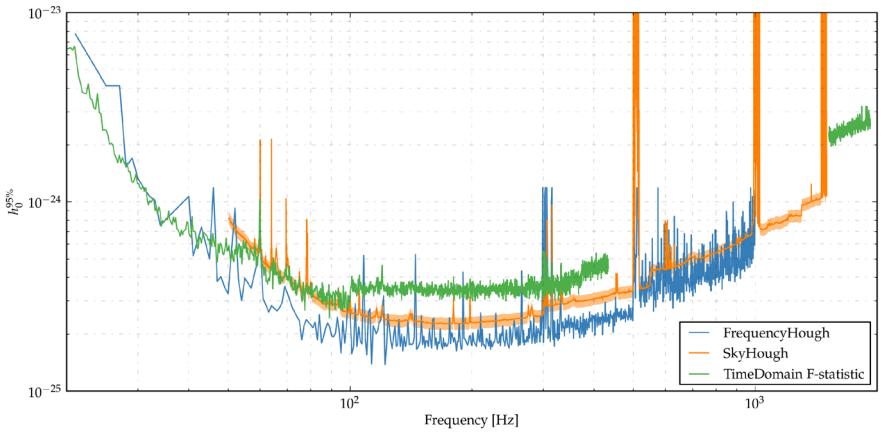

Fig. 34 O2 all-sky upper limits (95% CL) on h_0 for isolated stars from three semi-coherent search pipelines over the band 20–1922 Hz. As in Fig. 32, step changes in sensitivity correspond to reductions in FFT coherence time with increasing frequency. Image reproduced with permission from Abbott et al. (2019a), copyright by APS

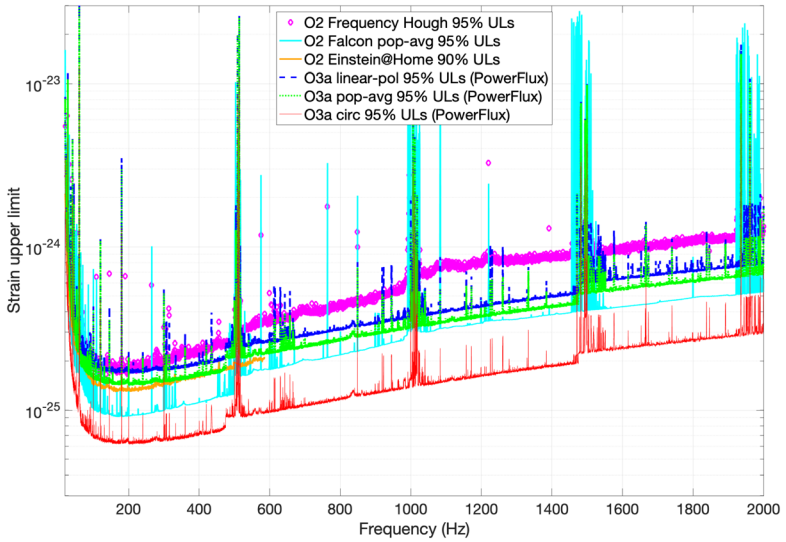

Fig. 35 O3a all-sky upper limits (95% CL) on h_0 for isolated stars from the O3a PowerFlux search in comparison with earlier O2 searches. The corresponding parameter space areas in f_{GW}–$\dot{f}_{\mathrm{GW}}$ are shown in Fig. 36. Image reproduced with permission from Abbott et al. (2021a), copyright by APS

in Fig. 37, in comparison with the O3a PowerFlux results (Abbott et al. 2021a) and with the results from the new Viterbi-based, less sensitive but blazing-fast, SOAP pipeline. Also shown are recent O3a Falcon results (Dergachev and Papa 2022) over a restricted spin-down range. Figure 38 shows a comparison of the parameter space coverages of these different searches.

4.5 All-sky searches for binary stars

Several methods have been proposed and implemented for carrying out a CW all-sky binary search. The first method, which was used in a published search of initial LIGO S6 data (Aasi et al. 2014a) is known as TwoSpect (Goetz and Riles 2011). The program carries out a semi-coherent search over an observation time long compared to the maximum orbital period considered, while using coherence times short with respect to the orbital period. Fourier transforms are carried out over each row (fixed frequency bin) in a $\sim$year-long spectrogram, and the resulting frequency-frequency plot is searched for characteristic harmonic patterns.

Another developed pipeline, known as Polynomial, (van der Putten et al. 2010) searches coherently using matched filters over an observation time short compared to the minimum orbital period considered. A bank of frequency polynomials in time is used for creating the matched filters, where for a small segment of an orbit, the frequency should vary as a low-order polynomial. Other proposed methods, which offer potentially substantial computational savings at a cost in sensitivity, include autocorrelations in the time-frequency plane (Viceré and Yvert 2016) and stochastic-background techniques (Ballmer 2006), with computational costs gains achieved by

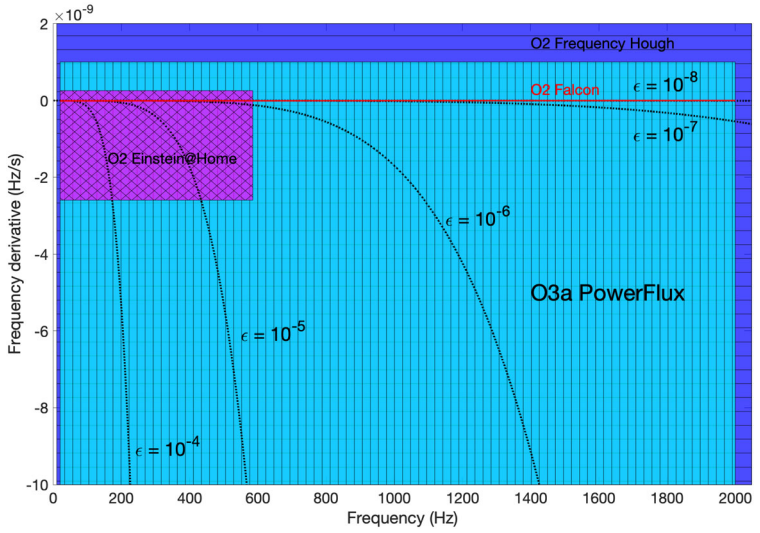

Fig. 36 Comparison of parameter space areas in O2 all-sky searches versus the O3a PowerFlux search. The shaded rectangle with vertical bars shows the 20–2000 Hz and -10^{-8}–10^{-9} Hz/s range for the O3a search (Abbott et al. 2021a). The slightly larger rectangle with horizontal bars shows the region searched in the O2 data with the Frequency Hough method (Abbott et al. 2019a; Palomba et al. 2019). The smaller rectangle with crossed diagonal bars shows the region searched by the distributed-computing project Einstein@Home (Steltner et al. 2021). The solid line at zero spin-down depicts the specialized O2 search for low-ellipticity millisecond pulsars using the Falcon method (Dergachev and Papa 2020b, 2021a, b) (the thickness of the line overstates the coverage in spin-down range). The dotted curves indicate contours of constant equatorial ellipticity $\epsilon = (10^{-8}, 10^{-7}, 10^{-6}, 10^{-5}$ and $10^{-4})$ for a star with stellar spin-down dominated by gravitational-wave emission. Image reproduced with permission from Abbott et al. (2021a), copyright by APS

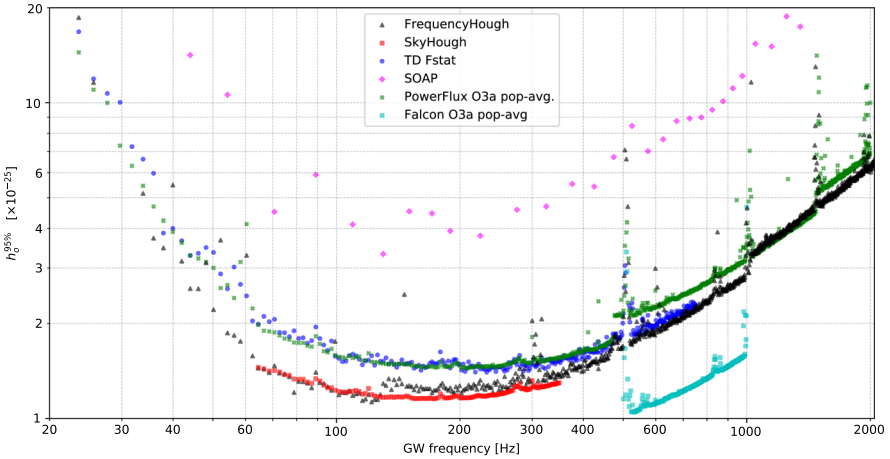

Fig. 37 O3 all-sky upper limits (95% CL) on h_0 for isolated stars from four pipelines (Abbott et al. 2022b), in comparison with the O3a PowerFlux (Abbott et al. 2021a) and Falcon results (Dergachev and Papa 2022). The corresponding parameter space areas in f_{GW}–$\dot{f}_{\mathrm{GW}}$ are shown in Fig. 38

using skymaps with sidereal-day folding (Thrane et al. 2015; Goncharov and Thrane 2018; Abbott et al. 2022a).

More recently, the implementation of graphics processor units software in the framework of the Sky Hough all-sky program has led to a breakthrough in all-sky binary search sensitivity (Covas and Sintes 2019). Upper limits were initially obtained over 100–300 Hz and over a broad range of binary orbital parameters from the LIGO O2 data (Covas and Sintes 2020). Although this approach does not yet cover the full orbital parameter space possible with the TwoSpect program, the intrinsic sensitivity is dramatically better, with extension of the method to shorter orbital periods a natural future improvement. A follow-up analysis in the O3a data (Abbott et al. 2021b; Tenorio 2021) expanded the search band slightly (50–300 Hz), and a parallel development using a similar Hough transform framework but with a $\mathcal{F}$-statistic (Covas and Prix 2022a, b) tailored to multi-hour segments, has been applied to the O3a data in the 300–500 Hz band (Covas et al. 2022). All of these results are shown in Fig. 39. See references for details on orbital parameter space regions covered by the different analyses, which vary considerably.

In addition, searches for isolated stars retain some sensitivity to long-period binaries, as shown in a recent studies (Singh et al. 2019; Singh and Papa 2023).

4.6 Searches for CW transients and other CW-like signals

The first dedicated search for CW transients following a known pulsar's glitch addressed glitches detected by radio astronomers during the Advanced LIGO / Virgo O2 data run. The search used the transient $\mathcal{F}$-statistic method (Prix et al. 2011) and focused on periods following glitches in the Crab and Vela pulsars (Keitel et al. 2019). A recent O3 analysis (Abbott et al. 2022f; Modafferi et al. 2021) searched for

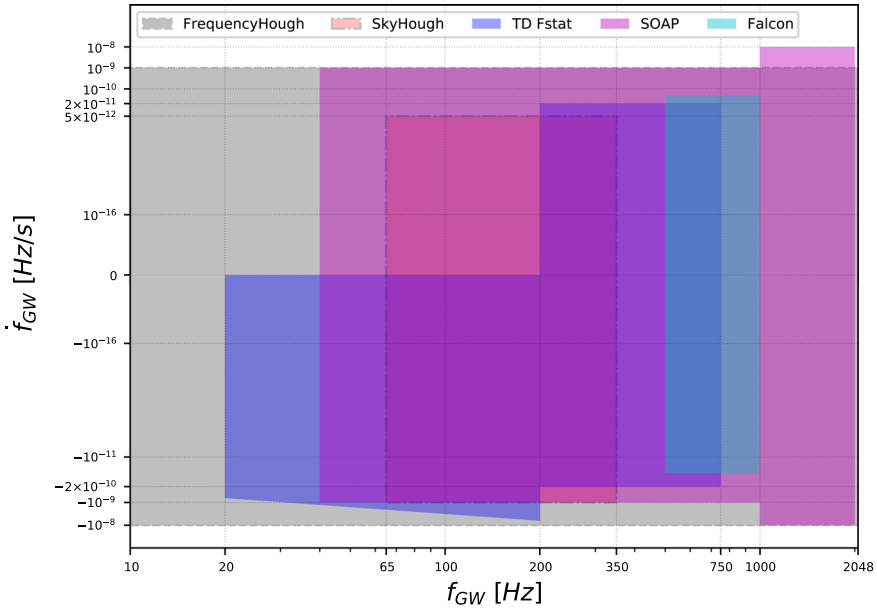

Fig. 38 Comparison of f_{GW}–$\dot{f}_{\mathrm{GW}}$ parameter space coverage for the four search pipelines used in the full-O3 all-sky searches (Abbott et al. 2022b) and for the restricted-spindown O3a Falcon search. (Abbott et al. 2022b)

CW transients following nine glitches across six pulsars (one glitch each from five stars: PSR J0534+2200, J0908−4913, J1105−6107, J1813−1749 and J1826−1334; and four glitches from the intriguing source, PSR J0537–6910—see Sects. 2.1.2, 2.1.4 and 4.2). No significant candidates were observed, although two marginal outliers were seen after one PSR J0537–6910 glitch, albeit with implied strengths well above those consistent with the inferred glitch energies. In fact, the upper limits obtained for post-glitch energy emission from all glitches examined lay above the maximum expected in a simple two-fluid model (Prix et al. 2011), with strain limits for PSR J1105–6107 approaching most closely to that benchmark (within a factor of $\sim$ 1.6).

The first dedicated search for long-lived, CW-like signals from a post-merger remnant looked for a signal from the post-GW170817 remnant, but as expected, given the $\sim$ 40 Mpc distance to the merger, no signal was detected in the immediate aftermath (Abbott et al. 2017o) ($\sim$ 500 s) or in a multi-hour to multi-day period afterward (Abbott et al. 2019d). Should another opportunity arise (from a nearby binary neutron star merger or a galactic supernova), search methods are available for use (Thrane et al. 2011; Miller et al. 2018; Sun and Melatos 2019; Oliver et al. 2019; Banagiri et al. 2019; Mytidis et al. 2019; Miller et al. 2019a).

More exotic recent analyses seeking CW or CW-like signals include:

- Searches for CW signals from Bose–Einstein clouds (D'Antonio et al. 2018; Abbott et al. 2022c) (see Sect. 2.2).

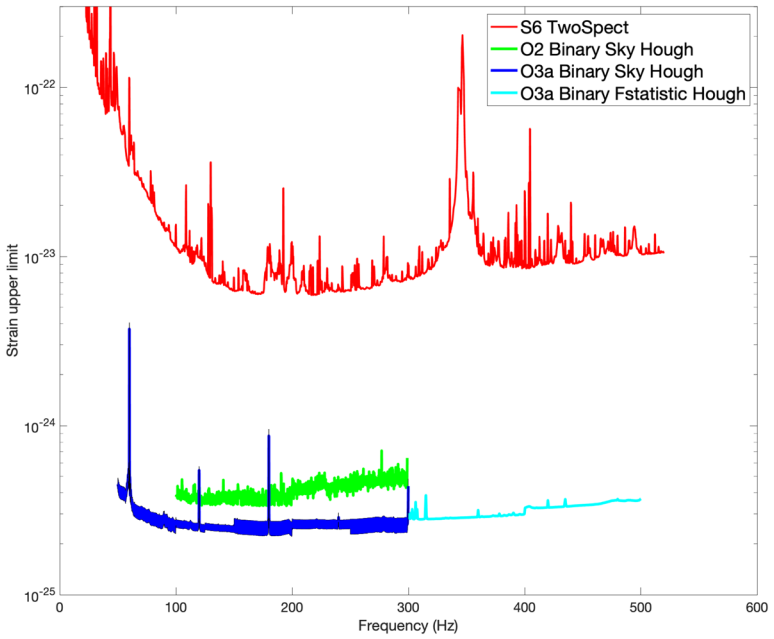

Fig. 39 All-sky upper limits (95% CL) on h_0 for stars in binary systems. Upper limits are shown from the inital LIGO S6 TwoSpect search (Aasi et al. 2014a), from the GPU-enhanced O2 Binary Sky Hough search (Covas and Sintes 2020) (100–300 Hz), from the O3a Binary Sky Hough search (Abbott et al. 2021b) (50–300 Hz) and from the O3a Binary $\mathcal{F}$-statistic search (Covas et al. 2022) (300–500 Hz). See references for details on orbital parameter space regions covered by the different analyses. The O2 and O3a Binary Sky Hough values shown are 95% sensitivities with bands to indicate uncertainties

- A search for non-black-hole weakly interacting compact dark objects with mass below $10^{-7}\ M_\odot$ orbiting within the Sun about its center (Horowitz et al. 2020).
- Searches for ultralight dark photon or scalar boson dark matter creating an extremely narrowband ($\Delta f/f \sim 10^{-6}$) spectral excess with stochastic phase (Pierce et al. 2018; Guo et al. 2019; Miller et al. 2021b; Abbott et al. 2022d; Grote and Stadnik 2019; Vermeulen et al. 2021).
- A search for binary systems of planetary-scale / asteroid-scale primordial black holes near to the Earth (Miller et al. 2021a, 2022; Abbott et al. 2022b).
- There has also been a proposal to apply CW search techniques to suspected Thorne–Żytkow objects (Thorne and Zytkow 1975) (TZOs) for which a neutron star orbiting inside of a giant star (slow inspiral decay) could produce signals in the band of ground-based gravitational-wave detectors (DeMarchi et al. 2021).

5 Outlook

5.1 Prospects for discovery

Over the next several years, the Advanced LIGO (Aasi et al. 2015a) and Virgo (Acernese et al. 2014) detectors are expected to approach and eventually surpass their original design sensitivities in strain, increasing the range within the galaxy which CW searches can access, thereby increasing detection likelihood. As the sensitive ranges of different search methods approach the dense galactic core, detection chances may rise more rapidly. In parallel to detector improvement, algorithms continue to improve, as researchers find more effective tradeoffs between computational cost and detection efficiency, while Moore's Law, including Graphics Processing Unit (GPU) exploitation (Keitel and Ashton 2018; Covas and Sintes 2019; Wette et al. 2021; Dunn et al. 2021; La Rosa et al. 2021), ensures increased computing resources for searches. All of these trends are encouraging for successful CW detection.

At the same time, theoretical uncertainties in what sensitivity is needed for the first CW detection are very large. While the spin-down limits based on gravitar assumptions and on either energy conservation or known age have been beaten for a handful of sources and will be beaten for more sources in the coming years, the gravitar model is surely optimistic—most stellar spin-downs are likely dominated by electromagnetic interactions. Whether the first detection is imminent or still many years distant remains unclear. A recent phenomenological population synthesis study (Cieślar et al. 2021), based on an exponentially decaying ellipticity that starts at its allowed maximum $\sim 10^{-5}$ with a supernova rate of once per century concluded that the expected number of detectable, young and isolated neutron stars for Advanced LIGO sensitivity is less than one and is $\sim$ 10 for Einstein Telescope.

Electromagnetic astronomers could prove pivotal in hastening detection by identifying new nearby or young neutron stars, or discovering pulsations from known stars, perhaps most usefully from the accreting Sco X-1 system (Galaudage et al. 2021). Given the computational challenges of most CW searches, narrowing the parameter space of a search exploiting electromagnetic observations could make the difference between a gravitational-wave miss and a discovery.

5.2 Confirming and exploiting a discovery

There are several aspects of confirming a nominal CW discovery, including establishing the statistical significance of the outlier, verifying consistency of the signal with the CW model, excluding an environmental or instrumental cause, and (optionally but ideally) confirming consistency with prior or follow-up electromagnetic observations. Once that discovery is established, exploiting it to understand neutron star astrophysics (or fundamental particle physics should a superradiant boson cloud be observed) will be a rich endeavor.

The degree of statistical confidence with which a putative CW signal detection can be confirmed depends on the type of search that leads to the candidate. The statistical

significance of an outlier depends on a trials factor that may range from ~ 1 for targeted searches for known pulsars using electromagnetically derived ephemerides to $\sim 10^{15}$ for all-sky searches. Hence the SNR threshold for, say, a "5-sigma" discovery varies too. In practice, though, for a candidate emerging from a hierarchical search with multiple stages of "zooming in", the SNR for a surviving outlier may be so much higher than the sensitivity-defining SNR threshold used in the first stage that the initial trials factor is irrelevant. Establishing the statistical confidence of a targeted-search candidate, on the other hand, may simply require steady accumulation of additional data while fully exploiting all data in hand from all detectors with appreciable sensitivity in that band. Empirically assessing the significance of loudest outliers is discussed in detail in Tenorio et al. (2022).

If known detector artifacts are degrading sensitivity in the frequency band of the candidate, it may be feasible to focus detector commissioning to mitigate the artifact prior to the next observing run. Another possible approach, although potentially detrimental to other GW observations, is "narrowbanding." In narrowbanding the detector sensitivity is improved in a narrow band at the expense of broadband sensitivity by adjusting the position of the "signal recycling" mirror at the output port of the interferometer (Aasi et al. 2015a); with the advent of quantum squeezing in advanced detectors (Tse et al. 2019), however, the potential gains from narrowbanding are less pronounced.

Even with a promising outlier, a discovery claim would need more than statistical inconsistency with detector noise. One would seek consistency with the signal model, particularly for candidates originating in hierarchical searches where early stages look primarily for excess power that is only roughly consistent with a particular template and where the spacing between templates is relatively coarse. The expected Doppler modulations due to the Earth's motion should be present (Zhu et al. 2017; Intini et al. 2020b). One wants to see a signal for which a fully coherent search over all data yields an SNR consistent with expectation from the putative source. Ideally, a residual spectrum from subtracting the reconstructed signal would be consistent with random background noise.

In the case of a targeted or directed search for which the source location is *a priori* known, one would want to verify that the highest-SNR template observed in that region of the sky and near the template's frequency parameters is indeed consistent with the correct sky location. Although one could impose a similar constraint on frequency and frequency derivatives for a targeted search, narrowband searches do allow those parameters to differ slightly from the nominal ones, to accommodate differential stellar rotation. Hence seeing the SNR peak at precisely the right location in parameter space for a known pulsar would lend credence to the signal, but seeing the SNR peak at a nearby point in parameter space can still mean discovery, albeit with a trials factor appropriate to a narrowband search.

The possibility of a rotational glitch during an observational period presents additional complications. One can no longer safely apply a fully coherent search over the time span and expect a monotonically increasing SNR. In the case of a targeted search with ephemerides in hand indicating a glitch, breaking the observation time into two (or more) segments is straightforward (Abbott et al. 2010), but in the case of

a source without independent timing information, one may have a true signal detection but lack the confidence to declare discovery without additional data taking because of apparent phase inconsistency in the available data.

In any gravitational-wave analysis using interferometers that push the frontier of technology (and which are routinely operated at maximum achievable sensitivity), one must consider whether or not instrumental or environmental contamination leads to a false signal. As discussed in Sect. 3.7, narrow lines can contribute to accumulated power in a templated search. As part of confirming a discovery, one would need to quantify that contamination for a putative signal lying near a known instrumental spectral line. More challenging and more realistic for a signal candidate surviving multiple hierarchical search stages are spectral lines that are *not* immediately apparent in the strain channel spectrum, especially lines that are non-stationary with respect to time or frequency ("wandering"). To address that possibility, one would look comprehensively at auxiliary data channels, such as readouts from magnetometers, accelerometers, seismometers, microphones and from any servo control channels that could impose tiny actuations on the gravitational-wave strain channel. Those investigations would include examination of averaged spectra for peaks coincident with the strain signal frequency and more probing searches for cross-coherence between the auxiliary channels and the strain channel that is inconsistent with statistical fluctuation.

The fact that the Virgo and KAGRA interferometers have made different technological choices means that instrumental contaminations differ, in general, from those of the LIGO interferometers, allowing better discrimination of astrophysical from instrumental sources. For example, a seemingly trivial but important difference is that the U.S. power mains used by LIGO, and the western Japanese power mains used by KAGRA provide alternating electrical currents at 60 Hz, but Virgo depends on Italian power mains which operate at 50 Hz. Since nearly all observatory electronics derive power from the mains, low-lying line contamination from the fundamental oscillation, from its higher harmonics and from sidebands due to non-linear interactions with mechanical and other electrical oscillations, are difficult to mitigate completely. Such technical differences reduce the chance of coincident false CW signals between the nominally identical LIGO detectors and the other two detectors.

Consistency in SNR detected by different interferometers offers another important astrophysical reality test. Unlike with transient GW detections, for which antenna pattern variations among detectors are critical to localization (Abbott et al. 2020b), any single interferometer can strongly localize a long-lived continous waves signal, largely removing antenna pattern / polarization ambiguity and permitting signal strength consistency comparisons across independent data sets in different interferometers (assuming the correctness of General Relativity GW polarization).

Finally, in confirming a continuous gravitational-wave signal one would, ideally, want confirmation via electromagnetic observations. For targeted or narrowband searches of known pulsars, the observations already exist, and the primary task is to establish statistical confidence of their consistency with gravitational data. For other known sources, however, gravitational-wave measurements may provide the necessary clues to allow detection of previously undetected pulsations. For example,

detection of a CW signal from Scorpius X-1 could permit discrimination of X-ray pulsations from a stochastic background dominated by accretion emission. For a previously unknown source found in an all-sky search, determining the source location from coherent integration over months of data (with sub-arcsecond resolution possible from the aperture formed by the Earth's orbit) may suffice for radio, X-ray, gamma-ray (and perhaps even optical) astronomers to find the counterpart. If electromagnetic pulsations were detected and agreed with expectation, the confirmation of the gravitational-wave signal would be ironclad.

An interesting challenge to confirmation would be continuous gravitational radiation due to boson cloud superradiance for an isolated black hole (see Sect. 2.2). If there were no accretion disk or companion to induce an electromagnetic signal, one would have to rely heavily upon the evolution of the gravitational-wave signal itself to infer the nature of the source. In particular, the source frequency governed by the boson's apparent mass in the potential of the black hole could spin *up* instead of down as the black hole loses mass energy to gravitational radiation, thereby reducing the magnitude of the negative binding energy correction to the unbound boson mass (Arvanitaki et al. 2015).

Once a continuous gravitational-wave detection has been confirmed electromagnetically, one will want to exploit the correlations to understand the source. Below are a sampling of potential measurements possible, along with questions they help to address:

- Relation between rotational and gravitational-wave frequencies, determining the fundamental mechanism of emission (see Sect. 2 and see Jones (2022) for a detailed discussion).
- Correlation of the gravitational and electromagnetic phase constants in the event of consistent frequency (phase) evolution. If an equatorial mass "bulge" explains the GW signal, how well does the implied quadrupolar axis align with a pulsar's inferred magnetic dipole projection? In an accreting system, for example, does added mass accumulate near the magnetic poles?
- Differential frequency (phase) evolution. Is there differential rotation between the stellar crust and its interior? If electromagnetic frequency glitches are observed, what is seen gravitationally before, during and after the glitch?
- If there is evidence for r-modes from, say, an approximate 4/3 ratio of GW signal frequency to stellar rotation frequency, how does the GW frequency evolve with time and how does the ratio evolve? Is there evidence of amplitude growth from instability? Decay from viscosity?
- Inferred quadrupole moment. Although ellipticity is a convenient dimensionless parameter, it is approximately the product of the ellipticity times the stellar moment of inertia about its spin axis that determines the signal strength for a mass-quadrupole radiator. Given the uncertainties in neutron star equation of state, there are large uncertainties in the moment of inertia and hence ambiguity in extracting ellipticity. Ambiguity at the level of near-degeneracy would arise in the absence of an independent determination of source distance from electromagnetic

observations (Sieniawska and Jones 2021). A CW detection in a binary system would offer an opportunity for determination of the stellar mass. Other stellar properties potentially accessible include the stellar radius (inferred from luminosity and temperature, if measurable). A precessing star with detectable electromagnetic pulsations offers additional opportunity for understanding internal structure (Gao et al. 2020).

- Even in the absence of detected electromagnetic pulsations, one can use the known source of an electromagnetic counterpart to infer a star's moment of inertia, equatorial ellipticity, and the component of the magnetic dipole moment perpendicular to its rotation axis (Lu et al. 2023). For a close enough neutron star without an electromagnetic counterpart, parallax inference from the GW signal alone could resolve the degeneracy among source distance, moment of inertia and equatorial ellipticity (Sieniawska et al. 2023) (see Eq. 14).
- Boson properties from superradiance. In the event of detecting superradiance from a boson cloud around a black hole, determining the boson's mass will be immediate from the signal frequency (at least for the annihilation channel expected to dominate) with the boson intrinsic spin determination more model dependent, based on signal strength and frequency evolution with some knowledge of the black hole source needed.

In addition to exploiting CW detection to understand the source, one can also carry out precise tests of General Relativity by measuring the polarization of the propagating gravitational wave. In Einstein's theory there should be two independent transverse, quadrupolar polarizations for which the relative strengths depend on the source orientation relative to the line of sight. In non-standard theories of gravity other polarization modes, including scalar, vector and longitudinal polarizations, may be present (Isi et al. 2015). Testing for these additional polarizations with transient gravitational-wave detections to date has been challenging because nearly all of the signal-to-noise ratio has come from the two nearly aligned LIGO detectors such that they mainly detect the same polarization projection. In contrast, even for a single detector, a CW signal permits disentangling multiple polarization contributions as the sidereal rotation of the Earth changes the detector's (polarimeter's) orientation with respect to the source direction deterministically (Isi et al. 2015; Kuwahara and Asada 2022). In fact, even in the absence of a CW signal, one can set upper limits on the non-standard polarizations (Abbott et al. 2018a), just as is possible for standard polarizations.

Nature has blessed the gravitational-wave community with a bounty of compact star mergers, including the remarkable first detected BBH merger, GW150914, and the even more remarkable and informative multi-messenger detection of the GW170817 BNS event. Should such kindness continue, one may hope soon for a multi-messenger detection of a CW source that not only could be observed into the foreseeable future, but could mark the first of a large collection to come, as GW150914 proved to be.

Acknowledgements The author is deeply grateful to current and former colleagues in the LIGO Scientific Collaboration and Virgo collaboration Continuous Waves Search Group for close collaboration from which he has benefited in preparing this article. The author also thanks Julian Carlin, Pep Covas, Vladimir Dergachev, Francesco Fidecaro, Bryn Haskell, Wynn Ho, Ian Jones, David Keitel, Andrew Melatos, Ben Owen, Maria Alessandra Papa, Lilli Sun, Rodrigo Tenorio, Karl Wette and Graham Woan for helpful suggestions concerning the manuscript. Special thanks to the two anonymous referees for their thorough readings and for many constructive suggestions (and corrections). Thanks too to LIGO, Virgo and the Max Planck Institute f. Gravitational Physics for the use of figures. This work was supported in part by National Science Foundation Awards PHY-2110181 and PHY-1806577. The author thanks the Institute of Nuclear Theory at the University of Washington and the Perimeter Institute of Waterloo for hosting workshops that proved helpful in composing this review. The author is grateful for computational resources provided by the LIGO Laboratory and is supported by the National Science Foundation. This material is based in part upon work supported by NSF's LIGO Laboratory which is a major facility fully funded by the National Science Foundation.

References

Aasi J et al (2013a) Directed search for continuous gravitational waves from the Galactic center. Phys Rev D. https://doi.org/10.1103/physrevd.88.102002

Aasi J et al (2013b) Einstein@Home all-sky search for periodic gravitational waves in LIGO S5 data. Phys Rev D 87(4):042001. https://doi.org/10.1103/PhysRevD.87.042001. arXiv:1207.7176 [gr-qc]

Aasi J et al (2014a) First all-sky search for continuous gravitational waves from unknown sources in binary systems. Phys Rev D 90(6):062010. https://doi.org/10.1103/PhysRevD.90.062010. arXiv:1405.7904 [gr-qc]

Aasi J et al (2014b) Gravitational waves from known pulsars: results from the initial detector era. Astrophys J 785(2):119. https://doi.org/10.1088/0004-637x/785/2/119

Aasi J et al (2014c) Implementation of an $\mathcal{F}$-statistic all-sky search for continuous gravitational waves in Virgo VSR1 data. Class Quantum Grav 31(16):165014. https://doi.org/10.1088/0264-9381/31/16/165014

Aasi J et al (2015a) Advanced LIGO. Class Quantum Grav 32(7):074001. https://doi.org/10.1088/0264-9381/32/7/074001

Aasi J et al (2015b) Characterization of the LIGO detectors during their sixth science run. Class Quantum Grav 32(11):115012. https://doi.org/10.1088/0264-9381/32/11/115012

Aasi J et al (2015c) Directed search for gravitational waves from Scorpius X-1 with initial LIGO data. Phys Rev D 91:062008. https://doi.org/10.1103/PhysRevD.91.062008

Aasi J et al (2015d) Narrow-band search of continuous gravitational-wave signals from Crab and Vela pulsars in Virgo VSR4 data. Phys Rev D 91:2. https://doi.org/10.1103/physrevd.91.022004

Aasi J et al (2015e) Searches for continuous gravitational waves from nine young supernova remnants. Astrophys J 813(1):39. https://doi.org/10.1088/0004-637x/813/1/39

Aasi J et al (2016a) First low frequency all-sky search for continuous gravitational wave signals. Phys Rev D 93:042007. https://doi.org/10.1103/PhysRevD.93.042007

Aasi J et al (2016b) Search of the Orion spur for continuous gravitational waves using a loosely coherent algorithm on data from LIGO interferometers. Phys Rev D 93:042006. https://doi.org/10.1103/PhysRevD.93.042006

Abadie J et al (2010) First search for gravitational waves from the youngest known neutron star. Astrophys J 722(2):1504–1513. https://doi.org/10.1088/0004-637x/722/2/1504
Abadie J et al (2011) Beating the spin-down limit on gravitational wave emission from the vela pulsar. Astrophys J 737(2):93. https://doi.org/10.1088/0004-637x/737/2/93
Abadie J et al (2012) All-sky search for periodic gravitational waves in the full S5 LIGO data. Phys Rev D 85(2):022001. https://doi.org/10.1103/physrevd.85.022001
Abazajian KN (2011) The consistency of Fermi-LAT observations of the galactic center with a millisecond pulsar population in the central stellar cluster. JCAP 03:010. https://doi.org/10.1088/1475-7516/2011/03/010. arXiv:1011.4275 [astro-ph.HE]
Abbott BP et al (2004) Setting upper limits on the strength of periodic gravitational waves from PSR J1939 + 2134 using the first science data from the GEO 600 and LIGO detectors. Phys Rev D 69:082004. https://doi.org/10.1103/PhysRevD.69.082004
Abbott BP et al (2005a) First all-sky upper limits from LIGO on the strength of periodic gravitational waves using the Hough transform. Phys Rev D 72:102004. https://doi.org/10.1103/PhysRevD.72.102004. arXiv:gr-qc/0508065
Abbott BP et al (2005b) Limits on gravitational-wave emission from selected pulsars using LIGO data. Phys Rev Lett 94:181103. https://doi.org/10.1103/PhysRevLett.94.181103
Abbott BP et al (2007a) Searches for periodic gravitational waves from unknown isolated sources and Scorpius X-1: results from the second LIGO science run. Phys Rev D 76:082001. https://doi.org/10.1103/PhysRevD.76.082001
Abbott BP et al (2007b) Upper limits on gravitational wave emission from 78 radio pulsars. Phys Rev D 76:042001. https://doi.org/10.1103/PhysRevD.76.042001
Abbott BP et al (2008a) All-sky search for periodic gravitational waves in LIGO S4 data. Phys Rev D 77:022001. https://doi.org/10.1103/PhysRevD.77.022001, [Erratum: Phys. Rev. D 80, 129904 (2009)]. arXiv:0708.3818 [gr-qc]
Abbott BP et al (2008b) Beating the spin-down limit on gravitational wave emission from the crab pulsar. Astrophys J Lett 683(1):L45. https://doi.org/10.1086/591526. arXiv:0805.4758 [astro-ph]
Abbott BP et al (2009a) All-sky LIGO search for periodic gravitational waves in the early S5 Data. Phys Rev Lett 102:111102. https://doi.org/10.1103/PhysRevLett.102.111102. arXiv:0810.0283 [gr-qc]
Abbott BP et al (2009b) Einstein@Home search for periodic gravitational waves in early S5 LIGO data. Phys Rev D 80:042003. https://doi.org/10.1103/PhysRevD.80.042003. arXiv:0905.1705 [gr-qc]
Abbott BP et al (2009c) The Einstein@Home search for periodic gravitational waves in LIGO S4 data. Phys Rev D 79:022001. https://doi.org/10.1103/PhysRevD.79.022001. arXiv:0804.1747 [gr-qc]
Abbott BP et al (2010) Searches for gravitational waves from known pulsars with science run 5 LIGO data. Astrophys J 713(1):671–685. https://doi.org/10.1088/0004-637x/713/1/671
Abbott BP et al (2016a) Comprehensive all-sky search for periodic gravitational waves in the sixth science run LIGO data. Phys Rev D 94(4):042002. https://doi.org/10.1103/PhysRevD.94.042002. arXiv:1605.03233 [gr-qc]
Abbott BP et al (2016b) GW150914: the advanced LIGO detectors in the era of first discoveries. Phys Rev Lett 116(13):131103. https://doi.org/10.1103/PhysRevLett.116.131103. arXiv:1602.03838 [gr-qc]
Abbott BP et al (2016c) GW150914: the advanced LIGO detectors in the era of first discoveries. Phys Rev Lett 116:131103. https://doi.org/10.1103/PhysRevLett.116.131103
Abbott BP et al (2016d) GW151226: observation of gravitational waves from a 22-solar-mass binary black hole coalescence. Phys Rev Lett 116:241103. https://doi.org/10.1103/PhysRevLett.116.241103
Abbott BP et al (2016e) Results of the deepest all-sky survey for continuous gravitational waves on LIGO S6 data running on the Einstein@Home volunteer distributed computing project. Phys Rev D 94(10):102002. https://doi.org/10.1103/PhysRevD.94.102002. arXiv:1606.09619 [gr-qc]
Abbott BP et al (2017a) All-sky search for periodic gravitational waves in the O1 LIGO data. Phys Rev D 96(6):062002. https://doi.org/10.1103/PhysRevD.96.062002. arXiv:1707.02667 [gr-qc]
Abbott BP et al (2017b) Directional limits on persistent gravitational waves from advanced LIGO's first observing run. Phys Rev Lett 118:121102. https://doi.org/10.1103/PhysRevLett.118.121102
Abbott BP et al (2017c) Exploring the sensitivity of next generation gravitational wave detectors. Class Quantum Grav 34(4):044001. https://doi.org/10.1088/1361-6382/aa51f4
Abbott BP et al (2017d) First low-frequency Einstein@Home all-sky search for continuous gravitational waves in Advanced LIGO data. Phys Rev D 96(12):122004. https://doi.org/10.1103/PhysRevD.96.122004. arXiv:1707.02669 [gr-qc]
Abbott BP et al (2017e) First narrow-band search for continuous gravitational waves from known pulsars in advanced detector data. Phys Rev D 96:122006. https://doi.org/10.1103/PhysRevD.96.122006

Abbott BP et al (2017f) First search for gravitational waves from known pulsars with Advanced LIGO. Astrophys J 839(1):12. https://doi.org/10.3847/1538-4357/aa677f, [Erratum: Astrophys. J. 851, 71 (2017)]. arXiv:1701.07709 [astro-ph.HE]
Abbott BP et al (2017g) Gravitational waves and gamma-rays from a binary neutron star merger: GW170817 and GRB 170817A. Astrophys J 848(2):L13. https://doi.org/10.3847/2041-8213/aa920c
Abbott BP et al (2017h) GW170104: observation of a 50-solar-mass binary black hole coalescence at redshift 0.2. Phys Rev Lett 118:221101. https://doi.org/10.1103/PhysRevLett.118.221101
Abbott BP et al (2017i) GW170608: observation of a 19-solar-mass binary black hole coalescence. Astrophys J 851(2):L35. https://doi.org/10.3847/2041-8213/aa9f0c. arXiv:1711.05578 [astro-ph.HE]
Abbott BP et al (2017j) GW170814: a three-detector observation of gravitational waves from a binary black hole coalescence. Phys Rev Lett 119:141101. https://doi.org/10.1103/PhysRevLett.119.141101
Abbott BP et al (2017k) GW170817: observation of gravitational waves from a binary neutron star inspiral. Phys Rev Lett 119:161101. https://doi.org/10.1103/PhysRevLett.119.161101
Abbott BP et al (2017l) Multi-messenger observations of a binary neutron star merger. Astrophys J Lett 848(2):L12. https://doi.org/10.3847/2041-8213/aa91c9. arXiv:1710.05833 [astro-ph.HE]
Abbott BP et al (2017m) Search for continuous gravitational waves from neutron stars in globular cluster NGC 6544. Phys Rev D 95:082005. https://doi.org/10.1103/PhysRevD.95.082005
Abbott BP et al (2017n) Search for gravitational waves from Scorpius X-1 in the first Advanced LIGO observing run with a hidden Markov model. Phys Rev D 95:122003. https://doi.org/10.1103/PhysRevD.95.122003
Abbott BP et al (2017o) Search for post-merger gravitational waves from the remnant of the binary neutron star merger GW170817. Astrophys J Lett 851(1):L16. https://doi.org/10.3847/2041-8213/aa9a35. arXiv:1710.09320 [astro-ph.HE]
Abbott BP et al (2017p) Upper limits on gravitational waves from Scorpius X-1 from a model-based cross-correlation search in advanced LIGO data. Astrophys J 847(1):47. https://doi.org/10.3847/1538-4357/aa86f0
Abbott BP et al (2018a) First search for nontensorial gravitational waves from known pulsars. Phys Rev Lett 120(3):031104. https://doi.org/10.1103/PhysRevLett.120.031104. arXiv:1709.09203 [gr-qc]
Abbott BP et al (2018b) Full band all-sky search for periodic gravitational waves in the O1 LIGO data. Phys Rev D 97(10):102003. https://doi.org/10.1103/PhysRevD.97.102003. arXiv:1802.05241 [gr-qc]
Abbott BP et al (2018c) GW170817: measurements of neutron star radii and equation of state. Phys Rev Lett 121:161101. https://doi.org/10.1103/PhysRevLett.121.161101
Abbott BP et al (2019a) All-sky search for continuous gravitational waves from isolated neutron stars using advanced LIGO O2 data. Phys Rev D 100(2):024004. https://doi.org/10.1103/PhysRevD.100.024004. arXiv:1903.01901 [astro-ph.HE]
Abbott BP et al (2019b) GWTC-1: a gravitational-wave transient catalog of compact binary mergers observed by LIGO and Virgo during the first and second observing runs. Phys Rev X 9:031040. https://doi.org/10.1103/PhysRevX.9.031040
Abbott BP et al (2019c) Narrow-band search for gravitational waves from known pulsars using the second LIGO observing run. Phys Rev D 99:12. https://doi.org/10.1103/physrevd.99.122002
Abbott BP et al (2019d) Search for gravitational waves from a long-lived remnant of the binary neutron star merger GW170817. Astrophys J 875(2):160. https://doi.org/10.3847/1538-4357/ab0f3d. arXiv:1810.02581 [gr-qc]
Abbott BP et al (2019e) Search for gravitational waves from Scorpius X-1 in the second Advanced LIGO observing run with an improved hidden Markov model. Phys Rev D. https://doi.org/10.1103/physrevd.100.122002
Abbott BP et al (2019f) Searches for continuous gravitational waves from 15 supernova remnants and Fomalhaut b with advanced LIGO. Astrophys J 875(2):122. https://doi.org/10.3847/1538-4357/ab113b. arXiv:1812.11656 [astro-ph.HE]
Abbott BP et al (2019g) Searches for gravitational waves from known pulsars at two harmonics in 2015–2017 LIGO data. Astrophys J 879(1):10. https://doi.org/10.3847/1538-4357/ab20cb. arXiv:1902.08507 [astro-ph.HE]
Abbott BP et al (2020a) GW190425: observation of a compact binary coalescence with total mass $\sim 3.4 M_{\odot}$. Astrophys J Lett 892(1):L3. https://doi.org/10.3847/2041-8213/ab75f5. arXiv:2001.01761
Abbott BP et al (2020b) Prospects for observing and localizing gravitational-wave transients with advanced LIGO, Advanced Virgo and KAGRA. Living Rev Relativ 23(1):3. https://doi.org/10.1007/s41114-020-00026-9

Abbott R et al (2020c) Gravitational-wave constraints on the equatorial ellipticity of millisecond pulsars. Astrophys J Lett 902(1):L21. https://doi.org/10.3847/2041-8213/abb655
Abbott R et al (2020d) GW190521: a binary black hole merger with a total mass of 150 $M_{\odot}$. Phys Rev Lett 125(10):101102. https://doi.org/10.1103/PhysRevLett.125.101102. arXiv:2009.01075 [gr-qc]
Abbott R et al (2020e) GW190814: gravitational waves from the coalescence of a 23 solar mass black hole with a 2.6 solar mass compact object. Astrophys J 896(2):L44. https://doi.org/10.3847/2041-8213/ab960f
Abbott R et al (2021a) All-sky search for continuous gravitational waves from isolated neutron stars in the early O3 LIGO data. Phys Rev D 104(8):082004. https://doi.org/10.1103/physrevd.104.082004
Abbott R et al (2021b) All-sky search in early O3 LIGO data for continuous gravitational-wave signals from unknown neutron stars in binary systems. Phys Rev D 103:064017. https://doi.org/10.1103/PhysRevD.103.064017
Abbott R et al (2021c) Constraints from LIGO O3 data on gravitational-wave emission due to R-modes in the glitching pulsar PSR J0537–6910. Astrophys J 922(1):71. https://doi.org/10.3847/1538-4357/ac0d52
Abbott R et al (2021d) Diving below the spin-down limit: constraints on gravitational waves from the energetic young pulsar PSR J0537–6910. Astrophys J Lett 913(2):L27. https://doi.org/10.3847/2041-8213/abffcd
Abbott R et al (2021e) GWTC-2: compact binary coalescences observed by LIGO and Virgo during the first half of the third observing run. Phys Rev X 11:021053. https://doi.org/10.1103/PhysRevX.11.021053
Abbott R et al (2021f) GWTC-3: compact binary coalescences observed by LIGO and Virgo during the second part of the third observing run. arXiv:2111.03606 [gr-qc]
Abbott R et al (2021g) Observation of gravitational waves from two neutron star-black hole coalescences. Astrophys J Lett 915(1):L5. https://doi.org/10.3847/2041-8213/ac082e. arXiv:2106.15163 [astro-ph.HE]
Abbott R et al (2021h) Search for anisotropic gravitational-wave backgrounds using data from Advanced LIGO and Advanced Virgo's first three observing runs. Phys Rev D 104(2):022005. https://doi.org/10.1103/PhysRevD.104.022005. arXiv:2103.08520 [gr-qc]
Abbott R et al (2021i) Searches for continuous gravitational waves from young supernova remnants in the early third observing run of Advanced LIGO and Virgo. Astrophys J 921(1):80. https://doi.org/10.3847/1538-4357/ac17ea. arXiv:2105.11641 [gr-qc]
Abbott R et al (2022a) All-sky, all-frequency directional search for persistent gravitational waves from Advanced LIGO's and Advanced Virgo's first three observing runs. Phys Rev D 105:122001. https://doi.org/10.1103/PhysRevD.105.122001. arXiv:2110.09834 [gr-qc]
Abbott R et al (2022b) All-sky search for continuous gravitational waves from isolated neutron stars using Advanced LIGO and Advanced Virgo O3 data. Phys Rev D 106:102008. https://doi.org/10.1103/PhysRevD.106.102008. arXiv:2201.00697 [gr-qc]
Abbott R et al (2022c) All-sky search for gravitational wave emission from scalar boson clouds around spinning black holes in LIGO O3 data. Phys Rev D 105:102001. https://doi.org/10.1103/PhysRevD.105.102001. arXiv:2111.15507 [astro-ph.HE]
Abbott R et al (2022d) Constraints on dark photon dark matter using data from LIGO's and Virgo's third observing run. Phys Rev D 105:063030. https://doi.org/10.1103/PhysRevD.105.063030. arXiv:2105.13085 [astro-ph.CO]
Abbott R et al (2022e) Model-based cross-correlation search for gravitational waves from the low-mass X-ray binary Scorpius X-1 in LIGO O3 data. Astrophys J Lett 941(2):L30. https://doi.org/10.3847/2041-8213/aca1b0
Abbott R et al (2022f) Narrowband searches for continuous and long-duration transient gravitational waves from known pulsars in the LIGO-Virgo third observing run. Astrophys J 932(2):133. https://doi.org/10.3847/1538-4357/ac6ad0. arXiv:2112.10990 [gr-qc]
Abbott R et al (2022g) Search for continuous gravitational waves from 20 accreting millisecond x-ray pulsars in O3 LIGO data. Phys Rev D 105:022002. https://doi.org/10.1103/PhysRevD.105.022002
Abbott R et al (2022h) Search for gravitational waves from Scorpius X-1 with a hidden Markov model in O3 LIGO data. Phys Rev D 106(6):062002. https://doi.org/10.1103/PhysRevD.106.062002. arXiv:2201.10104 [gr-qc]
Abbott R et al (2022i) Search of the early O3 LIGO data for continuous gravitational waves from the Cassiopeia A and Vela Jr. Supernova Remnants. Phys Rev D 105:082005. https://doi.org/10.1103/PhysRevD.105.082005. arXiv:2111.15116 [gr-qc]

Abbott R et al (2022j) Searches for gravitational waves from known pulsars at two harmonics in the second and third LIGO-Virgo observing runs. Astrophys J 935(1):1. https://doi.org/10.3847/1538-4357/ac6acf. arXiv:2111.13106 [astro-ph.HE]
Acernese F et al (2014) Advanced Virgo: a second-generation interferometric gravitational wave detector. Class Quantum Grav 32(2):024001. https://doi.org/10.1088/0264-9381/32/2/024001
Ackermann M et al (2017) The Fermi galactic center GeV excess and implications for dark matter. Astrophys J 840(1):43. https://doi.org/10.3847/1538-4357/aa6cab. arXiv:1704.03910 [astro-ph.HE]
Aharonian F et al (2005) A new population of very high energy gamma-ray sources in the milky way. Science 307(5717):1938–1942. https://doi.org/10.1126/science.1108643
Aharonian F et al (2008) HESS very-high-energy gamma-ray sources without identified counterparts. Astron Astrophys 477(1):353–363. https://doi.org/10.1051/0004-6361:20078516. arXiv:0712.1173 [astro-ph]
Alarie A, Bilodeau A, Drissen L (2014) A hyperspectral view of Cassiopeia A. Mon Not R Astron Soc 441:2996–3008. https://doi.org/10.1093/mnras/stu774
Alford MG, Schwenzer K (2014) Gravitational wave emission and spindown of young pulsars. Astrophys J 781:26. https://doi.org/10.1088/0004-637X/781/1/26. arXiv:1210.6091 [gr-qc]
Alford MG, Schwenzer K (2015) Gravitational wave emission from oscillating millisecond pulsars. Mon Not R Astron Soc 446(4):3631–3641. https://doi.org/10.1093/mnras/stu2361. arXiv:1403.7500 [gr-qc]
Allen B (2019) Spherical ansatz for parameter-space metrics. Phys Rev D 100(12):124004. https://doi.org/10.1103/PhysRevD.100.124004. arXiv:1906.01352 [gr-qc]
Allen B (2021) Optimal template banks. Phys Rev D 104(4):042005. https://doi.org/10.1103/PhysRevD.104.042005. arXiv:2102.11254 [astro-ph.IM]
Allen B, Hua W, Ottewill A (1999) Automatic cross-talk removal from multi-channel data. arXiv:gr-qc/9909083 [gr-qc]
Allen B, Papa MA, Schutz BF (2002) Optimal strategies for sinusoidal signal detection. Phys Rev D 66:102003. https://doi.org/10.1103/PhysRevD.66.102003
Allen GE, Chow K, DeLaney T, Filipovic MD, Houck JC, Pannuti TG, Stage MD (2015) On the expansion rate, age, and distance of the Supernova Remnant G266.2–1.2 (Vela Jr.). Astrophys J 798(2):82. https://doi.org/10.1088/0004-637X/798/2/82
Alpar MA, Cheng AF, Ruderman MA, Shaham J (1982) A new class of radio pulsars. Nature 300 (5894):728–730. https://doi.org/10.1038/300728a0
Althouse B, Jones L, Lazzarini A (1998) Determination of global and local coordinate axes for the LIGO sites. Tech. Rep. LIGO Report T980044, LIGO. https://dcc.ligo.org/T980044
Anderson DP, Cobb J, Korpela E, Lebofsky M, Werthimer D (2002) SETI@home: an experiment in public-resource computing. Commun ACM 45(11):56–61. https://doi.org/10.1145/581571.581573
Andersson N (1998) A new class of unstable modes of rotating relativistic stars. Astrophys J 502:708–713. https://doi.org/10.1086/305919. arXiv:gr-qc/9706075
Andersson N (2019) Gravitational-wave astronomy: exploring the dark side of the universe. Oxford Univ Press. https://doi.org/10.1093/oso/9780198568032.001.0001
Andersson N, Jones DI, Ho WCG (2014) Implications of an r-mode in XTE J1751–305: mass, radius and spin evolution. Mon Not R Astron Soc 442(2):1786–1793. https://doi.org/10.1093/mnras/stu870. arXiv:1403.0860 [astro-ph.SR]
Andersson N, Antonopoulou D, Espinoza CM, Haskell B, Ho WCG (2018) The enigmatic spin evolution of PSR J0537–6910: r-modes, gravitational waves, and the case for continued timing. Astrophys J 864(2):137. https://doi.org/10.3847/1538-4357/aad6eb. arXiv:1711.05550 [astro-ph.HE]
Antoniadis J, Freire PCC, Wex N, Tauris TM, Lynch RS, van Kerkwijk MH, Kramer M, Bassa C, Dhillon VS, Driebe T, Hessels JWT, Kaspi VM, Kondratiev VI, Langer N, Marsh TR, McLaughlin MA, Pennucci TT, Ransom SM, Stairs IH, van Leeuwen J, Verbiest JPW, Whelan DG (2013) A massive pulsar in a compact relativistic binary. Science 340(6131):448. https://doi.org/10.1126/science.1233232. arXiv:1304.6875 [astro-ph.HE]
Antonopoulou D, Espinoza CM, Kuiper L, Andersson N (2018) Pulsar spin-down: the glitch-dominated rotation of PSR J0537−6910. Mon Not R Astron Soc 473(2):1644–1655. https://doi.org/10.1093/mnras/stx2429. arXiv:1708.09459 [astro-ph.HE]
Antonucci F, Astone P, D'Antonio S, Frasca S, Palomba C (2008) Detection of periodic gravitational wave sources by Hough transform in the f versus $\dot{f}$ plane. Class Quantum Grav 25(18):184015. https://doi.org/10.1088/0264-9381/25/18/184015

Archibald AM, Stairs IH, Ransom SM, Kaspi VM, Kondratiev VI, Lorimer DR, McLaughlin MA, Boyles J, Hessels JWT, Lynch R, van Leeuwen J, Roberts MSE, Jenet F, Champion DJ, Rosen R, Barlow BN, Dunlap BH, Remillard RA (2009) A radio pulsar/X-ray binary link. Science 324(5933):1411–1414. https://doi.org/10.1126/science.1172740

Archibald RF, Gotthelf EV, Ferdman RD, Kaspi VM, Guillot S, Harrison FA, Keane EF, Pivovaroff MJ, Stern D, Tendulkar SP et al (2016) A high braking index for a pulsar. Astrophys J 819(1):L16. https://doi.org/10.3847/2041-8205/819/1/l16

Arras P, Flanagan EE, Morsink SM, Schenk A, Teukolsky SA, Wasserman I (2003) Saturation of the R mode instability. Astrophys J 591:1129–1151. https://doi.org/10.1086/374657. arXiv:astro-ph/0202345

Arvanitaki A, Dubovsky S (2011) Exploring the string axiverse with precision black hole physics. Phys Rev D 83:044026. https://doi.org/10.1103/PhysRevD.83.044026. arXiv:1004.3558 [hep-th]

Arvanitaki A, Dimopoulos S, Dubovsky S, Kaloper N, March-Russell J (2010) String axiverse. Phys Rev D 81:123530. https://doi.org/10.1103/PhysRevD.81.123530

Arvanitaki A, Baryakhtar M, Huang X (2015) Discovering the QCD axion with black holes and gravitational waves. Phys Rev D 91(8):084011. https://doi.org/10.1103/PhysRevD.91.084011. arXiv:1411.2263 [hep-ph]

Arvanitaki A, Baryakhtar M, Dimopoulos S, Dubovsky S, Lasenby R (2017) Black hole mergers and the QCD axion at advanced LIGO. Phys Rev D 95:043001. https://doi.org/10.1103/PhysRevD.95.043001

Arzoumanian Z, Brazier A, Burke-Spolaor S, Chamberlin S, Chatterjee S, Christy B, Cordes JM, Cornish NJ, Crawford F, Thankful Cromartie H, Crowter K, DeCesar ME, Demorest PB, Dolch T, Ellis JA, Ferdman RD, Ferrara EC, Fonseca E, Garver-Daniels N, Gentile PA, Halmrast D, Huerta EA, Jenet FA, Jessup C, Jones G, Jones ML, Kaplan DL, Lam MT, Lazio TJW, Levin L, Lommen A, Lorimer DR, Luo J, Lynch RS, Madison D, Matthews AM, McLaughlin MA, McWilliams ST, Mingarelli C, Ng C, Nice DJ, Pennucci TT, Ransom SM, Ray PS, Siemens X, Simon J, Spiewak R, Stairs IH, Stinebring DR, Stovall K, Swiggum JK, Taylor SR, Vallisneri M, van Haasteren R, Vigeland SJ, Zhu W, NANOGrav Collaboration (2018) The NANOGrav 11-year data set: high-precision timing of 45 millisecond pulsars. Astrophys J Suppl 235(2):37. https://doi.org/10.3847/1538-4365/aab5b0. arXiv:1801.01837 [astro-ph.HE]

Ashok A, Beheshtipour B, Papa MA, Freire PCC, Steltner B, Machenschalk B, Behnke O, Allen B, Prix R (2021) New searches for continuous gravitational waves from seven fast pulsars. Astrophys J 923(1):85. https://doi.org/10.3847/1538-4357/ac2582

Ashton G, Prix R (2018) Hierarchical multistage MCMC follow-up of continuous gravitational wave candidates. Phys Rev D 97(10):103020. https://doi.org/10.1103/PhysRevD.97.103020. arXiv:1802.05450 [astro-ph.IM]

Ashton G, Prix R, Jones DI (2017) Statistical characterization of pulsar glitches and their potential impact on searches for continuous gravitational waves. Phys Rev D 96(6):063004. https://doi.org/10.1103/PhysRevD.96.063004. arXiv:1704.00742 [gr-qc]

Ashton G, Lasky PD, Graber V, Palfreyman J (2019) Rotational evolution of the Vela pulsar during the 2016 glitch. Nat Astron 3(12):1143–1148. https://doi.org/10.1038/s41550-019-0844-6

Astone P et al (2002a) Search for periodic gravitational wave sources with the explorer detector. Phys Rev D 65:022001. https://doi.org/10.1103/PhysRevD.65.022001. arXiv:gr-qc/0011072

Astone P, Borkowski KM, Jaranowski P, Królak A (2002b) Data analysis of gravitational-wave signals from spinning neutron stars. IV. An all-sky search. Phys Rev D 65:042003. https://doi.org/10.1103/PhysRevD.65.042003

Astone P, Frasca S, Palomba C (2005) The short FFT database and the peak map for the hierarchical search of periodic sources. Class Quantum Grav 22(18):S1197–S1210. https://doi.org/10.1088/0264-9381/22/18/s34

Astone P, Bassan M, Bonifazi P, Borkowski KM, Budzyński RJ, Chincarini A, Coccia E, D'Antonio S, Emilio MDP, Fafone V et al (2008) All-sky search of NAUTILUS data. Class Quantum Grav 25(18):184012. https://doi.org/10.1088/0264-9381/25/18/184012

Astone P, Borkowski KM, Jaranowski P, Pietka M, Królak A (2010a) Data analysis of gravitational-wave signals from spinning neutron stars. V. A narrow-band all-sky search. Phys Rev D 82:022005. https://doi.org/10.1103/PhysRevD.82.022005

Astone P, D'Antonio S, Frasca S, Palomba C (2010b) A method for detection of known sources of continuous gravitational wave signals in non-stationary data. Class Quant Grav 27:194016. https://doi.org/10.1088/0264-9381/27/19/194016

Astone P, Colla A, D'Antonio S, Frasca S, Palomba C (2012) Coherent search of continuous gravitational wave signals: extension of the 5-vectors method to a network of detectors. J Phys: Conf Ser 363:012038. https://doi.org/10.1088/1742-6596/363/1/012038. arXiv:1203.6733 [astro-ph.IM]

Astone P, Colla A, D'Antonio S, Frasca S, Palomba C (2014a) Method for all-sky searches of continuous gravitational wave signals using the frequency-Hough transform. Phys Rev D 90:042002. https://doi.org/10.1103/PhysRevD.90.042002

Astone P, Colla A, D'Antonio S, Frasca S, Palomba C, Serafinelli R (2014b) Method for narrow-band search of continuous gravitational wave signals. Phys Rev D 89:062008. https://doi.org/10.1103/PhysRevD.89.062008

Baade W, Zwicky F (1934) Cosmic rays from Super-Novae. Proc Natl Acad Sci 20(5):259–263. https://doi.org/10.1073/pnas.20.5.259

Baiko DA, Chugunov AI (2018) Breaking properties of neutron star crust. Mon Not R Astron Soc 480 (4):5511–5516. https://doi.org/10.1093/mnras/sty2259. arXiv:1808.06415 [astro-ph.HE]

Baiotti L, Rezzolla L (2017) Binary neutron star mergers: a review of Einstein's richest laboratory. Rep Prog Phys 80(9):096901. https://doi.org/10.1088/1361-6633/aa67bb

Balasubramanian R, Sathyaprakash BS, Dhurandhar SV (1996) Gravitational waves from coalescing binaries: Detection strategies and Monte Carlo estimation of parameters. Phys Rev D 53:3033–3055. https://doi.org/10.1103/PhysRevD.53.3033, [Erratum: Phys. Rev. D 54, 1860 (1996)]. arXiv:gr-qc/9508011

Ballmer SW (2006) A radiometer for stochastic gravitational waves. Class Quantum Grav 23(8):S179–S185. https://doi.org/10.1088/0264-9381/23/8/s23

Banagiri S, Sun L, Coughlin MW, Melatos A (2019) Search strategies for long gravitational-wave transients: hidden Markov model tracking and seedless clustering. Phys Rev D 100:024034. https://doi.org/10.1103/PhysRevD.100.024034

Bassa CG, Pleunis Z, Hessels JWT, Ferrara EC, Breton RP, Gusinskaia NV, Kondratiev VI, Sanidas S, Nieder L, Clark CJ, Li T, van Amesfoort AS, Burnett TH, Camilo F, Michelson PF, Ransom SM, Ray PS, Wood K (2017) LOFAR discovery of the fastest-spinning millisecond pulsar in the galactic field. Astrophys J Lett 846(2):L20. https://doi.org/10.3847/2041-8213/aa8400. arXiv:1709.01453 [astro-ph.HE]

Baumann D, Chia HS, Stout J, ter Haar L (2019) The spectra of gravitational atoms. JCAP 12:006. https://doi.org/10.1088/1475-7516/2019/12/006. arXiv:1908.10370 [gr-qc]

Bayley J, Messenger C, Woan G (2020) Robust machine learning algorithm to search for continuous gravitational waves. Phys Rev D. https://doi.org/10.1103/physrevd.102.083024

Baym G, Pethick C, Pines D, Ruderman M (1969) Spin up in neutron stars: the future of the vela pulsar. Nature 224(5222):872–874. https://doi.org/10.1038/224872a0

Becker W (ed) (2009) Neutron stars and pulsars. Astrophysics and space science library, vol 357. Springer, Berlin, Heidelberg. https://doi.org/10.1007/978-3-540-76965-1

Becker W, Hui CY, Aschenbach B, Iyudin A (2006) Exploring the central compact object in the RX J0852.0-4622 Supernova Remnant with XMM-Newton. astro-ph/0607081. arXiv:astro-ph/0607081 [astro-ph]

Beheshtipour B, Papa MA (2020) Deep learning for clustering of continuous gravitational wave candidates. Phys Rev D. https://doi.org/10.1103/physrevd.101.064009

Beheshtipour B, Papa MA (2021) Deep learning for clustering of continuous gravitational wave candidates. II. Identification of low-SNR candidates. Phys Rev D 103:064027. https://doi.org/10.1103/PhysRevD.103.064027

Behnke B, Papa MA, Prix R (2015) Postprocessing methods used in the search for continuous gravitational-wave signals from the Galactic Center. Phys Rev D 91:064007. https://doi.org/10.1103/PhysRevD.91.064007

Bender P et al (1996) MPQ Reports, MPQ-208. Technical report, Max-Planck-Institut für Quantenoptik, Garching. https://www.elisascience.org

Beniwal D, Clearwater P, Dunn L, Strang L, Rowell G, Melatos A, Ottaway D (2022) Search for continuous gravitational waves from HESS J1427-608 with a hidden Markov model. Phys Rev D 106 (10):103018. https://doi.org/10.1103/PhysRevD.106.103018. arXiv:2210.09592 [astro-ph.HE]

Bernal CG, Lee WH, Page D (2010) Hypercritical accretion onto a magnetized neutron star surface: a numerical approach. Rev Mex Astron Astrof 46:309–322

Bero JJ, Whelan JT (2019) An analytic approximation to the Bayesian detection statistic for continuous gravitational waves. Class Quant Grav 36(1):015013. https://doi.org/10.1088/1361-6382/aaed6a, [Erratum: Class. Quant. Grav. 36, 049601 (2019)]. arXiv:1808.05453 [gr-qc]

Bertone G (2010) Particle dark matter: observations. Camb Univ Press Models Sear. https://doi.org/10.1017/CBO9780511770739
Beskin VS, Istomin AY (2022) Pulsar death line revisited-II 'The death valley'. Mon Not R Astron Soc 516(4):5084–5091. https://doi.org/10.1093/mnras/stac2423. arXiv:2207.04723 [astro-ph.HE]
Beskin VS, Litvinov PE (2022) Pulsar death line revisited—I. Almost vacuum gap. Mon Not R Astron Soc 510(2):2572–2582. https://doi.org/10.1093/mnras/stab3575. arXiv:2201.02875 [astro-ph.HE]
Bhattacharyya S (2020) The permanent ellipticity of the neutron star in PSR J1023+0038. Mon Not R Astron Soc 498(1):728–736. https://doi.org/10.1093/mnras/staa2304. arXiv:2008.01716 [astro-ph.HE]
Bhattacharyya S (2021) Spin evolution of neutron stars in two modes: implication for millisecond pulsars. Mon Not Roy Astronom Soc Lett 502(1):L45–L49. https://doi.org/10.1093/mnrasl/slab001
Bildsten L (1998) Gravitational radiation and rotation of accreting neutron stars. Astrophys J 501(1):L89–L93. https://doi.org/10.1086/311440
Biwer C, Barker D, Batch JC, Betzwieser J, Fisher RP, Goetz E, Kandhasamy S, Karki S, Kissel JS, Lundgren AP et al (2017) Validating gravitational-wave detections: the Advanced LIGO hardware injection system. Phys Rev D. https://doi.org/10.1103/physrevd.95.062002
Blaes O, Madau P (1993) Can we observe accreting, isolated neutron stars? Astrophys J 403:690. https://doi.org/10.1086/172240
Blair DG et al (1991) The detection of gravitational waves. Cambridge University Press, Cambridge
Blair DG et al (2012) Advanced gravitational wave detectors. Cambridge University Press, Cambridge
Bogdanov S, Guillot S, Ray PS, Wolff MT, Chakrabarty D, Ho WCG, Kerr M, Lamb FK, Lommen A, Ludlam RM, Milburn R, Montano S, Miller MC, Bauböck M, Özel F, Psaltis D, Remillard RA, Riley TE, Steiner JF, Strohmayer TE, Watts AL, Wood KS, Zeldes J, Enoto T, Okajima T, Kellogg JW, Baker C, Markwardt CD, Arzoumanian Z, Gendreau KC (2019a) Constraining the neutron star mass–radius relation and dense matter equation of state with NICER. I. The millisecond pulsar X-Ray Data Set. Astrophys J Lett 887(1):L25. https://doi.org/10.3847/2041-8213/ab53eb. arXiv:1912.05706 [astro-ph.HE]
Bogdanov S, Lamb FK, Mahmoodifar S, Miller MC, Morsink SM, Riley TE, Strohmayer TE, Tung AK, Watts AL, Dittmann AJ, Chakrabarty D, Guillot S, Arzoumanian Z, Gendreau KC (2019b) Constraining the neutron star mass–radius relation and dense matter equation of state with NICER. II. Emission from hot spots on a rapidly rotating neutron star. Astrophys J Lett 887(1):L26. https://doi.org/10.3847/2041-8213/ab5968. arXiv:1912.05707 [astro-ph.HE]
Bogdanov S, et al. (2021) Constraining the neutron star mass-radius relation and dense matter equation of state with NICER. III. Model description and verification of parameter estimation codes. Astrophys J Lett 914(1):L15. https://doi.org/10.3847/2041-8213/abfb79. arXiv:2104.06928 [astro-ph.HE]
Bonazzola S, Gourgoulhon E (1996) Gravitational waves from pulsars: emission by the magnetic field induced distortion. Astron Astrophys 312:675 arXiv:astro-ph/9602107
Bond HE, White RL, Becker RH, O'Brien MS (2002) FIRST J102347.6+003841: The first radio-selected cataclysmic variable. Publ Astronom Soc Pacific 114(802):1359–1363. https://doi.org/10.1086/344381
Bondi H, Hoyle F (1944) On the mechanism of accretion by stars. Mon Not R Astron Soc 104:273
Boztepe T, Göğüş E, Güver T, Schwenzer K (2020) Strengthening the bounds on the r-mode amplitude with X-ray observations of millisecond pulsars. Mon Not R Astron Soc 498(2):2734–2749. https://doi.org/10.1093/mnras/staa2503
Brady PR, Creighton T (2000) Searching for periodic sources with LIGO. II. Hierarchical searches. Phys Rev D 61:082001. https://doi.org/10.1103/PhysRevD.61.082001
Brady PR, Creighton T, Cutler C, Schutz BF (1998) Searching for periodic sources with LIGO. Phys Rev D 57:2101–2116. https://doi.org/10.1103/PhysRevD.57.2101. arXiv:gr-qc/9702050
Brito R, Ghosh S, Barausse E, Berti E, Cardoso V, Dvorkin I, Klein A, Pani P (2017a) Gravitational wave searches for ultralight bosons with LIGO and LISA. Phys Rev D 96:064050. https://doi.org/10.1103/PhysRevD.96.064050
Brito R, Ghosh S, Barausse E, Berti E, Cardoso V, Dvorkin I, Klein A, Pani P (2017b) Stochastic and resolvable gravitational waves from ultralight bosons. Phys Rev Lett 119(13):131101. https://doi.org/10.1103/PhysRevLett.119.131101. arXiv:1706.05097 [gr-qc]
Brito R, Grillo S, Pani P (2020) Black hole superradiant instability from ultralight spin-2 fields. Phys Rev Lett 124:211101. https://doi.org/10.1103/PhysRevLett.124.211101
Brogan CL, Gaensler BM, Gelfand JD, Lazendic JS, Lazio TJW, Kassim NE, McClure-Griffiths NM (2005) Discovery of a radio Supernova Remnant and nonthermal X-rays coincident with the TeV

source HESS J1813-178. Astrophys J Lett 629(2):L105–L108. https://doi.org/10.1086/491471. arXiv:astro-ph/0505145 [astro-ph]
Buballa M et al (2014) EMMI rapid reaction task force meeting on quark matter in compact stars. J Phys G 41(12):123001. https://doi.org/10.1088/0954-3899/41/12/123001. arXiv:1402.6911 [astro-ph.HE]
Buschauer R, Benford G (1976) General theory of coherent curvature radiation. Mon Not R Astron Soc 177(1):109–136. https://doi.org/10.1093/mnras/177.1.109
Caleb M, Heywood I, Rajwade K, Malenta M, Willem Stappers B, Barr E, Chen W, Morello V, Sanidas S, van den Eijnden J, Kramer M, Buckley D, Brink J, Motta SE, Woudt P, Weltevrede P, Jankowski F, Surnis M, Buchner S, Bezuidenhout MC, Driessen LN, Fender R (2022) Discovery of a radio-emitting neutron star with an ultra-long spin period of 76 s. Nat Astron. https://doi.org/10.1038/s41550-022-01688-x
Camilo F, Ransom SM, Halpern JP, Roshi DA (2021) Radio detection of PSR J1813-1749 in HESS J1813-178: the most scattered pulsar known. Astrophys J Lett 917(2):67. https://doi.org/10.3847/1538-4357/ac0720. arXiv:2106.00386 [astro-ph.HE]
Caplan ME, Horowitz CJ (2017) Colloquium: astromaterial science and nuclear pasta. Rev Mod Phys 89:041002. https://doi.org/10.1103/RevModPhys.89.041002
Cardoso V, Dias ÓJC, Hartnett GS, Middleton M, Pani P (2018) Constraining the mass of dark photons and axion-like particles through black-hole superradiance. J Cosmol Astropart Phys 03:043–043. https://doi.org/10.1088/1475-7516/2018/03/043
Cardoso V, Duque F, Ikeda T (2020) Tidal effects and disruption in superradiant clouds: a numerical investigation. Phys Rev D 101(6):064054. https://doi.org/10.1103/PhysRevD.101.064054. arXiv:2001.01729 [gr-qc]
Caride S, Inta R, Owen BJ, Rajbhandari B (2019) How to search for gravitational waves from *r*-modes of known pulsars. Phys Rev D 100(6):064013. https://doi.org/10.1103/PhysRevD.100.064013. arXiv:1907.04946 [gr-qc]
Cerda-Duran P, Elias-Rosa N (2018) Neutron stars formation and core collapse supernovae. In: Rezzolla L, Pizzochero P, Jones DI, Rea N, Vidaña I (eds) The physics and astrophysics of neutron stars. Springer, Cham, pp 1–56. https://doi.org/10.1007/978-3-319-97616-7_1
Chakrabarty D, Morgan EH, Muno MP, Galloway DK, Wijnands R, van der Klis M, Markwardt CB (2003) Nuclear-powered millisecond pulsars and the maximum spin frequency of neutron stars. Nature 424:42–44. https://doi.org/10.1038/nature01732. arXiv:astro-ph/0307029
Chamel N, Haensel P (2008) Physics of neutron star crusts. Living Rev Rel 11:10. https://doi.org/10.12942/lrr-2008-10
Chandrasekhar S (1970) Solutions of two problems in the theory of gravitational radiation. Phys Rev Lett 24:611–615. https://doi.org/10.1103/PhysRevLett.24.611
Chen WC (2020) Constraining the ellipticity of millisecond pulsars with observed spin-down rates. Phys Rev D. https://doi.org/10.1103/physrevd.102.043020
Chen K, Ruderman M (1993) Pulsar death lines and death valley. Astrophys J 402:264. https://doi.org/10.1086/172129
Chevalier RA (1989) Neutron star accretion in a supernova. Astrophys J 346:847. https://doi.org/10.1086/168066
Christodoulou D (1970) Reversible and irreversible transformations in black-hole physics. Phys Rev Lett 25:1596–1597. https://doi.org/10.1103/PhysRevLett.25.1596
Chung C, Melatos A, Krishnan B, Whelan JT (2011) Designing a cross-correlation search for continuous-wave gravitational radiation from a neutron star in the supernova remnant SNR 1987A. Mon Not R Astron Soc 414:2650. https://doi.org/10.1111/j.1365-2966.2011.18585.x. arXiv:1102.4654 [gr-qc]
Cieślar M, Bulik T, Curylo M, Sieniawska M, Singh N, Bejger M (2021) Detectability of continuous gravitational waves from isolated neutron stars in the Milky Way—the population synthesis approach. A &A 649:A92. https://doi.org/10.1051/0004-6361/202039503
Clark CJ et al (2016) The braking index of a radio-quiet gamma-ray pulsar. Astrophys J Lett 832(1):L15. https://doi.org/10.3847/2041-8205/832/1/L15. arXiv:1611.01292 [astro-ph.HE]
Clark CJ et al (2018) Einstein@Home discovers a radio-quiet gamma-ray millisecond pulsar. Sci Adv. https://doi.org/10.1126/sciadv.aao7228
Contopoulos I, Kazanas D, Fendt C (1999) The axisymmetric pulsar magnetosphere. Astrophys J 511:351. https://doi.org/10.1086/306652. arXiv:astro-ph/9903049
Cook GB, Shapiro SL, Teukolsky SA (1994) Rapidly rotating neutron stars in general relativity: realistic equations of state. Astrophys J 424:823. https://doi.org/10.1086/173934

Covas PB (2020) Effects of proper motion of neutron stars on continuous gravitational-wave searches. Mon Not R Astron Soc 500(4):5167–5176. https://doi.org/10.1093/mnras/staa3624
Covas PB, Prix R (2022) Improved all-sky search method for continuous gravitational waves from unknown neutron stars in binary systems. Phys Rev D 106(8):084035. https://doi.org/10.1103/PhysRevD.106.084035. arXiv:2208.01543 [gr-qc]
Covas PB, Prix R (2022) Improved short-segment detection statistic for continuous gravitational waves. Phys Rev D 105:124007. https://doi.org/10.1103/PhysRevD.105.124007. arXiv:2203.08723 [gr-qc]
Covas PB, Sintes AM (2019) New method to search for continuous gravitational waves from unknown neutron stars in binary systems. Phys Rev D 99(12):124019. https://doi.org/10.1103/PhysRevD.99.124019. arXiv:1904.04873 [astro-ph.IM]
Covas PB, Sintes AM (2020) First all-sky search for continuous gravitational-wave signals from unknown neutron stars in binary systems using advanced LIGO data. Phys Rev Lett 124(19):191102. https://doi.org/10.1103/PhysRevLett.124.191102. arXiv:2001.08411 [gr-qc]
Covas PB, Effler A, Goetz E, Meyers PM, Neunzert A, Oliver M, Pearlstone BL, Roma VJ, Schofield RMS, Adya VB et al (2018) Identification and mitigation of narrow spectral artifacts that degrade searches for persistent gravitational waves in the first two observing runs of advanced LIGO. Phys Rev D. https://doi.org/10.1103/physrevd.97.082002
Covas PB, Papa MA, Prix R, Owen BJ (2022) Constraints on r-modes and mountains on millisecond neutron stars in binary systems. Astrophys J Lett 929(2):L19. https://doi.org/10.3847/2041-8213/ac62d7. arXiv:2203.01773 [gr-qc]
Creighton JDE, Anderson WG (2011) Gravitational-wave physics and astronomy. Wiley-VCH, Weinheim
Cromartie HT, Fonseca E, Ransom SM, Demorest PB, Arzoumanian Z, Blumer H, Brook PR, DeCesar ME, Dolch T, Ellis JA, Ferdman RD, Ferrara EC, Garver-Daniels N, Gentile PA, Jones ML, Lam MT, Lorimer DR, Lynch RS, McLaughlin MA, Ng C, Nice DJ, Pennucci TT, Spiewak R, Stairs IH, Stovall K, Swiggum JK, Zhu WW (2020) Relativistic Shapiro delay measurements of an extremely massive millisecond pulsar. Nat Astron 4:72–76. https://doi.org/10.1038/s41550-019-0880-2. arXiv:1904.06759 [astro-ph.HE]
Cruces M, Reisenegger A, Tauris TM (2019) On the weak magnetic field of millisecond pulsars: Does it decay before accretion? Mon Not R Astron Soc 490(2):2013–2022. https://doi.org/10.1093/mnras/stz2701. arXiv:1906.06076 [astro-ph.SR]
Cutler C (2002) Gravitational waves from neutron stars with large toroidal B fields. Phys Rev D. https://doi.org/10.1103/physrevd.66.084025
Cutler C, Schutz BF (2005) Generalized F-statistic: multiple detectors and multiple gravitational wave pulsars. Phys Rev D. https://doi.org/10.1103/physrevd.72.063006
Cutler C, Gholami I, Krishnan B (2005) Improved stack-slide searches for gravitational-wave pulsars. Phys Rev D 72(4):042004. https://doi.org/10.1103/PhysRevD.72.042004
Dall'Osso S, Stella L (2022) Millisecond Magnetars. In: Bhattacharyya S, Papitto A, Bhattacharya D (eds) Millisecond pulsars. Astrophysics and Space Science Library, vol 465. Springer, Cham, pp 245–280. https://doi.org/10.1007/978-3-030-85198-9_8. arXiv:2103.10878 [astro-ph.HE]
D'Antonio S, Palomba C, Astone P, Frasca S, Intini G, La Rosa I, Leaci P, Mastrogiovanni S, Miller A, Muciaccia F et al (2018) Semicoherent analysis method to search for continuous gravitational waves emitted by ultralight boson clouds around spinning black holes. Phys Rev D. https://doi.org/10.1103/physrevd.98.103017
Davis D, Massinger T, Lundgren A, Driggers JC, Urban AL, Nuttall L (2019) Improving the sensitivity of advanced LIGO using noise subtraction. Class Quantum Grav 36(5):055011. https://doi.org/10.1088/1361-6382/ab01c5
Davis D et al (2021) LIGO detector characterization in the second and third observing runs. Class Quantum Grav 38(13):135014. https://doi.org/10.1088/1361-6382/abfd85. arXiv:2101.11673 [astro-ph.IM]
Daw EJ, Hollows IJ, Jones EL, Kennedy R, Mistry T, Edo TB, Fays M, Sun L (2022) IWAVE—an adaptive filter approach to phase lock and the dynamic characterization of pseudo-harmonic waves. Rev Sci Instrum 93(4):044502. https://doi.org/10.1063/5.0070394
de Araujo JCN, Coelho JG, Costa CA (2016) Gravitational waves from pulsars and their braking indices: the role of a time dependent magnetic ellipticity. Astrophys J 831(1):35. https://doi.org/10.3847/0004-637x/831/1/35
de Araujo JCN, Coelho JG, Costa CA (2017) Gravitational waves from pulsars in the context of magnetic ellipticity. Eur Phys J C. https://doi.org/10.1140/epjc/s10052-017-4925-3

De Lillo F, Suresh J, Miller AL (2022) Stochastic gravitational-wave background searches and constraints on neutron-star ellipticity. Mon Not R Astron Soc 513(1):1105–1114. https://doi.org/10.1093/mnras/stac984. arXiv:2203.03536 [gr-qc]
De Luca A (2008) Central Compact objects in supernova remnants. In: Bassa C, Wang Z, Cumming A, Kaspi VM (eds) 40 Years of pulsars: millisecond pulsars, magnetars and more. AIP conference series, vol 983. pp 311–319. https://doi.org/10.1063/1.2900173. arXiv:0712.2209 [astro-ph]
Degenaar N, Suleimanov VF (2018) Testing the equation of state with electromagnetic observations. In: Rezzolla L, Pizzochero P, Jones DI, Rea N, Vidaña I (eds) The physics and astrophysics of neutron stars. Astrophysics and Space Science Library, vol 457. Springer, p 185. https://doi.org/10.1007/978-3-319-97616-7_5
DeMarchi L, Sanders JR, Levesque EM (2021) Prospects for multimessenger observations of Thorne-Zytkow objects. Astrophys J 911(2):101. https://doi.org/10.3847/1538-4357/abebe1
Demorest PB, Pennucci T, Ransom SM, Roberts MSE, Hessels JWT (2010) A two-solar-mass neutron star measured using Shapiro delay. Nature 467(7319):1081–1083. https://doi.org/10.1038/nature09466. arXiv:1010.5788 [astro-ph.HE]
Deneva JS, Cordes JM, Lazio TJW (2009) Discovery of three pulsars from a galactic center pulsar population. Astrophys J 702(2):L177–L181. https://doi.org/10.1088/0004-637x/702/2/l177
Dergachev V (2005) Description of PowerFlux algorithms and implementation, LIGO Report LIGO-T050186
Dergachev V (2010a) Description of PowerFlux 2 algorithms and implementation. Technical Report. LIGO Report T1000272, LIGO. https://dcc.ligo.org/T1000272
Dergachev V (2010b) On blind searches for noise dominated signals: a loosely coherent approach. Class Quantum Grav 27(20):205017. https://doi.org/10.1088/0264-9381/27/20/205017
Dergachev V (2012) Loosely coherent searches for sets of well-modeled signals. Phys Rev D 85:062003. https://doi.org/10.1103/PhysRevD.85.062003
Dergachev V (2013) Novel universal statistic for computing upper limits in an ill-behaved background. Phys Rev D 87(6):062001. https://doi.org/10.1103/PhysRevD.87.062001. arXiv:1208.2007 [gr-qc]
Dergachev V (2018) Loosely coherent searches for medium scale coherence lengths. arXiv:1807.02351 [astro-ph.IM]
Dergachev V, Papa MA (2019) Sensitivity improvements in the search for periodic gravitational waves using O1 LIGO data. Phys Rev Lett 123:101101. https://doi.org/10.1103/PhysRevLett.123.101101
Dergachev V, Papa MA (2020a) Results from an extended falcon all-sky survey for continuous gravitational waves. Phys Rev D 101(2):022001. https://doi.org/10.1103/PhysRevD.101.022001. arXiv:1909.09619 [gr-qc]
Dergachev V, Papa MA (2020b) Results from the first all-sky search for continuous gravitational waves from small-ellipticity sources. Phys Rev Lett 125(17):171101. https://doi.org/10.1103/physrevlett.125.171101
Dergachev V, Papa MA (2021a) Results from high-frequency all-sky search for continuous gravitational waves from small-ellipticity sources. Phys Rev D 103:063019. https://doi.org/10.1103/PhysRevD.103.063019
Dergachev V, Papa MA (2021b) Search for continuous gravitational waves from small-ellipticity sources at low frequencies. Phys Rev D 104(4):043003. https://doi.org/10.1103/physrevd.104.043003
Dergachev V, Papa MA (2022) A frequency resolved atlas of the sky in continuous gravitational waves. arXiv:2202.10598 [gr-qc]
Dergachev V, Riles K (2005) PowerFlux polarization analysis, LIGO Report LIGO-T050187
Dergachev V, Papa MA, Steltner B, Eggenstein HB (2019) Loosely coherent search in LIGO O1 data for continuous gravitational waves from Terzan 5 and the Galactic Center. Phys Rev D 99:084048. https://doi.org/10.1103/PhysRevD.99.084048
Dhurandhar S, Krishnan B, Mukhopadhyay H, Whelan JT (2008) Cross-correlation search for periodic gravitational waves. Phys Rev D 77:082001. https://doi.org/10.1103/PhysRevD.77.082001. arXiv:0712.1578 [gr-qc]
Dhurandhar S, Krishnan B, Willis JL (2017) Marginalizing the likelihood function for modeled gravitational wave searches. arXiv:1707.08163 [gr-qc]
Dirichlet GL (1829) Sur la convergence des séries trigonométriques qui servent à représenter une fonction arbitraire entre des limites données. J Math 1829:157–169. https://doi.org/10.1515/crll.1829.4.157
Doneva DD, Kokkotas KD, Pnigouras P (2015) Gravitational wave afterglow in binary neutron star mergers. Phys Rev D 92:104040. https://doi.org/10.1103/PhysRevD.92.104040

Dreissigacker C, Prix R (2020) Deep-learning continuous gravitational waves: multiple detectors and realistic noise. Phys Rev D 102:2. https://doi.org/10.1103/physrevd.102.022005
Dreissigacker C, Prix R, Wette K (2018) Fast and accurate sensitivity estimation for continuous-gravitational-wave searches. Phys Rev D 98(8):084058. https://doi.org/10.1103/PhysRevD.98.084058. arXiv:1808.02459 [gr-qc]
Dreissigacker C, Sharma R, Messenger C, Zhao R, Prix R (2019) Deep-learning continuous gravitational waves. Phys Rev D 100:044009. https://doi.org/10.1103/PhysRevD.100.044009
Driggers JC, Vitale S, Lundgren AP, Evans M, Kawabe K, Dwyer SE, Izumi K, Schofield RMS, Effler A, Sigg D et al (2019) Improving astrophysical parameter estimation via offline noise subtraction for advanced LIGO. Phys Rev D 99:4. https://doi.org/10.1103/physrevd.99.042001
Dunn L, Clearwater P, Melatos A, Wette K (2021) Graphics processing unit implementation of the F-statistic for continuous gravitational wave searches. Class Quantum Grav. https://doi.org/10.1088/1361-6382/ac4616
Dupuis RJ, Woan G (2005) Bayesian estimation of pulsar parameters from gravitational wave data. Phys Rev D 72:102002. https://doi.org/10.1103/PhysRevD.72.102002. arXiv:gr-qc/0508096
Einstein A (1916) Näherungsweise Integration der Feldgleichungen der Gravitation. Sitzungber K Preuss Akad Wiss 1:688
Einstein A (1918) Über Gravitationswellen. Sitzungber K Preuss Akad Wiss 1:154
Ertan U, Alpar MA (2021) The minimum rotation period of millisecond pulsars. Mon Not R Astronom Soc Lett 505(1):L112–L114. https://doi.org/10.1093/mnrasl/slab060
Espinoza CM, Lyne AG, Kramer M, Manchester RN, Kaspi VM (2011) The braking index of PSR J1734–3333 and the magnetar population. Astrophys J 741(1):L13. https://doi.org/10.1088/2041-8205/741/1/l13
Espinoza CM, Lyne AG, Stappers BW (2017) New long-term braking index measurements for glitching pulsars using a glitch-template method. Mon Not R Astron Soc 466(1):147–162. https://doi.org/10.1093/mnras/stw3081. arXiv:1611.08314 [astro-ph.HE]
Essick R, Landry P, Holz DE (2020) Nonparametric inference of neutron star composition, equation of state, and maximum mass with GW170817. Phys Rev D 101(6):063007. https://doi.org/10.1103/PhysRevD.101.063007. arXiv:1910.09740 [astro-ph.HE]
Fattoyev FJ, Horowitz CJ, Lu H (2018) Crust breaking and the limiting rotational frequency of neutron stars. arXiv:1804.04952 [astro-ph.HE]
Ferdman RD, Archibald RF, Kaspi VM (2015) Long-term timing and emission behavior of the young crab-like pulsar PSR B0540-69. Astrophys J 812(2):95. https://doi.org/10.1088/0004-637X/812/2/95. arXiv:1506.00182 [astro-ph.SR]
Ferdman RD, Archibald RF, Gourgouliatos KN, Kaspi VM (2018) The glitches and rotational history of the highly energetic young pulsar PSR J0537−6910. Astrophys J 852(2):123. https://doi.org/10.3847/1538-4357/aaa198. arXiv:1708.08876 [astro-ph.HE]
Ferrand G, Safi-Harb S (2012) A census of high-energy observations of Galactic supernova remnants. Adv Space Res 49(9):1313–1319. https://doi.org/10.1016/j.asr.2012.02.004
Fesen RA, Hammell MC, Morse J, Chevalier RA, Borkowski KJ, Dopita MA, Gerardy CL, Lawrence SS, Raymond JC, van den Bergh S (2006) The expansion asymmetry and age of the Cassiopeia A Supernova Remnant. Astrophys J 645(1):283–292. https://doi.org/10.1086/504254
Fesik L, Papa MA (2020) First search for r-mode gravitational waves from PSR J0537-6910. Astrophys J 895(1):11. https://doi.org/10.3847/1538-4357/ab8193
Fomalont EB, Geldzahler BJ, Bradshaw CF (2001) Scorpius X-1: the evolution and nature of the twin compact radio lobes. Astrophys J 558(1):283–301. https://doi.org/10.1086/322479
Fonseca E, Cromartie HT, Pennucci TT, Ray PS, Kirichenko AY, Ransom SM, Demorest PB, Stairs IH, Arzoumanian Z, Guillemot L, Parthasarathy A, Kerr M, Cognard I, Baker PT, Blumer H, Brook PR, DeCesar M, Dolch T, Dong FA, Ferrara EC, Fiore W, Garver-Daniels N, Good DC, Jennings R, Jones ML, Kaspi VM, Lam MT, Lorimer DR, Luo J, McEwen A, McKee JW, McLaughlin MA, McMann N, Meyers BW, Naidu A, Ng C, Nice DJ, Pol N, Radovan HA, Shapiro-Albert B, Tan CM, Tendulkar SP, Swiggum JK, Wahl HM, Zhu WW (2021) Refined mass and geometric measurements of the high-mass PSR J0740+6620. Astrophys J Lett 915(1):L12. https://doi.org/10.3847/2041-8213/ac03b8. arXiv:2104.00880 [astro-ph.HE]
Freire PCC (2012) The pulsar population in globular clusters and in the galaxy. Proc Int Astron Union 8 (S291):243–250. https://doi.org/10.1017/s1743921312023770

Freire PCC, et al (2017) Long-term observations of the pulsars in 47 Tucanae—II. Proper motions, accelerations and jerks. Mon Not R Astron Soc 471(1):857–876. https://doi.org/10.1093/mnras/stx1533. arXiv:1706.04908 [astro-ph.HE]

Freise A, Strain K (2010) Interferometer techniques for gravitational-wave detection. Living Rev Rel 13:1. https://doi.org/10.12942/lrr-2010-1. arXiv:0909.3661 [gr-qc]

Friedman JL, Morsink SM (1998) Axial instability of rotating relativistic stars. Astrophys J 502:714–720. https://doi.org/10.1086/305920. arXiv:gr-qc/9706073

Friedman JL, Schutz BF (1978) Secular instability of rotating Newtonian stars. Astrophys J 222:281–296. https://doi.org/10.1086/156143

Fruchter AS, Stinebring DR, Taylor JH (1988) A millisecond pulsar in an eclipsing binary. Nature 333 (6170):237–239. https://doi.org/10.1038/333237a0

Gaensler BM, Slane PO (2006) The evolution and structure of pulsar wind nebulae. Ann Rev Astron Astrophys 44:17–47. https://doi.org/10.1146/annurev.astro.44.051905.092528. arXiv:astro-ph/0601081

Galaudage S, Wette K, Galloway DK, Messenger C (2021) Deep searches for X-ray pulsations from Scorpius X-1 and Cygnus X-2 in support of continuous gravitational wave searches. Mon Not R Astron Soc 509(2):1745–1754. https://doi.org/10.1093/mnras/stab3095

Galloway DK, Muno MP, Hartman JM, Psaltis D, Chakrabarty D (2008) Thermonuclear (type I) X-ray bursts observed by the Rossi X-ray timing explorer. Astrophys J Suppl 179(2):360–422. https://doi.org/10.1086/592044

Gao Y, Shao L, Xu R, Sun L, Liu C, Xu RX (2020) Triaxially deformed freely precessing neutron stars: continuous electromagnetic and gravitational radiation. Mon Not R Astron Soc 498(2):1826–1838. https://doi.org/10.1093/mnras/staa2476

Gáspár A, Rieke GH (2020) New HST data and modeling reveal a massive planetesimal collision around Fomalhaut. Proc Natl Acad Sci 117(18):9712–9722. https://doi.org/10.1073/pnas.1912506117

Geppert U, Page D, Zannias T (1999) Submergence and re-diffusion of the neutron star magnetic field after the supernova. Astron Astrophys 345:847–854

Ghosh P, Lamb FK (1979) Accretion by rotating magnetic neutron stars. III. Accretion torques and period changes in pulsating X-ray sources. Astrophys J 234:296–316. https://doi.org/10.1086/157498

Ghosh S, Berti E, Brito R, Richartz M (2019) Follow-up signals from superradiant instabilities of black hole merger remnants. Phys Rev D 99(10):104030. https://doi.org/10.1103/PhysRevD.99.104030. arXiv:1812.01620 [gr-qc]

Giliberti E, Cambiotti G (2022) Starquakes in millisecond pulsars and gravitational waves emission. Mon Not R Astron Soc 511(3):3365–3376. https://doi.org/10.1093/mnras/stac245

Gittins F, Andersson N, Jones DI (2020) Modelling neutron star mountains. Mon Not R Astron Soc 500 (4):5570–5582. https://doi.org/10.1093/mnras/staa3635. arXiv:2009.12794 [astro-ph.HE]

Glampedakis K, Gualtieri L (2018) Gravitational waves from single neutron stars: an advanced detector era survey. In: Rezzolla L, Pizzochero P, Jones DI, Rea N, Vidaña I (eds) The physics and astrophysics of neutron stars. Astrophysics and Space Science Library, vol 457. Springer, pp 673–736. https://doi.org/10.1007/978-3-319-97616-7_12. arXiv:1709.07049 [astro-ph.HE]

Goetz E, Riles K (2011) An all-sky search algorithm for continuous gravitational waves from spinning neutron stars in binary systems. Class Quantum Grav 28(21):215006. https://doi.org/10.1088/0264-9381/28/21/215006

Goetz E, Riles K (2016) Coherently combining data between detectors for all-sky semi-coherent continuous gravitational wave searches. Class Quantum Grav 33(8):085007. https://doi.org/10.1088/0264-9381/33/8/085007

Goetz E, et al (2021) Subtracting Narrow-band Noise from LIGO strain data in the third observing run. Technical Report LIGO Report T2100200, LIGO. https://dcc.ligo.org/T2100200

Gold T (1968) Rotating neutron stars as the origin of the pulsating radio sources. Nature 218(5143):731–732. https://doi.org/10.1038/218731a0

Goldreich P, Julian WH (1969) Pulsar electrodynamics. Astrophys J 157:869. https://doi.org/10.1086/150119

Goncharov B, Thrane E (2018) All-sky radiometer for narrowband gravitational waves using folded data. Phys Rev D 98:064018. https://doi.org/10.1103/PhysRevD.98.064018

Gotthelf EV, Halpern JP (2009) Discovery of a highly energetic X-ray pulsar powering HESS J1813–178 in the Young Supernova Remnant G1.282–0.02. Astrophys J 700(2):158–161. https://doi.org/10.1088/0004-637x/700/2/l158

Gottlieb EW, Wright EL, Liller W (1975) Optical studies of UHURU sources. XI. A probable period for Scorpius X-1 = V818 Scorpii. Astrophys J Lett 195:L33–L35. https://doi.org/10.1086/181703
Greco E et al (2022) Additional evidence for a pulsar wind nebula in the heart of SN 1987A from Multiepoch X-ray data and MHD modeling. Astrophys J 931(2):132. https://doi.org/10.3847/1538-4357/ac679d. arXiv:2204.06804 [astro-ph.HE]
Green DA (2014) A catalogue of 294 Galactic supernova remnants. Bull Astron Soc India 42:47 arXiv:1409.0637 [astro-ph.HE]
Grote H, Stadnik YV (2019) Novel signatures of dark matter in laser-interferometric gravitational-wave detectors. Phys Rev Res 1(3):033187. https://doi.org/10.1103/PhysRevResearch.1.033187. arXiv:1906.06193 [astro-ph.IM]
Guilet J, Müller E (2015) Numerical simulations of the magnetorotational instability in protoneutron stars-I. Influence of buoyancy. Mon Not R Astron Soc 450(2):2153–2171. https://doi.org/10.1093/mnras/stv727
Guo HK, Riles K, Yang FW, Zhao Y (2019) Searching for dark photon dark matter in LIGO O1 data. Commun Phys. https://doi.org/10.1038/s42005-019-0255-0
Gusakov ME, Chugunov AI, Kantor EM (2014) Instability windows and evolution of rapidly rotating neutron stars. Phys Rev Lett 112(15):151101. https://doi.org/10.1103/PhysRevLett.112.151101. arXiv:1310.8103 [astro-ph.HE]
Halpern JP, Gotthelf EV (2009) Spin-down Measurement of PSR J1852+0040 in Kesteven 79: central compact objects as anti-magnetars. Astrophys J 709(1):436–446. https://doi.org/10.1088/0004-637x/709/1/436
Harding AK, Contopoulos I, Kazanas D (1999) Magnetar spin-down. Astrophys J 525(2):L125–L128. https://doi.org/10.1086/312339
Haskell B, Patruno A (2011) Spin equilibrium with or without gravitational wave emission: the case of XTE J1814–338 and SAX J1808.4–365.8. Astrophys J Lett 738:L14. https://doi.org/10.1088/2041-8205/738/1/L14
Haskell B, Patruno A (2017) Are gravitational waves spinning down PSR J1023+0038? Phys Rev Lett 119(16):161103. https://doi.org/10.1103/PhysRevLett.119.161103. arXiv:1703.08374 [astro-ph.HE]
Haskell B, Priymak M, Patruno A, Oppenoorth M, Melatos A, Lasky PD (2015) Detecting gravitational waves from mountains on neutron stars in the advanced detector era. Mon Not R Astron Soc 450(3):2393–2403. https://doi.org/10.1093/mnras/stv726. arXiv:1501.06039 [astro-ph.SR]
Haskell B, Antonelli M, Pizzochero P (2022) Continuous gravitational wave emissions from neutron stars with pinned superfluids in the core. Universe 8(12):619. https://doi.org/10.3390/universe8120619. arXiv:2211.15507 [astro-ph.HE]
Hessels JWT, Ransom SM, Stairs IH, Freire PCC, Kaspi VM, Camilo F (2006) A radio pulsar spinning at 716 Hz. Science 311(5769):1901–1904. https://doi.org/10.1126/science.1123430
Hewish AR, Bell SJ, Pilkington J, Scott P, Collins R (1968) Observation of a rapidly pulsating radio source. Nature. https://doi.org/10.1038/217709a0
Heyl JS (2002) Low-mass X-ray binaries may be important laser interferometer gravitational-wave observatory sources after all. Astrophys J Lett 574(1):L57–L60. https://doi.org/10.1086/342263
Hirakawa H, Tsubono K, Fujimoto MK (1978) Search for gravitational radiation from the crab pulsar. Phys Rev D 17:1919–1923. https://doi.org/10.1103/PhysRevD.17.1919
Ho WCG (2011) Evolution of a buried magnetic field in the central compact object neutron stars. Mon Not R Astron Soc 414(3):2567–2575. https://doi.org/10.1111/j.1365-2966.2011.18576.x. arXiv:1102.4870 [astro-ph.HE]
Ho WCG (2015) Magnetic field growth in young glitching pulsars with a braking index. Mon Not R Astron Soc 452(1):845–851. https://doi.org/10.1093/mnras/stv1339. arXiv:1506.03933 [astro-ph.SR]
Ho WCG (2016) Gravitational waves within the magnetar model of superluminous supernovae and gamma-ray bursts. Mon Not R Astron Soc 463(1):489–494. https://doi.org/10.1093/mnras/stw2016. arXiv:1606.00454 [astro-ph.HE]
Ho WCG, Andersson N (2012) Rotational evolution of young pulsars due to superfluid decoupling. Nat Phys 8(11):787–789. https://doi.org/10.1038/nphys2424. arXiv:1208.3201 [astro-ph.SR]
Ho WCG, Heinke CO, Chugunov AI (2019) XMM-Newton detection and spectrum of the second fastest spinning pulsar PSR J0952–0607. Astrophys J 882(2):128. https://doi.org/10.3847/1538-4357/ab3578. arXiv:1905.12001 [astro-ph.HE]
Ho WCG, Espinoza CM, Arzoumanian Z, Enoto T, Tamba T, Antonopoulou D, Bejger M, Guillot S, Haskell B, Ray PS (2020) Return of the big Glitcher: NICER timing and glitches of PSR J0537–

6910. Mon Not R Astron Soc 498(4):4605–4614. https://doi.org/10.1093/mnras/staa2640. arXiv:2009.00030 [astro-ph.HE]
Ho WCG, Zhao Y, Heinke CO, Kaplan DL, Shternin PS, Wijngaarden MJP (2021) X-ray bounds on cooling, composition, and magnetic field of the Cassiopeia A neutron star and young central compact objects. Mon Not R Astron Soc 506(4):5015–5029. https://doi.org/10.1093/mnras/stab2081
Hobbs GB, Edwards RT, Manchester RN (2006) TEMPO2, a new pulsar-timing package-I. An overview. Mon Not R Astron Soc 369(2):655–672. https://doi.org/10.1111/j.1365-2966.2006.10302.x
Horowitz CJ, Kadau K (2009) Breaking strain of neutron star crust and gravitational waves. Phys Rev Lett 102:191102. https://doi.org/10.1103/PhysRevLett.102.191102
Horowitz CJ, Papa MA, Reddy S (2020) Search for compact dark matter objects in the solar system with LIGO data. Phys Lett B 800:135072. https://doi.org/10.1016/j.physletb.2019.135072
Hough PVC (1959) Machine analysis of bubble chamber pictures. Conf Proc 590914:554–558
Hough PVC (1962) Method and means for recognizing complex patterns. U.S. Patent 3,069,654
Hoyle F, Lyttleton RA (1939) The effect of interstellar matter on climatic variation. Proc Camb Philos Soc 35(3):405. https://doi.org/10.1017/S0305004100021150
Hughes DW (1980) Did Flamsteed see the Cassiopeia A supernova? Nature 285(5761):132–133. https://doi.org/10.1038/285132a0
Hutchins TJ, Jones DI (2022) Gravitational radiation from thermal mountains on accreting neutron stars: sources of temperature non-axisymmetry. arXiv:2212.07452 [astro-ph.HE]
Huth S, Pang PTH, Tews I, Dietrich T, Le Fèvre A, Schwenk A, Trautmann W, Agarwal K, Bulla M, Coughlin MW, Van Den Broeck C (2022) Constraining neutron-star matter with microscopic and macroscopic collisions. Nature 606(7913):276–280. https://doi.org/10.1038/s41586-022-04750-w
Idrisy A, Owen BJ, Jones DI (2015) R-mode frequencies of slowly rotating relativistic neutron stars with realistic equations of state. Phys Rev D. https://doi.org/10.1103/physrevd.91.024001
Intini G, Leaci P, Astone P, D'Antonio S, Frasca S, La Rosa I, Miller A, Palomba C, Piccinni O (2020) A Doppler-modulation based veto to discard false continuous gravitational-wave candidates. Class Quant Grav 37(22):225007. https://doi.org/10.1088/1361-6382/abac43
Intini G, Leaci P, Astone P, D'Antonio S, Frasca S, La Rosa I, Miller A, Palomba C, Piccinni O (2020) A Doppler-modulation based veto to discard false continuous gravitational-wave candidates. Class Quant Grav 37(22):225007. https://doi.org/10.1088/1361-6382/abac43
Isi M, Weinstein AJ, Mead C, Pitkin M (2015) Detecting beyond-Einstein polarizations of continuous gravitational waves. Phys Rev D 91:082002. https://doi.org/10.1103/PhysRevD.91.082002
Isi M, Sun L, Brito R, Melatos A (2019) Directed searches for gravitational waves from ultralight bosons. Phys Rev D 99:084042. https://doi.org/10.1103/PhysRevD.99.084042
Isi M, Mastrogiovanni S, Pitkin M, Piccinni OJ (2020) Establishing the significance of continuous gravitational-wave detections from known pulsars. Phys Rev D 102(12):123027. https://doi.org/10.1103/PhysRevD.102.123027. arXiv:2010.12612 [gr-qc]
Iyudin AF, Schönfelder V, Bennett K, Bloemen H, Diehl R, Hermsen W, Lichti GG, van der Meulen RD, Ryan J, Winkler C (1998) Emission from ^{44}Ti associated with a previously unknown Galactic supernova. Nature 396(6707):142–144. https://doi.org/10.1038/24106
Jaranowski P, Królak A (1999) Data analysis of gravitational-wave signals from spinning neutron stars. ii. accuracy of estimation of parameters. Phys Rev D 59:063003. https://doi.org/10.1103/PhysRevD.59.063003
Jaranowski P, Królak A (2009) Analysis of gravitational-wave data. Cambridge University Press, Cambridge
Jaranowski P, Królak A (2010) Searching for gravitational waves from known pulsars using the F and G statistics. Class Quantum Grav 27(19):194015. https://doi.org/10.1088/0264-9381/27/19/194015
Jaranowski P, Królak A, Schutz BF (1998) Data analysis of gravitational-wave signals from spinning neutron stars. 1. The signal and its detection. Phys Rev D 58:063001. https://doi.org/10.1103/PhysRevD.58.063001
Jasiulek M, Chirenti C (2017) R-mode frequencies of rapidly and differentially rotating relativistic neutron stars. Phys Rev D 95(6):064060. https://doi.org/10.1103/PhysRevD.95.064060. arXiv:1611.07924 [gr-qc]
Johnson-McDaniel NK, Owen BJ (2013) Maximum elastic deformations of relativistic stars. Phys Rev D 88:044004. https://doi.org/10.1103/PhysRevD.88.044004. arXiv:1208.5227 [astro-ph.SR]
Johnston S, Karastergiou A (2017) Pulsar braking and the P-$\dot{P}$ diagram. Mon Not R Astron Soc 467 (3):3493–3499. https://doi.org/10.1093/mnras/stx377. arXiv:1702.03616 [astro-ph.HE]

Jones DI (2010) Gravitational wave emission from rotating superfluid neutron stars. Mon Not R Astron Soc 402(4):2503–2519. https://doi.org/10.1111/j.1365-2966.2009.16059.x. arXiv:0909.4035 [astro-ph.SR]

Jones DI (2015) Parameter choices and ranges for continuous gravitational wave searches for steadily spinning neutron stars. Mon Not R Astron Soc 453(1):53–66. https://doi.org/10.1093/mnras/stv1584

Jones DI (2022) Learning from the frequency content of continuous gravitational wave signals. In: Vasconcellos CAZ (ed) Astrophysics in the XXI century with compact stars. World Scientific, pp 201–217. https://doi.org/10.1142/9789811220944_0006. arXiv:2111.08561 [astro-ph.HE]

Jones DI, Andersson N (2001) Freely precessing neutron stars: model and observations. Mon Not R Astron Soc 324(4):811–824. https://doi.org/10.1046/j.1365-8711.2001.04251.x

Jones DI, Andersson N (2002) Gravitational waves from freely precessing neutron stars. Mon Not R Astron Soc 331(1):203–220. https://doi.org/10.1046/j.1365-8711.2002.05180.x

Jones D, Sun L (2021) Search for continuous gravitational waves from Fomalhaut b in the second Advanced LIGO observing run with a hidden Markov model. Phys Rev D 103:023020. https://doi.org/10.1103/PhysRevD.103.023020

Jones DI, Owen B, Whitbeck D (2005) Parameter space metric for combined diurnal and orbital motion. Technical Report. LIGO-T0900500-v1, LIGO

Jones D, Sun L, Carlin J, Dunn L, Millhouse M, Middleton H, Meyers P, Clearwater P, Beniwal D, Strang L, Vargas A, Melatos A (2022) Validating continuous gravitational-wave candidates from a semicoherent search using doppler modulation and an effective point spread function. Phys Rev D 106:123011. https://doi.org/10.1103/PhysRevD.106.123011. arXiv:2203.14468 [gr-qc]

Jordana-Mitjans N, Mundell CG, Guidorzi C, Smith RJ, Ramírez-Ruiz E, Metzger BD, Kobayashi S, Gomboc A, Steele IA, Shrestha M, Marongiu M, Rossi A, Rothberg B (2022) A short gamma-ray burst from a protomagnetar remnant. Astrophys J 939(2):106. https://doi.org/10.3847/1538-4357/ac972b

Kalas P, Graham JR, Chiang E, Fitzgerald MP, Clampin M, Kite ES, Stapelfeldt K, Marois C, Krist J (2008) Optical images of an exosolar planet 25 light-years from earth. Science 322(5906):1345–1348. https://doi.org/10.1126/science.1166609

Kantor EM, Gusakov ME, Dommes VA (2020) Constraining neutron superfluidity with *r*-mode physics. Phys Rev Lett 125(15):151101. https://doi.org/10.1103/PhysRevLett.125.151101. arXiv:2009.12553 [astro-ph.HE]

Kargaltsev O, Pavlov GG, Sanwal D, Garmire GP (2002) The compact central object in the Supernova Remnant G266.2-1.2. Astrophys J 580(2):1060–1064. https://doi.org/10.1086/343852. arXiv:astro-ph/0207602 [astro-ph]

Kashiyama K, Murase K, Bartos I, Kiuchi K, Margutti R (2016) Multi-messenger tests for fast-spinning newborn pulsars embedded in stripped-envelope supernovae. Astrophys J 818(1):94. https://doi.org/10.3847/0004-637X/818/1/94. arXiv:1508.04393 [astro-ph.HE]

Keitel D (2016) Robust semicoherent searches for continuous gravitational waves with noise and signal models including hours to days long transients. Phys Rev D 93:084024. https://doi.org/10.1103/PhysRevD.93.084024

Keitel D, Ashton G (2018) Faster search for long gravitational-wave transients: GPU implementation of the transient $\mathcal{F}$-statistic. Class Quantam Grav 35(20):205003. https://doi.org/10.1088/1361-6382/aade34. arXiv:1805.05652 [astro-ph.IM]

Keitel D, Prix R (2015) Line-robust statistics for continuous gravitational waves: safety in the case of unequal detector sensitivities. Class Quantum Grav 32(3):035004. https://doi.org/10.1088/0264-9381/32/3/035004

Keitel D, Prix R, Papa MA, Leaci P, Siddiqi M (2014) Search for continuous gravitational waves: Improving robustness versus instrumental artifacts. Phys Rev D 89:064023. https://doi.org/10.1103/PhysRevD.89.064023

Keitel D, Woan G, Pitkin M, Schumacher C, Pearlstone B, Riles K, Lyne AG, Palfreyman J, Stappers B, Weltevrede P (2019) First search for long-duration transient gravitational waves after glitches in the Vela and Crab pulsars. Phys Rev D 100(6):064058. https://doi.org/10.1103/PhysRevD.100.064058. arXiv:1907.04717 [gr-qc]

Keitel D, Tenorio R, Ashton G, Prix R (2021) PyFstat: a python package for continuous gravitational-wave data analysis. J Open Source Softw 6(60):3000. https://doi.org/10.21105/joss.03000

Kerin AD, Melatos A (2022) Mountain formation by repeated, inhomogeneous crustal failure in a neutron star. Mon Not R Astron Soc 514(2):1628–1644. https://doi.org/10.1093/mnras/stac1351

Knispel B, Allen B (2008) Blandford's argument: the strongest continuous gravitational wave signal. Phys Rev D 78:044031. https://doi.org/10.1103/PhysRevD.78.044031
Kojima Y (1998) Quasitoroidal oscillations in rotating relativistic stars. Mon Not R Astron Soc 293:49–52. https://doi.org/10.1046/j.1365-8711.1998.01119.x. arXiv:gr-qc/9709003
Konno K, Obata T, Kojima Y (1999) Deformation of relativistic magnetized stars. Astron Astrophys 352:211–216 arXiv:gr-qc/9910038
Kramer M, Stappers B (2015) Pulsar Science with the SKA. In: Proceedings of advancing astrophysics with the square kilometre array—PoS(AASKA14). vol 215. SISSA, p 036. https://doi.org/10.22323/1.215.0036. arXiv:1507.04423 [astro-ph.IM]
Krastev PG, Li BA, Worley A (2008) Nuclear limits on gravitational waves from elliptically deformed pulsars. Phys Lett B 668:1–5. https://doi.org/10.1016/j.physletb.2008.07.105. arXiv:0805.1973 [astro-ph]
Krishnan B, Sintes AM, Papa MA, Schutz BF, Frasca S, Palomba C (2004) Hough transform search for continuous gravitational waves. Phys Rev D 70:082001. https://doi.org/10.1103/PhysRevD.70.082001
Kuwahara N, Asada H (2022) Earth rotation and time-domain reconstruction of polarization states for continuous gravitational waves from known pulsars. Phys Rev D 106:024051. https://doi.org/10.1103/PhysRevD.106.024051. arXiv:2202.00171 [gr-qc]
La Rosa I, Astone P, D'Antonio S, Frasca S, Leaci P, Miller AL, Palomba C, Piccinni OJ, Pierini L, Regimbau T (2021) Continuous gravitational-wave data analysis with general purpose computing on graphic processing units. Universe 7(7):218. https://doi.org/10.3390/universe7070218
Lander SK (2014) The contrasting magnetic fields of superconducting pulsars and magnetars. Mon Not R Astron Soc 437(1):424–436. https://doi.org/10.1093/mnras/stt1894. arXiv:1307.7020 [astro-ph.HE]
Lander SK, Andersson N, Glampedakis K (2011) Magnetic neutron star equilibria with stratification and type-II superconductivity. Mon Not R Astron Soc 419:732. https://doi.org/10.1111/j.1365-2966.2011.19720.x. arXiv:1106.6322 [astro-ph.SR]
Large MI, Vaughan AE, Mills BY (1968) A pulsar Supernova association? Nature 220(5165):340–341. https://doi.org/10.1038/220340a0
Lasky PD (2015) Gravitational waves from neutron stars: a review. Pubs Astron Soc Aust 32:e034. https://doi.org/10.1017/pasa.2015.35. arXiv:1508.06643 [astro-ph.HE]
Lasky PD, Leris C, Rowlinson A, Glampedakis K (2017a) The braking index of millisecond magnetars. Astrophys J Lett 843(1):L1. https://doi.org/10.3847/2041-8213/aa79a7
Lasky PD, Sarin N, Sammut L (2017b) Long-duration waveform models for millisecond magnetars born in binary neutron star mergers. Technical Report LIGO Report T1700408, LIGO. https://dcc.ligo.org/T1700408
Lattimer JM, Prakash M (2001) Neutron star structure and the equation of state. Astrophys J 550(1):426–442. https://doi.org/10.1086/319702
Lazio TJW, Cordes JM (1998) Hyperstrong radio-wave scattering in the galactic center. I. A survey for extragalactic sources seen through the galactic center. Astrophys J Suppl 118:201. https://doi.org/10.1086/313129
Leaci P (2015) Methods to filter out spurious disturbances in continuous-wave searches from gravitational-wave detectors. Phys Scr 90(12):125001. https://doi.org/10.1088/0031-8949/90/12/125001
Leaci P, Prix R (2015) Directed searches for continuous gravitational waves from binary systems: parameter-space metrics and optimal Scorpius X-1 sensitivity. Phys Rev D 91(10):102003. https://doi.org/10.1103/PhysRevD.91.102003. arXiv:1502.00914 [gr-qc]
Lee U (2014) Excitation of a non-radial mode in a millisecond X-ray pulsar XTE J1751–305. Mon Not R Astron Soc 442(4):3037–3043. https://doi.org/10.1093/mnras/stu1077. arXiv:1403.3476 [astro-ph.HE]
Levin Y (1999) Runaway heating by R modes of neutron stars in low mass x-ray binaries. Astrophys J 517:328. https://doi.org/10.1086/307196. arXiv:astro-ph/9810471
Levine J, Stebbins R (1972) Upper limit on the gravitational flux reaching the earth from the crab pulsar. Phys Rev D 6:1465–1468. https://doi.org/10.1103/PhysRevD.6.1465
LIGO Scientific Collaboration (2018) LIGO algorithm Library-LALSuite. free software (GPL). https://doi.org/10.7935/GT1W-FZ16
Lim Y, Holt JW (2019) Bayesian modeling of the nuclear equation of state for neutron star tidal deformabilities and GW170817. Eur Phys J A. https://doi.org/10.1140/epja/i2019-12917-9
Lindblom L, Detweiler SL (1977) On the secular instabilities of the Maclaurin spheroids. Astrophys J 211:565–567. https://doi.org/10.1086/154964

Lindblom L, Mendell G (1995) Does gravitational radiation limit the angular velocities of superfluid neutron stars? Astrophys J 444:804. https://doi.org/10.1086/175653
Lindblom L, Owen BJ (2020) Directed searches for continuous gravitational waves from twelve supernova remnants in data from Advanced LIGO's second observing run. Phys Rev D 101(8):083023. https://doi.org/10.1103/PhysRevD.101.083023. arXiv:2003.00072 [gr-qc]
Liu Y, Zou YC (2022) Directed search for continuous gravitational waves from the possible kilonova remnant G4.+6. Phys Rev D 106(12):123024. https://doi.org/10.1103/PhysRevD.106.123024
Livas J (1989) Broadband search techniques for periodic sources of gravitational radiation. In: Schutz BF (ed) Gravitational wave data analysis. NATO ASI series C, vol 253. Springer, Dordrecht, pp 217–238. https://doi.org/10.1007/978-94-009-1185-7
Livingstone MA, Kaspi VM (2011) Long-term X-ray monitoring of the young pulsar PSR B1509–58. Astrophys J 742:31. https://doi.org/10.1088/0004-637X/742/1/31. arXiv:1110.1312 [astro-ph.HE]
Livingstone MA, Kaspi VM, Gavriil FP, Manchester RN, Gotthelf EV, Kuiper L (2007) New phase-coherent measurements of pulsar braking indices. Astrophys Space Sci 308:317–323. https://doi.org/10.1007/s10509-007-9320-3. arXiv:astro-ph/0702196
Lorimer DR (2008) Binary and millisecond pulsars. Living Rev Relativ 11:80. https://doi.org/10.12942/lrr-2008-8
Lorimer DR, Kramer M (2005) Handbook of pulsar astronomy. Cambridge University Press, Cambridge
Lower ME, Johnston S, Dunn L, Shannon RM, Bailes M, Dai S, Kerr M, Manchester RN, Melatos A, Oswald LS, Parthasarathy A, Sobey C, Weltevrede P (2021) The impact of glitches on young pulsar rotational evolution. Mon Not R Astron Soc 508(3):3251–3274. https://doi.org/10.1093/mnras/stab2678
Lu N, Wette K, Scott SM, Melatos A (2023) Inferring neutron star properties with continuous gravitational waves. Mon Not R Astron Soc https://doi.org/10.1093/mnras/stad390. arXiv:2209.10981 [gr-qc]
Lyne A, Graham-Smith F (2006) Pulsar astronomy, 3rd edn. Cambridge University Press, Cambridge
Lyne A, Jordan C, Graham-Smith F, Espinoza C, Stappers B, Weltrvrede P (2015) 45 years of rotation of the Crab pulsar. Mon Not R Astron Soc 446:857–864. https://doi.org/10.1093/mnras/stu2118. arXiv:1410.0886 [astro-ph.HE]
Macquart JP, Kanekar N (2015) On detecting millisecond pulsars at the galactic center. Astrophys J 805 (2):172. https://doi.org/10.1088/0004-637X/805/2/172. arXiv:1504.02492 [astro-ph.HE]
Maggiore M (2008) Gravitational waves, volume 1: theory and experiments. Oxford University Press, Oxford
Maggiore M (2018) Gravitational waves, volume 2: astrophysics and cosmology. Oxford University Press, Oxford
Maggiore M, Broeck CVD, Bartolo N, Belgacem E, Bertacca D, Bizouard MA, Branchesi M, Clesse S, Foffa S, García-Bellido J et al (2020) Science case for the Einstein telescope. J Cosmol Astropart Phys 03:050–050. https://doi.org/10.1088/1475-7516/2020/03/050
Manchester RN (2012) Detection of gravitational waves using pulsar timing. In: The twelfth Marcel Grossmann meeting. World Scientific, pp 226–240. https://doi.org/10.1142/9789814374552_0011. arXiv:1004.3602 [astro-ph.HE]
Manchester RN (2018) Pulsar glitches. In: Weltevrede P, Perera BBP, Preston LL, Sanidas S (eds) Pulsar astrophysics the next fifty years. vol 337, pp 197–202. https://doi.org/10.1017/S1743921317009607. arXiv:1801.04332 [astro-ph.HE]
Manchester RN, Hobbs GB (2005) The ATNF pulsar catalogue. A. Teoh & M. Hobbs, Astron J 129, 1993–2006. http://www.atnf.csiro.au/research/pulsar/psrcat/
Mauceli E, McHugh MP, Hamilton WO, Johnson WW, Morse A (2000) Search for periodic gravitational radiation with the ALLEGRO gravitational wave detector. arXiv:gr-qc/0007023 [gr-qc]
McClintock JE, Narayan R, Steiner JF (2014) Black hole spin via continuum fitting and the role of spin in powering transient jets. Space Sci Rev 183(1–4):295–322. https://doi.org/10.1007/s11214-013-0003-9. arXiv:1303.1583 [astro-ph.HE]
McNolty F (1973) Some probability density functions and their characteristic functions. Math Comput 27 (123):495–504
Meadors GD, Kawabe K, Riles K (2014) Increasing LIGO sensitivity by feedforward subtraction of auxiliary length control noise. Class Quantum Grav 31(10):105014. https://doi.org/10.1088/0264-9381/31/10/105014
Meadors GD, Goetz E, Riles K (2016) Tuning into Scorpius X-1: adapting a continuous gravitational-wave search for a known binary system. Class Quantam Grav 33(10):105017. https://doi.org/10.1088/0264-9381/33/10/105017. arXiv:1512.02105 [gr-qc]

Meadors GD, Goetz E, Riles K, Creighton T, Robinet F (2017) Searches for continuous gravitational waves from Scorpius X-1 and XTE J1751–305 in LIGO's sixth science run. Phys Rev D 95:042005. https://doi.org/10.1103/PhysRevD.95.042005

Meadors GD, Krishnan B, Papa MA, Whelan JT, Zhang Y (2018) Resampling to accelerate cross-correlation searches for continuous gravitational waves from binary systems. Phys Rev D 97 (4):044017. https://doi.org/10.1103/PhysRevD.97.044017. arXiv:1712.06515 [astro-ph.IM]

Melatos A (1997) Spin-down of an oblique rotator with a current-starved outer magnetosphere. Mon Not R Astron Soc 288(4):1049–1059. https://doi.org/10.1093/mnras/288.4.1049

Melatos A, Payne DJB (2005) Gravitational radiation from an accreting millisecond pulsar with a magnetically confined mountain. Astrophys J 623:1044–1050. https://doi.org/10.1086/428600. arXiv:astro-ph/0503287

Melatos A, Douglass JA, Simula TP (2015) Persistent gravitational radiation from glitching pulsars. Astrophys J 807(2):132. https://doi.org/10.1088/0004-637X/807/2/132

Melatos A, Clearwater P, Suvorova S, Sun L, Moran W, Evans RJ (2021) Hidden Markov model tracking of continuous gravitational waves from a binary neutron star with wandering spin. III. tational phase tracking. Phys Rev D 104:042003. https://doi.org/10.1103/PhysRevD.104.042003

Melrose DB, Rafat MZ, Mastrano A (2021) Pulsar radio emission mechanisms: a critique. Mon Not R Astron Soc 500(4):4530–4548. https://doi.org/10.1093/mnras/staa3324. arXiv:2006.15243 [astro-ph.HE]

Mendell G, Landry M (2005) StackSlide and Hough search SNR and statistics. Technical Report. LIGO Report T050003, LIGO. https://dcc.ligo.org/T050003

Messenger C, Woan G (2007) A Fast search strategy for gravitational waves from low-mass X-ray binaries. Class Quantam Grav 24:S469–S480. https://doi.org/10.1088/0264-9381/24/19/S10. arXiv:gr-qc/0703155

Messenger C, Bulten HJ, Crowder SG, Dergachev V, Galloway DK, Goetz E, Jonker RJG, Lasky PD, Meadors GD, Melatos A, Premachandra S, Riles K, Sammut L, Thrane EH, Whelan JT, Zhang Y (2015) Gravitational waves from Scorpius X-1: a comparison of search methods and prospects for detection with advanced detectors. Phys Rev D 92:023006. https://doi.org/10.1103/PhysRevD.92.023006

Michel FC (1969) Relativistic stellar-wind torques. Astrophys J 158:727. https://doi.org/10.1086/150233

Michel FC, Li H (1999) Electrodynamics of neutron stars. Phys Rep 318(6):227–297. https://doi.org/10.1016/S0370-1573(99)00002-2

Michel FC, Tucker WH (1969) Pulsar emission mechanism. Nature 223(5203):277–279. https://doi.org/10.1038/223277a0

Middleditch J, Marshall FE, Wang QD, Gotthelf EV, Zhang W (2006) Predicting the starquakes in PSR J0537–6910. Astrophys J 652(2):1531–1546. https://doi.org/10.1086/508736

Middleton H, Clearwater P, Melatos A, Dunn L (2020) Search for gravitational waves from five low mass x-ray binaries in the second Advanced LIGO observing run with an improved hidden Markov model. Phys Rev D. https://doi.org/10.1103/physrevd.102.023006

Miller A, Astone P, D'Antonio S, Frasca S, Intini G, La Rosa I, Leaci P, Mastrogiovanni S, Muciaccia F, Palomba C, Piccinni OJ, Singhal A, Whiting BF (2018) Method to search for long duration gravitational wave transients from isolated neutron stars using the generalized frequency-Hough transform. Phys Rev D 98:102004. https://doi.org/10.1103/PhysRevD.98.102004

Miller AL et al (2019a) How effective is machine learning to detect long transient gravitational waves from neutron stars in a real search? Phys Rev D 100(6):062005. https://doi.org/10.1103/PhysRevD.100.062005. arXiv:1909.02262 [astro-ph.IM]

Miller MC et al (2019b) PSR J0030+0451 mass and radius from NICER data and implications for the properties of neutron star matter. Astrophys J 887(1):L24. https://doi.org/10.3847/2041-8213/ab50c5

Miller AL, Clesse S, De Lillo F, Bruno G, Depasse A, Tanasijczuk A (2021a) Probing planetary-mass primordial black holes with continuous gravitational waves. Phys Dark Univ 32:100836. https://doi.org/10.1016/j.dark.2021.100836. arXiv:2012.12983 [astro-ph.HE]

Miller AL et al (2021b) Probing new light gauge bosons with gravitational-wave interferometers using an adapted semicoherent method. Phys Rev D 103(10):103002. https://doi.org/10.1103/PhysRevD.103.103002. arXiv:2010.01925 [astro-ph.IM]

Miller MC et al (2021c) The Radius of PSR J0740+6620 from NICER and XMM-Newton data. Astrophys J Lett 918(2):L28. https://doi.org/10.3847/2041-8213/ac089b. arXiv:2105.06979 [astro-ph.HE]

Miller AL, Aggarwal N, Clesse S, De Lillo F (2022) Constraints on planetary and asteroid-mass primordial black holes from continuous gravitational-wave searches. Phys Rev D 105:062008. https://doi.org/10.1103/PhysRevD.105.062008. arXiv:2110.06188 [gr-qc]

Millhouse M, Strang L, Melatos A (2020) Search for gravitational waves from 12 young supernova remnants with a hidden Markov model in Advanced LIGO's second observing run. Phys Rev D 102:083025. https://doi.org/10.1103/PhysRevD.102.083025

Ming J, Krishnan B, Papa MA, Aulbert C, Fehrmann H (2016) Optimal directed searches for continuous gravitational waves. Phys Rev D 93(6):064011. https://doi.org/10.1103/PhysRevD.93.064011. arXiv:1510.03417 [gr-qc]

Ming J, Papa MA, Krishnan B, Prix R, Beer C, Zhu SJ, Eggenstein HB, Bock O, Machenschalk B (2018) Optimally setting up directed searches for continuous gravitational waves in Advanced LIGO O1 data. Phys Rev D 97(2):024051. https://doi.org/10.1103/PhysRevD.97.024051. arXiv:1708.02173 [gr-qc]

Ming J et al (2019) Results from an Einstein@Home search for continuous gravitational waves from Cassiopeia A, , Vela Jr. and G347.3. Phys Rev D 100(2):024063. https://doi.org/10.1103/PhysRevD.100.024063

Ming J, Papa MA, Eggenstein HB, Machenschalk B, Steltner B, Prix R, Allen B, Behnke O (2022) Results from an Einstein@Home search for continuous gravitational waves from G347.3 at low frequencies in LIGO O2 data. Astrophys J 925(1):8. https://doi.org/10.3847/1538-4357/ac35cb

Misner CW (1972) Interpretation of gravitational-wave observations. Phys Rev Lett 28:994–997. https://doi.org/10.1103/PhysRevLett.28.994

Misner CW, Thorne KS, Wheeler JA (1972) Gravitation. W.H. Freeman, San Francisco

Modafferi LM, Moragues J, Keitel D (2021) Search for long-duration transient gravitational waves from glitching pulsars during LIGO-Virgo third observing run. J Phys: Conf Ser 2156(12):012079. https://doi.org/10.1088/1742-6596/2156/1/012079. arXiv:2201.08785 [gr-qc]

Moragues J, Modafferi LM, Tenorio R, Keitel D (2023) Prospects for detecting transient quasi-monochromatic gravitational waves from glitching pulsars with current and future detectors. Mon Not R Astron Soc 519(4):5161–5176. https://doi.org/10.1093/mnras/stac3665. arXiv:2210.09907 [astro-ph.HE]

Morales JA, Horowitz CJ (2022) Neutron star crust can support a large ellipticity. Mon Not R Astron Soc 517(4):5610–5616. https://doi.org/10.1093/mnras/stac3058. arXiv:2209.03222 [gr-qc]

Mösta P, Ott CD, Radice D, Roberts LF, Schnetter E, Haas R (2015) A large-scale dynamo and magnetoturbulence in rapidly rotating core-collapse supernovae. Nature 528(7582):376–379. https://doi.org/10.1038/nature15755

Mukherjee A, Messenger C, Riles K (2018) Accretion-induced spin-wandering effects on the neutron star in Scorpius X-1: implications for continuous gravitational wave searches. Phys Rev D 97(4):043016. https://doi.org/10.1103/PhysRevD.97.043016. arXiv:1710.06185 [gr-qc]

Muno MP, Baganoff FK, Brandt WN, Morris MR, Starck JL (2008) A catalog of diffuse X-ray-emitting features within 20 pc of Sagittarius A*: twenty pulsar wind nebulae? Astrophys J 673(1):251–263. https://doi.org/10.1086/521641

Mytidis A, Coughlin M, Whiting B (2015) Constraining the R-mode saturation amplitude from a hypothetical detection of R-mode gravitational waves from a newborn neutron star: sensitivity study. Astrophys J 810:27. https://doi.org/10.1088/0004-637X/810/1/27. arXiv:1505.03191 [astro-ph.IM]

Mytidis A, Panagopoulos AA, Panagopoulos OP, Miller A, Whiting B (2019) Sensitivity study using machine learning algorithms on simulated r-mode gravitational wave signals from newborn neutron stars. Phys Rev D 99(2):024024. https://doi.org/10.1103/PhysRevD.99.024024. arXiv:1508.02064 [astro-ph.IM]

Narayan R (1987) The birthrate and initial spin period of single radio pulsars. Astrophys J 319:162. https://doi.org/10.1086/165442

Neuhäuser R, Hohle MM, Ginski C, Schmidt JG, Hambaryan VV, Schmidt TOB (2015) The companion candidate near Fomalhaut—a background neutron star? Mon Not R Astron Soc 448(1):376–389. https://doi.org/10.1093/mnras/stu2751

Neunzert A (2019) Searching for continuous gravitational waves from unknown isolated neutron stars in advanced LIGO data. PhD thesis, University of Michigan. https://hdl.handle.net/2027.42/151632

Ng CY, Romani RW (2004) Fitting pulsar wind tori. Astrophys J 601(1):479–484. https://doi.org/10.1086/380486

Ng KKY, Vitale S, Hannuksela OA, Li TGF (2021) Constraints on ultralight scalar bosons within black hole spin measurements from the LIGO-Virgo GWTC-2. Phys Rev Lett 126:151102. https://doi.org/10.1103/PhysRevLett.126.151102

Nieder L, Clark CJ, Bassa CG, Wu J, Singh A, Donner JY, Allen B, Breton RP, Dhillon VS, Eggenstein HB, Hessels JWT, Kennedy MR, Kerr M, Littlefair S, Marsh TR, Sánchez DM, Papa MA, Ray PS, Steltner B, Verbiest JPW (2019) Detection and timing of gamma-ray pulsations from the 707 Hz pulsar J0952–0607. Astrophys J 883(1):42. https://doi.org/10.3847/1538-4357/ab357e

Nieder L, Clark CJ, Kandel D, Romani RW, Bassa CG, Allen B, Ashok A, Cognard I, Fehrmann H, Freire P, Karuppusamy R, Kramer M, Li D, Machenschalk B, Pan Z, Papa MA, Ransom SM, Ray PS, Roy J, Wang P, Wu J, Aulbert C, Barr ED, Beheshtipour B, Behnke O, Bhattacharyya B, Breton RP, Camilo F, Choquet C, Dhillon VS, Ferrara EC, Guillemot L, Hessels JWT, Kerr M, Kwang SA, Marsh TR, Mickaliger MB, Pleunis Z, Pletsch HJ, Roberts MSE, Sanpa-arsa S, Steltner B (2020) Discovery of a gamma-ray black widow pulsar by GPU-accelerated Einstein@home. Astrophys J Lett 902(2):L46. https://doi.org/10.3847/2041-8213/abbc02

Oliver M, Keitel D, Sintes AM (2019) Adaptive transient Hough method for long-duration gravitational wave transients. Phys Rev D. https://doi.org/10.1103/physrevd.99.104067

Oppenheimer JR, Volkoff GM (1939) On massive neutron cores. Phys Rev 55:374–381. https://doi.org/10.1103/PhysRev.55.374

Osborne EL, Jones DI (2020) Gravitational waves from magnetically-induced thermal neutron star mountains. Mon Not R Astron Soc 494(2):2839–2850. https://doi.org/10.1093/mnras/staa858. arXiv:1910.04453 [astro-ph.HE]

Ostriker JP, Rees MJ, Silk J (1970) Some observable consequences of accretion by defunct pulsars. Astrophys J Lett 6:179

Owen BJ (1996) Search templates for gravitational waves from inspiraling binaries: choice of template spacing. Phys Rev D 53:6749–6761. https://doi.org/10.1103/PhysRevD.53.6749

Owen BJ (2005) Maximum elastic deformations of compact stars with exotic equations of state. Phys Rev Lett. https://doi.org/10.1103/physrevlett.95.211101

Owen BJ (2010) How to adapt broad-band gravitational-wave searches for *r*-modes. Phys Rev D 82:104002. https://doi.org/10.1103/PhysRevD.82.104002

Owen BJ, Lindblom L, Cutler C, Schutz BF, Vecchio A, Andersson N (1998) Gravitational waves from hot young rapidly rotating neutron stars. Phys Rev D 58:084020. https://doi.org/10.1103/PhysRevD.58.084020

Owen BJ, Lindblom L, Pinheiro LS (2022) First constraining upper limits on gravitational-wave emission from NS 1987A in SNR 1987A. Astrophys J Lett 935(1):L7. https://doi.org/10.3847/2041-8213/ac84dc. arXiv:2206.01168 [gr-qc]

Özel F, Freire PCC (2016) Masses, radii, and the equation of state of neutron stars. Annu Rev Astron Astrophys 54(1):401–440. https://doi.org/10.1146/annurev-astro-081915-023322

Pacini F (1967) Energy emission from a neutron star. Nature 216(5115):567–568. https://doi.org/10.1038/216567a0

Pacini F (1968) Rotating neutron stars, pulsars, and Supernova Remnants. Nature 219:145. https://doi.org/10.1038/219145a0

Page D, Beznogov MV, Garibay I, Lattimer JM, Prakash M, Janka HT (2020) NS 1987A in SN 1987A. Astrophys J 898(2):125. https://doi.org/10.3847/1538-4357/ab93c2

Palomba C (2000) Pulsars ellipticity revised. Astron Astrophs 354:163–168

Palomba C (2005) Simulation of a population of isolated neutron stars evolving through the emission of gravitational waves. Mon Not R Astron Soc 359:1150–1164. https://doi.org/10.1111/j.1365-2966.2005.08975.x. arXiv:astro-ph/0503046

Palomba C (2012) Searches for continuous gravitational wave signals and stochastic backgrounds in LIGO and Virgo data. arXiv:1201.3176. arXiv:1201.3176 [astro-ph.IM]

Palomba C, Astone P, Frasca S (2005) Adaptive Hough transform for the search of periodic sources. Class Quantum Grav 22(18):S1255–S1264. https://doi.org/10.1088/0264-9381/22/18/s39

Palomba C et al (2019) Direct constraints on ultra-light boson mass from searches for continuous gravitational waves. Phys Rev Lett 123:171101. https://doi.org/10.1103/PhysRevLett.123.171101. arXiv:1909.08854 [astro-ph.HE]

Pandharipande VR, Pines D, Smith RA (1976) Neutron star structure: theory, observation, and speculation. Astrophys J 208:550–566. https://doi.org/10.1086/154637

Papa MA et al (2016) Hierarchical follow-up of subthreshold candidates of an all-sky Einstein@Home search for continuous gravitational waves on LIGO sixth science run data. Phys Rev D 94 (12):122006. https://doi.org/10.1103/PhysRevD.94.122006. arXiv:1608.08928 [astro-ph.IM]

Papa MA, Ming J, Gotthelf EV, Allen B, Prix R, Dergachev V, Eggenstein HB, Singh A, Zhu SJ (2020) Search for continuous gravitational waves from the central compact objects in Supernova Remnants Cassiopeia A, Vela Jr., and G347.3–0.5. Astrophys J 897(1):22. https://doi.org/10.3847/1538-4357/ab92a6

Papaloizou J, Pringle JE (1978) Gravitational radiation and the stability of rotating stars. Mon Not R Astron Soc 184:501–508. https://doi.org/10.1093/mnras/184.3.501

Parthasarathy A, Shannon RM, Johnston S, Lentati L, Bailes M, Dai S, Kerr M, Manchester RN, Oslowski S, Sobey C, van Straten W, Weltevrede P (2019) Timing of young radio pulsars-I. Timing noise, periodic modulation, and proper motion. Mon Not R Astron Soc 489(3):3810–3826. https://doi.org/10.1093/mnras/stz2383

Parthasarathy A et al (2020) Timing of young radio pulsars. II. Braking indices and their interpretation. Mon Not R Astron Soc 494(2):2012–2026. https://doi.org/10.1093/mnras/staa882

Paschalidis V, Stergioulas N (2017) Rotating stars in relativity. Living Rev Relativ 20:7. https://doi.org/10.1007/s41114-017-0008-x. arXiv:1612.03050 [astro-ph.HE]

Patel P, Siemens X, Dupuis R, Betzwieser J (2010) Implementation of barycentric resampling for continuous wave searches in gravitational wave data. Phys Rev D. https://doi.org/10.1103/physrevd.81.084032

Patruno A (2017) The slow orbital evolution of the accreting millisecond pulsar IGR J0029+5934. Astrophys J 839(1):51. https://doi.org/10.3847/1538-4357/aa6986

Patruno A, Haskell B, D'Angelo C (2012) Gravitational waves and the maximum spin frequency of neutron stars. Astrophys J 746(1):9. https://doi.org/10.1088/0004-637x/746/1/9

Patruno A, Haskell B, Andersson N (2017) The spin distribution of fast-spinning neutron stars in low-mass X-ray binaries: evidence for two subpopulations. Astrophys J 850(1):106. https://doi.org/10.3847/1538-4357/aa927a. arXiv:1705.07669 [astro-ph.HE]

Pavlov GG, Sanwal D, Kiziltan B, Garmire GP (2001) The compact central source in the RX J0852–4622 supernova remnant. Astrophys J Lett 559:L131. https://doi.org/10.1086/323975. arXiv:astro-ph/0108150

Payne DJB, Melatos A (2004) Burial of the polar magnetic field of an accreting neutron star-I. Self-consistent analytic and numerical equilibria. Mon Not R Astron Soc 351(2):569–584. https://doi.org/10.1111/j.1365-2966.2004.07798.x

Penrose R (1969) Gravitational collapse: the role of general relativity. Riv Nuovo Cim 1:252–276. https://doi.org/10.1023/A:1016578408204, [Gen. Rel. Grav.34,1141(2002)]

Pétri J (2019) The illusion of neutron star magnetic field estimates. Mon Not R Astron Soc 485(4):4573–4587. https://doi.org/10.1093/mnras/stz711. arXiv:1903.01528 [astro-ph.HE]

Piccinni OJ (2022) Status and perspectives of continuous gravitational wave searches. Galaxies. https://doi.org/10.3390/galaxies10030072

Piccinni OJ, Astone P, D'Antonio S, Frasca S, Intini G, Leaci P, Mastrogiovanni S, Miller A, Palomba C, Singhal A (2018) A new data analysis framework for the search of continuous gravitational wave signals. Class Quantum Grav 36(1):015008. https://doi.org/10.1088/1361-6382/aaefb5

Piccinni OJ, Astone P, D'Antonio S, Frasca S, Intini G, La Rosa I, Leaci P, Mastrogiovanni S, Miller A, Palomba C (2020) Directed search for continuous gravitational-wave signals from the Galactic Center in the Advanced LIGO second observing run. Phys Rev D 101(8):082004. https://doi.org/10.1103/PhysRevD.101.082004. arXiv:1910.05097 [gr-qc]

Pierce A, Riles K, Zhao Y (2018) Searching for dark photon dark matter with gravitational-wave detectors. Phys Rev Lett. https://doi.org/10.1103/physrevlett.121.061102

Pierini L, Astone P, Palomba C, Nyquist A, Dall'Osso S, D'Antonio S, Frasca S, La Rosa I, Leaci P, Muciaccia F, Piccinni OJ, Rei L (2022) Impact of signal clusters in wide-band searches for continuous gravitational waves. Phys Rev D 106:042009. https://doi.org/10.1103/PhysRevD.106.042009

Piro AL, Giacomazzo B, Perna R (2017) The fate of neutron star binary mergers. Astrophys J 844(2):L19. https://doi.org/10.3847/2041-8213/aa7f2f

Pisarski A, Jaranowski P (2015) Banks of templates for all-sky narrow-band searches of gravitational waves from spinning neutron stars. Class Quantam Grav 32(14):145014. https://doi.org/10.1088/0264-9381/32/14/145014. arXiv:1302.0509 [gr-qc]

Pisarski A, Jaranowski P, Pietka M (2011) Banks of templates for directed searches of gravitational waves from spinning neutron stars. Phys Rev D 83:043001. https://doi.org/10.1103/PhysRevD.83.043001. arXiv:1010.2879 [gr-qc]

Pitkin M, Reid S, Rowan S, Hough J (2011) Gravitational wave detection by interferometry (ground and space). Living Rev Rel 14:5. https://doi.org/10.12942/lrr-2011-5

Pitkin M, Gill C, Jones DI, Woan G, Davies GS (2015) First results and future prospects for dual-harmonic searches for gravitational waves from spinning neutron stars. Mon Not R Astron Soc 453(4):4399–4420. https://doi.org/10.1093/mnras/stv1931

Pitkin M, Doolan S, McMenamin L, Wette K (2018) Reduced order modelling in searches for continuous gravitational waves-I. Barycentring time delays. Mon Not R Astron Soc 476(4):4510–4519. https://doi.org/10.1093/mnras/sty548

Pletsch HJ (2008) Parameter-space correlations of the optimal statistic for continuous gravitational-wave detection. Phys Rev D 78:102005. https://doi.org/10.1103/PhysRevD.78.102005

Pletsch HJ (2010) Parameter-space metric of semicoherent searches for continuous gravitational waves. Phys Rev D 82:042002. https://doi.org/10.1103/PhysRevD.82.042002. arXiv:1005.0395 [gr-qc]

Pletsch HJ, Allen B (2009) Exploiting global correlations to detect continuous gravitational waves. Phys Rev Lett 103:181102. https://doi.org/10.1103/PhysRevLett.103.181102. arXiv:0906.0023 [gr-qc]

Pletsch HJ, Guillemot L, Allen B, Kramer M, Aulbert C, Fehrmann H, Ray PS, Barr ED, Belfiore A, Camilo F et al (2011) Discovery of nine gamma-ray pulsars in Fermi Large Area Telescope data using a new blind search method. Astrophys J 744(2):105. https://doi.org/10.1088/0004-637x/744/2/105

Popov SB, Postnov KA, Shakura NI (2015) Settling accretion on to isolated neutron stars from interstellar medium. Mon Not R Astron Soc 447(3):2817–2820. https://doi.org/10.1093/mnras/stu2643

Poppenhaeger K, Auchettl K, Wolk SJ (2017) A test of the neutron star hypothesis for Fomalhaut b. Mon Not R Astron Soc 468(4):4018–4024. https://doi.org/10.1093/mnras/stx565

Potekhin AY, Pons JA, Page D (2015) Neutron stars-cooling and transport. Space Sci Rev 191(1–4):239–291. https://doi.org/10.1007/s11214-015-0180-9. arXiv:1507.06186 [astro-ph.HE]

Premachandra SS, Galloway DK, Casares J, Steeghs DT, Marsh TR (2016) Precision ephemerides for gravitational wave searches: II. Cyg X-2. Astrophys J 823(2):106. https://doi.org/10.3847/0004-637X/823/2/106. arXiv:1604.03233 [astro-ph.HE]

Prix R (2007a) Search for continuous gravitational waves: Metric of the multidetector $\mathcal{F}$-statistic. Phys Rev D 75:023004. https://doi.org/10.1103/PhysRevD.75.023004

Prix R (2007b) Template-based searches for gravitational waves: efficient lattice covering of flat parameter spaces. Class Quantum Grav 24(19):S481–S490. https://doi.org/10.1088/0264-9381/24/19/s11

Prix R (2009) Gravitational waves from spinning neutron stars. In: Becker W (ed) Neutron stars and pulsars. Astrophysics and Space Science Library, vol 357. Springer, pp 651–685. https://doi.org/10.1007/978-3-540-76965-1_24

Prix R (2018) The F-statistic and its implementation in ComputeFstatistic_v2. Technical Report LIGO Report T0900149-v6, LIGO. https://dcc.ligo.org/T0900149

Prix R, Itoh Y (2005) Global parameter-space correlations of coherent searches for continuous gravitational waves. Class Quantum Grav 22:S1003. https://doi.org/10.1088/0264-9381/22/18/S14

Prix R, Krishnan B (2009) Targeted search for continuous gravitational waves: Bayesian versus maximum-likelihood statistics. Class Quant Grav 26:204013. https://doi.org/10.1088/0264-9381/26/20/204013. arXiv:0907.2569 [gr-qc]

Prix R, Shaltev M (2012) Search for continuous gravitational waves: optimal stackslide method at fixed computing cost. Phys Rev D 85:084010. https://doi.org/10.1103/PhysRevD.85.084010. arXiv:1201.4321 [gr-qc]

Prix R, Giampanis S, Messenger C (2011) Search method for long-duration gravitational-wave transients from neutron stars. Phys Rev D 84:023007. https://doi.org/10.1103/PhysRevD.84.023007

Raaijmakers G, Riley TE, Watts AL, Greif SK, Morsink SM, Hebeler K, Schwenk A, Hinderer T, Nissanke S, Guillot S, Arzoumanian Z, Bogdanov S, Chakrabarty D, Gendreau KC, Ho WCG, Lattimer JM, Ludlam RM, Wolff MT (2019) A NICER view of PSR J0030+0451: implications for the dense matter equation of state. Astrophys J Lett 887(1):L22. https://doi.org/10.3847/2041-8213/ab451a. arXiv:1912.05703 [astro-ph.HE]

Raaijmakers G, Greif SK, Hebeler K, Hinderer T, Nissanke S, Schwenk A, Riley TE, Watts AL, Lattimer JM, Ho WCG (2021) Constraints on the dense matter equation of state and neutron star properties from NICER's mass-radius estimate of PSR J0740+6620 and multimessenger observations. Astrophys J Lett 918(2):L29. https://doi.org/10.3847/2041-8213/ac089a. arXiv:2105.06981 [astro-ph.HE]

Radhakrishnan V, Srinivasan G (1982) On the origin of the recently discovered ultra-rapid pulsar. Curr Sci 51:1096–1099

Rajbhandari B, Owen BJ, Caride S, Inta R (2021) First searches for gravitational waves from *r*-modes of the Crab pulsar. Phys Rev D 104:122008. https://doi.org/10.1103/PhysRevD.104.122008

Ravenhall DG, Pethick CJ, Wilson JR (1983) Structure of matter below nuclear saturation density. Phys Rev Lett 50:2066–2069. https://doi.org/10.1103/PhysRevLett.50.2066

Ravi V, Lasky PD (2014) The birth of black holes: neutron star collapse times, gamma-ray bursts and fast radio bursts. Mon Not R Astron Soc 441(3):2433–2439. https://doi.org/10.1093/mnras/stu720. arXiv:1403.6327 [astro-ph.HE]

Reardon DJ, Shannon RM, Cameron AD, Goncharov B, Hobbs GB, Middleton H, Shamohammadi M, Thyagarajan N, Bailes M, Bhat NDR, Dai S, Kerr M, Manchester RN, Russell CJ, Spiewak R, Wang JB, Zhu XJ (2021) The Parkes pulsar timing array second data release: timing analysis. Mon Not R Astron Soc 507(2):2137–2153. https://doi.org/10.1093/mnras/stab1990

Reed JE, Hester JJ, Fabian AC, Winkler PF (1995) The three-dimensional structure of the Cassiopeia A Supernova Remnant. I. The spherical shell. Astrophys J 440:706. https://doi.org/10.1086/175308

Reed BT, Deibel A, Horowitz CJ (2021) Modeling the galactic neutron star population for use in continuous gravitational-wave searches. Astrophys J 921(1):89. https://doi.org/10.3847/1538-4357/ac1c04. arXiv:2104.00771 [astro-ph.HE]

Regimbau T, de Freitas Pacheco JA (2006) Gravitational wave background from magnetars. Astron Astrophys 447:1. https://doi.org/10.1051/0004-6361:20053702. arXiv:astro-ph/0509880

Renaud M, Marandon V, Gotthelf EV, Rodriguez J, Terrier R, Mattana F, Lebrun F, Tomsick JA, Manchester RN (2010) Discovery of a highly energetic pulsar associated with IGR J14003–6326 in the young uncataloged galactic supernova remnant G310.6–1.6. Astrophys J 716(1):663–670. https://doi.org/10.1088/0004-637x/716/1/663

Reynolds CS (2014) Measuring black hole spin using X-ray reflection spectroscopy. Space Sci Rev 183(1–4):277–294. https://doi.org/10.1007/s11214-013-0006-6. arXiv:1302.3260 [astro-ph.HE]

Reynolds SP, Borkowski KJ, Green DA, Hwang U, Harrus I, Petre R (2008) The youngest galactic supernova remnant: G1.9+0.3. Astrophys J Lett 680:L41. https://doi.org/10.1086/589570

Riles K (2013) Gravitational waves: sources, detectors and searches. Prog Part Nucl Phys 68:1–54. https://doi.org/10.1016/j.ppnp.2012.08.001. arXiv:1209.0667 [hep-ex]

Riles K (2017) Recent searches for continuous gravitational waves. Mod Phys Lett A 32(39):1730035. https://doi.org/10.1142/S021773231730035X. arXiv:1712.05897 [gr-qc]

Riley TE, Watts AL, Bogdanov S, Ray PS, Ludlam RM, Guillot S, Arzoumanian Z, Baker CL, Bilous AV, Chakrabarty D, Gendreau KC, Harding AK, Ho WCG, Lattimer JM, Morsink SM, Strohmayer TE (2019) A NICER view of PSR J0030+0451: millisecond pulsar parameter estimation. Astrophys J 887(1):L21. https://doi.org/10.3847/2041-8213/ab481c. arXiv:1912.05702 [astro-ph.HE]

Riley TE, Watts AL, Ray PS, Bogdanov S, Guillot S, Morsink SM, Bilous AV, Arzoumanian Z, Choudhury D, Deneva JS, Gendreau KC, Harding AK, Ho WCG, Lattimer JM, Loewenstein M, Ludlam RM, Markwardt CB, Okajima T, Prescod-Weinstein C, Remillard RA, Wolff MT, Fonseca E, Cromartie HT, Kerr M, Pennucci TT, Parthasarathy A, Ransom S, Stairs I, Guillemot L, Cognard I (2021) A NICER view of the massive pulsar PSR J0740+6620 informed by radio timing and XMM-Newton spectroscopy. Astrophys J Lett 918(2):L27. https://doi.org/10.3847/2041-8213/ac0a81. arXiv:2105.06980 [astro-ph.HE]

Roberts MSE, van Leeuwen J (eds) (2013) Neutron stars and pulsars: challenges and opportunities after 80 years, IAU symposium, vol 291. Cambridge University Press

Romani RW (1990) A unified model of neutron-star magnetic fields. Nature 347(6295):741–743. https://doi.org/10.1038/347741a0

Romano JD, Cornish NJ (2017) Detection methods for stochastic gravitational-wave backgrounds: a unified treatment. Living Rev Relativ 20:2. https://doi.org/10.1007/s41114-017-0004-1. arXiv:1608.06889 [gr-qc]

Roy J, Gupta Y, Lewandowski W (2012) Observations of four glitches in the young pulsar J1833–1034 and study of its glitch activity. Mon Not R Astron Soc 424(3):2213–2221. https://doi.org/10.1111/j.1365-2966.2012.21380.x

Ruderman M (1969) Neutron starquakes and pulsar periods. Nature 223(5206):597–598. https://doi.org/10.1038/223597b0

Ruderman MA, Sutherland PG (1975) Theory of pulsars: polar gaps, sparks, and coherent microwave radiation. Astrophys J 196:51–72. https://doi.org/10.1086/153393

Sammut L, Messenger C, Melatos A, Owen BJ (2014) Implementation of the frequency-modulated sideband search method for gravitational waves from low mass X-ray binaries. Phys Rev D 89 (4):043001. https://doi.org/10.1103/PhysRevD.89.043001. arXiv:1311.1379 [gr-qc]

Sanders J (2016) Advanced gravitational wave detectors and detection: arm length stabilization and directed searches for isolated neutron stars. PhD thesis, University of Michigan. https://hdl.handle.net/2027.42/120826

Sancho de la Jordana L (2010) Hierarchical Hough all-sky search for periodic gravitational waves in LIGO S5 data. J Phys: Conf Ser 228:012004. https://doi.org/10.1088/1742-6596/228/1/012004. arXiv:1001.3754 [gr-qc]

Sancho de la Jordana L, Sintes AM (2008) A χ^2 veto for continuous wave searches. Class Quantam Grav 25:184014. https://doi.org/10.1088/0264-9381/25/18/184014. arXiv:0804.1007 [gr-qc]

Sarin N, Lasky PD, Sammut L, Ashton G (2018) X-ray guided gravitational-wave search for binary neutron star merger remnants. Phys Rev D 98(4):043011. https://doi.org/10.1103/PhysRevD.98.043011. arXiv:1805.01481 [astro-ph.HE]

Sarin N, Lasky PD, Ashton G (2020) Interpreting the X-ray afterglows of gamma-ray bursts with radiative losses and millisecond magnetars. Mon Not R Astron Soc 499(4):5986–5992. https://doi.org/10.1093/mnras/staa3090. arXiv:2008.05745 [astro-ph.HE]

Sathyaprakash BS, Dhurandhar SV (1991) Choice of filters for the detection of gravitational waves from coalescing binaries. Phys Rev D 44:3819–3834. https://doi.org/10.1103/PhysRevD.44.3819

Sathyaprakash BS, Schutz BF (2009) Physics astrophysics and cosmology with gravitational waves. Living Rev Rel 12:2. https://doi.org/10.12942/lrr-2009-2

Saulson PR (2017) Fundamentals of interferometric gravitational wave detectors, 2nd edn. World Scientific, Singapore

Sauter O, Dergachev V, Riles K (2019) Efficient estimation of barycentered relative time delays for distant gravitational wave sources. Phys Rev D. https://doi.org/10.1103/physrevd.99.044006

Schutz BF (1985) A first course in general relativity. Cambridge University Press, Cambridge

Schutz BF (1991) Data processing, analysis, and storage for interferometric antennas. In: Blair DG (ed) The detection of gravitational waves. Cambridge University Press, pp 406–452. https://doi.org/10.1017/CBO9780511600104.018

Serim D, Serim MM, Baykal A (2022) Pulse frequency fluctuations of persistent accretion powered pulsars. Mon Not R Astron Soc 518(1):1–12. https://doi.org/10.1093/mnras/stac3076. arXiv:2207.00248 [astro-ph.HE]

Seto N (2005) Gravitational wave astrometry for rapidly rotating neutron stars and estimation of their distances. Phys Rev D 71:123002. https://doi.org/10.1103/PhysRevD.71.123002

Shaltev M (2016) Optimizing the StackSlide setup and data selection for continuous-gravitational-wave searches in realistic detector data. Phys Rev D 93(4):044058. https://doi.org/10.1103/PhysRevD.93.044058. arXiv:1510.06427 [gr-qc]

Shaltev M, Leaci P, Papa MA, Prix R (2014) Fully coherent follow-up of continuous gravitational-wave candidates: an application to Einstein@Home results. Phys Rev D 89(12):124030. https://doi.org/10.1103/PhysRevD.89.124030. arXiv:1405.1922 [gr-qc]

Shapiro SL, Teukolsky SA (1983) Black holes. The physics of compact objects. White Dwarfs and Neutron Stars. Wiley, New York

Shklovskii IS (1970) Possible causes of the secular increase in pulsar periods. Sov Astron 13:562

Siemonsen N, East WE (2020) Gravitational wave signatures of ultralight vector bosons from black hole superradiance. Phys Rev D 101(2):024019. https://doi.org/10.1103/PhysRevD.101.024019. arXiv:1910.09476 [gr-qc]

Sieniawska M, Bejger M (2019) Continuous gravitational waves from neutron stars: current status and prospects. Universe 5(11):217. https://doi.org/10.3390/universe5110217. arXiv:1909.12600 [astro-ph.HE]

Sieniawska M, Jones DI (2021) Gravitational waves from spinning neutron stars as not-quite-standard sirens. Mon Not R Astron Soc 509(4):5179–5187. https://doi.org/10.1093/mnras/stab3315

Sieniawska M, Bejger M, Królak A (2019) Follow-up procedure for gravitational wave searches from isolated neutron stars using the time-domain $\mathcal{F}$-statistic method. Class Quantum Grav 36(22):225008. https://doi.org/10.1088/1361-6382/ab3ee5

Sieniawska M, Jones DI, Miller AL (2023) Measuring neutron-star distances and properties with gravitational-wave parallax. Mon Not R Astron Soc 521(2):1924–1930. https://doi.org/10.1093/mnras/stad624. arXiv:2212.07506 [astro-ph.HE]

Singh A, Papa MA (2023) Opportunistic search for continuous gravitational waves from compact objects in long-period binaries. Astrophys J 943(2):99. https://doi.org/10.3847/1538-4357/acaf80. arXiv:2208.14117 [gr-qc]

Singh A, Papa MA, Eggenstein HB, Walsh S (2017) Adaptive clustering procedure for continuous gravitational wave searches. Phys Rev D 96(8):082003. https://doi.org/10.1103/PhysRevD.96.082003. arXiv:1707.02676 [gr-qc]

Singh A, Papa MA, Dergachev V (2019) Characterizing the sensitivity of isolated continuous gravitational wave searches to binary orbits. Phys Rev D 100(2):024058. https://doi.org/10.1103/PhysRevD.100.024058. arXiv:1904.06325 [gr-qc]

Singh N, Haskell B, Mukherjee D, Bulik T (2020) Asymmetric accretion and thermal 'mountains' in magnetized neutron star crusts. Mon Not R Astron Soc 493(3):3866–3878. https://doi.org/10.1093/mnras/staa442. arXiv:1908.05038 [astro-ph.HE]

Singhal A et al (2019) A resampling algorithm to detect continuous gravitational-wave signals from neutron stars in binary systems. Class Quantam Grav 36(20):205015. https://doi.org/10.1088/1361-6382/ab4367

Sintes AM, Krishnan B (2006) Improved Hough search for gravitational wave pulsars. J Phys: Conf Ser 32:206–211. https://doi.org/10.1088/1742-6596/32/1/031. arXiv:gr-qc/0601081

Slane P, Gaensler BM, Dame TM, Hughes JP, Plucinsky PP, Green A (1999) Nonthermal X-ray emission from the shell-type supernova remnant G347.3–0.5. Astrophys J 525(1):357–367. https://doi.org/10.1086/307893

Smith DA, Bruel P, Cognard I, Cameron AD, Camilo F, Dai S, Guillemot L, Johnson TJ, Johnston S, Keith MJ, Kerr M, Kramer M, Lyne AG, Manchester RN, Shannon R, Sobey C, Stappers BW, Weltevrede P (2019) Searching a thousand radio pulsars for gamma-ray emission. Astrophys J 871(1):78. https://doi.org/10.3847/1538-4357/aaf57d

Soida K, Ando M, Kanda N, Tagoshi H, Tatsumi D, Tsubono K, the TAMA Collaboration (2003) Search for continuous gravitational waves from the SN1987A remnant using TAMA300 data. Class Quantum Grav 20(17):S645–S654. https://doi.org/10.1088/0264-9381/20/17/308

Spitkovsky A (2004) Electrodynamics of pulsar magnetospheres. IAU Symp 218:357 arXiv:astro-ph/0310731

Staelin DH, Reifenstein EC (1968) Pulsating radio sources near the Crab nebula. Science 162(3861):1481–1483. https://doi.org/10.1126/science.162.3861.1481

Starobinskiĭ AA (1973) Amplification of waves during reflection from a rotating "black hole". Soviet J Exp Theor Phys 37:28

Steltner B, Papa MA, Eggenstein HB, Allen B, Dergachev V, Prix R, Machenschalk B, Walsh S, Zhu SJ, Behnke O et al (2021) Einstein@Home all-sky search for continuous gravitational waves in LIGO O2 public data. Astrophys J 909(1):79. https://doi.org/10.3847/1538-4357/abc7c9

Steltner B, Menne T, Papa MA, Eggenstein HB (2022a) Density-clustering of continuous gravitational wave candidates from large surveys. Phys Rev D 106:104063. https://doi.org/10.1103/PhysRevD.106.104063

Steltner B, Papa MA, Eggenstein HB (2022b) Identification and removal of non-Gaussian noise transients for gravitational-wave searches. Phys Rev D 105:022005. https://doi.org/10.1103/PhysRevD.105.022005

Stockinger G et al (2020) Three-dimensional models of core-collapse supernovae from low-mass progenitors with implications for crab. Mon Not R Astron Soc 496(2):2039–2084. https://doi.org/10.1093/mnras/staa1691. arXiv:2005.02420 [astro-ph.HE]

Strader J et al (2019) Optical spectroscopy and demographics of redback millisecond pulsar binaries. Astrophys J 872(1):42. https://doi.org/10.3847/1538-4357/aafbaa. arXiv:1812.04626 [astro-ph.HE]

Strang LC, Melatos A, Sarin N, Lasky PD (2021) Inferring properties of neutron stars born in short gamma-ray bursts with a plerion-like X-ray plateau. Mon Not R Astron Soc 507(2):2843–2855. https://doi.org/10.1093/mnras/stab2210. arXiv:2107.13787 [astro-ph.HE]

Strohmayer T, Mahmoodifar S (2014a) A non-radial oscillation mode in an accreting millisecond pulsar? Astrophys J 784:72. https://doi.org/10.1088/0004-637X/784/1/72. arXiv:1310.5147 [astro-ph.HE]

Strohmayer T, Mahmoodifar S (2014b) Discovery of a neutron star oscillation mode during a superburst. Astrophys J Lett 793(2):L38. https://doi.org/10.1088/2041-8205/793/2/L38. arXiv:1409.2847 [astro-ph.HE]

Sturrock PA (1970) Pulsar radiation mechanisms. Nature 227(5257):465–470. https://doi.org/10.1038/227465a0

Sun L (2018) Hidden Markov model and cross-correlation searches for continuous gravitational waves. PhD thesis, University of Melbourne. http://hdl.handle.net/11343/213141

Sun L, Melatos A (2019) Application of hidden Markov model tracking to the search for long-duration transient gravitational waves from the remnant of the binary neutron star merger GW170817. Phys Rev D 99:123003. https://doi.org/10.1103/PhysRevD.99.123003

Sun L, Melatos A, Lasky PD, Chung CTY, Darman NS (2016) Cross-correlation search for continuous gravitational waves from a compact object in SNR 1987A in LIGO Science run 5. Phys Rev D 94:082004. https://doi.org/10.1103/PhysRevD.94.082004

Sun L, Melatos A, Suvorova S, Moran W, Evans RJ (2018) Hidden Markov model tracking of continuous gravitational waves from young supernova remnants. Phys Rev D. https://doi.org/10.1103/physrevd.97.043013

Sun L, Melatos A, Lasky PD (2019) Tracking continuous gravitational waves from a neutron star at once and twice the spin frequency with a hidden Markov model. Phys Rev D 99:123010. https://doi.org/10.1103/PhysRevD.99.123010

Sun L, Brito R, Isi M (2020) Search for ultralight bosons in Cygnus X-1 with Advanced LIGO. Phys Rev D. https://doi.org/10.1103/physrevd.101.063020

Suvorov AG, Melatos A (2019) Relaxation by thermal conduction of a magnetically confined mountain on an accreting neutron star. Mon Not R Astron Soc 484(1):1079–1099. https://doi.org/10.1093/mnras/sty3518. arXiv:1812.10029 [astro-ph.HE]

Suvorova S, Sun L, Melatos A, Moran W, Evans RJ (2016) Hidden Markov model tracking of continuous gravitational waves from a neutron star with wandering spin. Phys Rev D 93(12):123009. https://doi.org/10.1103/PhysRevD.93.123009. arXiv:1606.02412 [astro-ph.IM]

Suvorova S, Clearwater P, Melatos A, Sun L, Moran W, Evans RJ (2017) Hidden Markov model tracking of continuous gravitational waves from a binary neutron star with wandering spin . II. Binary orbital phase tracking. Phys Rev D 96:102006. https://doi.org/10.1103/PhysRevD.96.102006

Suzuki T (1995) Search for continuous gravitational wave from pulsars with resonant detector. In: Coccia E (ed) First Edoardo Amaldi conference on gravitational wave experiments. World Scientific, p 115

Tan CM, Bassa CG, Cooper S, Dijkema TJ, Esposito P, Hessels JWT, Kondratiev VI, Kramer M, Michilli D, Sanidas S, Shimwell TW, Stappers BW, van Leeuwen J, Cognard I, Grießmeier JM, Karastergiou A, Keane EF, Sobey C, Weltevrede P (2018) LOFAR discovery of a 23.5 s radio pulsar. Astrophys J Lett 866(1):54. https://doi.org/10.3847/1538-4357/aade88.[astro-ph.HE]

Tananbaum H (1999) Cassiopeia A. IAU Circ 7246:1

Tauris TM (2012) Spin-down of radio millisecond pulsars at genesis. Science 335(6068):561–563. https://doi.org/10.1126/science.1216355

Tauris TM, Konar S (2001) Torque decay in the pulsar (P, dot P) diagram. Effects of crustal ohmic dissipation and alignment. Astron Astrophys 376:543–552. https://doi.org/10.1051/0004-6361:20010988

Taylor JH (1992) Pulsar timing and relativistic gravity. Philos Trans A Math Phys Eng Sci 341(1660):117–134. https://doi.org/10.1098/rsta.1992.0088

Tenorio R (2021) An all-sky search in early O3 LIGO data for continuous gravitational-wave signals from unknown neutron stars in binary systems. In: 55th Rencontres de Moriond on Gravitation. arXiv:2105.07455 [gr-qc]

Tenorio R, Keitel D, Sintes AM (2021a) Application of a hierarchical MCMC follow-up to Advanced LIGO continuous gravitational-wave candidates. Phys Rev D 104(8):084012. https://doi.org/10.1103/physrevd.104.084012

Tenorio R, Keitel D, Sintes AM (2021b) Search methods for continuous gravitational-wave signals from unknown sources in the advanced-detector era. Universe. https://doi.org/10.3390/universe7120474

Tenorio R, Keitel D, Sintes AM (2021c) Time-frequency track distance for comparing continuous gravitational wave signals. Phys Rev D 103(6):064053. https://doi.org/10.1103/PhysRevD.103.064053

Tenorio R, Modafferi LM, Keitel D, Sintes AM (2022) Empirically estimating the distribution of the loudest candidate from a gravitational-wave search. Phys Rev D 105(4):044029. https://doi.org/10.1103/PhysRevD.105.044029. arXiv:2111.12032 [gr-qc]

Thorne KS (1980) Multipole expansions of gravitational radiation. Rev Mod Phys 52:299–339. https://doi.org/10.1103/RevModPhys.52.299

Thorne KS (1989) Gravitational radiation. In: Hawking SW, Israel W (eds) Three hundred years of gravitation. Cambridge University Press, Cambridge, p 330

Thorne KS, Zytkow AN (1975) Red giants and supergiants with degenerate neutron cores. Astrophys J 199:L19–L24. https://doi.org/10.1086/181839

Thorstensen JR, Armstrong E (2005) Is FIRST J102347.6+003841 Really a Cataclysmic Binary? Astrophys J 130(2):759–766. https://doi.org/10.1086/431326. arXiv:astro-ph/0504523 [astro-ph]

Thrane E, Kandhasamy S, Ott CD, Anderson WG, Christensen NL, Coughlin MW, Dorsher S, Giampanis S, Mandic V, Mytidis A et al (2011) Long gravitational-wave transients and associated detection strategies for a network of terrestrial interferometers. Phys Rev D. https://doi.org/10.1103/physrevd.83.083004

Thrane E, Mitra S, Christensen N, Mandic V, Ain A (2015) All-sky, narrowband, gravitational-wave radiometry with folded data. Phys Rev D 91:124012. https://doi.org/10.1103/PhysRevD.91.124012

Tiwari V, Drago M, Frolov V, Klimenko S, Mitselmakher G, Necula V, Prodi G, Re V, Salemi F, Vedovato G, Yakushin I (2015) Regression of environmental noise in LIGO data. Class Quantum Grav 32 (16):165014. https://doi.org/10.1088/0264-9381/32/16/165014

Torres MAP, Jonker PG, Steeghs D, Roelofs GHA, Bloom JS, Casares J, Falco EE, Garcia MR, Marsh TR, Mendez M, Miller JM, Nelemans G, Rodriguez-Gil P (2008) Observations of the 599 Hz accreting x-ray pulsar IGR J00291+5934 during the 2004 outburst and in quiescence. Astrophys J 672(2):1079–1090. https://doi.org/10.1086/523831

Treves A, Turolla R, Zane S, Colpi M (2000) Isolated neutron stars: accretors and coolers. Publ Astron Soc Pac 112(769):297

Tse M et al (2019) Quantum-enhanced advanced LIGO detectors in the era of gravitational-wave astronomy. Phys Rev Lett 123:231107. https://doi.org/10.1103/PhysRevLett.123.231107

Tsukada L, Callister T, Matas A, Meyers P (2019) First search for a stochastic gravitational-wave background from ultralight bosons. Phys Rev D 99:103015. https://doi.org/10.1103/PhysRevD.99.103015

Tsukada L, Brito R, East WE, Siemonsen N (2021) Modeling and searching for a stochastic gravitational-wave background from ultralight vector bosons. Phys Rev D 103:083005. https://doi.org/10.1103/PhysRevD.103.083005

University of California B (2002) The Einstein@Home project is built upon the BOINC (Berkeley Open Infrastructure for Network Computing) architecture described at http://boinc.berkeley.edu/

Ushomirsky G, Cutler C, Bildsten L (2000) Deformations of accreting neutron star crusts and gravitational wave emission. Mon Not R Astron Soc 319:902. https://doi.org/10.1046/j.1365-8711.2000.03938.x. arXiv:astro-ph/0001136

Vajente G, Huang Y, Isi M, Driggers JC, Kissel JS, Szczepańczyk MJ, Vitale S (2020) Machine-learning nonstationary noise out of gravitational-wave detectors. Phys Rev D. https://doi.org/10.1103/physrevd.101.042003

Valluri SR, Dergachev V, Zhang X, Chishtie FA (2021) Fourier transform of the continuous gravitational wave signal. Phys Rev D 104:024065. https://doi.org/10.1103/PhysRevD.104.024065

Van Den Broeck C (2005) The gravitational wave spectrum of non-axisymmetric, freely precessing neutron stars. Class Quantum Grav 22(9):1825–1839. https://doi.org/10.1088/0264-9381/22/9/022

van der Putten S, Bulten HJ, van den Brand JFJ, Holtrop M (2010) Searching for gravitational waves from pulsars in binary systems: an all-sky search. J Phys: Conf Ser 228:012005. https://doi.org/10.1088/1742-6596/228/1/012005

Vermeulen SM, Relton P, Grote H, Raymond V, Affeldt C, Bergamin F, Bisht A, Brinkmann M, Danzmann K, Doravari S, Kringel V, Lough J, Lück H, Mehmet M, Mukund N, Nadji S, Schreiber E, Sorazu B, Strain KA, Vahlbruch H, Weinert M, Willke B, Wittel H (2021) Direct limits for scalar field dark matter from a gravitational-wave detector. Nature 600(7889):424–428. https://doi.org/10.1038/s41586-021-04031-y

Viceré A, Yvert M (2016) An autocorrelation method to detect periodic gravitational waves from neutron stars in binary systems. Class Quantum Grav 33(16):165006. https://doi.org/10.1088/0264-9381/33/16/165006

Viets A, Wade M (2021) Subtracting narrow-band noise from LIGO strain data in the third observing run. Technical Report. LIGO Report T2100058, LIGO. https://dcc.ligo.org/T2100058

Vigelius M, Melatos A (2010) Gravitational-wave spin-down and stalling lower limits on the electrical resistivity of the accreted mountain in a millisecond pulsar. Astrophys J 717:404–410. https://doi.org/10.1088/0004-637X/717/1/404. arXiv:1005.2257 [astro-ph.HE]

Viterbi A (1967) Error bounds for convolutional codes and an asymptotically optimum decoding algorithm. IEEE Transact Informat Theory 13(2):260–269

Wade L, Siemens X, Kaplan DL, Knispel B, Allen B (2012) Continuous gravitational waves from isolated Galactic neutron stars in the advanced detector era. Phys Rev D 86:124011. https://doi.org/10.1103/PhysRevD.86.124011

Wagoner RV (1984) Gravitational radiation from accreting neutron stars. Astrophys J 278:345–348. https://doi.org/10.1086/161798

Walsh S et al (2016) Comparison of methods for the detection of gravitational waves from unknown neutron stars. Phys Rev D 94(12):124010. https://doi.org/10.1103/PhysRevD.94.124010. arXiv:1606.00660 [gr-qc]

Walsh S, Wette K, Papa MA, Prix R (2019) Optimizing the choice of analysis method for all-sky searches for continuous gravitational waves with Einstein@Home. Phys Rev D. https://doi.org/10.1103/physrevd.99.082004

Wang L, Steeghs D, Galloway DK, Marsh T, Casares J (2018) Precision ephemerides for gravitational-wave searches-III. Revised system parameters of Sco X-1. Mon Not R Astron Soc 478(4):5174–5183. https://doi.org/10.1093/mnras/sty1441

Watts A, Krishnan B, Bildsten L, Schutz BF (2008) Detecting gravitational wave emission from the known accreting neutron stars. Mon Not R Astron Soc 389:839–868. https://doi.org/10.1111/j.1365-2966.2008.13594.x. arXiv:0803.4097 [astro-ph]

Weltevrede P, Johnston S, Espinoza CM (2011) The glitch-induced identity changes of PSR J1119–6127. Mon Not R Astron Soc 411(3):1917–1934

Weltevrede P, Perera BBP, Preston L, Sanidas S (eds) (2018) Pulsar astrophysics: the next 50 years, IAU symposium, vol 337. Cambridge University Press

Wette K (2012) Estimating the sensitivity of wide-parameter-space searches for gravitational-wave pulsars. Phys Rev D 85:042003. https://doi.org/10.1103/PhysRevD.85.042003. arXiv:1111.5650 [gr-qc]

Wette K (2014) Lattice template placement for coherent all-sky searches for gravitational-wave pulsars. Phys Rev D 90:122010. https://doi.org/10.1103/PhysRevD.90.122010

Wette K (2015) Parameter-space metric for all-sky semicoherent searches for gravitational-wave pulsars. Phys Rev D 92:082003. https://doi.org/10.1103/PhysRevD.92.082003

Wette K (2016) Empirically extending the range of validity of parameter-space metrics for all-sky searches for gravitational-wave pulsars. Phys Rev D 94(12):122002. https://doi.org/10.1103/PhysRevD.94.122002. arXiv:1607.00241 [gr-qc]

Wette K (2021) Geometric approach to analytic marginalisation of the likelihood ratio for continuous gravitational wave searches. Universe 7(6):174. https://doi.org/10.3390/universe7060174. arXiv:2104.14829 [gr-qc]

Wette K, Prix R (2013) Flat parameter-space metric for all-sky searches for gravitational-wave pulsars. Phys Rev D 88:123005. https://doi.org/10.1103/PhysRevD.88.123005

Wette K, Owen BJ, Allen B, Ashley M, Betzwieser J, Christensen N, Creighton TD, Dergachev V, Gholami I, Goetz E, Gustafson R, Hammer D, Jones DI, Krishnan B, Landry M, Machenschalk B, McClelland DE, Mendell G, Messenger CJ, Papa MA, Patel P, Pitkin M, Pletsch HJ, Prix R, Riles K, de la Jordana LS, Scott SM, Sintes AM, Trias M, Whelan JT, Woan G (2008) Searching for gravitational waves from Cassiopeia A with LIGO. Class Quantum Grav 25(23):235011. https://doi.org/10.1088/0264-9381/25/23/235011

Wette K, Walsh S, Prix R, Papa MA (2018) Implementing a semicoherent search for continuous gravitational waves using optimally constructed template banks. Phys Rev D. https://doi.org/10.1103/physrevd.97.123016

Wette K, Dunn L, Clearwater P, Melatos A (2021) Deep exploration for continuous gravitational waves at 171–172 Hz in LIGO second observing run data. Phys Rev D. https://doi.org/10.1103/physrevd.103.083020

Whelan JT, Prix R, Cutler CJ, Willis JL (2014) New coordinates for the amplitude parameter space of continuous gravitational waves. Class Quantam Grav 31:065002. https://doi.org/10.1088/0264-9381/31/6/065002. arXiv:1311.0065 [gr-qc]

Whelan JT, Sundaresan S, Zhang Y, Peiris P (2015) Model-based cross-correlation search for gravitational waves from Scorpius X-1. Phys Rev D 91:102005. https://doi.org/10.1103/PhysRevD.91.102005. arXiv:1504.05890 [gr-qc]

Whitbeck DM (2006) Observational consequences of gravitational wave emission from spinning compact sources. PhD thesis, The Penn State University. https://etda.libraries.psu.edu/catalog/7132

Williams PR, Schutz BF (2000) An Efficient matched filtering algorithm for the detection of continuous gravitational wave signals. In: Meshkov S (ed) Gravitational waves: third Edoardo Amaldi

Conference. AIP Conference Series, vol 523. pp 473–476. https://doi.org/10.1063/1.1291918. arXiv:gr-qc/9912029
Woan G, Pitkin MD, Haskell B, Jones DI, Lasky PD (2018) Evidence for a minimum ellipticity in millisecond pulsars. Astrophys J 863(2):L40. https://doi.org/10.3847/2041-8213/aad86a
Worley A, Krastev PG, Li BA (2008) Nuclear constraints on the moments of inertia of neutron stars. Astrophys J 685(1):390–399. https://doi.org/10.1086/589823
Yamamoto TS, Tanaka T (2021) Use of an excess power method and a convolutional neural network in an all-sky search for continuous gravitational waves. Phys Rev D 103(8):084049. https://doi.org/10.1103/PhysRevD.103.084049. arXiv:2011.12522 [gr-qc]
Yao JM, Manchester RN, Wang N (2017) A new electron-density model for estimation of pulsar and FRB distances. Astrophys J 835(1):29. https://doi.org/10.3847/1538-4357/835/1/29
Yim G, Jones DI (2020) Transient gravitational waves from pulsar post-glitch recoveries. Mon Not R Astron Soc 498(3):3138–3152. https://doi.org/10.1093/mnras/staa2534. arXiv:2007.05893 [astro-ph.HE]
Yoshida S, Yoshida S, Eriguchi Y (2005) R-mode oscillations of rapidly rotating barotropic stars in general relativity: analysis by the relativistic Cowling approximation. Mon Not R Astron Soc 356(1):217–224. https://doi.org/10.1111/j.1365-2966.2004.08436.x
Yoshino H, Kodama H (2014) Gravitational radiation from an axion cloud around a black hole: Superradiant phase. PTEP 2014:043E02. https://doi.org/10.1093/ptep/ptu029. arXiv:1312.2326 [gr-qc]
Yoshino H, Kodama H (2015) The bosenova and axiverse. Class Quantum Grav 32(21):214001. https://doi.org/10.1088/0264-9381/32/21/214001
Yunes N, Miller MC, Yagi K (2022) Gravitational-wave and x-ray probes of the neutron star equation of state. Nat Rev Phys 4(4):237–246. https://doi.org/10.1038/s42254-022-00420-y
Zel'dovich YB (1971) Generation of waves by a rotating body. Sov J Exp Theor Phys Lett 14:180
Zhang B, Harding AK, Muslimov AG (2000) Radio pulsar death line revisited: Is PSR J2144–3933 anomalous? Astrophys J Lett 531:L135–L138. https://doi.org/10.1086/312542. arXiv:astro-ph/0001341
Zhang Y, Papa MA, Krishnan B, Watts AL (2021) Search for continuous gravitational waves from Scorpius X-1 in LIGO O2 data. Astrophys J Lett 906(2):L14. https://doi.org/10.3847/2041-8213/abd256
Zhu SJ, Papa MA, Eggenstein HB, Prix R, Wette K, Allen B, Bock O, Keitel D, Krishnan B, Machenschalk B, Shaltev M, Siemens X (2016) Einstein@Home search for continuous gravitational waves from Cassiopeia A. Phys Rev D 94:082008. https://doi.org/10.1103/PhysRevD.94.082008
Zhu SJ, Papa MA, Walsh S (2017) New veto for continuous gravitational wave searches. Phys Rev D 96(12):124007. https://doi.org/10.1103/PhysRevD.96.124007. arXiv:1707.05268 [gr-qc]
Zhu SJ, Baryakhtar M, Papa MA, Tsuna D, Kawanaka N, Eggenstein HB (2020) Characterizing the continuous gravitational-wave signal from boson clouds around Galactic isolated black holes. Phys Rev D. https://doi.org/10.1103/physrevd.102.063020
Zimmermann M (1978) Revised estimate of gravitational radiation from Crab and Vela pulsars. Nature 271(5645):524–525. https://doi.org/10.1038/271524a0
Zimmermann M, Szedenits E (1979) Gravitational waves from rotating and precessing rigid bodies: simple models and applications to pulsars. Phys Rev D 20:351–355. https://doi.org/10.1103/PhysRevD.20.351
Zweizig J, Riles K (2021) Information on self-gating of $h(t)$ used in O3a continuous-wave searches. Technical Report. LIGO Report T2000384, LIGO. https://dcc.ligo.org/T2000384